Ludwig-Maximilians-Universität

Sigillum Universitatis Ludovici Maximiliani

Probing Early Dark Energy and primordial non-Gaussianity with cosmological simulations

Dissertation der Fakultät für Physik

der Ludwig-Maximilians-Universität München

für den Grad des

Doctor rerum naturalium

vorgelegt von Margherita Grossi

presented by / presentata da

aus Atina (Italien)

from / da

München, 9.12.2009

Sigillum Universitatis Ludovici Maximiliani

1. Gutachter: Prof. Dr. Simon D. M. White

2. Gutachter: Prof. Dr. Jochen Weller

Tag der mündlichen Prüfung: 5.2.2010

Ai miei genitori

Contents

List of Figures

List of Tables

Zusammenfassung

Die Dichteverteilung der Materie im Universum bestimmt nicht nur die fundamentalen Parameter kosmologischer Modelle, sondern gibt auch Aufschluß über die physikalischen Prozesse, die zur Bildung der kosmischen Strukturen und Galaxien führen. Die Entwicklung des ersten präzisen kosmologischen Modells, des ΛCDM Modells, ist eine bedeutende Errungenschaft der modernen, beobachtenden Kosmologie. Trotzdem bleiben eine Reihe von wichtigen Fragen über Zusammensetzung und Entwicklungsgeschichte des Universums unbeantwortet: Abgesehen von der Natur der Dunklen Materie ist der physikalische Ursprung der Dunklen Energie eine der ganz großen Fragen der theoretischen Physik. Ebenso bedürfen die statistischen Eigenschaften der anfänglichen Dichtefluktuationen im frühen Universum einer genauen Überprüfung. Kleinste Abweichungen von den Gauß'schen Fluktuationen des Standardmodells würden, sofern sie nachgewiesen werden, eine Vielzahl von Informationen über die Physik des frühen Universums enthalten. In dieser Arbeit benutze ich numerische Verfahren, um neue, hochpräzise Vorhersagen zur kosmischen Strukturbildung in generalisierten Dunkle Energie Kosmologien zu treffen. Außerdem berücksichtige ich Modelle mit nicht - Gauß'schen Anfangbedingungen.

Im ersten Abschnitt untersuche ich die nicht-lineare Strukturentstehung in sogenannten "Early Dark Energy" (EDE) Modellen und vergleiche sie mit dem ΛCDM Standardmodell. In diesen EDE Szenarien beeinflußt die Dunkle Energie die Strukturentstehung besonders stark, da sie, anders als in Modellen mit zeitabhängiger Zustandsgleichung, bereits bei hohen Rotverschiebungen dynamisch nicht vernachlässigbar ist. Interessanterweise zeigen meine Ergebnisse, dass der Sheth and Tormen (1999) Formalismus, mit dem üblicherweise die Anzahldichte von Halos aus Dunkler Materie geschätzt wird, in EDE Kosmologien weiterhin anwendbar ist, im Widerspruch zu analytischen Berechnungen. Dies zeigt, dass Simulationen einen wichtigen Beitrag zu unserem Verständnis von kosmologischen Modellen mit generalisierter Dunkler Energie liefern können. In diesem Zusammenhang untersuche ich auch das Verhältnis zwischen Masse und Geschwindigkeitsdispersion der Dunklen Materie in Halos. Dabei finde ich eine gute Übereinstimmung mit der Normalisierung der ΛCDM Kosmologien, wie sie in Evrard et al. (2008) beschrieben ist. Allerdings führt das frühere Anwachsen der Dichtestrukturen in EDE Modellen zu großen Unterschieden in der Massenfunktion der Halos bei hohen Rotverschiebun-

gen. Dies könnte direkt in Beobachtungen gemessen werden, indem man die Anzahl der Gruppen als Funktion der Geschwindigkeitsdispersion der enthaltenen Galaxien entlang der Sichtlinie bestimmt. Insbesondere würde dadurch das Problem der mehrdeutigen Massebestimmung von Halos umgangen. Schließlich ermittele ich die Beziehung zwischen dem Konzentrationsparameter von Halos und der Halomasse in den EDE Kosmologien. Hier finde ich, dass sich die Differenz der Konzentrationen relativ zu denen in der ΛCDM Kosmologie gut durch den von Eke et al. (2001) vorgeschlagenen Formalismus beschreiben läßt.

Der zweite Teil meiner Arbeit widmet sich beobachtbaren Effekten, die sich besonders gut zum Test kosmologischer Modelle eignen: den globalen Eigenschaften der thermischen und kinetischen Sunyaev Zeldovich (SZ) Effekte. Unter Verwendung einer Reihe von hochaufgelösten hydrodynamischen Simulationen berechne ich künstliche SZ-Beobachtungskarten für eine Reihe alternativer Kosmologien, die zu frühen Zeiten mehr Galaxienhaufen aufweisen aber heute die gleiche Normalisierung wie ΛCDM haben. Dabei zeigen meine Ergebnisse, dass in den EDE Modellen der jeweils über die gesamte Karte gemittelte Compton-y-Parameter systematisch größer ist als im ΛCDM Modell. Während dort der Hauptteil des Signals von Rotverschiebungen kleiner als 1 kommt, weisen die Karten in den EDE Modellen nicht vernachlässigbare Beiträge auch bei sehr hohen Rotverschiebungen auf. Erwartungsgemäß finde ich daher auch, dass das Leistungsspektrum der thermischen und kinetischen SZ Fluktuationen in EDE Kosmologien größer ist als im Standardmodell. Allerdings reicht diese Steigerung für realistische EDE Modelle nicht aus, um die theoretischen Voraussagen in Übereinstimmung mit aktuellen Messungen der Mikrowellenhintergrundanisotropie bei großen Multipolwerten zu bringen. Eine Zählung der durch den SZ Effekt detektierbaren Halos in den simulierten Karten zeigt nur einen leichten Anstieg in den massereichsten Haufen für EDE Kosmologien. Nur eine Beschränkung der Stichprobe auf hohe Rotverschiebungen führt zu ausgeprägten Unterschieden zwischen den Modellen. Ebenso sind Voraussagen für zukünftige Zählungen von SZ-detektierten Haufen durch das South Pole Telescope (SPT Ruhl, 2004) stark durch Unsicherheiten in der Kosmologie beeinträchtigt. Das trifft insbesondere auf den kombinierten Effekt von Variationen in σ_8, h und Ω_M zu, der den Unterschied zwischen kosmologischen Modellen mit unterschiedlichen Dunkle Energie Szenarien mühelos übertrifft. Schließlich finde ich, dass die Normalisierung und die Steigung der Relation zwischen thermischem SZ-Effekt und Halomasse in vielen EDE Kosmologien unverändert bleibt, was die Interpretation von Beobachtungen des SZ Effekts in Galaxienhaufen vereinfacht.

In weiteren Untersuchungen berechne ich eine Reihe von hochaufgelösten Vielteilchensimulationen für physikalisch motivierte nicht - Gauß'sche Kosmologien. Dabei folge ich der Standardprozedur, in der die nicht - Gauß'schen Merkmale in die Anfangsverteilung durch einen quadratischen Term im primordialen Gravitationspotenzial realisiert werden. Hierbei bestimmt ein dimensionsloser Nichtlin-

earitätsparameter f_{NL} die Stärke des Effekts in den unterschiedlichen Modellen. In umfangreichen Studien untersuche ich die Massenverteilungsfunktion der Halos und deren Entwicklung in nicht - Gauß'schen Modellen. Zudem vergleiche ich meine numerischen Experimente mit analytischen Vorhersagen von Matarrese et al. (2000) und Lo Verde et al. (2008). Dabei finde ich eine sehr gute Übereinstimmung zwischen Simulation und analytischer Vorhersage, vorausgesetzt bestimmte Korrekturen für die Dynamik des nicht-sphärischen Kollapses werden berücksichtigt. Dazu werden die Vorhersagen dahingehend modifiziert, dass sie im Grenzfall sehr seltener Ereignisse einem geeignet veränderten Grenzwert der kritischen Dichte entsprechen. Desweiteren bestätige ich jüngste Ergebnisse, nach denen primordiale nicht - Gauß'sche Dichtefluktuationen eine starke skalenabhänginge Verzerrung auf großen Skalen verursachen, und ich lege einen physikalisch motivierten mathematischen Ausdruck vor, der es erlaubt, die Verzerrung zu messen und der eine gute Näherung für die Simulationsergebnisse darstellt. Die gefundene Korrektur hat zudem wichtige Auswirkungen auf in früheren Arbeiten vorhergesagte Schranken für Modelle mit nicht - Gauß'schen Dichtefluktuationen.

Summary

The large-scale structure of the Universe encodes information about the fundamental cosmological parameters and the physical processes governing the formation of cosmic structures and galaxies. The development of the first precision cosmological model, now known as ΛCDM, is a major achievement in modern observational cosmology. However, there remain a number of open questions regarding the basic history and composition of the Universe. Besides the unknown nature of dark matter, the physical origin of dark energy represents a major puzzle for theoretical physics. Many phenomenological field-theoretical models suggest that dark energy should not behave like a cosmological constant, but rather change its equation of state slowly over time. The hope is that upcoming observations will be able to constrain this evolution, and assist in theoretical studies of the physical nature of dark energy.

A prerequisite for the correct interpretation of observational data and hence, for the successful constraint of dark energy, is the calculation of structure formation in dark energy cosmologies with sufficient precision to tell the different models apart. Similarly, the statistical nature of the initial perturbations in the Universe needs to be investigated with great care, because even small deviations from Gaussianity, if detected, would contain rich information about the physics of the early universe. In particular, the occurrence of massive objects at early epochs provides an important observational test for non-Gaussian models. This explains the recently renewed interest in studying deviations from Gaussianity in the primordial density field.

Numerical N-body simulations are arguably the most accurate tool available to study structure formation in cosmology, since they are largely free of simplifying assumptions (apart from numerical limitations) and allow high accuracy calculations also in the non-linear regime of structure formation. Simulations are also crucial for testing the results of more simplified analytic treatments and for the interpretation of future large galaxy cluster surveys at high redshift. Therefore, we extensively use numerical methods for obtaining new, high-precision predictions for cosmic structure formation in generalized dark energy cosmologies, and in models that contain non-Gaussianity in their initial conditions. The primary goal of our research is to explore the link between theory and observations in physically motivated non-standard models and to work on cosmological tests relevant to probe the nature of

13

dark energy.

In the first part of this Thesis we focus on the study of non-linear structure formation in high-resolution simulations of Early Dark Energy (EDE) cosmologies, and we compare their evolution with the standard ΛCDM model. In EDE models, the impact of dark energy on structure formation is expected to be particularly strong because of the presence of a non-negligible dark energy component even at very high redshift, unlike in most other alternative models with a time-varying equation of state. An interesting consequence of EDE is that extensions of the spherical top-hat collapse model predict that the virial overdensity and linear threshold density for collapse should be modified, yielding significant differences in the expected halo mass function based on the Press and Schechter (1974) or Sheth and Tormen (1999) formalisms. Interestingly, we found that the Sheth and Tormen (1999) formalism for estimating the abundance of dark matter halos continues to work very well in its standard form for the EDE cosmologies, contrary to the analytic expectations. This highlights the importance of simulations for understanding even basic phenomena in generalized dark energy scenarios. With regards to the halo properties, we study the virial relationship between mass and dark matter velocity dispersion in different dark energy cosmologies, finding excellent agreement with the normalization for ΛCDM as calibrated by Evrard et al. (2008). However, the earlier growth of structure in EDE models, relative to the standard model, produces large differences in mass functions at high redshift. This could be measured directly by counting groups as a function of the line-of-sight velocity dispersion of their member galaxies, skirting the ambiguous problem of assigning a mass to the halo. Finally, we determine the concentration-mass relationship for our EDE cosmologies. Consistent with the expectation due to their earlier formation time, the EDE halos show higher concentrations at a given halo mass. We find that the magnitude of the difference in concentration is well described by the model of Eke et al. (2001) for estimating halo concentrations.

The second part of the Thesis is dedicated to the study of one particular cosmological probe in more detail, namely the global properties of the thermal and kinetic Sunyaev Zeldovich (SZ) effects. In fact, the SZ effect is presently actively pursued as a promising method to constrain the properties of an early dark energy component, and might provide complementary information on the expansion rate of the Universe through the study of baryon physics. Using a set of high-resolution hydrodynamical simulations, we create mock SZ maps for a wide range of alternative cosmologies that predict higher cluster abundance at early times but have the same normalization today. We observe that the value of the Comptonization y-parameter averaged over the total maps is systematically higher in the EDE models. Whereas in the ΛCDM case most of the signal comes from redshifts smaller than one, in the EDE cases the contribution is non-negligible up to very high redshift. We consistently confirm the expectation that also the levels of the thermal and kinetic SZ power

in the EDE cosmologies are higher than in the standard model, but the increase in viable models is not yet consistent with current measurements of CMB anisotropy at high multipole values. The enhancement in the thermal SZ maps is the direct manifestation of the boosted cluster abundance in generalized dark energy models. However, examining the plain number counts of SZ detected halos in the simulated maps, we estimate only a slight increase in the number counts for the EDE cosmologies for the most massive halos. Only when the analysis is restricted to high redshift clusters, the differences in the distribution become really pronounced. This result suggests that a promising strategy for obtaining stringent constraints on the dark energy is to perform deep cluster surveys together with optical follow-up in order to determine redshift estimates for a large number of clusters. All the same, forecasts for future measurements of the SZ number counts as the one carried out with the South Pole Telescope (SPT Ruhl, 2004), will be strongly limited by the uncertainties due to the cosmology, in particular the combined effects of variations in σ_8, h and Ω_M, that can easily overcome the differences due to the dark energy physics. Finally, we use the simulated SZ maps in order to fine-tune the known scaling relation, in particular the thermal SZ-mass correlation, in the EDE cosmologies and improve their prediction. We find that the slope and normalization of the relation remains unchanged over a wide range of EDE cosmologies, simplifying the interpretation of observations of SZ clusters.

As a complementary line of investigation, we perform high resolution N-body simulations of physically motivated non-Gaussian cosmologies in order to study the formation and evolution of structures in the non-linear regime, and to compare, in detail, with the concordance ΛCDM model. Following a standard procedure, we model the specific non-Gaussian features imprinted on the initial distribution of particles through a quadratic Gaussian term in the primordial gravitational potential. In this scenario, a dimensionless non-linearity parameter, $f_{\rm NL}$, quantifies the magnitude of the effect in the different models. According to our convention, positive values of $f_{\rm NL}$ are responsible for an increased occurrence of massive objects at every redshift, due to the anticipated onset of the non-linear regime of clustering. However, the validity of theoretical extrapolations to the non-Gaussian case needs to be tested in details. In the third part of this Thesis, we extensively investigate the halo mass function and its evolution in non-Gaussian models and compare the outcome of our numerical experiments to analytic predictions by Matarrese et al. (2000) and Lo Verde et al. (2008). We find that correcting for non-spherical collapse dynamics yields excellent agreement between the simulations and the analytic predictions. The effect can be accounted for by modifying the theoretical predictions in such a way that, in the rare events limit, they correspond to a suitable modified critical density threshold for collapse. We also perform numerical tests to study analytical descriptions of the halo clustering. We confirm the recent claim (Dalal et al., 2008) that primordial non-Gaussianity induces a strong scale-dependent bias on large scales and we provide the reader with a physically motivated mathematical

expression to measure it, which provides good fits to the simulated data. The correction we find has implications for previously reported and forecasted constraints on non-Gaussianity. Nevertheless we can safely state that the non-Gaussian halo bias offers a robust and highly competitive test of primordial non-Gaussianity of the local type.

1

The standard cosmological model and beyond

1.1 Introduction

One hundred years ago our picture of the Universe was that of a small, young, static cosmos. Today we know that we inhabit an evolving Universe filled with billions of galaxies in our sphere of observation, all held together by dark matter, an invisible component whose presence is only known through its gravitational effect. Moreover, the optical light we receive from distant galaxies allows us to observe the Universe in different epochs of its evolution: the more distant we watch, the younger are the cosmic structures we can see. This peculiarity suggests that we can understand the origin of the Universe and predict its future by simply applying the laws of physics starting from the present configuration. In brief, the most surprising achievement of all is the awareness that the cosmos, even if huge, is finite in a well definite way, therefore it can be comprehensively studied despite the standard rule of science, the repeatability, cannot be applied to cosmology.

The attempt to reach such a complete description led in the 1960s to the so called hot *Big Bang* scenario, which provides a quantitative understanding of a great part of the history of the Universe, from a fraction of a second after the beginning (t$\approx 10^{-2} - 10^2$ sec) until the present epoch (t≈ 15 Gyr). The basic idea is that the Universe has expanded from a primordial hot and dense initial condition at some finite time in the past, and continues to expand to this day. The attribute "hot" makes fundamental physics an inseparable part of standard cosmology, since the history of the Universe starts from singularities and temperatures well beyond our laboratory access and carries information on the strongest and weakest forces

in Nature.

Our ability to study the Universe has improved dramatically also from the observational point of view. A century ago the only window on the cosmos consisted of visible images taken from photographic plates using small aperture telescopes. Today, we observe the Universe with eyes that are sensitive from the radio waves to gamma rays energy. Moreover, rapid advances in technologies such as detectors, telescopes, and observatories on the ground and in space, have given us a rough picture of what happened as our cosmos evolved from a quite simple state early on to its present complexity. A substantial body of observations supports directly or indirectly the hot Big Bang model. Equally important, there are no data that are inconsistent.

A few characteristics hold that we can briefly remind here. The Universe is essentially electrically neutral and its large scale dynamics is governed by gravity; it is nearly in thermal equilibrium and the geometry of the space is maximally symmetrical. However, this symmetry does not expand to space-time. Indeed, the most important cosmological discovery in 20th century was certainly the observation of the cosmic expansion of space: that is, we do not live in a steady state Universe.

To understand what kind of laws shape the cosmos and its contents, the answer from the time of Galileo onwards has to be essentially dynamics, which is the specification of how a system will develop with time. Therefore, a mathematical description of the laws of dynamics tells us how the system will evolve into the future, from data specified in the past. Starting from this approach, the results would depend only on a small number of parameters: namely, the composition of the Universe, its current expansion rate and the initial distribution of matter. To precisely determine these quantities has become a main issue in cosmology.

Recent cosmological observations of unprecedented accuracy by the WMAP satellite have measured the material and energetic content of the Universe and established a *Standard Model* of cosmology, which we will discuss extensively in this Chapter. Despite many successes, the Standard Model of cosmology is still unsatisfactory. Just like the Standard Model of particle physics, it fits almost all the data in its respective field, but it is equally incomplete, since it leaves important questions about the origin and evolution of the Universe unanswered. This thesis addresses our current knowledge of these aspects and our prospects for exploring them in details.

One of the most important statements of the Standard Model is that ordinary matter, that is everything we can directly observe, accounts for only a few percent of the total Universe content. Almost a quarter of the matter in our cosmos is made of dark matter, an invisible component that manifests itself through its gravitational influence. The missing and predominant component is a very mysterious substance called dark energy. This unexpected prediction was made with the discovery that the Universe is expanding at approximately twice the velocity required to overcome

the gravitational pull of all the matter contained. Today, the nature of the dark energy along with the ultimate fate of our Universe, are two of the greatest unsolved mysteries faced by modern astrophysicists. Will this expansion continue at its current rate, will it stop or maybe even reverse? These are a number of questions that need to be explored.

The simplest interpretation, the Standard Cosmological Model or ΛCDM, requires this dark component to have been negligible in early stages of the evolution of our Universe. It has become important only recently, in the last 5 billion years or so, allowing the formation of galaxies and life on Earth. It is especially difficult to deal with such a cosmic coincidence: we happen to be living at the exact time when dark energy has become important. These considerations, combined with the uncertainty of the actual nature of cosmic acceleration, show the importance of studying alternative cosmological models. In particular, in this Thesis we will explore the possibility that dark energy properties are evolving with time in physically motivated theories and try to set up cosmological tests to distinguish the plethora of existing theoretical models.

Another open question is the character and the origin of the inhomogeneities that give rise to the observable Universe. According to the theory of structure formation, the high level of clustering proper to the distribution of matter in the Universe is a late-time consequence of a process of gravitational instability which started over initial irregularities in the primordial density field. However, the Standard Cosmological Model does not account for the origin of such primordial fluctuations, whose existence is raised to a postulate. The complementary theory of Cosmological Inflation, besides releasing the Standard Model from the embarrassing sensitivity to its initial conditions, provides a natural explanation to the origin of these seed fluctuations: in this context, they arise as quantum-mechanical fluctuations in the inflaton. Other perceived benefits of the proposed inflationary period is that it can provide an explanation of the remarkable uniformity of the matter distribution and space-time geometry and the thermalization of far distant regions in the Universe. The idea is that, with inflation, the initial state of the Universe might have been very irregular in details, but the enormous expansion during the inflationary stage would have served to iron out these irregularities. A closely flat and uniform universe is thereby anticipated.

When treating the issue of cosmological perturbations within linear perturbation theory, the response on the statistical features of initial perturbations is straightforward: they are Gaussian. This hypothesis has so far been used as a standard starting point in the study of structure formation, due also to the advantages provided by assuming such a simple statistics. However, it is possible that some departures from Gaussianity were already present in the early stage of evolution. This is a possibility we will pursue in this Thesis. The study of primordial non-Gaussianity stands out as a key instrument to discriminate among competing models for the generation of

the seed fluctuations and thus can provide us with a rare glimpse into the nature of the initial conditions of the Universe.

To conclude, the Standard Model of cosmology is today a widely accepted idea. However, we cannot yet demonstrate that there is not other physics, applied to cosmology, that equally well agrees with cosmological tests and observational data. Therefore, we still need to carefully check the Inflation $+ \Lambda$CDM model as to demonstrate whether those models are a convincing approximation to the way the world really is.

In the remainder of this Chapter we review the foundations of cosmology which are relevant for the following discussion on the structure formation in non-standard cosmological models. In Section 2 we introduce the current cosmological model based on the cosmological principle and we define the dynamics and the evolution of the Universe by means of the Friedmann equations and the cosmological parameters. We introduce the concept of distance in cosmology and we discuss observational evidences in Section 3. Section 4 is completely dedicated to the currently favoured model of structure formation, illustrating both the results of the linear theory of perturbations and the spherical collapse model. Moreover, numerical simulations are presented as a fundamental tool in the investigation of the non-linear regime. The problems of the Standard Cosmological Models are summarized in Section 5, while Section 6 focuses on the inflationary solutions. Finally, we introduce non-standard cosmology characterized by the presence of primordial non-Gaussianity (Section 6.1) and dynamical dark energy, with particular attention to early dark energy models (Section 7). A brief outline of the Thesis contents concludes the Chapter (Section 8).

1.2 The homogeneous and isotropic universe

The basic assumption of modern cosmology is that the Universe is *homogeneous* (constant density) and *isotropic* (the same in every direction), when observed on sufficiently large scales, bigger than several hundred Mpc or so. This idea was proposed by Einstein for the first time, not really on the basis of observations, but to simplify the mathematical analysis and to restrict the range of the possible cosmological predictions. In fact, he shared Mach's firm belief that the physical laws are determined by the distribution and the motion of matter on large scale.

In 1933, Milne discovered that this idea, immediately named the *Cosmological Principle*, has as a direct consequence the Hubble expansion law. If we consider, for example, an observer surrounded by isotropically distributed matter, we can notice that the density of the mass surrounding him is only a function of radius. Thus the only velocity field allowed is an expansion (or contraction) with velocity

$\vec{v}$ proportional to the distance $\vec{r}$, according to

$$\vec{v} = H\vec{r}. \qquad (1.1)$$

The Hubble parameter $H = \dot{a}/a$ describes how fast the most distant galaxies are receding from us, and its value at present can be parametrized as $H_0 = 100h$ km/s/Mpc, where h is a dimensionless fudge factor that we will largely use in many quantitative results in this work. Recent measurements, done by the Hubble Space Telescope Key Project on the extragalactic scale, give $h = 0.72 \pm 0.08$ (Freedman et al., 2001), which is consistent with other methods (e.g. Freedman, 2000; Riess et al., 2009); for a review see Jackson (2007). The value of h is confirmed to be about 0.7 also in the analysis of the WMAP data ($H_0 = 70.5 \pm 1.3$ km/s/Mpc; Komatsu et al., 2009a). The Hubble parameter is very important because it allows to establish a time scale for the expansion of the Universe, $t_H = 1/H_0 \approx 14$ billion years, consistent with recent age estimates of the Universe.

Today, the best evidence for the validity of the cosmological principle is the uniformity of the temperature of the Cosmic Microwave Background, whose spectrum is consistent with a black body with temperature 2.725K and does not present any significant anisotropy. Therefore we can infer that, at the epoch when the background was generated (about 380.000 years after the Big Bang), the Universe was homogeneous and isotropic at a higher degree of precision (of the order 10^{-5}).

The form of the space-time metric is determined if one adopts a coordinate system that accounts for homogeneity and isotropy. From General Relativity, the space-time must admit a slicing in space-like hypersurfaces which are homogenous and isotropic on large scale. We can then define a preferred geodesic time coordinate, which is called the cosmic time t, and can be identified as a global time variable. The more general space-time interval $\mathrm{d}s^2$ can be expressed in the following way:

$$\mathrm{d}s^2 = g_{ij}\mathrm{d}x^i\mathrm{d}x^j = g_{00}\mathrm{d}t^2 + 2g_{0i}\mathrm{d}t\mathrm{d}x^i - \sigma_{ij}\mathrm{d}x^i\mathrm{d}x^j, \qquad (1.2)$$

where g_{ij} represents the metric tensor that describes the space-time geometry, the index 0 refers to the time components, while σ_{ij} is a defined spatial metric (the space isotropy implies that all terms g_{0i} are null). From simple geometric considerations one can demonstrate that the only metric compatible with the Hubble discovery and the cosmological principal is the *Friedmann-Lemaître-Robertson-Walker metric* (FLRW), described by the line element:

$$\mathrm{d}s^2 = (c\,\mathrm{d}t)^2 - a^2(t)\left[\frac{\mathrm{d}r^2}{1 - Kr^2} + r^2\left(\mathrm{d}\theta^2 + \sin^2\theta\mathrm{d}\phi^2\right)\right], \qquad (1.3)$$

where we used the polar spherical coordinates: r, θ, ϕ. The distance between two points depends only for the functional form of $a(t)$, called *expansion factor* or *scale factor of the Universe*, while the space curvature is constant and is determined by

the value of the *curvature parameter* K in units of inverse length square. The scale factor can be renormalized to be unity today, so we can write $a(t_0) = 1$. Since a random displacement of the line element does not affect K, we adopt the following convention for the global geometry of the Universe:

- $K = +1$ denotes a spherical geometry with a positive curvature;

- $K = 0$ denotes flat Minkowski space, or Eulerian space;

- $K = -1$ denotes hyperbolic geometry with negative curvature.

The Friedmann's universes with $K = -1$, 0 and $+1$ are called open, flat and closed, respectively, according to the topological nature of the three-dimensional space traced by them.

The dynamics of the expanding Universe is embodied in the cosmic scale factor $a(t)$, which describes the scaling up of all physical distances in the Universe (like separations of galaxies and wavelengths of photons). Since the scale factor $a(t)$ grows with time, i.e. the Universe is expanding, the wavelength of the radiation produced by photons emitted from a distant source seems shifted towards lower frequencies with respect to the radiation of nearer objects. We define the *redshift z* as:

$$z \equiv \frac{a(t_0)}{a(t_e)} - 1 = \frac{\lambda_0}{\lambda_e} - 1 = \frac{\Delta\lambda}{\lambda_e}, \tag{1.4}$$

where λ_0 is the observed wavelength and λ_e is the wavelength of the emitted radiation. The redshift is a convenient label for epochs in the Universe, as it directly encodes a certain age (t_e) of the Universe, so we will frequently use it as a convenient time variable. We note that z exceeds unity for the early universe, making it clear that the cosmological redshift can not be interpreted as a simple Doppler shift.

1.2.1 Friedmann Equations and Cosmological Constant

The equations of motion for the scale factor can be obtained by inserting the FLRW metric in the field equations of general relativity. This yields:

$$R_{ij} - \frac{1}{2}g_{ij}R = \frac{8\pi G}{c^4}T_{ij}, \tag{1.5}$$

where R_{ij} and R are, respectively, the Ricci tensor and the Ricci scalar. The quantity T_{ij} is the stress-energy tensor, which describes the distribution of the matter and energy density. For a perfect fluid characterized by a pressure $p(t)$ and energy density $\rho(t)$, this term reads

$$T_{ij} = \left(p + \rho c^2\right) U_i U_j - p g_{ij}, \tag{1.6}$$

where the vector U_i is the four-velocity of the fluid and g_{ij} are the components of the metric tensor.

Solving (1.5), we obtain the following set of ordinary differential equations, one for the temporal component:

$$\ddot{a} = -\frac{4\pi}{3} G \left(\rho + 3\frac{p}{c^2} \right) a, \tag{1.7}$$

and three identical ones for the spatial components:

$$a\dot{a} + 2\dot{a}^2 + 2Kc^2 = 4\pi G \left(\rho - \frac{p}{c^2} \right) a^2. \tag{1.8}$$

These so-called *Friedmann equations* completely determine the background time-evolution of the Universe. The two relations (1.7 and 1.8) are not independent, and applying the condition of adiabatic expansion, we can rewrite equation (1.8) in the following form:

$$\left(\frac{\dot{a}}{a_0} \right)^2 - \frac{8\pi}{3} G\rho \left(\frac{a}{a_0} \right)^2 = -\frac{Kc^2}{a_0^2}, \tag{1.9}$$

which allows to recover the scale factor $a(t)$[1]. However, these equations lead to a contradiction when we consider a static solution: either the pressure or the energy density should be negative in this case, since

$$\rho = -\frac{3p}{c^2}, \tag{1.10}$$

which is called Strong Energy Condition.

In an attempt to reconcile the theory with the, at the time popular, idea of a static Universe, Einstein modified in 1917 his original field equations and introduced a cosmological term proportional to the metric, the cosmological constant[2] Λ:

$$R_{ij} - \frac{1}{2} g_{ij} R - \Lambda g_{ij} = \frac{8\pi G}{c^4} T_{ij}. \tag{1.11}$$

Consequently, also the Friedmann equations must be modified, replacing p and ρ with an effective pressure, $\tilde{p} = p - \Lambda c^4/(8\pi G)$, and an effective density, $\tilde{\rho} = \rho + \Lambda c^2/(8\pi G)$, so that:

$$\ddot{a} = -\frac{4\pi}{3} G \left(\rho + 3\frac{p}{c^2} \right) a + \frac{\Lambda}{3} c^2 a, \tag{1.12}$$

$$\dot{a}^2 + Kc^2 = \frac{8}{3} \pi \rho G a^2 + \frac{\Lambda}{3} c^2 a^2. \tag{1.13}$$

It is important to notice that the introduction of the cosmological constant is not purely an ad hoc artifact, but this form naturally arises as a constant of integration of the theory, and may be related to the issue of the zero point energy.

After the expansion of the Universe had been discovered, this extended theory was distrusted by Einstein itself, who regarded the Λ-term as the biggest mistake

---

[1] This result can be obtained also using a Newtonian approach and applying the Birkhoff's theorem.
[2] Einstein interpreted this contribution as a modification of the field equations, while today the cosmological constant is viewed as a contribution to the stress-energy tensor.

he made in his life. However, with the adoption of the inflationary paradigm in cosmology, and the discovery of observational evidence for an accelerated expansion of the Universe, the cosmological constant has again assumed a fundamental role in explaining the dynamics of the Universe. This quantity is now interpreted as an intrinsic, fundamental energy density of the quantum vacuum (Weinberg, 1989), and is believed to contribute today more than two-third of the total energy density. Indeed, the Friedmann equations directly relate the rate of increase of the scale factor, as encoded by the Hubble parameter, to the total energy density of all matter in the Universe.

One additional piece of information is required before the cosmological Friedman equations can be solved: we need to specify an equation of state for the fluid in the form $p = w\rho c^2$, where w is the equation of state parameter, which lies in the Zeldovich interval $0 \leqslant w \leqslant 1$. For a matter dominated Universe the pressure can be neglected, implying $w = 0$; when radiation dominates, the pressure is equal to $p = \rho c^3/3$, and finally $w = -1$ corresponds to the cosmological constant case.

Applying the adiabatic condition we deduce that the relativistic matter grows more rapidly than the ordinary matter. In fact, during the expansion, the matter density decreases as the inverse of the total volume ($\rho_m(z) = \rho_{0m}(1+z)^3$), while for relativistic matter, e.g. photons, also the wavelength increases by a factor a, and the total energy is proportional to $(1+z)^4$. An important consequence of the value of w for the cosmological constant is that the energy density has always been (and always will be) the same thorough the expansion history of the Universe: $\rho_\Lambda(z) = \rho_{0\Lambda}$. Its value can be considered a fundamental constant of Nature.

We may use the Friedmann equations to define, at any given time, a critical energy density ρ_{cr}, for which the spatial sections must be precisely flat, and introduce the density parameter: [3]

$$\Omega \equiv \frac{\rho}{\rho_{0,cr}} = \frac{8\pi G\rho}{3H^2}. \tag{1.14}$$

Since ρ and H change with time this defines an epoch-dependent density parameter, while the current value is denoted by Ω_0. Starting from (1.9) and remembering that:

$$\rho(a) = \rho_0 \left(\frac{a}{a_0}\right)^{-3(1+w)}, \tag{1.15}$$

we can write:

$$\left(\frac{\dot{a}(t)}{a}\right)^2 = H_0^2 \left[\Omega_{m,0}\left(\frac{a}{a_0}\right)^{-3} + \Omega_{r,0}\left(\frac{a}{a_0}\right)^{-4} + \Omega_{\Lambda,0} + (1-\Omega_{\text{TOT},0})\left(\frac{a}{a_0}\right)^{-2}\right], \tag{1.16}$$

with $\Omega_{\text{TOT},0} = \Omega_{m,0} + \Omega_{r,0} + \Omega_{\Lambda,0}$, where Ω_i defines the fraction of energy density in the different components: matter, radiation and cosmological constant, respectively.

---

[3]It is possible to demonstrate that Ω keeps his sign at every time ($\Omega < 1$ if $K = -1$, $\Omega = 1$ if $K = 0$, $\Omega > 1$ if $K = +1$), so that also the geometry of the Universe is time invariant.

If the equation of state of a particular component varies with time, the energy density involves an integral over its time evolution:

$$\rho_X \propto \exp\left(-3\int d\ln a \left[1 + w\left(a\right)\right]\right).$$ (1.17)

Of particular interest to us will be the case of an evolving dark energy density, since we will study the effect of different parametrizations of the equation of state parameter on structure formation.

There are particular cases in which is very simple to describe the evolution of the scale factor analytically. Among them, the most important one is the Einstein-de-Sitter universe in which $K = 1$, $\Omega_{m,0} = 1$, and all the other components are zero. However, this model is attractive only on theoretical grounds. The expansion of the Universe depends on the total density of matter and energy due to all the components, but observations suggest that this sum is well below the critical density. In particular, the radiation contribution is almost negligible: $\Omega_{r,0} \cong 10^{-5}$, as we can deduce from the black body temperature measured by the COBE satellite ($T_r = 2.725K$, Fixsen et al., 1994). The matter component $\Omega_{m,0}$ can be computed by summing up the luminous and diffuse baryonic matter, as well as a non-baryonic non-collisional dark matter component. The theory of Big Bang nucleosynthesis puts an upper limit for the baryonic content, of about $\Omega_{b,0} = 0.05$, while from the rotation curves of spiral galaxies and the dynamics of galaxy clusters we have evidence that the remaining $\Omega_{DM,0} \cong 0.3$ must be contributed by dark matter. Since, on the other hand, from CMB observations the spatial geometry of the Universe appears to be flat, about $\cong 70\%$ of the total energy density should be constituted by dark energy, in the form of a cosmological constant or an evolving component called quintessence. This implies that the Universe is apparently vacuum dominated at present.

1.3 Distance measures

Distance measurements provide a clear and direct method to map the expansion history and the geometrical properties of the Universe. In cosmology, there are many ways to specify the distance between two points. Indeed, since the Universe is expanding, observers on Earth look back in time as they look out in distance, and the separation between two comoving objects is constantly changing. The radial comoving coordinate r is directly connected to the physical distance, expressed as the line element $\mathrm{d}s^2$ in the Robertson-Walker metric. Once we choose a reference system common to two specific points, their spatial separation can be obtained considering space-like hypersurfaces, under the hypothesis $\mathrm{d}t = 0$. The *proper distance* is then defined as the distance between two generic points which would be measured with rulers at the time they are being observed.

The expression for the proper distance is:

$$D_p = \int_0^r \frac{a \, dr'}{(1 - Kr'^2)^{1/2}} = af(r), \tag{1.18}$$

where

$$f(r) = \begin{cases} \sin^{-1} r & \text{if} \quad K = +1, \\ r & \text{if} \quad K = 0, \\ \sinh^{-1} r & \text{if} \quad K = -1. \end{cases} \tag{1.19}$$

Simply by differentiating the quantity D_p we can obtain the expression for the radial velocity of a point due to the expansion of the Universe,

$$v_{pr} = \frac{d}{dt} D_p(t) = \dot{a}f(r) = \frac{\dot{a}}{a} D_p(t), \tag{1.20}$$

which expresses the Hubble law.

The *comoving distance* D_c between two nearby objects in the Universe is the separation between two points following the cosmic expansion flow. The total line-of-sight comoving distance is computed by integrating the infinitesimal contributions (δD_c) between nearby events along the radial ray from $z = 0$ to the object. Following Peebles (1993) we can define:

$$D_c = \frac{a_0}{a} D_p = f(r) = \frac{c}{H_0} \int_1^a \frac{d a'}{a'^2 E(a')}, \tag{1.21}$$

where, for a ΛCDM cosmology:

$$E(a) = \sqrt{\Omega_{m,0}/(a)^3 + \Omega_{k,0}/(a)^2 + \Omega_{\Lambda,0}}. \tag{1.22}$$

This term is proportional to the time derivative of the logarithm of the scale factor (i.e., $\dot{a}(t)/a(t)$) and thus the integrand in Eq. (1.21) is proportional to the time-of-flight of a photon travelling across the redshift interval dz. This is the fundamental distance measure in cosmology for quantifying aspects of large scale structure imprinted on the Hubble flow. In dark energy models that have an equation of state parameter different from $w = -1$, the expansion rate is an integrated function of w (see Eq. 1.17). Since almost all cosmological tests measure an integrated function of the expansion rate itself (e.g. distance measurements), the information they carry on the (possible) time evolution of the equation of state is integrated twice.

The *angular diameter distance*, D_a, is defined as the ratio of an object's physical and angular size (in radians) and it is used to convert angular separations in telescope images into proper separations at the source. It increases till redshift $z \sim 1$ for the standard ΛCDM cosmology, while more distant objects appear larger in angular size. The angular diameter distance is related to the comoving distance by

(Weinberg, 1972):

$$D_a = \frac{D_c}{1+z}. \tag{1.23}$$

Finally, the *luminosity distance* D_l is the distance preserving the Euclidean relationship between bolometric (integrated over all frequencies) flux S and the bolometric luminosity L:

$$D_l \equiv \sqrt{\frac{L}{4\pi\,S}}. \tag{1.24}$$

This quantity is related to the comoving distance and angular diameter distance by (Weinberg, 1972),

$$D_{\mathrm{L}} = (1+z)\,D_{\mathrm{M}} = (1+z)^2\,D_{\mathrm{A}} \tag{1.25}$$

since the surface brightness of a receding object is reduced by a factor $(1+z)^{-4}$, and the angular area goes down as D_{A}^{-2}.

As a final remark, because distances are integrals over the expansion history, they contain about as much information as the Hubble parameter. Moreover, they are degenerate with respect to the cosmological parameters (see Eq. 1.22), with the greatest sensitivity to the energy densities of dark matter and dark energy. Surveys that explore this innate cosmological dependence trying to minimize systematic uncertainties in the measurements are a powerful tool to constraint the physics behind the standard cosmological models.

Type Ia supernovae

Empirically, the peak luminosity of a class of exploding stars called Type Ia supernovae (SN) can be used as an efficient distance indicator. These objects are the results of the thermonuclear disruption of carbon-oxygen white dwarfs in a binary system and can be observed to a great distance. Having a modest intrinsic scatter in luminosity, the SN type Ia can be calibrated to serve as standardized candles. In 1998 two major studies, the Supernova Cosmology project (Perlmutter, 1999) and the High-z Supernovae Search (Riess et al., 1998), with samples of ~ 50 objects, found evidence for an accelerating Universe by observing that distant supernovae appear to be fainter than expected in a flat matter-dominated Universe. This means that, at fixed redshift, they are at larger distances than expected and thus the expansion of the Universe is accelerated, a phenomenon interpreted as being due to a cosmological constant, or to a more general 'dark energy' component.

The data consist in a series of flux measurements (the light curve) with high signal to noise ratio before and after the peak flux. This is done in multiple wavelengths to permit dust and intrinsic colour corrections, together with a spectroscopy of the sources to identify the objects as SN type Ia. The distances are derived in terms of the equivalent magnitude or logarithmic flux known as the distance modulus:

$$m - M = 5\log\left(H_0 D_L\right) - 5\log H_0 + 25, \tag{1.26}$$

where m and M are the apparent and absolute magnitude, respectively. The first term, which contains the luminosity distance D_L, varies logarithmically with redshift up to corrections which depend on the geometry. Expanding in z, we obtain (Weinberg, 1972):

$$H_0 D_L = cz \left[1 + \frac{1 - q_0}{2} z + \cdots \right], \tag{1.27}$$

where $q_0 \equiv -a\ddot{a}/\dot{a}^2$ is the deceleration parameter. From Eq. (1.7), we derive that only a component that has $p < -\rho/3$, and therefore $w < -1/3$, can cause the expansion to accelerate: $\ddot{a} > 0$ ($q < 0$). This is the defining property of *dark energy*.

Current compilations cover between 300 and 400 SN type Ia with measurement quality suitable for cosmological constraints (Kowalski, 2008), and the outlook is that future probes will increase this number to tens of thousands of objects (Howell et al., 2009), thereby drastically improving the statistical significance of the data. The published data sets are consistent with a ΛCDM cosmological model, but also with a great variety of other dark energy cosmologies. Considering a flat Universe dominated by the cosmological constant, SNe type Ia can only constrain a combination of Ω_m and Ω_Λ: $q = \Omega_m/2 - \Omega_\Lambda$. In the top panel of Figure 1.1, we show the join constraints on the parameter plane (Ω_m,Ω_Λ) obtained from SN data together with CMB and BAO data (that we will discuss in the following). The constraints of SN in the plane (Ω_m,w) (bottom panel), show that even for a flat universe with constant equation of state there is a considerable uncertainty in dark energy characteristics. It is very important to reduce the systematic uncertainties in SN Ia data for future experiments that aim to put constraints on the equation of state w from a larger sample of SNe.

Baryon acoustic oscillations

The Baryonic Acoustic Oscillations (BAO) arise from the competition between gravitational attraction and gas pressure in the primordial photon-baryon fluid. These oscillations leave their imprints on structures at every epoch of the evolution of the Universe, providing a robust standard ruler from which we can derive the expansion history.

In particular, the peak we observe in the large-scale correlation function of galaxies at a separation of about $100\,h^{-1}$ Mpc is a remnant of the sound waves in the primordial plasma. The comoving distance that the sound waves can travel from the initial seed of the primordial perturbation up to the recombination time is called 'sound horizon', and is given by:

$$s = \int_{z_\mathrm{dec}}^{\infty} \mathrm{d}z \frac{c_s}{H(z)}, \tag{1.28}$$

where c_s is the speed of sound in the photon-baryon fluid, given approximately by $c_s \approx c\,[3(1 + 3\Omega_b/4\Omega_r)]^{-1/2}$, and $z_\mathrm{dec} \approx 1100$ is the redshift of the decoupling
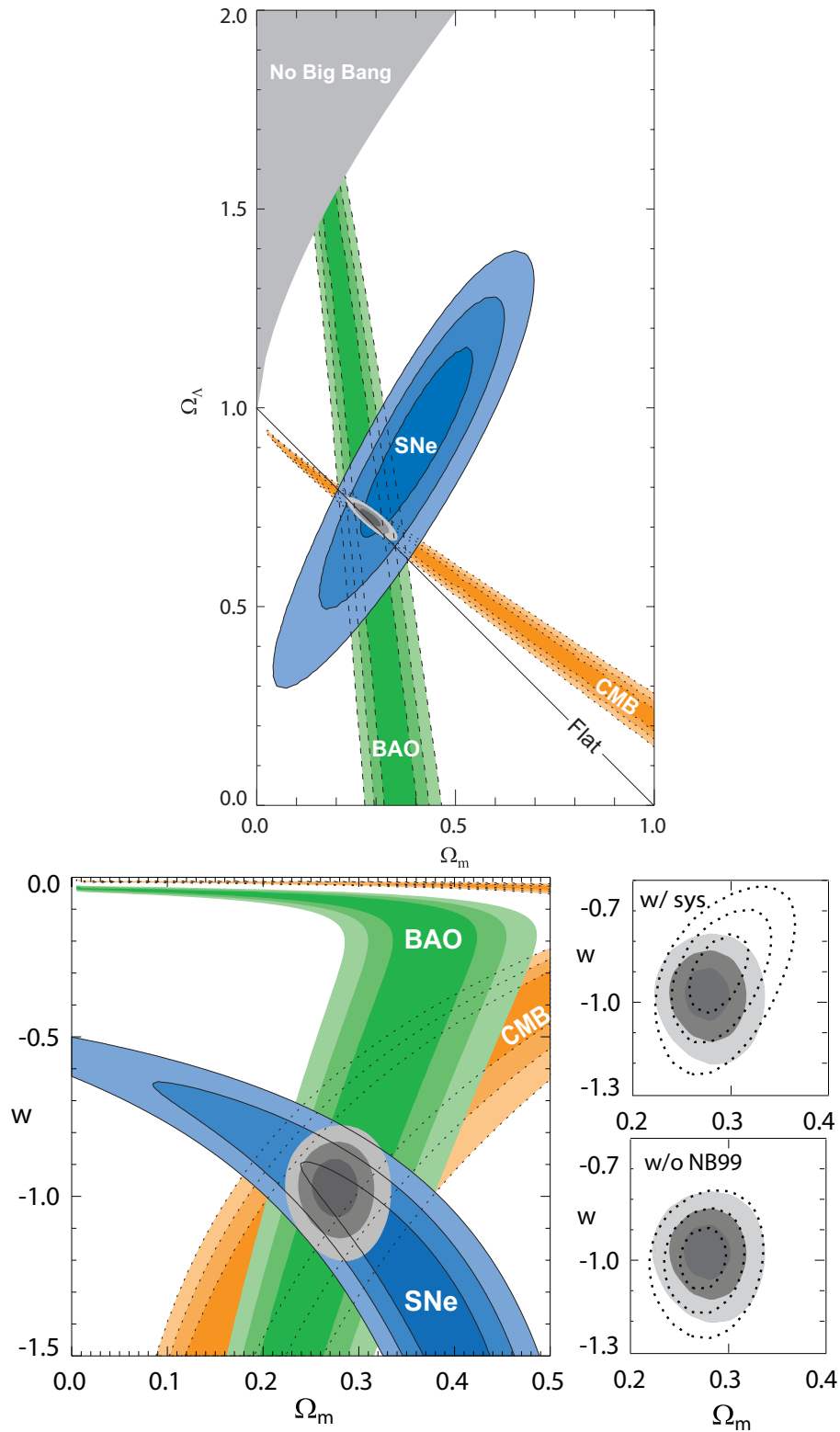
Figure 1.1 Top panel: 68.3 %, 95.4 % and 99.7% confidence level contours on Ω_Λ and Ω_m obtained from CMB, BAO and the Union SN set, as well as their combination (assuming $w = -1$). Bottom panel: Differences in 68.3 %, 95.4 % and 99.7% confidence level contours on w and Ω_m, for a flat Universe. The plot shows the individual constraints from CMB, BAO and the Union SN set, as well as the combined constraints (filled grey contours, statistical errors only). From Kowalski (2008).

between photons and baryons. Measuring this scale in the clustering of galaxies for spatial density patterns transverse to the line-of-sight give the angular diameter distance, $\tilde{d} = D_a/s$, while along the line-of-sight this gives the proper distance interval, $\tilde{H} = sH$. The strength of this methods stems from the fact that we can calibrate the sound horizon at very high redshift from the CMB data. The measured quantities give complementary information with respect to the SNIa data, since they are ratios relative to the high redshift Universe.

The BAO scale was first measured in 2005 using the Sloan Digital Sky survey data (SDSS) (Eisenstein et al., 2005; Hütsi, 2006; Padmanabhan et al., 2007) and the 2dF survey data (Cole et al., 2005) with a current precision of 3.6% in the angular diameter distance at $z = 0.35$. The two different data sets confirm the current model of cosmology, even though they present some residual tensions (Sánchez and Cole, 2008). The main observational obstacle is the weakness of the acoustic signal in the correlation function. Moreover, the oscillations leave their imprint on very large scales, and this poses a tremendous challenge to observations, as surveys must cover large volumes of the Universe. On the other hand, the physics of structure formation on those scales is well understood, and the detection of BAOs provides an important confirmation of the existence of the dark energy and of the validity of the current paradigm of structure formation, that we will explore in the following Section.

Cosmic microwave background

Independent constraints on the evolution and composition of the Universe can be derived from the analysis of the Cosmic Microwave Background (CMB) radiation, that was predicted by the Big Bang theory and discovered in 1965 by A. Penzias and R. Wilson. Geometric distance information in the CMB arises from the angular scale of the acoustic peaks in the angular power spectrum of the CMB temperature anisotropies, which were first detected by the COBE satellite (Wright et al., 1992). In a typical cosmology, the anisotropy power spectrum (usually plotted as $l(l+1)C_l$) features a flat plateau at large angular scales (small l), followed by a series of oscillations at higher angular scale. These features represent the oscillations of the photon-baryon fluid around the time of decoupling, after which the interactions between matter and radiation become negligible.

Careful analysis of all the features of the CMB power spectrum (the positions and height of the peaks and troughs) provides tight constraints on essentially all the cosmological parameters. In particular, the first acoustic peak is related to the Hubble radius at the time of last scattering, and the angular scale l at which the peak is observed depends directly on the total energy density of the Universe: $l \simeq 220\,\Omega_{\text{TOT}}$ The most recent CMB constraints on the total energy density are (Komatsu et al., 2009a):

$$\Omega_{\text{TOT}} = 1.005 + / - 0.0066 \tag{1.29}$$

at 95% confidence, consistent with spatial flatness and completely excluding significantly curved universes[4].

Moreover, as explained before, if we can predict independently the sound horizon scale, then we can use it as a standard ruler, since the angular scale of the CMB measures the ratio between the distance to the last scattering surface, D_{lss}, and the sound horizon, s, much more precisely than the single distances themselves. Related to that, the reduced shift parameter, $R = \sqrt{(\Omega_m h^2)} D_{\mathrm{lss}}$, gives a good approximation of the full CMB leverage on the cosmic expansion for models close to the ΛCDM scenario (Efstathiou and Bond, 1999). For non-standard models, where the sound horizon and the conformal distance change, this relation needs to be corrected. The tightly constrained geometric information means that certain combinations of cosmological parameters can be well determined, but it is necessary to take into account an additional error due to the fact that we assume external priors on the models, for example deciding a-priori whether or not to account for the possibility of an evolving dark energy. In this case, taking the wrong cosmology would then lead to a miscalibration of the standard ruler (see e.g. Linder and Robbers, 2008)) and a bias in the theoretical interpretation of the results.

1.4 Structure formation

Observations confirm that the Universe has quite the same properties on very large scales, but on the other hand we can observe that the matter is irregularly distributed on smaller scales, where in fact the space is populated by galaxies, clusters and superclusters. The standard model assumes that these structures originated from gravitational instability, which caused the primordial fluctuations in the density field to grow and decouple from the background expansion, and to eventually collapse to form bound structures. The physical origin of these perturbations in the first place is still not fully clear, but the general idea is that they were generated during an early inflationary epoch from quantum fluctuations (Guth 1981).

The currently favored theory of structure formation classifies and studies small fluctuations around the FLRW metric, so that the large-scale structure can still be described as a homogeneous and isotropic background against which small inhomogeneities stand out that represent the variety of the Universe we observe.

Jeans was the first to demonstrate, in 1902, that starting from a uniform distribution of density and matter, small fluctuations in the density, $\delta\rho$, and velocity, δv, should evolve with time. Given a spherical overdense region with radius R and mass $M \propto \rho R^3$, the evolution of the system depends on the balance between two forces: the first is the pressure force, which acts as to cancel the density perturbation, the second is gravity, which tends to amplify it. The characteristic scale at which the

---

[4]This result does however assume a prior on the Hubble parameter from other measurements, and that the dark energy is a cosmological constant.

two opposing forces are equal is known as *Jeans length*, $R(J)$, and can be computed as:

$$R_J \simeq \frac{v_s}{\sqrt{2G\rho}}, \tag{1.30}$$

where G is the universal gravitational constant, ρ is the gas density and v_s is the sound speed. Similar resoning also turns out to hold for collisionless fluid, as long as we replace v_s, the adiabatic sound speed, with the mean square velocity of the particles making up the fluid. In this case, if $R < R_J$, the velocity dispersion of the particles is too large for them to be held by self-gravity and they undergo free streaming; the fluctuations are dissipated by this process. On the other hand, for $R > R_J$, the perturbation can grow by gravitational instability.

The growth of density perturbations proceeds in two phases, that can be classified into the linear and non-linear regime, according to the value of the density contrast:

$$\delta(x) \equiv \frac{\rho(x) - \rho_b}{\rho_b}, \tag{1.31}$$

which quantifies the density inhomogeneity at comoving coordinates (x) relative to the mean density of the Universe ρ_b. When $\delta << 1$, the perturbations can be treated by first order linear perturbation theory, while when $\rho \cong 1$, the solutions found by perturbation theory do not give good approximations any more, so usually numerical techniques are employed. In this thesis, we will focus on probing the formation of structure during the non-linear regime through accurate N-body simulations.

We should remember that the evolution of cosmological structures takes place in a scenario where the dominant matter component is the dark matter, a non-relativistic fluid interacting only gravitationally. Although dissipative gas physics plays an important role in galaxy formation, gravitation is the interaction that dominates the dynamics of the Universe. Gravity has an amplifying effect on the initial fluctuations. Any region with a density higher than its surroundings will increase its level of density contrast. The increase in $\delta(x)$ will be reflected in the gravitational field and tend to attract even more matter into the initial perturbation. This will result in a runaway process in which any existing perturbation will be amplified, eventually creating bound objects. The opposite effect occurs in underdense regions, so-called *voids*, where the gravitational force will be weaker and more and more mass will escape.

1.4.1 The linear theory of structure growth

Under the hypothesis that the perturbations are much smaller than the horizon scale of the Universe, the curvature effects can be neglected, and a Newtonian treatment is sufficient to describe their growth. On cosmological scales, we can, to a good approximation, describe the evolution the cosmic density field by a set of three

coupled differential equations involving the density contrast δ, the peculiar velocity **v** and the gravitational potential ϕ :

- the *Continuity equation*,

$$\frac{\partial \rho}{\partial t} + \vec{\nabla} \cdot (\rho \vec{v}) \equiv \frac{D\rho}{Dt} + \rho \vec{\nabla} \cdot \vec{v} = 0, \tag{1.32}$$

which ensures mass conservation;

- the *Euler equation*,

$$\frac{\partial \vec{v}}{\partial t} + \left(\vec{v} \cdot \vec{\nabla} \right) \vec{v} \equiv \frac{D\vec{v}}{Dt} = -\frac{1}{\rho} \vec{\nabla} p - \vec{\nabla} \phi, \tag{1.33}$$

which ensures moment conservation and describes the motion of the fluid element; and finally

- the *Poisson equation*,

$$\nabla^2 \phi = 4\pi G \rho, \tag{1.34}$$

that relates the distribution of matter and the gravitational field.

A usual assumption in the analysis is that the system considered is adiabatic. Therefore, the time evolution of the entropy is described by reads $dS/dt = 0$ and the equation of state reduces to the simple form $p = p(\rho)$. To include the expansion of the background universe, we modify the perturbation equations by considering the following linear evolution:

$$\rho = \rho_b (1 + \delta), \tag{1.35}$$

$$\vec{u} = H\vec{r} + \vec{v}, \tag{1.36}$$

$$p = p_b + \delta p, \tag{1.37}$$

$$\Phi = \Phi_0 + \phi, \tag{1.38}$$

and introduce a comoving reference frame. The system, once written in Fourier space, can be easily solved considering solutions in the form of plane waves:

$$f(r, t) = f_k \cdot \exp\left(i\vec{k} \cdot \vec{r} + iwt \right), \tag{1.39}$$

where w and k are the frequency and wavenumber, respectively, and f_k is the amplitude of the quantity that perturbs the system, and can be equal to $\delta\rho$, δv, $\delta\phi$, or δs. In the case of small fluctuations ($\delta \ll 1$) and small streaming motions, δ and v can be computed from linear perturbation theory (Peebles, 1980). In the linear approximation, the evolution equation of δ is given by:

$$\ddot{\delta}_k + 2H\dot{\delta}_k + \left(v_s^2 k^2 - 4\pi G\rho_b \right) \delta_k = 0, \tag{1.40}$$

33

where the expansion of the universe acts as a friction term, thus slowing down the gravitational instability.

The linear equation has two independent solutions. For an EdS model:

$$\delta_{k;+}(t) \propto t^{2/3} \propto a; \qquad \delta_{k;-}(t) \propto t^{-1} \propto a^{-3/2}, \tag{1.41}$$

where δ_k is the Fourier transform of the density contrast of matter perturbations. The first solution, the so called growing mode, determines the growth of the density fluctuations, while the second defines a decaying perturbation. These results are valid both for the baryonic and non-baryonic matter if we consider v_s as an estimate of the velocity dispersion in the case of collisionless matter. For a universe dominated by radiation, we have instead: $\delta_{k;+}(t) \propto t \propto a^2$. Perturbations of the other components follow the trend of the dominant component at any given epoch, because they are coupled together via gravity.

Without going into the details of the analytical derivation, the solutions for the perturbations within the cosmological horizon can be summarized as follows. Before the equivalence between matter and radiation, the Universe is radiation dominated, but the dark matter is already decoupled from radiation, so that its perturbations cannot grow, $\delta_{\mathrm{DM}} \sim const$ (stagnation effect). Between equivalence and recombination (i.e. the era when electrons and protons combine to form hydrogen atoms, about 380000 years after Big Bang), the fluctuations of the radiation-baryon fluid oscillate, while the dark matter perturbations can start growing, in particular $\delta_{\mathrm{DM}}(t) \propto a(\Omega = 1)$. After recombination, the dark matter density is still the dominant contribution; the density fluctuations of the baryonic matter, finally decoupled from radiation, undergo an accelerated growth until they reach the dark matter perturbation level, and $\delta_{\mathrm{B}} \sim \delta_{\mathrm{DM}}$. The trends described above refer to perturbations larger than the corresponding Jeans scale, $\lambda_J = 2\pi/k_J$, called the Jeans length. In case fluctuations have $\lambda < \lambda_J$, gravity is not the dominating force and dissipative gas-dynamical processes tend to smooth and eventually cancel the perturbations. The mass scales for this dissipative process in the baryonic matter is known as the Silk mass, and no structures are expected to formed at scales smaller than that.

Growth factor and dark energy

The solutions described above in Eq. (1.41) refer to a flat Universe with $\Omega \sim 1$, which is a good approximation at very early times, such as before the equivalence epoch. For later times, Eq. (1.40) must be solved separately for each cosmological model to obtain an accurate description.

With respect to the formation of cosmic structures we are interested in perturbations with $\lambda >> \lambda_J$, and the general solution for δ can be rewritten as:

$$\delta(x,t) = \delta_+(x,t_i)D(t) + \delta_-(x,t_i)D(t), \tag{1.42}$$

where t_i is some reference time and $D_+(t)$ ($D_-(t)$) replaces $\delta_+(t)$ ($\delta_-(t)$). The growing mode $D_+(t)$ is usually referred to as *linear growth factor* and quantifies the growth of the density contrast from an initial value $\delta_0 = \delta(a = 1)$. Generally, the normalized growth factor obeys:

$$D'' + \frac{3}{2}\left[1 - \frac{w(a)}{1 + X(a)}\right]\frac{D'}{a} + \frac{3}{2}\left[\frac{X(a)}{1 + X(a)}\right]\frac{D}{a^2} = 0, \tag{1.43}$$

where $X(a)$ is the ratio of the matter density to the energy density:

$$X(a) = \frac{\Omega_{m,0}}{\Omega_{de,0}}\exp\left[-3\int_a^1 d\ln a' w(a')\right]. \tag{1.44}$$

and we allowed for a time dependent equation of state, $w(a)$. The evolution of a matter density perturbation is reduced from the Newtonian exponential growth to a power-law growth on a Hubble time scale by the drag induced by the cosmological expansion. Thus, the expansion history can in principle be reconstructed from the growth rate of inhomogeneous density perturbations in the non-relativistic matter component on scales significantly less than the Hubble radius[5].

In general, the equation for the growing mode requires numerical integration, with $\dot{a}(a)$ given by the Friedmann equation, but a very good approximation to the answer is given by the fitting formula of Carroll et al. (1992)

$$\delta_0(\Omega_{m,0}, \Omega_{\Lambda,0}) \approx \frac{5}{2}\Omega_{m,0}\left[\Omega_{m,0}^{4/7} - \Omega_{\Lambda,0} + \left(1 + \frac{1}{2}\Omega_m\right)\left(1 + \frac{1}{70}\Omega_{\Lambda,0}\right)\right]^{-1} \tag{1.45}$$

for the growth suppression in low density universes, where $\delta_0(\Omega_{m,0}, \Omega_{\Lambda,0})$ denotes the ratio of the current linear amplitude to the fiducial case. For flat models this formulation says that the growth suppression is less marked than for an open Universe: $\Omega^{0.23}$ instead of $\Omega^{0.65}$. It also implies that structures form earlier in a low density Universe, and at late times a more rapid expansion retards their growth. Therefore, if the cosmological constant is important dynamically, it only becomes so very recently. For a flat Universe, the epoch where the cosmological constant starts to dominate is $a \sim (\Omega_m/\Omega_\Lambda)^{1/3}$.

In early dark energy models the growth of linear perturbation is suppressed (Ferreira and Joyce, 1998), hence structures grow slower. To quantify this effect, we consider an average of the dark energy contribution towards the total energy density during structure formation (Doran et al., 2001):

$$\bar{\Omega}_{de,sf} = -\ln a_{eq}^{-1}\int_{\ln a_{eq}}^0 \Omega_{de}(a)\,d\ln a, \tag{1.46}$$

where a_{eq} is the scale factor at the matter-radiation equivalence. In an early dark

---

[5]Provided perturbations in the dark energy component can be neglected and the effective gravitational constant does not change with time

energy cosmology with $\Omega_m < 1$, the solution of Eq. (1.40) is:

$$\delta \propto a^{\left[\sqrt{25-24\Omega_{sf}^d}-1\right]/4} \sim a^{1-3\Omega_{sf}^d/5}. \tag{1.47}$$

Hence, all k-modes inside the horizon at a given time will suffer the same suppression.

Growth measurements, being integrals from high redshift to the preset epoch, can probe the high redshift universe. For example, if measurements of the linear growth factor at $z = 2$ deviate by more than 5% with respect to the expected ΛCDM model, then, for a monotonically varying dark energy model of the kind $w(a) = w_0 + w_a(1 - a)$, we can obtain the limit $w_a < 0.6$ or $w(z = 2) < -0.6$. However, the growth also depends on the initial conditions, the coupling of different mass/energy components, potential deviations of gravity from general relativity, and a precise knowledge of Ω_m is required to truly use this approach.

Density fluctuation spectrum

We can describe structure formation in terms of statistical quantities, relying on two hypothesis: the cosmological principle and the ergodic hypothesis[6].

It is very convenient to think of linear perturbations as of a superposition of plane waves that evolve independently in the linear regime. In other words, we can decompose the density contrast δ into Fourier modes:

$$\hat{\delta}\left(\vec{k}\right) = \int \delta\left(\vec{x}\right) \exp\left(-i\vec{k}\cdot\vec{x}\right) d^3k, \tag{1.48}$$

where $\hat{\delta}$ denotes the Fourier transform of δ. The fluctuations in a Gaussian random field are fully described by their *power spectrum*, $P(k)$:

$$P(k) = \left\langle |\delta_k|^2 \right\rangle, \tag{1.49}$$

which measures the power over a scale k for a generic perturbation. Back in real space, the Fourier transform of the power spectrum is the two-point correlation function, $\xi(\vec{r})$, which measures the coherence of the density contrast for all points of the Universe separated by a distance $\vec{r}$.

It is conventionally assumed that the primordial power spectrum has a power law behavior: $Pk = Ak^n$, where A is a normalization constant that can be inferred from observations, for example of the local abundance of galaxy clusters (White et al., 1993; Eke et al., 1996; Viana and Liddle, 1996; Tegmark and Zaldarriaga, 2002), and n is the spectral index ($n \approx 0.96$ Komatsu et al. (2009a)). If we require that the primordial power spectrum is scale invariant, i.e. the fluctuations in the gravitational potential are independent of the length scale, then the spectral index must be $n = 1$.

---

[6]This hypothesis states that the average taken over all the possible realizations of an ensemble are equal to the averages done over a sample of that population

This power spectrum is called *Harrison-Zeldovich spectrum* and is compatible with predictions from the inflationary model (see Section 1.6).

Historically, the normalization of the power spectrum is usually expressed in terms of the variance of the density contrast inside spheres of radius $8\,h^{-1}\mathrm{Mpc}$, namely σ_8. If we consider mass fluctuations inside a generic volume δ_M, we can define the variance as:

$$\sigma_M^2 = \frac{\left\langle (M - \langle M \rangle)^2 \right\rangle}{\langle M \rangle^2} = \frac{1}{2\pi^2} \int P(k)\, \hat{W}^2(kR)\, k^2 dk, \qquad (1.50)$$

where $\hat{W}(kR)$ is a window function, usually the Fourier transform of a Gaussian or top-hat filter in real space. The observational determination of σ_8 is still a highly debated subject in modern cosmology.

The primordial power spectrum is later modified by physical processes which affect the growth of density perturbations, in particular the suppression of the fluctuations before the epoch of equivalence. The cumulative effect of all processes is parametrized by a transfer function, so that the primordial power spectrum changes its shape according to: $P(k,t) = P(k,t_0)T^2(k)D(t)^2/D(t_0)^2$, where $T(k)$ is the transfer function (see Bardeen et al. for a fitting formula) and $D(t)$ is the growing mode of Eq. (1.43). In a Universe dominated by Cold Dark Matter with Zeldovich primordial spectrum, the kinematic suppression of the growth on large scales leads to a bottom-up structure formation scenario in which large systems like galaxy clusters form via hierarchical merging of smaller structures.

1.4.2 The non-linear evolution

The Jeans theory of gravitational instability fails when the density fluctuations approach unity. Typical examples of non-linear density fluctuations are galaxy clusters, for which $\delta \approx 10^3$. Once the density field enters into the non-linear regime, it becomes non-Gaussian and its probability distribution function for the density assumes a skewed shape towards high values of δ.

The study of the perturbation growth in this case is usually carried out with numerical methods, but analytical results can be found for systems with a particularly simple symmetry and by using certain approximations. In particular, the spherical collapse model and the Zeldovich approximation are useful tools to qualitatively understand the processes leading to the formation of virialized dark matter halos.

The spherical collapse-model

The spherical collapse model provides an analytical approximation to the non-linear growth of a top-hat (spherical and homogeneous) sub-horizon fluctuation. In this approach, we treat the spherical inhomogeneity in the field as a separate FLRW uni-

verse, that separates itself with respect to a flat expanding background. Similarly to what happens in a closed universe, the perturbation will initially expand together with the background until it reaches a maximum radius, corresponding to the minimum of the density, and then it will detach from the background Hubble expansion and undergo gravitational collapse. The theoretical description of the model would lead to a singularity due to the assumed perfect spherical symmetry; in reality, because of the radial orbit instability, small asphericities, and the gas pressure, the overdense region will stop the contraction before a singularity is reached and the system settles into virial equilibrium. This model, though simple, has been widely studied (Gunn and Gott, 1972). Here we just review some of the basic concepts we will need to understand the formation of structures in non-standard cosmological models.

Starting from the assumption that the initial perturbation is spherically symmetric, we consider an overdense region of radius R and total mass M. The additional constraint of vanishing initial velocity for the perturbation, $v_i = 0$, make the role of the pressure important with respect to gravitational attraction, particularly in the initial phase. Since the overdense region is a finite-size perturbation, the corresponding density contrast is meant to be the mean overdensity within the spherical volume considered, obtained via integration of the spherically symmetric density fluctuation field (averaged on the volume itself) over that region.

The solution for the density perturbation in the case of a matter dominated universe reads:

$$\delta\left(t\right) = \delta_+\left(t_i\right)\left(\frac{t}{t_i}\right)^{2/3} + \delta_-\left(t_i\right)\left(\frac{t}{t_i}\right)^{-1}. \tag{1.51}$$

Combining this equation with the continuity equation, and with the condition $v_i = 0$, it is easy to verify that $\delta_-\left(t_i\right) = 2/3\delta_+\left(t_i\right)$. Therefore, the relation between the linear growing mode of the perturbation and the initial overdensity extrapolated from the linear theory predictions gives $\delta_+ = 3/5\,\delta(t_i)$.

On the other hand, the requirement of the perturbation to recollapse gives $\Omega_p = \Omega(t_i)(1+\delta_i) > 1$, where $\Omega(t_i)$ is the background density parameter at the reference initial time t_i. Applying the Friedmann solutions for a closed dust universe in parametric form:

$$a\left(\theta\right) = a_0 \frac{\Omega_0}{2\left(\Omega_0 - 1\right)}\left(1 - \cos\theta\right); \tag{1.52}$$

$$t\left(\theta\right) = \frac{1}{2H_0}\frac{\Omega_0}{\left(\Omega_0 - 1\right)^{3/2}}\left(\theta - \sin\theta\right), \tag{1.53}$$

with θ within the range $[0, 2\pi]$, we can compute the evolution of the perturbation in the non-linear regime in different phases.

1. **Turn around**. After a period of expansion, the sphere reaches its maximum (a_{MAX}) at $\theta = \pi$ (see Eq. 1.53). This very instant, the ratio between the

background density $\rho\,(t_m)$ and the perturbation density $\rho_p\,(t_m)$ is equal to:

$$\chi_m = \frac{\rho_p\,(t_m)}{\rho\,(t_m)} = \left(\frac{3\pi}{4}\right)^2 \simeq 5.55. \qquad (1.54)$$

As a comparison, the linear theory extrapolation at the same time gives:

$$\delta_+\,(t_m) = \delta_+\,(t_i) \left(\frac{t_m}{t_i}\right)^{2/3} \simeq 1.07. \qquad (1.55)$$

2. **Collapse**. Considering only the gravitational physics, a perfectly symmetric sphere would collapse to a singularity for $\theta = 2\pi$. According to linear theory, the density contrast at this time would be:

$$\delta_+\,(t_c) = \delta_+\,(t_m) \left(\frac{t_{\,c}}{t_m}\right)^{2/3} \simeq 1.68. \qquad (1.56)$$

3. **Virialization**. In reality, the collapse to a point does not happen in non-linear dynamics. For the gas, the dissipative physics intervenes and convert the kinetic energy into heat. For collisionless matter, it is transformed into unordered random motions instead. Assuming that the total energy of the fluctuation at the time of virialization, t_{vir}, should be equal to the energy at the time of turn around t_m, we obtain that the radius at turnaround is twice the virial radius, i.e. $R_m = 2\,R_{vir}$, thus $\rho_{p(t_{\mathrm{vir}})} = 8\rho_p\,(t_m)$. The numerical simulations give $t_{\mathrm{vir}} \simeq 3t_m$. Therefore the density parameter at t_c is:

$$\chi_c = \frac{\rho_p\,(t_c)}{\rho\,(t_c)} = 2^2 8\chi \simeq 178. \qquad (1.57)$$

We note that at this time, the linear theory prediction

$$\delta_+\,(t_{vir}) = \delta_+\,(t_m) \left(\frac{t_{vir}}{t_m}\right)^{2/3} \simeq 2.20, \qquad (1.58)$$

represents a large underestimate of the spherical collapse model results:

$$\chi_{\mathrm{vir}} = \frac{\rho_p\,(t_{\mathrm{vir}})}{\rho\,(t_{\mathrm{vir}})} = 3^2 8\chi_m \simeq 400. \qquad (1.59)$$

Clearly, linear theory is hence only applicable till $\delta_{\mathrm{lin}} \approx \delta_c$ or slightly larger than one (~ 1.68). In the strong non-linear evolution that leads to virialization, this density contrast is corrected to 178. In order to clearly mark the difference between the two regimes in the following Chapters of this Thesis, the non-linear overdensity corresponding to virialization will therefore be denoted with a different notation than the linear one. To this end we will replace χ by Δ_{vir}.

The concept that the value of the overdensity distinguishes the collapsed sys-

tems from the ones that are still forming allows one to find the collapsed objects in numerical simulations. The non-linear overdensity inferred from the top-hat model usually leads to the definition of a corresponding virial radius. Although the derivation we have carried out above is restricted to the case of an Einstein-de Sitter background, Eq. (2.46) shows why an overdensity of about 200 is usually considered as typical for a dark matter halo which has reached the virial equilibrium.

Moreover, the contribution of quintessence in the equation of motions relevant for the top-hat collapse is still under debate. If quintessence reduces to the cosmological constant, then it does not affect the treatment. In the case of a constant equation of state parameter w, the non-linear overdensity corresponding to the virialization, Δ_{vir}, can be computed via the best fit functional form proposed by Weinberg and Kamionkowski (2003), that is

$$\Delta_{\mathrm{vir}}(z) = 18\pi^2[1 + a\Theta^b(z)] \tag{1.60}$$

where

$$a = 0.399 - 1.309(|w|^{0.426} - 1) b = 0.941 - 0.205(|w|^{0.938} - 1) \tag{1.61}$$

and, according to the evolution of the matter energy density parameter $\Theta(z) = 1/\Omega_m(z) - 1 = (1/\Omega_{m,0} - 1)(1+z)^{3w}$.

The dark energy influences the evolution of the perturbations via its equation of state. In models with larger w structures do form earlier and then the virialization overdensity at the redshift of collapse rises with increasing w. If we consider a scalar field, two cases must be distinguished. Caldwell et al. (1998) showed that quintessence cannot be perfectly smooth, but it is generally believed that the clustering of the field should be negligible for scales smaller than $\approx 100\,h^{-1}\mathrm{Mpc}$ and Maor (2007) argued that including the quintessence explicitly in the equations could not lead to energy-conservation. So, including or excluding clustering of the quintessence field will lead to different results.

The Zeldovich approximation

To study the evolution of a perturbation with a generic shape, we can use the so-called *Zeldovich approximation*. In this model, whose validity is limited to the quasi-linear regime, the effects due to the pressure force are neglected and the structure formation is analyzed using a kinematic approach. Given an ensemble of particles uniformly distributed, we assume that they continue to move in the direction of their initial displacement.

The comoving position of a particle $\vec{x}(t)$ is related to the proper coordinate $\vec{r}(t)$ through the relation $\vec{x}(t) = \vec{r}(t)/a(t)$. The generic solution of the motion equation

can be written as:

$$\vec{x}(\vec{q}, t) = \vec{q} + s(\vec{q}, t),$$ (1.62)

where $\vec{q}$ is the initial (Lagrangian) position and x is the final (Eulerian) and $s(\vec{q}, t)$ is the displacement vector. For a non-collisional, self-gravitating fluid in an expanding background we obtain:

$$s(\vec{q}, t) = b(t) \nabla \psi(\vec{q}),$$ (1.63)

where $b(t)$ is the growing mode of the density fluctuations, and $\psi(t)$ is the gravitational potential, which is related to the density fluctuations by the Poisson equation (Eq. 1.34).

Similarly, equations (1.62) and (1.63) describe a trajectory in which the particles move with constant velocity:

$$v = \frac{dr}{dt} - H t = a \frac{dx}{dt} = a H(a) f(\Omega) \delta.$$ (1.64)

The term $f(\Omega)$ is the logarithmic derivative of the grow factor and, in a ΛCDM universe, can be approximated by $f(\Omega) \equiv d\log D / d\log a \approx (\Omega_m(a))^{0.6}$, but is different in non standard cosmology.

In the Zeldovich approximation, the collapse is described by three eigenvalues of the deformation tensor between $\vec{r}$ and $\vec{q}$. For an ellipsoidal distribution, in general the collapse takes place along the smaller axis, i.e. the gravity tends to accentuate the asphericity, leading to the formation of a flat structure known as *pancake*. In three dimensions, the collapse of aspherical structures creates, in the final stages, almost one-dimensional structures, the filaments. This method describes quite well the dynamics of the density field up to the point when particles start to intersect each other, known as shell-crossing time. The advantage of the Zeldovich approximation is that it gives surprisingly accurate results in the computation of the peculiar velocities, and it is also particularly useful for initializing the particle velocities and positions in N-body simulations.

1.4.3 Abundance tests

Galaxy clusters provide a unique tool for cosmology, being the most massive collapsed objects we observe in the final stage of the evolved primordial density perturbations (Press and Schechter, 1974). Clusters trace efficiently the structure of the Universe on large scales (Eisenstein et al., 2005; Hütsi, 2006) and their distribution strongly depends on cosmological parameters (Weller and Battye, 2003; Sefusatti et al., 2007). Therefore, a detailed study of the their aboundance can provide us with useful information on the underlying cosmology. However, using this connection is not so straightforward in practice.

Several groups have tried to constraint the cosmology by comparing observations with theoretical models, based on the mass function formalism we will describe below (e.g. Bahcall and Fan, 1998) or with simulated data from N-body experiments (e.g. Bahcall and Cen, 1993; Bode et al., 2001). These approaches, even if shown to be very useful, are intrinsically limited by the quality of the data. Cluster masses are not very well determined for intermediate-high redshift clusters, and standard methods to determine them (based on velocity dispersions, cluster richness, gravitational lensing, X-ray surface brightness de-projection) usually give different answers. Moreover, observations do not actually measure the abundance of structures per comoving volume. They rather measure the number of objects as a function of redshift, which involves also the distances, and thus furnishes a mixed probe of the growth rate and the geometry of the universe.

Today, a new generation of experiments is underway to count the abundance of sources as a function of mass and redshift, through optical observations, X-ray flux, weak lensing and the Sunyaev-Zeldovich effect. Among several possible tests, the latter has received great interest in recent years. The Sunyaev Zeldovich (SZ) effect is simply the distortion of the CMB due to the inverse scattering of photons that cross the high energy cluster electrons, and it is of fundamental importance for two reasons. First, it is a contamination of the CMB signal, therefore a good understanding of this effect is required in order to perform an appropriate data analysis. Secondly, it can also be considered as a very sensitive tool to measure the cluster distribution as a function of mass, as we will underline in this Thesis (see Chapter 3).

Particularly interesting in this respect is that the SZ effect is the preferred way to observe high redshift clusters. In fact, when looking for clusters at mm wavelengths, it is easier to detect the furthest ones because the effect drops very slowly with distance (or even increases). These high redshift objects are very important for understanding the physics of cluster formation and also to establish the evolution of cluster scaling laws. The number of available clusters with measured SZ effect is expected to rapidly growth with the higher sensitivity of the detectors now available, making the SZ effect an important tool to explore the far Universe.

In the following we will exploit the subject of the aboundance of structures introducing the mathematical formulation of the mass function.

The mass function

Under gravitational instability, it is possible to model the formation of virialized halos from the growth of peaks in the primordial mass fluctuation distribution. Estimating the abundance of a particular class of objects as a function of redshift involves, among other variables, the initial power spectrum, the expansion rate of the Universe, astrophysical processes such as dissipation and feedback, and a robust observational proxy for the mass.

Invoking the hypothesis that the initial perturbation field follows a Gaussian random-phase statistic, the distribution function of the density filtered on a spatial scale R (corresponding to a mass scale M), $\delta\left(\vec{x}, R\right) = \delta_M$, can be written as:

$$P\left(\delta_M\right) \mathrm{d}\delta_M = \frac{1}{\left(2\pi\sigma_M^2\right)^{1/2}} \exp\left(-\frac{\delta_M^2}{2\sigma_M^2}\right) \mathrm{d}\delta_M, \tag{1.65}$$

where σ_M^2 is the variance defined in Eq. (1.50). The probability that the fluctuation exceeds a generic threshold δ_c is given by:

$$P_{>\delta_c}\left(M\right) = \int_{\delta_c}^{\infty} P\left(\delta_M\right) \mathrm{d}\delta_M. \tag{1.66}$$

One can now assume that the number of cosmic structures is proportional to this probability, which characterizes density perturbations greater than δ_c. In the spherical collapse theory, the formation of a virialized halo happens when the density contrast reaches the linearly extrapolated value $\delta_c = 1.686$. Therefore, the difference between $P_{>\delta_c}\left(M\right)$ and $P_{>\delta_c}\left(M + dM\right)$ will be proportional to the number of objects included in a given mass interval, the so called *mass function*. Press and Schechter (1974) derived an analytical expression for the mass function based on the ansatz:

$$n\left(M\right) M \, \mathrm{d}M = 2\rho_m \left[P_{>\delta_c}\left(M\right) - P_{>\delta_c}\left(M + dM\right)\right] = 2\rho_m \left|\frac{\mathrm{d}P_{>\delta_c}}{\mathrm{d}\sigma_M}\right| \left|\frac{\mathrm{d}\sigma_M}{\mathrm{d}M}\right| \mathrm{d}M, \tag{1.67}$$

where the factor 2 is included to take into account the so called *cloud-in-cloud problem*, which is the possibility that at a given instant some object, which is nonlinear on a scale M, can be later contained in another object, at a larger mass scale.

If we express the variance with a power law $\sigma_M = \left(M/M_0\right)^{-\alpha}$, Eq. (1.67) becomes:

$$\frac{dn\left(M, z\right)}{dM} = \sqrt{\frac{2}{\pi}} \frac{\rho_m}{M^2} \frac{\delta_c\left(z\right)}{\sigma_M} \left|\frac{d\ln\sigma}{d\ln M}\right| \exp\left\{-\frac{\delta_c^2\left(z\right)}{2\sigma^2\left(M\right)}\right\} = \tag{1.68}$$

$$\frac{2}{\sqrt{\pi}} \frac{\rho_m \alpha}{M_*^2} \left(\frac{M}{M_*}\right)^{\alpha-2} \exp\left\{-\left(\frac{M}{M_*}\right)^{2\alpha}\right\}. \tag{1.69}$$

The differential mass function is thus a power law relation, with an exponential 'cut-off' at the scale $M_* = \left(2/\delta_c^2\right)^{1/2\alpha} M_0$.

A more rigorous derivation of this relation is possible using the *excursion set* model Bond et al. (1991). In this theory, the field is rescaled at the initial time $\delta\left(\vec{x}\right) \equiv \delta\left(\vec{x}, t_0\right)$ and the temporal dependence is transferred on the critical threshold, $\delta_c\left(t\right) = \delta_c D\left(t_0\right)/D\left(t\right)$. An infinitesimal element belongs to a halo of mass M at time t if the linear fluctuation $\delta_f\left(\vec{x}; R\right)$, centered on $\vec{x}$ and filtered over a sphere of

radius $R \propto M^{1/3}$, has a value greater or equal to the threshold:

$$\vec{x} \in M \qquad \Leftrightarrow \qquad \delta_f(\vec{x}, R) \geqslant \delta_c(t). \qquad (1.70)$$

The evolution of dark matter halos can be described by Brownian random motions in two-dimensional space, and $\delta_c(t)$ is such that points with trajectories hitting the barrier are removed by counting them as being part of halos.

Under this approach we can also correct the Press-Schechter formula (1.68) for the effects due to the asphericity of the collapse. If we write the mass function in terms of the fraction of collapsed objects, $\nu \equiv \frac{\delta_c(z)}{\sigma_M}$, we obtain:

$$n(M, z)\, \mathrm{d}M = \frac{\bar{\rho}}{M} f(\nu) \frac{\mathrm{d}\nu}{\mathrm{d}M}\, \mathrm{d}M, \qquad (1.71)$$

where

$$\frac{\mathrm{d}f}{\mathrm{d}\nu} = C\sqrt{\frac{2A}{\pi}} \left(1 + \frac{1}{(A\nu^2)^q}\right) \exp\left(-\frac{A\nu^2}{2}\right), \qquad (1.72)$$

and the parameters are $A = 0.707$, $C = 0.3222$, and $q = 0.3$, as derived by Sheth and Tormen (1999) for the case of ellipsoidal collapse. This expression reduces to the original Press-Schechter form for $A = 1$, $C = 0.5$ and $q = 0$. Moreover, fitting the results of N-body simulations directly, Jenkins et al. (2001) obtained an empirical formula very similar to Eq. (1.72) with $A = 0.75$, and therefore with a somewhat steeper decay in the number of objects in the high mass end. More recently, Warren et al. (2006) found another best-fit assuming q as a free parameter and removing the arbitrary collapsing scale δ_c, that was already modified in the Sheth and Tormen formulation. Their multiplicity function, $f(\sigma)$, reads:

$$f(\sigma) \equiv \frac{M}{\bar{\rho}} \frac{\mathrm{d}n}{\mathrm{d}\ln\sigma^{-1}} = A\left(\sigma^{-a} + b\right) e^{-c/\sigma^2}, \qquad (1.73)$$

with $A = 0.723$, $a = 1.625$, $b = 0.254$ and $c = 1.198$. These two mass functions are almost independent of the statistical uncertainty of the cosmological parameters and turn out to be very accurate to relate, e.g., cluster counts with the properties of the primordial density field.

The Press-Schechter model, and especially its improved variants, are well supported by cosmological simulations, as we will observe in the following Chapters, and is therefore a useful analytic predictive tool in many circumstances. In spite of the statistical derivation of the theory, using the so-called *extended* Press-Schechter, we can also obtain the mass function for the progenitors of a given halo and an analytical expression for the mean formation time of objects.

Another application of the excursion set approach is the modeling of the spatial clustering of dark halos (Mo and White, 1996). As discussed in Section 1.4.1, the correlation function and the power spectrum completely specify the mass density

field. If galaxies trace the mass, the two point correlation function and power spectrum of the galaxies, ξ_{gg} and P_{gg}, coincide with ξ and P. However, this is probably not a good representation of reality. Galaxy formation involves complex gas dynamics and dissipative processes, and it is more natural to think that galaxies form in the highest peaks of the density distribution (Kaiser, 1984; Bardeen et al.). Thus, we need to allow for some *biasing* (Davis et al., 1985) towards the highest perturbations over the mean background. Quantitatively, biasing can be defined by introducing a *bias factor* b such that $\xi_{gg}(r) = b^2 \xi(r)$. Mo and White (1996) constructed a model for the spatial clustering of dark halos by extending the Press Schechter theory. They find that:

$$b\left(\nu, z\right) = 1 + \left(\nu^2 - 1\right)/\delta_c, \tag{1.74}$$

where δ_c is the critical linear overdensity at collapse which depends slightly on cosmology, and $\nu = \delta_c/\sigma(M, z)$ is the dimensionless amplitude of fluctuations that produce halos of mass M at redshift z. An updated version of the formula considering the ellipsoidal collapse model can be found in Sheth et al. (2001). It should be noticed that these approaches need to assume that the initial density perturbations are Gaussian. In Chapter 4 we present a more detailed and quantitative study of biasing in non-Gaussian cosmologies.

1.4.4 Numerical methods

Although analytical techniques provide a physical understanding of the processes involved in structure formation, they necessarily involve some kind of approximations, and they provide solutions only to special configurations and symmetries. Furthermore, the complications that arise in the study of higher order perturbation theory prevent analytical models from presenting detailed theoretical predictions that can be tested against observations. The only general methods for following the fully non-linear evolution of structure growth are therefore numerical simulations.

Nowadays, simulations have become a fundamental tool to construct a standard model for the formation of structures in the Universe, the so-called ΛCDM model, which represents a major theoretical paradigm of modern cosmology. Important achievements of numerical simulations include the study of the density profile of virialized dark matter halos, the non-linear parts of the clustering of dark matter, the temperature profile of galaxy clusters, among many others. The rapid growth of computer performance and, at the same time, the development of more sophisticated numerical algorithms are the key prerequisites to obtain accurate theoretical predictions with simulations. Hereafter, we will summarize some of the basic ideas of numerical simulations.

Since a large fraction of the mass in the Universe (about 90%) is constituted by dark matter, it is essential to model the collisionless component accurately. The

method used for this purpose is the N-body technique, which allows the representation of a portion of the Universe using a large number N of particles, which moves under their mutual gravitational attraction. Running an N-body simulation involves following the trajectories of a set of particles interacting within a rectangular box (most often cubic), assumed to be representative of the Universe as a whole. This means discretising the mass through N point-like particles and integrating their equations of motion till the present time.

The detailed procedure is essentially standard, in the sense that it identically applies whatever the model is one wishes to simulate. The information on the specific cosmology is embodied in the initial conditions (positions and velocities) of the distribution of particles. The N-body integrator starts acting upon these initial conditions at the beginning of the simulation and evolves them forward in time. Of course, the set-up of initial conditions is a delicate issue in its own right since inaccuracies or numerical artifacts may survive and be imprinted on the non-linear evolution of structures till the end of the computation.

The efficiency of the N-body simulations depends mainly on the algorithm used to compute the gravitational force. The simplest way to compute the force acting on a single particle is to sum up the contribution of all the particles in the simulations. In the Particle-Particle (PP) algorithm, the Newton force equation is modified as:

$$\vec{F}_j = \sum_{i \neq j}^{N} \frac{Gm_i\vec{r}_{ij}}{\left(\vec{r}_{ij}^2 + \epsilon_s^2\right)^{3/2}}, \tag{1.75}$$

where ϵ_s is the *softening length*, introduced to suppress two-body forces at very small separations. This parameter is equivalent to replacing a point mass by an extended body of size of order ϵ_s. A softening must be introduced for collisionless matter in order to ensure that two-body relaxation is not important, and also that no bound two-particle pairs can form. One can also view ϵ_s as a spatial resolution limit; structures smaller than this scale can not be represented.

Whereas the PP-method is really accurate, it cannot handle systems with a number of particles greater than $\sim 10^5 - 10^6$, because the computational time prohibitively scales as $O(N^2)$. The Particle-Mesh (PM) method offers a solution to this problem. The gravitational potential is here computed on a Cartesian grid with periodic boundary conditions, taking advantage of the Fast Fourier Transform (FFT) algorithms to speed up the solution of the Poisson equation in Fourier space. This method requires $N + N_g \log N_g$ operations for N particles and N_g grid points. Unfortunately, the force resolution on small scales is quite poorly resolved, since it is limited by the finite size of the grid, a serious limitation for the strong clustering occurring during cosmic structure formation. To combine the accuracy of the PP method with the computational efficiency of PM, in 1971 Hockney proposed a hybrid scheme, the P^3M approach, in which the long range forces are computed on a grid,

while the contribution due to the nearby particles, which change rapidly with time, is treated with the PP method.

Another revolution in the numerical simulation efficiency comes with the use of the hierarchical *Tree* algorithm (Appel 1985; Barnes and Hut 1986). The key point of Tree methods is to divide the space recursively into a hierarchy of cells, each containing one or more particles. If a cell of size l and distance d (from the point where forces need to be computed) satisfies the opening criteria $d > l/\theta$ (where θ is the accuracy parameter), the internal structure of the cell can be neglected and its gravitational field is approximated with a multipole expansion. Otherwise, the space is further subdivided in sub cells, if needed up to the point where the smallest cells contain at most one particle. The total computation time in this scheme is reduced by replacing the summation over all particles with a much shorter set of low-order multipole expansions of the gravitational potential of particle groups.

So far we have only discussed the numerical evolution of the collisionless material in the Universe. To model the visible matter it is necessary to also address the dynamics of the baryonic matter together with the non-baryonic component and to study hydrodynamical processes besides gravity. In fact, in the late time non-linear phase of structure formation, hydrodynamical and radiative effects become very important for galaxy formation. The simplest case of non-relativistic, non-radiative simulations of an ideal gas is a reasonable approximation for the hot plasma in clusters of galaxies. To add further realism to the simulations it is necessary to take into account radiative cooling and heating processes, as well as feedback to prevent excessive gas cooling.

A powerful technique used to model the hydrodynamical processes is the Smoothed Particle Hydrodynamic (SPH) approach. In SPH, the basic fluid equations are solved numerically by employing an ensemble of discrete particles, characterized by their positions, velocities and internal thermodynamic variables (like the thermal energy per unit mass). These particles have an associated spatial smoothing length h over which their properties are interpolated by a kernel function. Being a Lagrangian method, SPH allows for an accurate treatment of the self-gravity together with hydrodynamics, and is particularly well suited for cosmological simulations of structure formation, where an automatically adaptive resolution is required due to the high collapse factors of the mass.

In this thesis, we will make extensive use of these simulation techniques, all performed using the Lagrangian code GADGET (Springel et al., 2001b; Springel, 2005). In this simulation code, the gravitational interaction is computed with a Tree method, combined with a PM approach for long-range forces, yielding the so-called *Tree*PM method. The hydrodynamical processes are modelled with the SPH technique.

1.5 Problems of the Standard Model

In the previous paragraphs we have described what is known as standard cosmology. This framework is a remarkable achievement, describing with impressive accuracy the physical processes leading to the complex Universe around us. However, there remain some outstanding problems in cosmology. We will discuss below some of these problems of the standard model and delineate the development of the Inflationary Theory.

Small-scale inhomogeneity

The cosmological model we have outlined so far is incapable of explaining the origin of the primordial density fluctuations, whose existence is postulated as one of the fundamental aspects of the model's initial conditions. The large scale smoothness of the Universe is in contrast with the existence of small scale structures, such as galaxies and clusters of galaxies, which grow from primordial density inhomogeneity. Since none of the established physics that forms the basis of the standard model seems able to generate such perturbations, it is natural to place their origin within the uncertainties of the very early Universe, where quantum mechanical effects played a fundamental role and the classical, standard laws of physics lose their validity.

The theory of cosmic inflation provides a natural explanation for the existence of primordial perturbations, that in this scenario arise from quantum mechanical fluctuations being stretched by a period of super-expansion. Although this result represents the most important aspect of the theory, we will see that historical motivations which led to the introduction of inflation were rather different, stemming from the embarrassing fine-tuning problem of the initial conditions needed in the standard model to account for the properties of our observable Universe.

The flatness problem

Within the context of the standard cosmology, there is no explanation for the so called *flatness problem*, that simply concerns the fact that, among all the possible universes, the one we live in appears to represent an extremely peculiar entity.

From the Friedmann equations (1.9) we get after some manipulations,

$$\Omega(t) - 1 = \frac{Kc^2}{a^2 H^2}, \tag{1.76}$$

meaning that, for a Universe dominated by either matter or radiation, the combination $a\,H$ is a decreasing function of time, thus Ω deviates very rapidly from a value of unity. The flat geometry is then an unstable situation for the Universe (Liddle,

2003): if there is any deviation from it, this will get more and more emphasized with time. We can be more quantitative about this. If the only matter in the universe is radiation and dust, then in order to have Ω in the range observed today requires

$$\Omega(t_p) \simeq 1 + (\Omega_0 - 1)10^{-60}, \tag{1.77}$$

i.e. the kinetic term computed at the Planck time ($t_p = 10^{-43}$ sec) should differ from the gravitational one by less than 10^{-60}, which means an extremely tiny deviation from the critical value. Almost all initial conditions for Ω should lead to either open or closed "extreme" models, but no evolution comparable to what we observe today should ever be possible.

This fine tuning problem is related to the so called "oldness problem": if Ω, instead of being so close to unity, was exactly 1 at the Planck time, the universe would have either (for $K > 0$) recollapsed in few 10^{-43} sec, or (for $K < 0$) it would have reached a temperature of 3K after 10^{-1} sec. So the problem translates into asking why the universe has been able to last so long (≈ 15 Gyr).

The horizon problem

There seems to be a fundamental incompatibility between the Cosmological Principle and the existence, in the Friedmann models, of a *particle horizon*, unless we require that large-scale homogeneity and isotropy of the Universe is part of its initial conditions. We have already mentioned that the strongest piece of evidence in favour of the Cosmological Principle is the striking uniformity of the temperature field of the cosmic background radiation. Such observational evidence can only be explained assuming that the entire universe was in causal contact when the radiation last scattered; in this way any temperature fluctuation would have been smoothed out. However, within the standard cosmological model the existence of particle horizons forbids such causal connection at the last scattering epoch.

Light signal can only propagate a finite distance between the Big Bang and present. The set of points capable of sending light signals that could have been received by an observer O up to some generic time t is said to be causally connected with the observer. These points must be located inside a sphere centered upon O, with proper radius:

$$R_H(t) = a(t) \int_0^t c \frac{dt'}{a(t')}.$$

If, at $t = 0$, the integral converges to a finite value, then R_H exists and is called "particle horizon" at time t. Such a horizon therefore exists in conventional Big Bang models, which are dominated by radiation at early time. When we look at the CMB we are observing the universe at redshift $z_{ls} \approx 1000$; meanwhile, the comoving distance between an observer located at t_0 and a point on the last scattering surface

is related to the proper radius by:

$$r_{ls} \approx \frac{a}{a_0} D_C = \frac{c(t_0 - t_{ls})}{(1 + z_{ls})} \approx c \frac{t_0}{z_{ls}}.$$

However, the radius of the particle horizon at this epoch is given by:

$$R_H(z_{ls}) \approx 3ct_0 z_{ls}^{-3/2} \approx 3r_{ls} z_{ls}^{-1/2} \approx 10^{-3/2} r_{ls}.$$

Hence, following the standard model $R_H < r_{ls}$, which means that an observer located at t_0 sees different zones on the last scattering surface that are causally disconnected, because they have non-overlapping horizons. This in contrast with observations.

In reality, the horizon problem has even deeper implications. Not only homogeneity represents a problem, but also the existence of small irregularities in the temperature field, which cannot be generated casually in this framework, and need to be acknowledged as pre-existing.

Missing relics

Within the context of unified gauge theories there are several stable, super-heavy particle species, produced in the very early universe, which should have survived till today, i.e. not being annihilated during the evolution of the universe. An estimate of the contribution that such particles should bring to the present energy density gives $\Omega_X \ll 1$, a value largely above the observational constraints. An example of this kind of particles is the magnetic monopole, which should be present in large abundances but has never been found. The expected number density of monopoles works out to be $\Omega_M \simeq 10^{16}$, completely incompatible with current limits. Therefore, it is necessary to find some physical way to dilute their density in the early universe.

1.5.1 The cosmological constant problem(s)

In the next sections we will see how cosmological inflation can elegantly solve the three critical issues we have mentioned so far. However, there is anyway another central problem, which inflation does not solve and which remains the most significant concern of modern cosmology.

The most general form of Einstein's equations takes into account a term containing the so-called cosmological constant Λ. From the Friedmann equations, corrected for the presence of a cosmological constant term, along with already mentioned observational constraints, we can set an upper limit for the present-day density of the Λ component:

$$|\rho_\Lambda| \leqslant 10^{-48} \text{ GeV}^4,$$

corresponding to $|\Lambda| < 10^{-55} \text{ cm}^{-2}$ and $m_\Lambda < 10^{-32} \text{ eV} \approx 10^{-43} \text{ g}$. This limit

is hard to account for with 'natural' explanations, at least within the dominant interpretative scenario for the cosmological constant term. Indeed, this would imply that at the Planck time the ratio of the cosmological constant energy density to the ambient density would be $\rho_\Lambda/\rho_{t_p} \approx 10^{123}$. Therefore, the cosmological constant problem is another *fine tuning problem*, resulting from the fact that the dark energy appears to be so unnaturally small compared to any fundamental scale of physics.

One modern interpretation of the existence of a dark energy term regards Λ as a measure of the energy density of the *vacuum*, identified with the state of lowest energy for a quantum system. This interpretation is strengthened by the finding that the energy momentum tensor of the vacuum, when compared to that of a generic perfect fluid, leads to an equation of state $p_{\text{vac}} = -\rho_{\text{vac}}c^2$. The vacuum can therefore be thought as a perfect fluid with $w = -1$, hence the identification with Λ.

In addition to the small dark energy density, the vacuum energy presents another puzzle: the coincidence between the observed vacuum energy and the current matter density. Our best fit model for the Universe (Riess et al., 1998) features vacuum and matter density of roughly the same order of magnitude today, but the ratio of these quantities changes rapidly as the Universe expands: $\Omega_\Lambda/\Omega_m = \rho_\Lambda/\rho_M \propto a^3$. As a consequence, at early time the vacuum energy should have been negligible compared to matter and radiation. There exists only a brief epoch during the history of the universe in which it is possible to witness the transition from the domination of one type of component to another. Comparing the energy density of matter and dark energy, we infer that the crossover must have taken place at a recent cosmological time, $z \simeq 0.4$. This is the so-called *coincidence problem*: we happen to live around the time when the dark energy has started to become important.

1.6   The inflationary solution

Among the issues just mentioned, the horizon problem is an especially serious one. Any solution seems to require an important modification to how information can propagate in the early Universe. Cosmological inflation is such a mechanism.

The basic idea is that during the early stages of the evolution there has been an epoch in which the vacuum energy density of some scalar field Φ gives the dominant contribution to the total energy density. During this phase the universe undergoes an accelerated expansion in which the scale factor a grows nearly exponentially. As a consequence of such an expansion, a small causally connected region can grow to a size exceeding the present size of our universe (which is of order H_0^{-1}). If the horizon radius is greatly increased, distant points in the CMB have actually been in casual contact before, and unwanted relics are tremendously diluted, solving the monopole problem. In addition, the effect of the acceleration is to quickly expand a

small region of the Universe to a huge size, thus diminishing the spatial curvature of the space and making the Universe extremely close to flat.

In all viable models, inflation occurs at an energy scale of $\approx 10^{14}$ GeV ($t \approx 10^{-34}$ sec), when the GUT transition occurred, leading to an increase of the scale factor of order $\sim e^{70}$. Inflationary theories provide a full model accounting for the physical origin of such an expansion, and eventually reconcile the inflationary scenario with the standard model, which must take over at $t \sim 1$ sec. Assuming validity of general relativity, the requirement $\ddot{a} > 0$ results in the constraint $\rho + 3p < 0$ for the nature of the material driving the expansion, which implies the peculiar property of a negative pressure.

According to fundamental particle physics, the key idea at the basis of the unification of fundamental interactions is that of *phase transitions*, which can be naively defined as the mechanism by which a system, initially in a ordered phase characterised by a certain symmetry, moves towards an unordered phase with a smaller degree of symmetry. Phase transitions are controlled by an unusual form of matter known as a *scalar field*, describing spin-0, scalar particles. Depending on the nature of the transition, scalar fields can behave as if they possess negative pressure, satisfying the inflationary condition. Once the phase transition comes to an end, the scalar field decays away and the inflationary expansion terminates. No specific particle physics phase transition has so far been identified to be the one giving rise to inflation, and a large number of different models still coexist, mainly relying on motivations from modern supersymmetry theories.

The dynamics of inflation

We here illustrate some basic concepts of the dynamics of the inflationary field. For further details and an extensive treatment, we refer the reader to the text by Liddle & Lith (2000).

In the local rest-frame, a homogeneous scalar field ϕ behaves as a perfect fluid with:

$$\rho_\phi = \frac{1}{2}\dot{\phi}^2 + V(\phi), \tag{1.78}$$

$$p_\phi = \frac{1}{2}\dot{\phi}^2 - V(\phi). \tag{1.79}$$

The condition for inflation, $\ddot{a} > 0$, is therefore satisfied provided $\dot{\phi}^2 \ll V(\phi)$; the potential energy of the scalar field is the dominant contribution to both the energy density and the pressure, and the resulting equation of state approximates that of a cosmological constant ($p \simeq \rho$). The equation of motion of the scalar field, taking into account the expansion of the Universe, is given by:

$$\ddot{\Phi} + 3H\dot{\Phi} + \frac{\partial V}{\partial \Phi} = 0, \tag{1.80}$$

where H assumes the form

$$H^2 = \frac{8\pi G}{3}\left[V(\phi) + \frac{1}{2}\dot{\phi}^2\right] = \frac{1}{3M_{Pl}^2}\left[V(\phi) + \frac{1}{2}\dot{\phi}^2\right], \tag{1.81}$$

and M_{Pl} is the reduced Planck mass. Eq. (1.80) can be interpreted as describing the field ϕ rolling down towards a minimum ϕ_0, under the action of a force $\partial V/\partial \phi$ and against a source of friction given by the term in H.

The standard technique for analysing inflation consists of the *slow-roll* approximation, which throws away the last term of Eq. (1.81) and the first term of Eq. (1.80), leaving:

$$H^2 \simeq \frac{V(\phi)}{3M_{Pl}^2}, \tag{1.82}$$

$$3H\dot{\phi} \simeq -\frac{\partial V(\phi)}{\partial \phi}. \tag{1.83}$$

For this approximation to be valid, it is necessary that:

$$\epsilon(\phi), \quad |\eta(\phi)| \quad \ll 1, \tag{1.84}$$

where

$$\epsilon(\phi) \equiv \frac{M_{Pl}^2}{2}\left(\frac{V'}{V}\right)^2, \tag{1.85}$$

$$\eta(\phi) \equiv M_{Pl}^2\left(\frac{V''}{V}\right), \tag{1.86}$$

and primes denote derivatives with respect to ϕ. The smallness of the slow-roll parameters ϵ and η constrains the potential V to be approximately flat: this is anyway just a necessary consistency condition for the slow-roll approximation to be valid, and not a sufficient one, as no requirements are set for the size of the kinetic term in $\dot{\phi}$, which could in principle be as large as one wants. A further assumption is then required, namely that the solution for a given potential satisfies Eq. (1.83).

The physical meaning of the slow-roll approximation is to consider a very gentle evolution of ϕ towards ϕ_0; this allows one to neglect the kinetic term in Eq. (1.81) and the acceleration in Eq. (1.80). The importance of this approximation lies in the fact that it can follow the evolution of the inflaton field for almost any choice of the potential, unlike the full equations. In typical models, the "slowly-rolling" phase lasts $\sim 10^{-32}$ s. At the beginning of this phase, the extension of the causally connected region is of the order of $\sim H(t_b)^{-1}$; then, in a very short time interval Δt it expands by an enormous factor ($\sim \exp(\Delta t)$). Hence, any inhomogeneity and anisotropy present at the beginning can be soon smoothed out. As Φ approaches the minimum, it begins to oscillate on a short time scale compared to the Hubble time. Such oscillations are damped by particle creation or by the decay of Φ into lighter

particles. The thermalization of these particles is responsible for the reheating of the universe to a temperature $T_{rh} \leqslant T_c$ (where the equality holds if the conversion of vacuum energy into new particles is perfectly efficient). At the end of this stage, the Universe starts evolving like a radiative Friedmann universe, and the standard model finally takes over.

Solving the problems of Standard Cosmology

During inflation the energy density of the universe $\rho_{\text{TOT}} \simeq \rho_\Phi$ is approximately constant, because ρ_Φ varies slowly with time, while the scale factor grows exponentially so that the initial value of Ω becomes very close to unity. From the hypothesis that the duration of the process is large than a certain number N of *e-foldings* :

$$N \equiv \ln\left(\frac{a_f}{a_i}\right) \geqslant 60 \left[\frac{2.3 + \frac{1}{30}\ln\left(\frac{T_f}{T_P}\right) - \frac{1}{60}\ln z_{eq}}{|1 + 3w|}\right], \qquad (1.87)$$

where t_{end} sets the end of inflation, we infer that only in recent epochs we can have measurable deviations of Ω from the initial value. The inflationary solution to the flatness problem ensures that *regardless* of its initial value, the phase of inflationary expansion will drive Ω extremely close to 1, such that in all the subsequent evolution up to the present day it remains indistinguishably close to unity.

The solution to the horizon problem also arises naturally from the general definition of inflation we just have given. The cosmological horizon (or radius of the Hubble sphere) has comoving size $r_c = c\, a_0/\dot{a}$. A given comoving scale l_0 enters the cosmological horizon (and gets causally connected) at a finite time $t_H(l_0) \neq 0$, due to the fact that r_c grows with time. This comoving scale can eventually escape from the horizon if there exists a time interval $t_i < t < t_f$ during which $r_c < l_0$. This can happen only if:

$$\dot{r}_c < 0 \iff -\frac{\ddot{a}}{\dot{a}} < 0 \iff \ddot{a} > 0.$$

Hence, an accelerated expansion is required during this interval. Therefore, regions outside the horizon would present a high degree of homogeneity because they have been causally connected in the past. Such accelerated expansion is provided by inflation with the condition:

$$r_c(t_f) \ll r_c(t_i),$$

which requires a number of e-foldings $N > 60$.

Finally, provided the GUT transition occurred before the inflationary epoch, the number density of magnetic monopoles can get dramatically diluted by the expansion, down to a level consistent with current observations. In any case, it is clear that the extent to which the inflationary solution is valid depends entirely on how much expansion it effectively caused, and this is measured in terms of e-foldings. To fully solve the issues of the standard model, around seventy e-foldings

during inflation are required.

1.6.1 Cosmological perturbations: the rise of non-Gaussianity

The most attractive aspect of inflation is that it provides an explanation for the
very existence of cosmic structures, since it can explain the production of the seed
perturbations. These are believed to originate as quantum mechanical fluctuations
of the inflaton field, whose existence is a direct consequence of the uncertainty
principle. The reason why these fluctuations survive and eventually give rise to
irregularities in the radiation and matter field must be sought within the inflationary
dynamics and critically depends upon the characteristic scales of the fluctuations
themselves.

The overall evolution can be summarized as follows: quantum fluctuations arise
on scales which are much smaller than the comoving Hubble radius $(aH)^{-1}$, the scale
beyond which casual processes cannot operate. On such small scales, flat space-
time quantum field theory is valid and accounts for the temporal evolution of the
perturbations. The inflationary expansion stretches the wavelength of fluctuations
to scales outside the horizon, where they follow the classical evolution and have
their amplitude "frozen-in" at the value of horizon crossing. The perturbations in
the scalar field show up as irregularities in the energy density ρ_ϕ, which are then
inherited by the radiation and matter field to which the inflaton field decays during
reheating. After the end of the inflationary stage, the Hubble radius increases faster
than the scale factor and perturbations will eventually re-enter the horizon at some
point in the radiation or matter dominated era (see Bartolo et al., 2004, for further
details).

The applicability of linear theory to the generic cosmological perturbations prob-
lem has a natural justification when we consider that the local deviations from the
homogeneous background field are small. Nevertheless, the technique has the limit
of being completely blind to second-order dynamics involving the inflaton field,
basically any interactions with other fields or itself. Within this approach, primor-
dial perturbations have uncorrelated Fourier components: in other words, they are
Gaussian. Given a generic perturbation $\delta\phi(\vec{x}, t)$, the probability distribution of the
Fourier space coefficients $\delta_{\vec{k}}$ can be expressed as:

$$\delta\phi_{\vec{k}} = |\delta\phi_{\vec{k}}| \, \exp(i\theta_{\vec{k}}) = Re \, \delta\phi_{\vec{k}} + i \, Im \, \delta\phi_{\vec{k}}. \tag{1.88}$$

The perturbation in configuration space is just a sum over a large number of Fourier
modes and, according to the central limit theorem, their independence guarantees
that the resulting superposition will be Gaussian distributed. Asking for Gaussianity
in this case results in two separate requirements:

 - random phases, i.e. θ_k uniformly distributed over $[0, 2\pi]$;

- Rayleigh distribution for the moduli of the Fourier amplitudes, i.e.

$$P(|\delta\phi_k|)\,\mathrm{d}|\delta\phi_k| = \frac{|\delta\phi_k|}{\delta\phi_k^2}\,\exp\left(-\frac{|\delta\phi_k|^2}{2\delta\phi_k^2}\right)\,\mathrm{d}|\delta\phi_k|. \tag{1.89}$$

These assumptions do not result in too much of an error though, when the standard, single-field, slow-roll inflationary model is investigated. In this case, self-interactions of the inflaton field are present, but suppressed as a consequence of the flatness of the inflaton potential, or smallness of the slow-roll parameters.

However, second-order effects are not always negligible: they are in fact predominant in less-simplistic, non-standard inflationary scenarios. In these cases interactions cannot be neglected, vacuum fluctuations of different Fourier modes will couple, and a characteristic non-Gaussianity will arise in the perturbation field[7].

The phase association induced by quadratic non-linearities is termed *quadratic phase coupling* (Coles and Chiang, 2000); as a consequence of the non-randomness of phases, the evolution of the Fourier modes at different wave-numbers becomes coupled and the resulting superposition will not be Gaussian distributed. In the framework of single-field models, whenever a flat potential is required for inflation to occur, the existence of self-interactions and gravitational coupling brings no effective deviation from the results of linear theory, and the perturbations can effectively be regarded as Gaussian. This is not the end of the story, though, as it seems more natural to expect that several scalar fields other than the inflaton co-existed during the inflationary epoch. The constraints on the magnitude of non-linearities need not to be obeyed by these collateral fields, whose contribution to the total energy density is sub-dominant with respect to the inflaton; the latter still remains the only field responsible of the inflationary dynamics.

Perturbations arising in the dominant and subordinate fields have different imprints on the subsequent matter and radiation fluctuations: the former are referred to as *adiabatic*, while the latter are *isocurvature* perturbations. Perturbations of the adiabatic type involve fluctuations in the existing field such that the entropy does not vary spatially, while those of isocurvature type have zero net fluctuation in the energy-density and conversely involve entropy fluctuations. The combined study of CMB anisotropies and the large-scale matter distribution constrains the amount of allowed isocurvature perturbations to only a small fractional contribution, thus reducing the role of sub-dominant fields in the context of cosmological perturbations. Nevertheless, couplings between these fields and the inflaton are naturally expected and could have resulted in an effective production of considerable non-Gaussianity. Bartolo et al. (2001) have shown that such a coupling gives rise to a new mechanism for generating quantum fluctuations in the scalar fields, the oscillation mechanism, according to which the fluctuations in a scalar field χ can

---

[7]Accounting for interactions means allowing for terms beyond the quadratic term to be present in the inflaton potential V

evolve into fluctuations of the inflaton field ϕ, with a calculable probability, in a way similar to the phenomenon of neutrino oscillations.

We will not go any further in this subject, and just remark that there are physically motivated models where the existence of primordial non-Gaussianity is naturally accounted for. In Chapter 4, we will study the effect of primordial non-Gaussianity on structure formation through the use of numerical simulations in the case of standard, single-field models of inflation. We shall examine a simple class of mildly non-Gaussian perturbations described by a sort of Taylor expansion around the Gaussian case:

$$\Phi(\vec{x}) = \Phi_{(1)}(\vec{x}) + f_{\mathrm{NL}}^{\Phi} \left[\Phi_{(1)}^2(\vec{x}) - \left\langle \Phi_{(1)}^2(\vec{x}) \right\rangle \right], \qquad (1.90)$$

where $\Phi^{(1)}(\vec{k})$ is a Gaussian random field and f_{NL} is the *non-linearity parameter* controlling the magnitude of non-Gaussianity in the gravitational potential. The value and functional dependence of f_{NL} is of central importance in the study of the effects of primordial non-Gaussianity on the evolution of structures in the Universe, which is one of the subjects of this Thesis.

1.7 Dark energy

As seen in the previous sections, the most favoured cosmological model predicts that the Universe contains close to homogeneous dark energy which approximates a cosmological constant. The so-called Λ seems to be a good dark energy candidate in order to give an interpretation of the observed large-scale dynamics of the Universe; in particular it explains very well the recent phase of acceleration in the cosmological expansion. However, it theoretically lacks a meaningful underlying physical motivation and is affected by the fine tuning and coincidence problems (see Section 1.5.1). In fact, the cosmological constant, which is strongly connected to the energy density of the vacuum, is of the same order of magnitude as the amount of dark and baryonic matter energy density today. This number is very tiny in terms of the natural scale of primordial energy density given by the Planck mass, and assuming that the vacuum energy density is constant, it is very difficult to understand why it should be so small at the present epoch.

In order to solve this problem, it has been proposed that Λ might be very small now because it has been rolling towards zero for a very long time. Therefore, the dark energy can be explained in terms of the large age of the Universe (Wetterich, 1988). Much discussed nowadays are scenarios in which the dark energy is a homogeneous scalar field, named quintessence and slowly evolves in a runaway potential which decrease monotonically to zero (Wetterich, 1988; Ratra and Peebles, 1988; Caldwell et al., 1998). This idea arose also in particle physics, through the discussion of phase transitions in the early universe and the search for a dynamical

cancellation of the vacuum energy density. We refer the reader to the reviews by Peebles and Ratra (2003) and by Wetterich (2002) for a thorough discussion of the subject.

The dynamical evolution of dark energy is modelled through the study of a homogeneous scalar field ϕ, whose kinetic energy is $T_{\text{kin}} = \dot{\phi}^2/2$ and the potential is $V(\phi)$. If the spatial curvature can be neglected, the field equation is:

$$\ddot{\phi} + 3\frac{\dot{a}}{a}\dot{\phi} + \frac{\partial V}{\partial \phi} = 0. \tag{1.91}$$

In the rest frame of an observer moving such that the Universe appears isotropic, the energy momentum tensor of the scalar field is diagonal, and its time and space parts define the energy density and pressure, as

$$\rho_\phi = \frac{1}{2}\dot{\phi}^2 + V(\phi), \tag{1.92}$$

$$p_\phi = \frac{1}{2}\dot{\phi}^2 - V(\phi). \tag{1.93}$$

Therefore, the general form of the equation of state relating ρ_ϕ and p_ϕ becomes:

$$w = \frac{\frac{1}{2}\dot{\phi}^2 - V(\phi)}{\frac{1}{2}\dot{\phi}^2 + V(\phi)}, \tag{1.94}$$

with the condition $w < 1/3$ to have an accelerated expansion. In analogy to what happens during the inflationary dynamics, if the scalar field varies slowly in time, $\dot{\phi}^2 \ll V(\phi)$ (slow-rolling condition), the dark energy reduces to the cosmological constant. At the end of the inflationary phase, however, the scalar field is supposed to vary rapidly enough to produce the entropy of the Universe, and therefore the baryons, leaving ρ_ϕ close to zero. The dark energy may patch on to the part of the scalar field responsible for inflation, if the time evolution of ρ_ϕ starts to slow down and become slower than that of the matter density.

There are many well justified choices of scalar potentials that asymptote gradually to zero, namely in the form of power laws (Lucchin and Matarrese, 1985; Peebles and Ratra, 1988), inverse power laws (Ratra and Peebles, 1988), and exponential potentials (Ratra and Peebles, 1988; Wetterich, 1988; Ferreira and Joyce, 1998). One of the prototypical quintessence models is a scalar field ϕ with an exponential potential (Wetterich, 1988) of the form:

$$V(\phi) = M_P^4 \exp(-\alpha\phi/M_P). \tag{1.95}$$

The constant α determines the fraction that the dark energy contributes to the total energy density as compared to the critical energy density, via:

$$\Omega_d = \frac{\rho_\phi}{\rho_c} = \frac{n}{2\alpha^2}, \tag{1.96}$$

where $n = 4$ for radiation and $n = 3$ for non-relativistic matter. In the case where the background density dominates, one finds an attractor scaling solution, or *tracker solution*, where the scalar kinetic and potential energy density scale proportional to matter or radiation.

Two features are particularly interesting in this respect. The first is that the scaling solution is obtained independently of the precise initial conditions (Zlatev et al., 1999), i.e. whether ρ_ϕ at the beginning is of the same order or much smaller than the background energy density. Under the condition that the dark energy density is emerging only now, we can determine the characteristic energy scale set by the value of Λ: for example, for $\alpha = 2$, the required value for Λ is ~ 10 MeV, which falls in a reasonable range from a high energy physics point of view. Secondly, the solution has also the property that ρ_ϕ is decreasing less rapidly than the mass density in matter and radiation, and the final attractor corresponds to scalar field dominance.

Modifications of a pure exponential potential (Albrecht and Skordis, 2000) can lead to a local minimum in the potential in which the field can be trapped and can explain the emergence of the quintessence component out of the background density. These models, however, do not provide a solution to the coincidence problem.

The k-essence scenario (Armendariz-Picon et al., 2000) is based on the idea that the scalar field has a dynamics which is sensitive to the differences between matter and radiation-dominated universes, and its energy density becomes constant only after the equivalence epoch. This would explain why the scalar field becomes important now. Also, the introduction of a direct interaction between the dark energy fluids and other cosmic components is a way to account for late time dark energy domination, in particular for models with strong coupling (Amendola, 2000; Amendola et al., 2008). Another possibility is that the acceleration happens from time to time, so that there is nothing special about the present era. This scenario can be accomplished by oscillating dark energy (Dodelson et al., 2000).

A very interesting feature of dynamical dark energy is that it is experimentally testable, through the study of distances and structure growth. In particular, different dark energy models produce a different value of the equation of state parameter, both today and in the past. A wealth of phantom (or ghost) models (Caldwell, 2002; Kujat et al., 2006) have been proposed to account for the possibility, allowed by observational data, that w is slightly more negative than -1. Moreover, attempts to explain the recent acceleration without invoking a dark energy field have also been developed: within the framework of general relativity, an inhomogeneous world model, with a metric different from the FLRW one, while a more radical approach to the problem is the idea that general relativity itself breaks down on large scales (modified gravity theories, see e.g. Durrer and Maartens, 2008). The study of such models goes however well beyond the scope of this work. Instead we will provide in the following Section a detailed description of the parametric approach we will follow in our research work.

1.7.1 Parametrizing dark energy

Another much discussed approach to the study of the dark energy is to characterize dark energy models through parameters that fit and describe observational measurements. Since a clear front runner for a comprehensive model does not exist, instead of considering a specific potential for the scalar field, it is more convenient to trace the evolution of the dark energy in terms of few quantities which accurately portray its key physical properties. Different parametrizations have been proposed for the evolution of the energy density, $\Omega_\Lambda(z)$, and the equation of state parameter, $w(z)$. Of course, a successful fitting function should be able to faithfully reproduce the properties of an entire class of dark energy models.

Introducing a dynamical energy component generally modifies the equation of state to the more general form $p = w(z)\rho$, with negative pressure. For the sake of simplicity, the first assumption we can make is that the equation-of-state parameter of the dark energy component is constant but not strictly equal to 1, so that the energy density associated to this component does evolve with time. As proposed in the literature (e.g., see Wang and Steinhardt, 1998; Weinberg and Kamionkowski, 2003) and studied in this Thesis, this difference with respect to the standard case with $w = -1$ is indeed enough to affect the growth of density perturbations and their evolution.

Nevertheless, there are no strong theoretical reasons for restricting our attention to a constant w. The equation of state can be studied in terms of an unknown variable whose behavior is guessed by means of a suitable fitting function $w(z)$, under the assumption of a moderate evolution with redshift. Several possibilities for this have been proposed in literature. In particular, two parameters representations, e.g. $w(a) = w_0 + w_a(1 + a)$, based on the physical formulation proposed by Chevallier and Polarski (2001), and, later, by Linder and Jenkins (2003), have been shown to be a robust and widely applicable way to match a great variety of dark energy physics. In this case the two key parameters are the value of the equation of state parameter today, w_0, and its time variation, $w' = \mathrm{d}w/\mathrm{d}\ln a$. Indeed, it has been shown (Linder and Huterer, 2005) that even with observational data corresponding to the next generation of supernovae distances, CMB and weak lensing shear, it is extremely challenging to accurately measure the dark energy with a more elaborate parametrization. Moreover, a larger number of parameters than two is not viable for a general fit if we are interested in parameters that are directly related to the nature and dynamics of the dark energy. A main virtue of the parametrized forms is their model independence and the fact that they embrace the behavior of a wide class of dark energy models. On the other hand, a primitive fit may distract our attention from a more fundamental explanation of the phenomenon.

In this Thesis we study more restricted, local parametrizations, in an effort to distinguish finely between physical models. We focus on the so-called *early dark energy* models, in which the contribution of the energy density at early times is

not negligible. In this case the evolution of the equation of state parameter is directly related to the asymptotic early value of the energy density, Ω_E, which constitutes the second parameter of the model, besides w_0. Experimental data may constrain this component with the requirement that the dark energy is subdominant during the radiation era, and for a large fraction of the matter domination. Current upper limits on the fraction of dark energy density at the last scattering surface are $\Omega_{\mathrm{EDE}}(z_{lss}) < 2.3 \times 10^2$ (Xia and Viel, 2009). We also adopt a specific model for early dark energy that parametrizes the evolution of the dark energy density (see Doran and Robbers, 2006). Remembering that the general expression of the energy density contributed by a generic form of dark energy, neglecting radiation, is (see Eq. 1.17):

$$\Omega_{\mathrm{de}}(z) = \Omega_{\mathrm{de},0} \exp\left(-3 \int \mathrm{d} \ln a \left[1 + w\left(a\right)\right]\right),\tag{1.97}$$

we can directly relate it to the equation of state by:

$$w_{\mathrm{de}}(a) = \frac{-\mathrm{d}\Omega_{\mathrm{de}}/\mathrm{d}\ln a}{3(1 - \Omega_{\mathrm{de}})\Omega_{\mathrm{de}}}.\tag{1.98}$$

In the same vein, also the potential $V(a)$ of the scalar field can be reconstructed given a functional form of the equation of state.

Early Dark energy models have been investigated by several authors (see, for instance, Wetterich, 2004; Bartelmann et al., 2006; Doran and Robbers, 2006; Linder, 2006). Direct consequences of these models are a decrease of the distance measurements and of the age of the Universe. Moreover, they affect the density perturbations and the growth of cosmic structures, so that an observational confirmation of these theoretical predictions would give an important clue to the physics of dark energy.

1.8 Thesis outline

Cosmology is nowadays going through an era of important advances and discoveries. Precision observations of the Cosmic Microwave Background and of the large-scale clustering of galaxies have confirmed earlier indications that the Universe is undergoing an epoch of accelerated expansion in the present epoch, driven by some form of dark energy. Observations also suggest that the Universe underwent a period of accelerated expansion in its early history, known as inflation. In this Thesis we present research that probes the nature of these two cosmological periods.

The primary aim of this work is to make accurate predictions for the non-linear structures that develop in specific non-standard cosmologies, which consider alternatives to the simple concordance model of the Universe and try to solve some of its problems. Examples for such non-standard cosmologies that we analyze in detail include models where an Early Dark Energy component impacts the linear and non-

linear growth of the structures, and models where the primordial density fluctuation field has a non-Gaussian contribution. We will also discuss whether the observations can be equally well explained in these alternative cosmological scenarios and the possibility of testing their predictions by forthcoming data.

High-resolution numerical simulations are used as a primary tool to explore the outcome of both Early Dark Energy and non-Gaussian cosmological models. Numerical methods are arguably the most general and accurate method for investigating the non-linear growth of structures in its full geometrical complexity, and they constitute the link between theoretical models, which provide the initial conditions of the Universe, and observations of clusters and galaxies today. Such comparisons will provide important hints for the physics that need to be included in viable models for the formation and evolution of structure in the Universe.

This Thesis is structured as follows. We begin our investigation in Chapter 2 with the study of the non-linear structure formation in Early Dark Energy (hereafter, EDE) cosmologies. As mentioned before, in these scenarios, the dark energy contributes a substantial fraction of the energy density even at early times, unlike for example a cosmological constant. By comparing theoretical predictions with a comprehensive set of simulated data, we accurately measure the quantitative impact of EDE on the abundance and structure of dark matter halos. Extensions of the spherical top-hat collapse model (Bartelmann et al., 2006) predict that the virial overdensity and linear threshold density for collapse should be modified in EDE cosmologies, yielding significant modifications in the expected halo mass function based on the Press and Schechter (1974) or Sheth and Tormen (1999) formalisms. Therefore, we pay particular attention to measurements of the halo mass function and to tests whether analytical predictions and fitting formula still work reliably in such cosmologies. In the second part of the Chapter, we study the properties of halos by looking at the virial relationship between mass and dark matter velocity dispersion in different dark energy cosmologies. We compare our results with previous calibrations (Evrard et al., 2008). We also verify that the earlier formation of structure in EDE models affects the concentration of halos and we estimate this effect. Finally, we test how well the growth of the mass function can be tracked by counting halos as a function of the line-of-sight velocity dispersion of their substructures, skirting the ambiguous problem of assigning a mass to the halo. This method can serve as a proxy for the directly measurable line-of-sight motion of galaxies in observations, and looks very promising to put constraints on the equation of state parameter.

We will then move on in Chapter 3 to the study of one particular question in more detail, namely the impact of EDE on the Sunyaev Zeldovich (SZ) effect. Indeed, the most significant observable consequence of EDE models is that the counts of cluster-sized halos should decrease more slowly towards higher redshift than in the standard cosmological model (Bartelmann et al., 2006). Therefore, future cluster surveys

of the thermal SZ-effect should provide ideally suitable data for testing the dark energy physics. In this work we perform several high-resolution hydrodynamical simulations that cover a wide range of viable dark energy cosmology and generate synthetic maps both of the thermal and kinetic SZ effect. The global properties of the SZ effect, given in terms of statistical properties of the maps and source number counts, are analyzed in detail, focusing on the aspects connected with the different physical models adopted. We also present forecasts for future measurements of the SZ number counts and we discuss the prospects of constraining the properties of a dark energy component with ongoing SZ surveys, in particular the one carried out with the South Pole Telescope (SPT Ruhl, 2004). Of most interest here is also to understand how well clusters behave as 'SZ standard candles" and how large their intrinsic scatter in the Y-M relation is. Therefore, we will extend the analysis of the Y-M correlation to the early dark energy case and show at what radius (or overdensity) one should measure the integrated SZ effect and define cluster masses so as to achieve the tightest possible scaling. In the last part of this Chapter, we investigate whether early dark energy models have a distinct signature in the power spectra of the Cosmic Microwave Background and we quantify this effect.

While the first part of the Thesis deals with early dark energy cosmologies, in Chapter 4 we turn to the question of non-Gaussian initial conditions. Based on N-body simulations, we present tests of analytical formulae describing the halo abundance and clustering for non-Gaussian initial conditions. Following a standard procedure, we model departures of non-Gaussianity through a quadratic Gaussian term in the primordial gravitational potential, characterized by the dimensionless non-linearity parameter f_{NL}. Using a series of high-resolution N-body simulations, we calibrate the analytic formulation of the mass function in non-Gaussian cosmology by Matarrese et al. (2000) and Lo Verde et al. (2008), and we verify the theoretical prediction of a strong scale-dependence of the halo bias (Dalal et al., 2008). The description of the abundance and clustering of halos for non-Gaussian initial conditions has recently received renewed interest, motivated by the forthcoming large galaxy and cluster surveys, which can potentially yield constraints of order unity on the non-Gaussianity parameter f_{NL}. Therefore, we discuss the implications of this correction on present and forecasted primordial non-Gaussianity constraints, confirming that the non-Gaussian halo bias offers a robust and highly competitive test of primordial non-Gaussianity.

Finally, we summarize the main findings of this Thesis in Chapter 5, and provide an outlook on future work.

2

Dark matter structures in early dark energy cosmologies

2.1 Introduction

Arguably the most surprising result of modern cosmology is that all matter (including both atoms and non-baryonic dark matter) accounts for only a quarter of the total energy density of the Universe today, while the rest is contributed by a *dark energy* field. In 1999, observations of type Ia supernovae by the Supernovae Cosmology Project (Riess et al., 1999; Riess, 2004) and the relative accurate measurements of the distances to this objects (Perlmutter, 1999; Kowalski, 2008) demonstrated that the expansion of the Universe is accelerated today; there hence exists a mysterious force that acts against the pull of gravity. Nowadays, the inference that this is caused by dark energy can be made with significant confidence, as the observational evidence has further firmed up. In fact, we have good reason to believe that we live in a flat universe with an upper limit of $\Omega_m \leqslant 0.3$ for the matter density today, based on cosmic microwave background measurements and a host of other observational probes (Komatsu et al., 2009a, e.g.). These observations yield a consistent picture, the so-called concordance cosmology, and are in agreement with predictions of the inflationary theory.

The physical origin of dark energy is however unknown and a major puzzle for theoretical physics. A nagging outstanding problem is that most quantum field theories predict a huge cosmological constant from the energy of the quantum vacuum, up to 120 orders of magnitude too large. There is hence no simple natural explanation for dark energy, and one has to be content with phenomenological models at this point. Two proposed forms of dark energy are the cosmological constant, a constant

energy density filling space homogeneously, and scalar fields such as quintessence. In particular, 'tracking quintessence' models attempt to alleviate the coincidence problem of the cosmological constant model. More exotic models where the dark energy couples to matter fields or can cluster itself have also been proposed.

In light of the many theoretical possibilities, the hope is that future observational constraints on dark energy will enable progress in the understanding of this puzzling phenomenon. This requires the exploitation of the subtle influence of dark energy on structure formation, both on linear and non-linear scales. As the expected effects are generally small for many of the viable dark energy scenarios, it is crucial to be able to calculate structure formation in dark energy cosmologies with sufficient precision to tell the different models apart, and to be able to correctly interpret observational data. For example, in order to use the abundance of clusters of galaxies at different epochs to measure the expansion history of the universe, one needs to reliably know how the cluster mass function evolves with time in different dark energy cosmologies. Numerical simulations are the most accurate tool available to obtain the needed theoretical predictions, and they are also crucial for testing the results of more simplified analytic calculations.

In this study, we carry out such non-linear simulations for a particular class of dark energy cosmologies, so-called Early Dark Energy (EDE) models where dark energy might constitute an observable fraction of the total energy density of our Universe at the time of matter radiation equality or even big-bang nucleosynthesis. While in the cosmological constant scenario, the fraction in dark energy is negligible at high redshift, in such models the energy fraction is a few per cent during recombination and structure formation, which introduces interesting effects due to dark energy already at high redshift. In particular, for an equal amplitude of clustering today, we expect structures to form earlier in such cosmologies than in ΛCDM. This could be useful to alleviate the tension between a low σ_8 normalization suggested by current observational constraints from the CMB on one hand, and the observations of relatively early reionization and the existence of a population of massive halos present already at high redshift on the other hand.

Recently, Bartelmann et al. (2006) studied two particular EDE models, evaluating the primary quantities relevant for structure formation, such as the linear growth factor of density perturbation, the critical density for spherical collapse and the overdensity at virialization, and finally the halo mass function. In the two models analyzed, they found that the effect of EDE on the geometry of the Universe is only moderate, for example, distance measures can be reduced by 8%. Assuming the same expansion rate today, such models are younger compared to ΛCDM. At early times, the age of the universe should differ by approximately $5 - 10\%$.

However, when Bartelmann et al. (2006) repeated the calculation of the spherical collapse model in the EDE cosmology, a few nontrivial modifications appeared. The evolution of a homogeneous, spherical overdensity can be traced utilizing both the

virial theorem and the energy conservation between the collapse and the turn around time (see also Lacey and Cole, 1993; Wang and Steinhardt, 1998). Bartelmann et al. (2006) obtained the value of the virial overdensity as a function of the collapse redshift, translating the effect of the early dark energy in an extra contribution to the potential energy at early times. They found that the virial overdensity should be slightly enlarged by EDE, because a faster expansion of the universe means that, by the time a perturbation has turned around and collapsed to its final radius, a larger density contrast has been produced. However, at the same time they found that the linearly extrapolated density contrast corresponding to the collapsed object should be significantly reduced.

These two results based on analytic expectations have a pronounced influence on the predicted mass function of dark matter halos. In EDE models, the cluster population expected from the Press-Schechter or Sheth-Tormen formalism grows considerably relative to ΛCDM, as a result of the lowered value of the critical linear density contrast δ_c for collapse. This effect can be compensated for by lowering the normalization parameter σ_8 in order to obtain the same abundance of clusters today. In this case, one would however still expect a higher cluster abundance in EDE at high redshift, due to the earlier growth of structure in this model.

An open question is whether the EDE really participates in the virialization process in the way assumed in the analytic modeling. Similarly, it is not clear whether the excursion set formalism of Sheth & Tormen yields an equally accurate description of the non-linear mass function of halos in EDE cosmologies as in ΛCDM. Because accurate theoretical predictions for the halo mass function are a critical ingredient for constraining cosmological parameters (in particular Ω_m and Ω_Λ) as well as models of galaxy formation, it is important to test these predictions for the EDE cosmology in detail with numerical N-body simulations. In particular, we want to probe whether the fraction f of matter ending up in objects larger than a given mass M at some redshift z can be found by *only* looking at the properties of the linearly evolved density field at this epoch, using the ordinary ST formalism, or whether there is some dependence on redshift, power spectrum or dark energy parameters, as suggested by Bartelmann et al. (2006).

A further interest in EDE cosmologies stems from the fact that for a given σ_8, the EDE models predict a substantially slower evolution of the halo population than in the ΛCDM model. This could explain the higher normalization cosmology expected from cluster studies relative to analysis of the CMB. The value of σ_8, for a given cosmology, provides also a measure of the expected biasing parameter that relates the galaxy and the mass distribution. The early dark energy cosmologies could hence reduce the current mild tension between cluster data and the CMB observations. We note that halos in cosmologies with EDE are also expected to be more concentrated than in ΛCDM; because the density of the Universe was greater at early times, objects that virialized at high redshift are more compact than those

that virialized more recently.

Previous numerical simulations of a quintessence component with a changing equation of state (EOS) explored two particular potentials: SUGRA and Ratra Peebles (RP), which differ because RP has a more smoothly decreasing w and consequently a very different evolution in the past. Both Linder and Jenkins (2003) and Klypin et al. (2003) analyzed the influence of the dark energy on the halo mass function in order to extrapolate the abundance of structure at different epochs and to compare it with existent theoretical models. They used different numerical codes: the publicly available code GADGET, in the first project, and the Adaptive Refinement Tree code (Kravtsov et al., 1997), in the second. They concluded that the best way to understand which dark energy Universe fit the observations best is to look at the growth history of halos and the evolution of their properties with time. Dolag et al. (2004) focused on the modification of the concentration parameter with mass and redshift, for the same cosmologies, based on high resolution simulations of a sample of massive halos. A limited number of numerical studies also considered the possibility of a coupling of the dark energy field with dark matter (Mainini et al., 2003; Macciò et al., 2004).

In this Chapter, we carry out several high resolution simulations of dark energy cosmologies in order to accurately measure the quantitative impact of early dark energy on abundance and structure of dark matter halos. To this end, we in particular measure halo mass functions and evaluate the agreement/disagreement with different analytic fitting functions. We also test how well the growth of the mass function can be tracked with dynamical measure based on the velocity dispersion of dark matter substructures, which can serve as a proxy for the directly measurable line-of-sight motion of galaxies or line widths in observations, and gets around the usual ambiguities arising from different possible mass definitions for halos. Finally, we also present measurements of halo concentrations, and of the relation between dark matter velocity dispersion and halo mass. While finalizing this work, Francis et al. (2008) submitted a preprint which also studies numerical simulations of EDE cosmologies. Their work provides a different analysis and is complementary to our study, but it reaches similar basic conclusions about the halo mass function.

This Chapter is organized as follows. After a brief introduction to the Early Dark Energy models in Section 2, we present the simulations and also give details on our numerical methods in Section 3. In Section 4, we study the mass function of halos for the different cosmologies, and as a function of redshift. Then, in Section 5 we investigate the properties of halos by studying the virial relation between mass and dark matter velocity dispersion, as well as the mass–concentration relationship. In Section 6, we consider the velocity distribution function and prospects for measuring it in observations. Finally, we discuss our results and present our conclusions in Section 7.

2.2 Early dark energy models

The influence of dark energy on the evolution of the Universe is governed by its equation of state,

$$p = w\rho c^2. \tag{2.1}$$

A cosmological constant has $w_\Lambda = -1$ at all redshift, while a distinctive feature of the Early Dark Energy (hereafter EDE) models as well as of other models such as quintessence is that their equation of state parameter, $w_{\rm de}(z)$, varies during cosmic history.

Negative pressure at all times implies that the energy density parameter will fall to zero very steeply for increasing redshift. If, however, we allow the equation of state parameter to rise above zero, we can construct models in which $\Omega_{\rm de}(z)$ has a small positive value at all epochs, depending on the cosmological background model we adopt. While canonical dark energy models with near constant behaviour for w do not predict any substantial dark energy effect at $z > 2$, in such EDE models the contribution of dark energy to the cosmic density can be of order of a few percent even at very high redshift.

We are here investigating this interesting class of models which are characterized by a low but non-vanishing dark energy density at early times. Note that while the acceleration of the expansion of the Universe is a quite recent phenomenon, the dark energy responsible for this process could have an old origin. In fact, field theoretical models have been constructed that generically cause such a dynamical behaviour (Ratra and Peebles, 1988; Wetterich, 1988; Ferreira and Joyce, 1998; Liddle and Scherrer, 1999).

Wetterich (2004) proposed a useful parameterization of a family of cosmological models with EDE in terms of three parameters:

- the amount of dark energy today, $\Omega_{\rm de,0}$ (we assume a flat universe, so $\Omega_{m,0} = 1 - \Omega_{\rm de,0}$),

- the equation-of-state parameter w_0 today, and

- an average value $\Omega_{\rm de,e}$ of the energy density parameter at early times (to which it asymptotes for $z \mapsto \infty$).

Figure 2.1 shows the redshift evolution of the equation-of-state parameter in the four different cosmologies that we examine in this study. As can be noticed, the EDE models approach the cosmological constant scenario at very low redshift. We can compute the equation-of-state parameter for these early dark energy models from the fitting formula:

$$w(z) = \frac{w_0}{(1 + by)^2}, \tag{2.2}$$

69
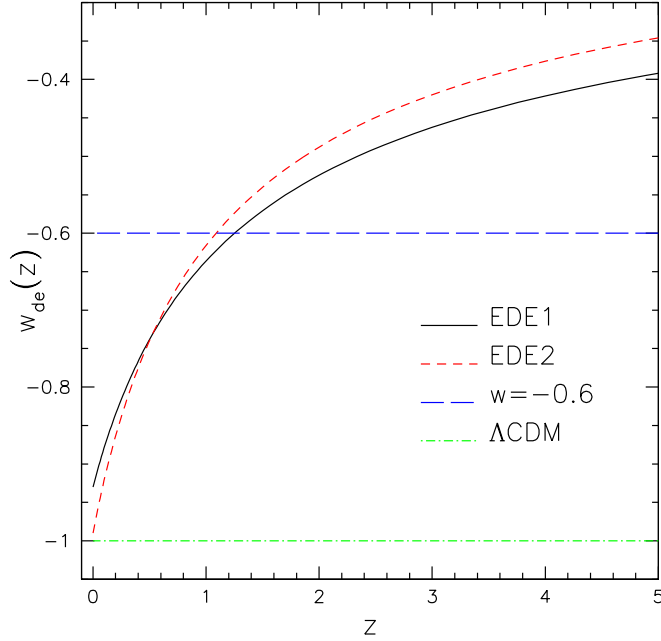
Figure 2.1 Equation of state parameter w shown as a function of redshift for the four different cosmological models considered in this work. In the two early dark energy models EDE1 and EDE2, shown with black solid and red dotted lines respectively, the value of w today is close to that of ΛCDM, but the amount of dark energy at early times is non vanishing, as described by the parameterization (2.2).

where

$$b = -\frac{3w_0}{\ln\left(\frac{1-\Omega_{\mathrm{de,e}}}{\Omega_{\mathrm{de,e}}}\right) + \ln\left(\frac{1-\Omega_{m,0}}{\Omega_{m,0}}\right)}, \tag{2.3}$$

and $y = \ln\left(1+z\right) = -\ln a$. The parameter b characterizes the time at which an approximately constant equation-of-state changes its behaviour.

In Figure 2.2, we plot the evolution of the matter and energy density parameters up to redshift $z = 30$. The dark energy parameter for EDE models evolves relatively slowly with respect to a standard ΛCDM cosmology. In fact, the critical feature of this parameterization is a non-vanishing dark energy contribution during recombination and structure formation (see also Doran et al., 2001):

$$\bar{\Omega}_{\mathrm{de,sf}} = -\ln a_{\mathrm{eq}}^{-1} \int_{\ln a_{\mathrm{eq}}}^{0} \Omega_{\mathrm{de}}\left(a\right) \mathrm{d}\ln a. \tag{2.4}$$

For sufficiently low $\Omega_{\mathrm{de,e}}$, EDE models reproduce quite well the accelerated cosmic expansion in the present-day Universe and they can be fine-tuned to agree both with low-redshift observations and CMB temperature fluctuation results (Doran et al., 2005, 2007).
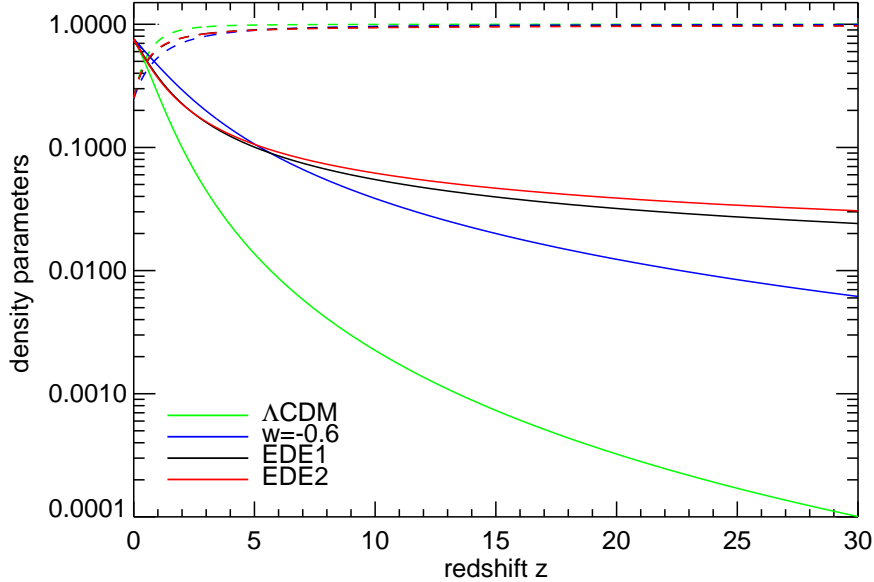
Figure 2.2 Evolution of the density parameters $\Omega_m(z)$ (dashed lines) and $\Omega_{\mathrm{de}}(z)$ (solid line) for the four cosmological models studied in this work. At redshift $z = 30$, the dark energy contribution is orders of magnitude higher for EDE models compared with a ΛCDM cosmology.

	$\Omega_{m,0}$	$\Omega_{\mathrm{de},0}$	h_0	σ_8	w_0	$\Omega_{\mathrm{de},e}$
ΛCDM	0.25	0.75	0.7	0.8	-1.	0.
DECDM	0.25	0.75	0.7	0.8	-0.6	0.
EDE1	0.25	0.75	0.7	0.8	-0.93	2×10^{-4}
EDE2	0.25	0.75	0.7	0.8	-0.99	8×10^{-4}

Table 2.1 Parameters of the N-Body simulations. The parameter $\Omega_{\mathrm{de},e}$ describes the amount of dark energy at early times, see equation (2.3). This value, together with w_0, the value of the equation state parameter today, and $\Omega_{\mathrm{de},0}$, the amount of dark energy today, completely describes our EDE models.

2.3 Numerical simulations

We performed a series of cosmological N-body simulations for two early dark energy models 'EDE1' and 'EDE2', which have $w_0 = -0.93$ and $w_0 = -0.99$, respectively, and a dark energy density at early times of about 10^{-4} (see Tab. 2.1). For comparison, we have also calculated a model 'DECDM' with constant equation of state parameter equal to $w = -0.6$, and a conventional ΛCDM reference model. We shall refer with these labels to the different models throughout the Chapter.

In all our models, the matter density parameter today was chosen as $\Omega_m = 0.25$, and we consider a flat universe. The Hubble parameter is $h = H_0/(100\,\mathrm{km\,s^{-1}Mpc^{-1}}) = 0.7$ and we assume Gaussian density fluctuations with a scale-invariant primordial

power spectrum. The normalization of the linear power spectrum extrapolated to $z = 0$ is $\sigma_8 = 0.8$ for all our simulations as given by present day observations. We also used the same spectral index $n = -1$ throughout in order to focus our attention on possible differences due to the dark energy contribution alone. For these choices, the models EDE1 and EDE2 are almost degenerate, but their proximity serves as a useful test for how well differences in the results can be detected even for small variations in the EDE parameters. This gives a useful illustration on how well one can hope to be able to distinguish them in practice and provides realistic data for testing the discriminative power of specific statistics.

For our largest calculations we used 512^3 particles in boxes of volume $100^3 \, h^{-3}$ Mpc^3, resulting in a mass resolution of $m_p = 5.17 \times 10^8 \, h^{-1} M_\odot$ and a gravitational softening length of $\epsilon = 4.2 \, h^{-1}$kpc, kept fixed in comoving coordinates. All the simulations were started at redshift $z_{\mathrm{init}} = 49$, and evolved to the present. For the simulations, we adapted the cosmological code GADGET-3 (based on Springel et al., 2001b; Springel, 2005) and the initial condition code N-GENIC, in order to allow simulations with a time-variable equation of state. These simulations can be used to determine the mass function also in the high-mass tail with reasonably small cosmic variance error, while at the same time probing down to interestingly small mass scales.

In Figure 2.3, we plot the expansion function of the EDE models relative to the ΛCDM case. We note that the only modification required in the simulation code was to update the expression for calculating the Hubble expansion rate, which needs to include the quintessence component. This term enters in both the kinematics and the dynamics of the cosmological models.

According to the Friedmann equation within a flat universe we have

$$H(a) = H_0 \left[\frac{\Omega_{m,0}}{a^3} + \Omega_{\mathrm{de},0} \, \exp\left(-3 \int \left[1 + w\left(a\right) \right] \mathrm{d}\ln a \right) \right]^{1/2}. \tag{2.5}$$

The density of dark energy changes with the scale factor as:

$$\Omega_{\mathrm{de}}(z) = \Omega_{\mathrm{de},0} \exp\left(-3 \int d\ln a \left[1 + w\left(a\right) \right] \right), \tag{2.6}$$

instead of simply being equal to $\Omega_{\mathrm{de},0}$, as in the usual scenario. For $w = -1$, the behaviour of a cosmological constant is recovered.

If we interpret the modified expansion rate as being due to $w(z)$, as defined in equation (2.2), we find:

$$H^2\left(z\right)/H_0^2 = \Omega_{\mathrm{de},0}\left(1+z\right)^{3+3\bar{w}_h(z)} + \Omega_{m,0}\left(1+z\right)^3, \tag{2.7}$$

where

$$\bar{w}_h\left(z\right) = \frac{w_0}{1 + b\ln\left(1+z\right)}, \tag{2.8}$$
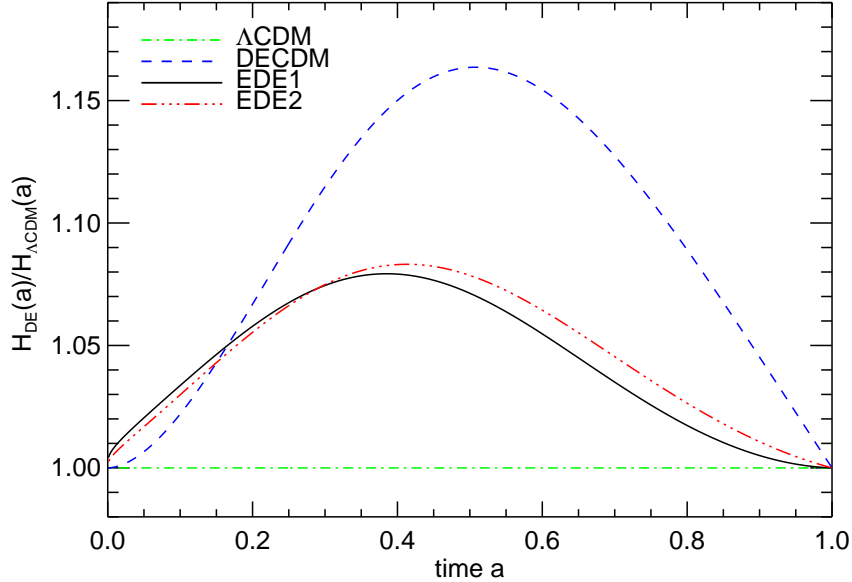
Figure 2.3 Hubble expansion rate for the models studied in this work. All models are normalized with respect to the reference ΛCDM case. In the models EDE1, EDE2, and in the model with constant w, the expansion rate of the universe is higher at early times. This has a strong effect on the evolution of the growth factor.

and b is given by the Eqn. (2.3).

We can see that effectively the EDE models predict the observed effect of an acceleration in the expansion rate, and this has consequences on the global geometry of the Universe. We note that the dark energy term in Eqn. (2.6) just parametrizes our ignorance concerning the physical mechanism leading to an increase in expansion rate. However, once the dependence of H on the scale factor is fixed, the mathematical problem of calculating structure growth is then unambiguously defined.

The evolution of $\Omega_{\mathrm{de,a}}$ affects not only the expansion rate of the background but also the formation of structures. The primary influence of dark energy on the growth of matter density perturbations is however indirect and arises through the sensitive dependence of structure growth on the expansion rate of the universe. In Figure 2.4, we show the linear growth factor D divided by the scale factor D/a as a function of time for all our models. All curves are normalized so that they start from unity at early times.

In order to rescale the power spectrum of matter fluctuations to the redshift of the initial conditions ($z = 49$ for all simulations), we introduced in our initial condition code the calculation of the growth factor for a general equation-of-state as given by Linder and Jenkins (2003):

$$D'' + \frac{3}{2}\left[1 - \frac{w\left(a\right)}{1 + X\left(a\right)}\right]\frac{D'}{a} + \frac{3}{2}\left[\frac{X\left(a\right)}{1 + X\left(a\right)}\right]\frac{D}{a^2} = 0, \qquad (2.9)$$
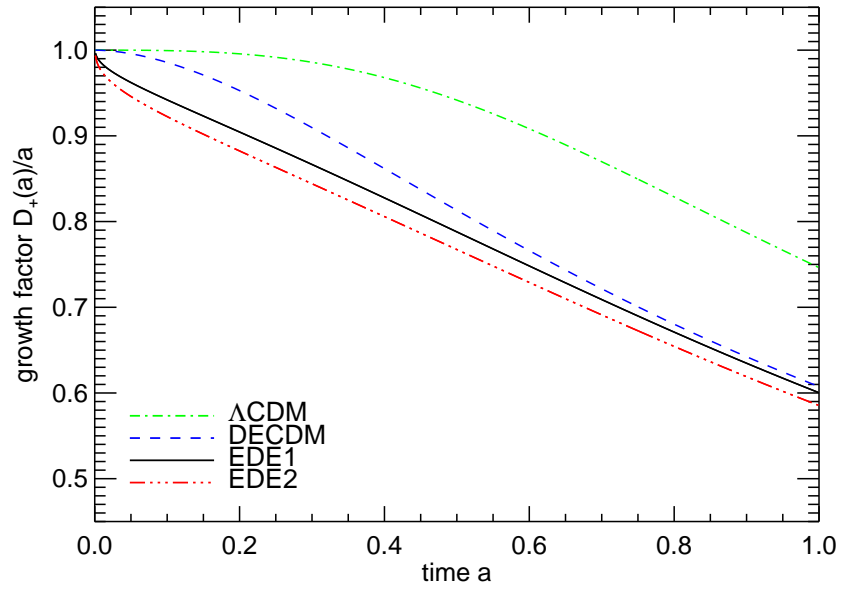
Figure 2.4 Ratio of the growth factor of linear density perturbations and the scale factor a, as a function of a. The four models are described in Table 2.1. The curves are normalized to unity at early times, i.e. we here assume that the starting density contrast is the same in the four cosmologies. The models EDE1 and EDE2 show a significant difference in the growth factor evolution even with small energy density at high redshift: structures have to grow earlier to reach the same abundance as the ΛCDM model today.

where $X(a)$ is the ratio of the matter density to the energy density:

$$X(a) = \frac{\Omega_{m,0}}{\Omega_{\text{de},0}} \exp\left[-3 \int_a^1 d\ln a' w(a')\right], \qquad (2.10)$$

and we allowed for a time-dependent equation of state, $w(a)$. Here we define the growth factor as the ratio $D = \delta(a)/\delta(a_i)$ of the perturbation amplitude at scale factor a relative to the one at a_i, and we use the normalization condition $D(a_{\text{eq}}) = a_{\text{eq}}$.

We can easily see that for very large redshift we recover the matter dominated behaviour in the ΛCDM case: $D(a) \propto a$. On the other hand, as expected, the linear growth in the two EDE models falls behind the green curve in Fig. 2.4, implying that they reach a given amplitude at earlier times. In fact, the expansion rate in the ΛCDM cosmology is lower than in EDE models, which governs the friction term $(\dot{a}/a)$ in the growth equation

$$\ddot{\delta} + 2\frac{\dot{a}}{a}\dot{\delta} - 4\pi G\rho\delta = 0 \qquad (2.11)$$

of the perturbations.

These formulae can be used to derive a suitable expression for the reduced linear overdensity δ_c for collapse expected in EDE models (Bartelmann et al., 2006), which in turn suggests that there are significant consequences for the process of non-linear structure formation, an expectation that we will analyse later in detail. In sum, structures need to grow earlier in EDE models than in ΛCDM in order to reach the same amplitude at the present time. At an equal redshift, the initial conditions must hence be more evolved in order to produce comparable results today. The DECDM shows a behaviour qualitatively similar to EDE1 and EDE2 (blue long-dashed line).

In all our simulations, we have identified dark matter halos using two methods: the friends-of-friends (FOF) algorithm with linking length $b = 0.2$, and the spherical overdensity (SO) group finder. Candidate groups with a minimum of 32 particles were retained by the FOF group finder. In the SO algorithm, we first identify FOF groups, and then select the particle with the minimum gravitational potential as their centres, around which spheres are grown that enclose a fixed prescribed mean density $\Delta \times \rho_{\text{crit}}$, where ρ_{crit} is the critical density. Different definitions of virial overdensity are in use in the literature, and we consider different values for Δ where appropriate. The classical definition of NFW adopts $\Delta = 200$ independent of cosmology, while sometimes also $\Delta = 200\,\Omega_m$ is used, corresponding to a fixed overdensity relative to the background density. Finally, a value of $\Delta \sim 178\,\Omega_m^{0.45}$ based on a generalization of the spherical top-hat collapse model to low density cosmologies can also be used. Note however that this may in principle depend on the dark energy cosmology (Bartelmann et al., 2006), and is hence slightly ambiguous in these cosmologies.
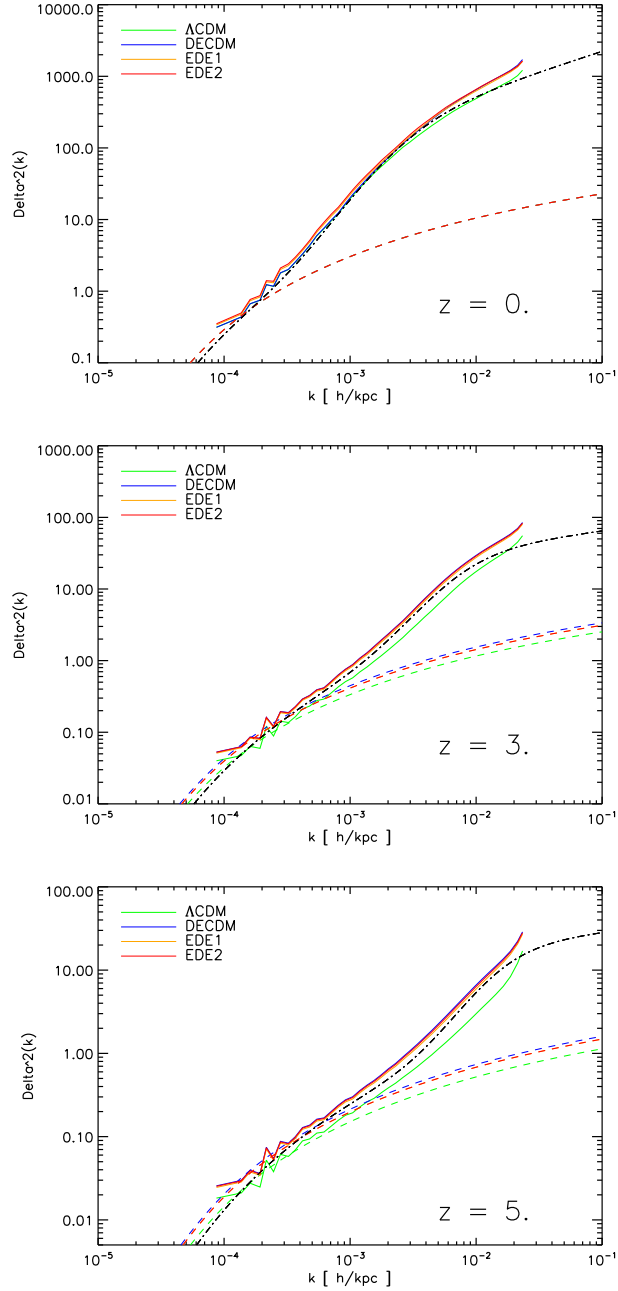
Figure 2.5 Comparison of the non-linear power spectra of the four different cosmological models studied here. The three panels give results for redshifts $z = 0$, $z = 3$ and $z = 5$, from top to bottom. The y-axes shows the dimensionless power $\Delta^2 = k^3 P(k)$ as a function of k computed from the dark matter density field using a grid of 512^3 points. All the simulations are normalized to $\sigma_8 = 0.8$ for the linearly extrapolated density field today. The dashed lines indicate the expected linear power spectra. The prediction from Smith et al. (2003) for the ΛCDM cosmology is shown by the black dot-dashed line.

76

We have verified the correctness of our implementation of early dark energy in the simulation code by checking that it accurately reproduces the expected linear growth rate in these non-standard cosmologies. Recall that rather than normalizing the density perturbations of the initial conditions to the same value at the (high) starting redshift, we determine them such that they should grow to the same linear amplitude today in all of the models. In practice, we fix σ_8, the linearly extrapolated *rms* fluctuations in top-hat spheres of radius $8\,h^{-1}\mathrm{Mpc}$ to the value 0.8 for the epoch $z = 0$.

In Figure 2.5, we show measurements of the power spectrum of our different models at three different redshifts. While the models differ significantly at high redshift, the four different realizations show the same amplitude of the power spectrum, at least on large scales, at redshift $z = 0$ (left panel). The underlying assumption of this approach is that the transfer function used in the computation is that of a cosmological constant model. This is a good approximation at cluster scales for early dark energy models. We would like to stress that in what follows we do not assume that halo number density is normalized to the present day halo abundance in the ΛCDM model. Instead we consider that all models have a fixed power spectrum normalization. The fluctuations on small scales probably reflect the earlier structure formation time in the EDE models and the resulting differences in the non-linear halo structures. The good agreement of the power spectrum at the end, as well as a detailed comparison of the growth rate of the largest modes in the box with the linear theory expectation (not shown), demonstrate explicitly that the EDE models are simulated accurately by the code, as intended.

Note also that the power spectrum measurements show that due to the slower evolution of the linear growth factor in EDE models, the degeneracy between the models is lifted towards high-z since this corresponds to more time for the different growth dynamics to take effect. Consequently, we expect a different evolution of structures back in time. Our main focus in the following will be to study the impact of a different equation of state for the dark energy upon the mass function of dark matter halos and its evolution with redshift.

2.4   The mass function

In this section we measure the halo abundance at different redshifts and compare with analytic fitting functions proposed in the literature. Our primary goal is to see to which extent dark energy models can still be described by these fitting formulae, and whether there is any numerical evidence that supports the higher halo abundance predicted for the EDE cosmologies (Bartelmann et al., 2006). We will mostly focus on halo mass functions determined with the FOF algorithm with a linking length of 0.2, but we shall also consider SO mass functions later on.
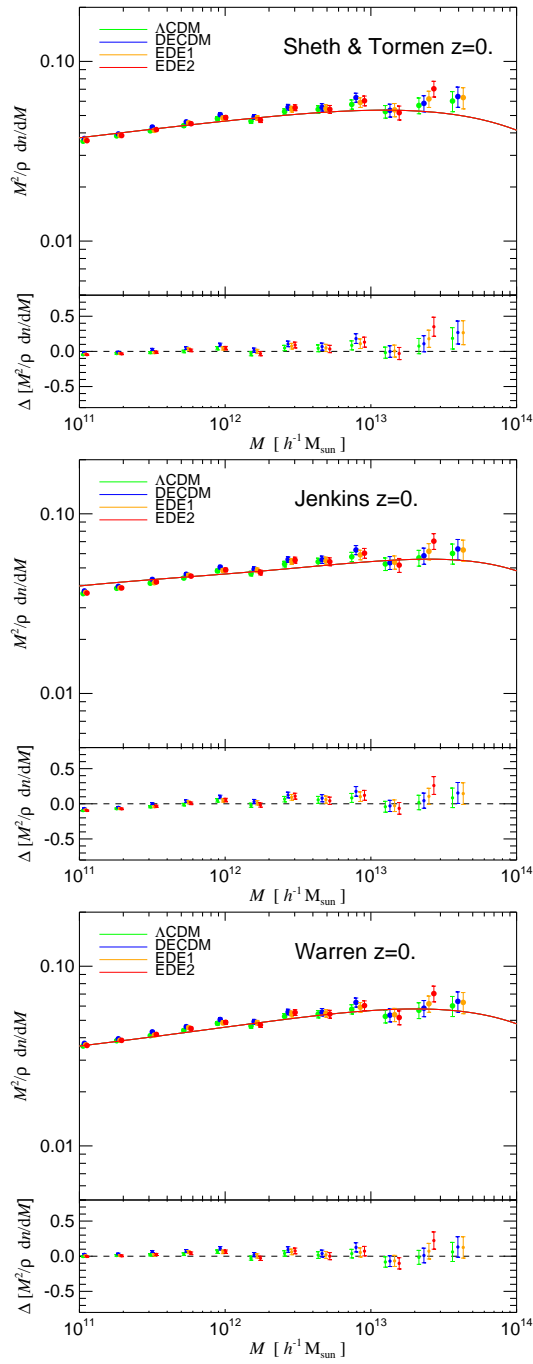
Figure 2.6 Friends-of-friends multiplicity mass functions at $z = 0$ for the four dark energy models studied here. The solid lines in each panel represent the multiplicity function computed analytically either from the Sheth & Tormen formula (left panel), the Jenkins formula (central panel) or the Warren model (right panel). The symbols are the numerical simulation results for ΛCDM (green), DECDM (blue), EDE1 (orange) and EDE2 (red). We consider only halos with more than 200 particles and we apply an upper mass cut-off where the Poisson error reaches 14%. In the lower plot of each figure we show the residuals between analytically expected and numerically determined mass functions for all models. The differences are typically below 10%. The error bars show Poisson uncertainties due to counting statistics for all models. At $z = 0$, the simulation results for all cosmologies are basically identical, which reflects the fact that we normalized the models such that they have the same linear power spectra today, with a normalization of $\sigma_8 = 0.8$.
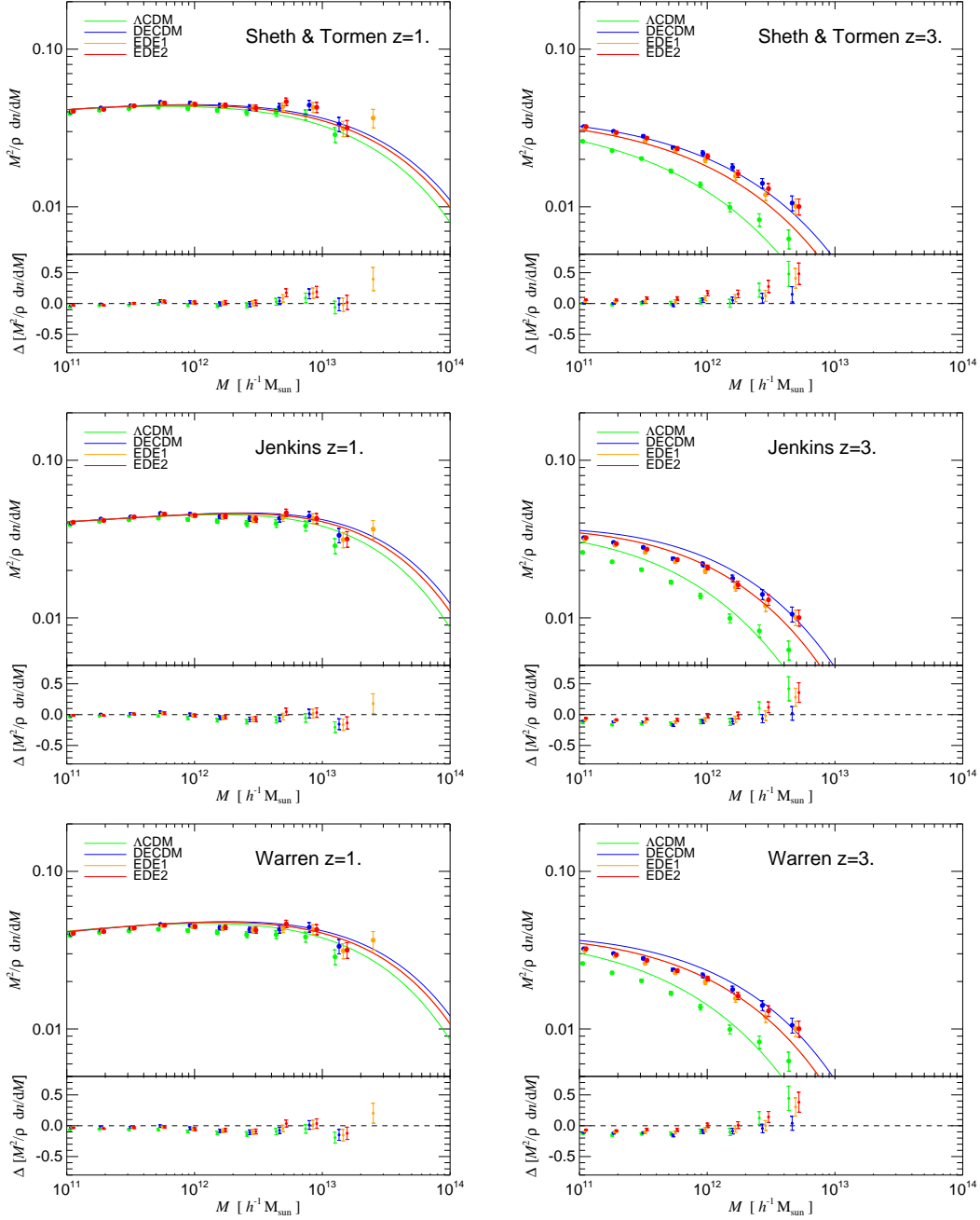
Figure 2.7 Friends-of-friends multiplicity mass functions for the four dark energy models studied here. The evolution towards high redshift is shown in terms of results at $z = 1$ (left column) and at $z = 3$ (right column). The solid lines in each plot represent the multiplicity function computed analytically from the Sheth & Tormen formula (top row), the Jenkins formula (middle row) and the Warren formula (bottom row). The points are the numerical simulation results for ΛCDM model (green), DECDM (blue), EDE1 (orange) and EDE2 (red). We consider only halos with more than 200 particles and we apply an upper mass cut-off where the Poisson error reaches 14%. In the lower plot of each figure we show the residuals between analytically expected and numerically determined mass functions for all models. The differences are typically below 15%. The error bars show Poisson uncertainties due to counting statistics for all models.

79

In Figure 2.6, we show our measured halo mass functions in terms of the multiplicity function, which we define as

$$f\left(\sigma, z\right) = \frac{M}{\rho_0} \frac{\mathrm{d}n(M, z)}{\mathrm{d}\ln \sigma^{-1}} \tag{2.12}$$

where ρ_0 is the background density, $n(M, z)$ is the abundance of halos with mass less than M at redshift z, and σ is the mass variance of the power spectrum filtered with a top-hat mass scale equal to M. Note that for a fixed σ_8 the predicted number density of dark matter halos given by the above formula is uniquely affected by the dark energy models through the ratio $\delta_c(z)/D$ (Haiman et al., 2001; Nunes et al., 2006, see discussions here). The overdensity is expected to be different for different dark energy models and therefore the number density of halos at $z = 0$ may also differ if we assume the same power spectrum normalization for all models. In particular, the peculiar form of the quintessence potentials and different behaviors of the field in highly non linear regions can significantly alter the evolution of the perturbations and the time of the collapse (Mota and van de Bruck, 2004; Nunes and Mota, 2006; Manera and Mota, 2006). Numerical simulations may allow to further distinguish between different prescriptions and to investigate in how far perturbations in the quintessence field affect the analytical predictions of the spherical collapse model. This is really important because the physical properties of clusters, such as the density contrast and virial radius strongly depend on clustering properties of dark energy. In the present study, we refer the work of Bartelmann et al. (2006) for the value of δ_c in the early dark energy models: in this work they show significant variations of the linearly extrapolated overdensity with redshift within the early dark energy models.

We give results for the cosmological models ΛCDM, DECDM, EDE1 and EDE2, plotted as symbols, while the solid lines show various theoretical predictions. Note that we plot the mass function only in a limited mass range in order to avoid being dominated by counting statistics or resolution effects. To this end we only consider halos above a minimum size of 200 particles. At the high mass end, individual objects are resolved well, but the finite volume of the box limits the number of massive rare halos we can detect. We therefore plot the mass function only up to the point where the Poisson error reaches $\sim 14\%$ (corresponding to minimum number of ~ 50 objects per bin).

As well known, the Press & Schechter mass function (Press and Schechter, 1974), while qualitatively correct, disagrees in detail with the results of N-body simulations (Efstathiou et al., 1988b; White et al., 1993; Lacey and Cole, 1994; Eke et al., 1996), specifically, the PS formula overestimates the abundance of halos near the characteristic mass $M_\star$ and underestimates the abundance in the high-mass tail. We therefore omit it in our comparison. The discrepancy is largely resolved by replacing the spherical collapse model of the standard Press & Schechter theory with

the refined ellipsoidal collapse model (Sheth and Tormen, 1999; Sheth et al., 2001; Sheth and Tormen, 2002). Indeed, in the top left panel of Figure 2.6 we can see quite good agreement of the Sheth & Tormen mass function (ST) with our simulations at $z = 0$. We stress that here the standard value of $\delta_c = 1.689$ for the linear collapse threshold has been used irrespective of the cosmological model. Two other well-known fitting formulae are that from Jenkins (central panel, Jenkins et al., 2001, 'J') and that from Warren (right panel, Warren et al., 2006, 'W'), which differ only very slightly in the low-mass range. We compare our measurements with these models in the panels of the middle and right columns. As we can see from the comparison between the solid lines and the numerical data points, the differences between the different theoretical models (which only rely on the linearly evolved power spectrum at each epoch) and the simulation results is very small. The universality of the Jenkins and Warren fitting formulae only obtains when we define haloes in our simulations at fixed overdensity independent of the cosmological parameters we consider. It is important to notice that at redshift zero we can extend this result also to quintessence models, because this analysis allows us to directly address the question of how dark energy participates in the virialization process. Therefore, the mass function formalism of Jenkins and Warren is sufficiently well determined that the effects due to the change in the δ_c collapsing threshold, if present at all, are negligible compared to the overall uncertainties due to the theoretical fitting functions. This conclusion disagrees with previous analytical computations from Bartelmann et al. (2006).

Figure 2.7 shows the redshift evolution of the mass function, in the form of separate comparison panels at redshifts $z = 1$ and $z = 3$. While at $z = 0$ the different cosmologies agree rather well with each other, as expected based on the identical linear power spectra, at redshift $z = 1$ we begin to see differences between the models, and finally at $z = 3$, we can observe a significantly higher number density of groups and clusters in the non-standard dark energy models. Notice that the model with constant w (blue line) behaves qualitatively rather similar to the EDE models. In each of the panels, we include a separate plot of the residuals with respect to the analytic fitting functions. This shows that at $z = 3$ the agreement is clearly best for the ST formula. However, we can clearly quantify the predicted evolution of the halo mass function also using the Warren and Jenkins formalism, as well as any cosmological dependence of the halo mass multiplicity function. Also at higher redshift we could not find any systematic error in the halo model when we apply the crude fitting formulae calibrated on the ΛCDM reference model.

A further step is to see how the possible virialization of dark energy affect cluster abundances and so to disentangle which approach provides a better fit to simulations. The differences between the models are most evident in the exponential tail of the mass function where it begins to fall off quite steeply, in agreement with what is expected from the power spectrum analysis. We can see that, at high-z, replacing

the cosmological constant by an early dark energy scenario has a strong impact on the history of structure formation. In particular, non-linear structures form substantially earlier in such a model, such that a difference in abundance of a factor of ~ 2 is reached already by $z = 3$. This underlines the promise high redshift cluster surveys hold for distinguishing different cosmological models, and in particular for constraining the dynamical evolution of dark energy.

We now want to assess in a more quantitative fashion the differences between our numerical halo mass functions and the analytic fitting functions. In particular we are interested in the question whether we can objectively determine a preference for one of the analytic models, and whether there is any evidence that the ordinary mass function formalism does work worse for the generalized dark energy models than for ΛCDM. The latter would indicate that the critical linear overdensity threshold δ_c needs to be revised for EDE models, as suggested by the analytic spherical collapse theory (Bartelmann et al., 2006).

To this end we directly measure the goodness of the fit, which we define for the purposes of this analysis as:

$$\chi^2 = \left(\sum_j 1/\sigma_j^2 \right)^{-1} \sum_i \frac{(\mathrm{MF}_i - \mathrm{MF}_{\mathrm{TH},i})^2}{\sigma_i^2 \, \mathrm{MF}_{\mathrm{TH},i}^2}, \tag{2.13}$$

where $\mathrm{MF}_{\mathrm{TH},i}$ are the theoretical values, MF_i are the simulations results, and we took into account a simple Poisson error in the definition of the goodness of fit. In Figure 2.8, we plot this value expressed in percent for all simulations when compared with the theoretical formulae of ST (solid line), Jenkins (dotted line) and Warren (dashed line). We cannot identify a clearly superior behaviour of any the three fitting functions, at least at this level of resolution; the models lie in a strip between approximately 5 and 15% error between $z = 0$ and $z = 5$. There is some evidence that the ST model does a bit better than the other fitting formulae for the ΛCDM cosmology at high redshift, but the opposite is true for the two EDE cosmologies and the Jenkins and Warren functions.

Interestingly, the overall agreement between simulation results and fitting functions is actually slightly worse for ΛCDM than for the non-standard dark energy cosmologies. There is hence no tangible evidence that a revision of the mass function formalism is required to accurately describe EDE cosmologies. Our finding of a universal $f(\sigma)$ is quantitatively different from the expectation based on the analysis of the EDE models by Bartelmann et al. (2006). We find that only the different linear growth rate has to be taken into account for describing the mass function in the early dark energy cosmologies with the ST formalism, but there is no need to modify the linear critical overdensity value. To make this point more explicit, we show in Figure 2.10 the mass function for the EDE models and compare it to standard ST (solid lines), and to the expectations obtained taking into
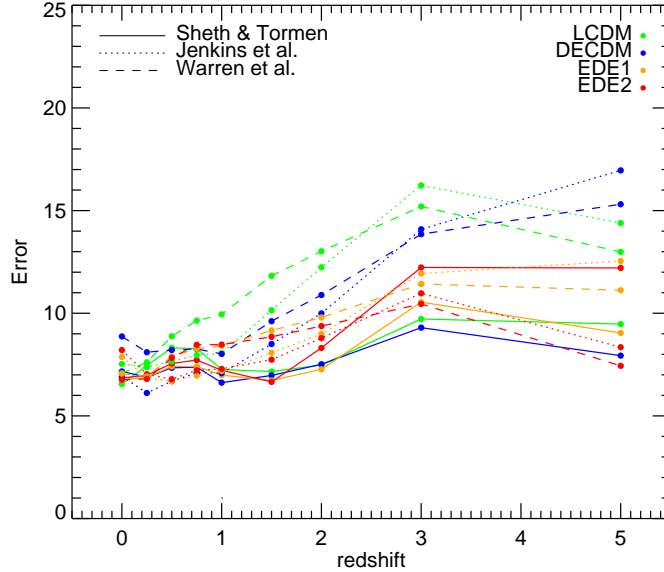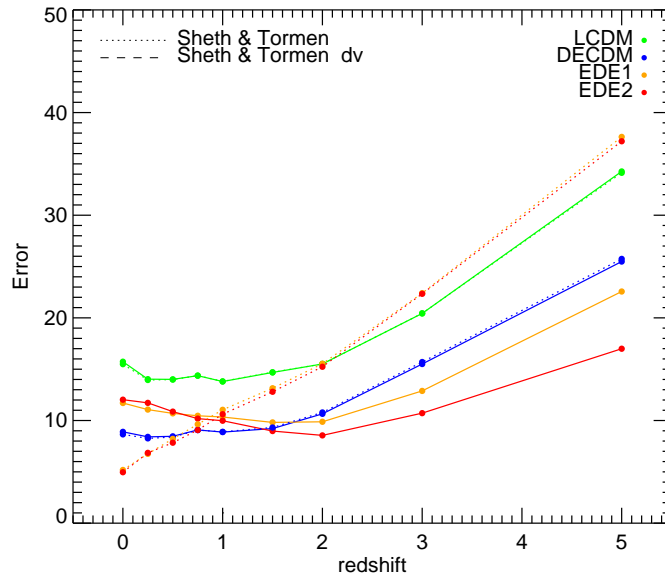
Figure 2.8 Redshift dependence of our goodness of fit parameter χ^2 (see Eqn. 2.13), expressed as percent, computed by comparing the theoretical expectation for the multiplicity mass function with the simulation results. All cosmological models are compared. The deviations are computed with respect to the Sheth & Tormen model (solid lines), the Jenkins et al. (dotted lines) and the Warren (dashed lines).

account a different density contrast for EDE models (dashed lines). The predictions in the second case are based on the analytic study of Bartelmann et al. (2006) and the critical overdensity is proportional to $(a)^{3\Omega_{\mathrm{de,sf}}/5}$ (see Eqn. 2.4).[1] Clearly, the proposed modification of δ_c actually worsens the agreement, both for the halos selected according the FOF algorithm (top panel) or defined with respect to the virial overdensity (bottom panel).

In the plots we discussed above, we always employed the FOF halo finder with standard linking length of $b = 0.2$ to find the halos, and the masses were simply the FOF group masses, which effectively correspond to the mass within an isodensity surface of constant overdensity relative to the background density. As the analytic mass function formulae have been calibrated with FOF halo mass functions, we expect that they work best if the mass is defined in this way. However, we may alternatively also employ a different mass definition based on the spherical overdensity (SO) approach, which allows one to take into account the time-dependent virial overdensity Δ predicted by generalizations of the spherical collapse model for dark energy cosmologies. In the bottom panel of Figure 2.10 we can see that an even more marked disagreement results when we take into account this arguably more consistent halo definition.

---

[1]In order to obtain the new values for the critical overdensity it is necessary to compute the virial overdensity by solving the equation of the generalized spherical collapse model.

Figure 2.9 Redshift dependence of our goodness of fit parameter χ^2 (see Eqn. 2.13), expressed as percent, computed by comparing the theoretical expectation for the multiplicity mass function with the simulation results. All models are considered. Here we use the top hat halo mass definition to compute the mass function from the simulations, and the deviations are computed with respect to the standard Sheth & Tormen model (dotted-dashed lines), and the Sheth & Tormen formula computed from a generalization of the top-hat collapse theory (dashed lines).

To stress this conclusion, in Figure 2.9, we show the residuals of our SO halo mass functions compared with the Sheth & Tormen prediction, as a function of redshift and for our different cosmological models, using the same procedure already applied to the FOF halo finder results. In this case, the halos were defined as virialized regions that are overdense by a variable density threshold equal to

$$\Delta_c = 18\pi^2 + 82x - 39x^2, \tag{2.14}$$

where $x = \Omega_m(z) - 1$, see Bryan and Norman (1998). This is the predicted dependence of Δ for ΛCDM, which we used for simplicity also for the other dark energy cosmologies. As expected, we see that the error increases relative to the FOF mass functions, with discrepancies of order 10% at $z = 0$. However, there is again no evidence that the non-standard dark energy cosmologies are described worse by the ST formalism than ΛCDM. Also, there is no improvement in the accuracy of the fit when we introduce the modified linear density contrast for the EDE models. On the contrary, as seen by the dotted lines, which represent the theoretical mass function (based on Sheth & Tormen) modified according to the spherical top hat collapse theory proposed by Bartelmann et al. (2006). We want to remark that using the exact value of Δ computed for the EDE cosmologies in the SO algorithm would not change the main conclusion of this analysis, it would actually increase slightly the discrepancies between simulation results and expectations with a modified δ_c.

Our results thus suggest that the mass function depends primarily on the linear power spectrum and is only weakly, if at all, dependent on the details of the expansion history. This disagrees with the expectations from the generalization of the top hat collapse theory, which are not confirmed by our numerical data. In fact, our simulations show that a description of the mass function based on the generalized TH calculation is incorrect at the accuracy level reached here. While the dynamic range of our results could be improved by increasing the resolution and box-size of our simulations, it appears unlikely that this could affect our basic conclusions. Nevertheless, better resolution would be required if one seeks to still further reduce the present residuals of order 5-15% between the fitting functions of ST, Jenkins or Warren.

2.5 Halo properties

2.5.1 The virial scaling relation

Evrard et al. (2008) have shown that the dark matter velocity dispersion of halos provides for accurate mass estimates once the relationship between mass and velocity dispersion is accurately calibrated with the help of numerical simulations. They have demonstrated that there exists a quite tight power-law relation between the mass
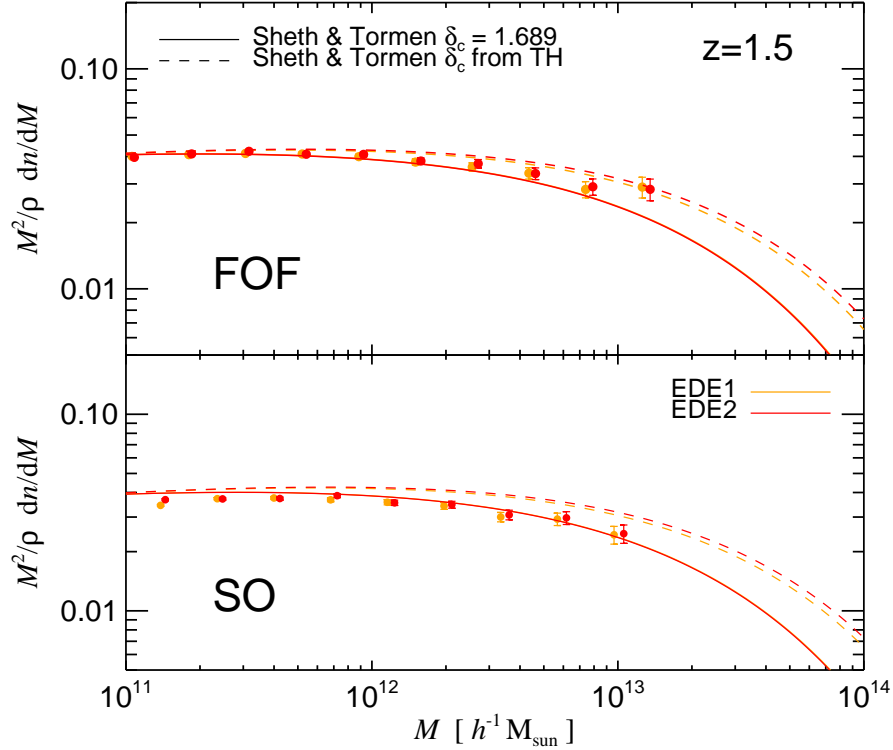
Figure 2.10 Multiplicity mass function at $z = 1.5$ for the two EDE models studied here. We want to highlight that the introduction of a modified overdensity motivated by the generalized spherical collapse theory (Bartelmann et al., 2006) reduces the agreement between the simulation results and the theoretical ST mass function. The measured points are in better agreement with the solid line (standard ST model) than with the dashed lines (ST modified model), the latter systematically overestimate the halo abundance. This holds true both if we consider the halos obtained from the FOF halo finder (top panel) or the one obtained by taking into account the theoretically motivated virial overdensity with the appropriate SO mass definition (bottom panel).
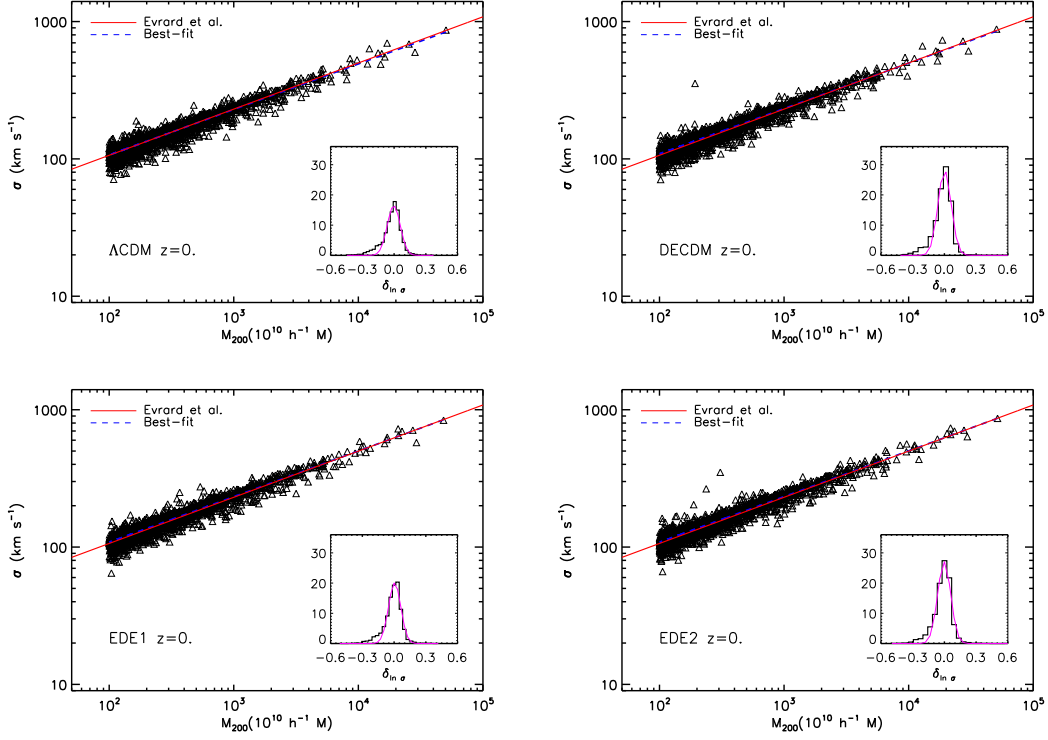
Figure 2.11 The virial scaling relation at the present epoch for primary halos with mass larger than $10^{12}\,\mathrm{M}_\odot$ for the four models considered (from left to right and top to bottom: ΛCDM, DECDM, EDE1, EDE2). The red solid line in each plot represents the Evrard et al. (2008) relation, while the blue dashed line is our best fit. The triangles are the simulation results: we employ a fixed critical threshold of $\Delta = 200$ to identify the dark matter halos. The insets show the distributions of deviations in $\ln\sigma_{\mathrm{DM}}$ around the Evrard et al. (2008) fit.

of a halo and its one-dimensional velocity dispersion σ_{DM}, where

$$\sigma_{\mathrm{DM}}^2 = \frac{1}{3N_p} \sum_{i=1}^{N_p} \sum_{j=1}^{3} |v_{i,j} - \bar{v}_j|^2 , \qquad (2.15)$$

with $v_{i,j}$ being the j_{th} component of the physical velocity of particle i in the halo, N_p is total number of halo particles within a radius that encloses a mean overdensity of $\Delta = 200$ with respect to the critical density, and $\bar{v}$ is the mean halo velocity. When virial equilibrium is satisfied, we expect that the specific thermal energy in a halo of mass M and of radius R will scale with its potential energy, GM/R, while the kinetic energy is proportional to $M^{2/3}$. Since σ_{DM} expresses the specific thermal energy in dark matter, we can express the mean expected velocity dispersion as a function of mass as

$$\sigma_{\mathrm{DM}}\left(M, z\right) = \sigma_{\mathrm{DM},15} \left(\frac{h(z) M_{200}}{10^{15} M_\odot} \right)^\alpha . \qquad (2.16)$$

Here the fit parameters are the slope α of the relation, and the normalization $\sigma_{\mathrm{DM},15}$ at a mass scale of $10^{15} h^{-1} M_\odot$. While the slope α just follows from the virial theorem if halos form a roughly self-similar family of objects (which they do to good approximation), the amplitude $\sigma_{\mathrm{DM},15}$ of the relationship is a non-trivial outcome of numerical simulations and reflects properties of the virialization process of the halos as well as their internal structure. Evrard et al. (2008) showed that a single fit is consistent with the numerical data of a large set of N-body simulations of the ΛCDM cosmology, covering a substantial dynamic range.

However it is conceivable that the amplitude of the relationship will be slightly different in early dark energy cosmologies, as a result of the different virial overdensity that is predicted by the top hat collapse in these cosmologies. If true, this would then also hint at a different normalization of the relationship between total Sunyaev-Zeldovich decrement and mass, which would hence directly affect observationally accessible probes of the cluster mass function at high redshift.

We here test whether we can find any difference in this relationship for our different dark energy cosmologies. In Figure 2.11, we plot the velocity dispersion of halos as a function of mass, in the four different cosmologies we simulated. The halos were identified using a spherical overdensity definition, where the virial radius r_{200} was determined as the radius that encloses a fixed multiple of 200 times the critical density at the redshift z, and M_{200} being the corresponding enclosed mass. We then determined the best-fit relation obtained from our numerical data (red solid lines). This fit is in very good agreement with the results obtained by Evrard et al. (2008) (dotted blue lines), given by $\sigma_{\mathrm{DM},15} = 1082 \pm 4.0 \, \mathrm{km\,s^{-1}}$ and $\alpha = 0.3361 \pm 0.0026$, a value consistent with the virial expectation of $\alpha = 1/3$. The insets show the residuals about the fit at redshift $z = 0$. They have a log-normal distribution with a maximum of 6% dispersion (for the DECDM model) around the power-law relation.

The histograms are well fit by a log-normal with zero mean.

We find that the halos closely follow a single virial relation, insensitive of the cosmological parameters, the epoch and also the resolution of the simulation. In particular, we do not find any significant differences for the EDE models, instead, the same form of the virial relation is preserved across the entire range of mass and redshift in the four simulations. We wanted also to verify whether part of the symmetry is due to the definition used for the halo mass function. We then analyze the same statistic taking into account both $\Delta = 200$ times the mean density of the Universe and the value directly derived from the Top Hat spherical collapse model. We find out that in these two cases the normalization and slope of the relation should be slightly reduced (α at $z = 0$ is always between 0.325 and 0.33), but the decrease is of the same order of magnitude in the ΛCDM reference case and for EDE models. We can conclude that the velocity dispersion-mass correlation hence appears to be global and very robust property of dark matter halos which is not affected by different contributions of dark energy to the total energy density of the universe.

This is a reassuring result as it means that also in the case of early dark energy, clusters can be studied as a one parameter family and the calibration of dynamical mass estimates from internal cluster dynamics does not need to be changed. Differences in the normalization should only reflect more or less frequent halo mergers and interactions, which can introduce an additional velocity component (Espino-Briones et al., 2007; Faltenbacher and Mathews, 2007).

2.5.2 Halo concentrations

As we have seen, for an equal normalization of the present-day linear power spectrum, the dark matter halo mass function at $z = 0$ does not depend on the nature of dark energy. On one hand this is a welcome feature, as it simplifies using the evolution of the mass function to probe the expansion history of the universe, but on the other hand it disappointingly does not provide for an easy handle to tell different evolutions apart based only on the present-day data. However, a discrimination between the models may still be made if the *internal structure* of halos is affected by the formation history, which would show up for example in their concentration distribution.

Cosmological simulations have consistently shown that the spherically averaged mass density profile of equilibrium dark matter halos are approximately universal in shape. As a result, we can describe the halo profiles by the NFW formula (Navarro et al., 1995, 1996, 1997):

$$\frac{\rho\left(r\right)}{\rho_{\mathrm{crit}}} = \frac{\delta_c}{(r/r_s)(1 + r/r_s)^2},$$
(2.17)
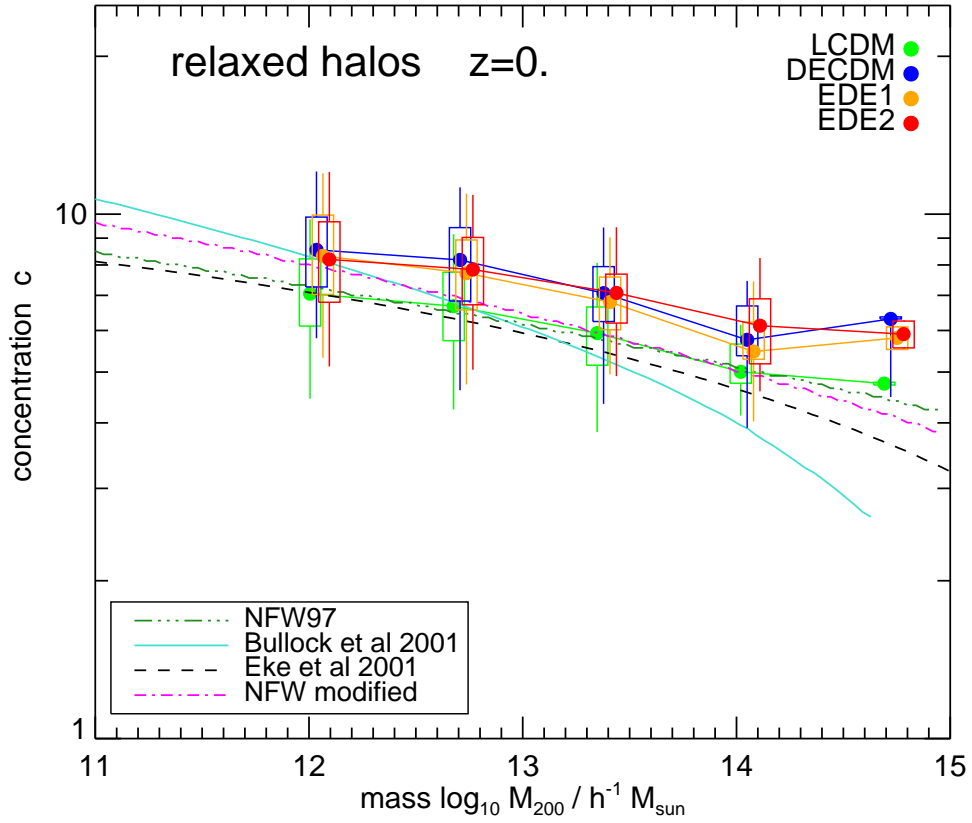
Figure 2.12 Mass-concentration relation for relaxed halos in all our simulations. The boxes represent the 25 and 75 percentiles of the distribution with respect to the median value, while the whiskers show the 5 and 95 percentiles. We compare our results with the theoretical expectations from NFW, ENS, B01. Also, a modified NFW prescription with slightly modified parameters as updated by Gao et al. (2008) is shown (see Section 5 for details).

where $\rho_{\text{crit}} = 3H_0^2/8\pi G$ is the critical density, δ_c is the characteristic density contrast and r_s is the scale radius of the halo. The concentration c is defined as the ratio between r_{200} and r_s. The quantities δ_c and c are directly related by

$$\delta_c = \frac{200}{3} \frac{c^3}{[\ln(1+c) - c/(1+c)]}. \tag{2.18}$$

The concentration c is the only free parameter in Eqn. (2.18) at a given halo mass and these two quantities are known to be correlated. In fact, characteristic halo densities reflect the density of the universe at the time the halos formed; the later a halo is assembled, the lower is its average concentration.

We have measured concentrations for our halos in the different cosmologies using the same procedures as applied to the analysis of the Millennium simulation (Neto et al., 2007; Gao et al., 2008). For our measurements, we take into account both relaxed and unrelaxed halos. In the second case, the equilibrium state is assessed by means of three criteria: (1) the fraction of mass in substructures with centers inside the virial radius is small, $f_{\text{sub}} < 0.1$, (2) the normalized offset between the center-of-mass of the halo $\vec{r}_{\text{cm}}$ and the potential minimum $\vec{r}_c$ is small, $s = |\vec{r}_c - \vec{r}_{\text{cm}}|/r_{200} < 0.07$ and (3) the virial ratio is sufficiently close to unity, $2T/|U| < 1.35$. These quantities provide a measure for the dynamical state of a halo, and considering these three conditions together guarantees in practice that a halo is close to an equilibrium configuration, excluding the ones with ongoing mergers, or with strong asymmetric configurations due to massive substructures.

For all relaxed halos selected in this way, we computed a spherically averaged density profile by storing the halo mass in equally spaced bins in $\log_{10}(r)$ between the virial radius r_{200} and $\log_{10}(r/r_{200}) = -2.5$. We used 32 bins for each halo and we choose a uniform radial range in units of r_{200} for the fitting procedure so that all halos are treated equally, regardless of the mass. We find that we obtain stable results when we use halos with more than 3000 particles, consistent with the Power et al. (2003) criteria, while with fewer particles we notice resolution effects in the concentration measurements, as both the gravitational softening and discreteness effects can artificially reduce the concentration. The final mass range we explored is hence 10^{12} to $10^{15}\,h^{-1}\mathrm{M}_\odot$.

In Figure 2.12, we show our measured mass-concentration relation for the different dark energy models at $z = 0$. The four solid lines show the median concentration as a function of mass. The boxes represent the 25 and 75 percentiles of the distribution, while the whiskers indicate the 5 and 95 percentiles of the distributions. We note that the scatter of the concentration at a given mass is very close to a log-normal distribution. It is interesting to remark that both the mean and the dispersion decrease with mass. In fact, massive halos form in some sense a more homogeneous population, because they have collapsed recently and so the formation redshift is relatively close to the present epoch. On the other hand, less massive

halos have a wider distribution of assembly redshifts and the structure of individual objects strongly depends on their particular accretion histories. For them, the assumption that objects we observe are just virialized is therefore inappropriate, especially for very low mass halos. In Fig. 2.12 we take into account only the relaxed halos, but we did an analogue measurement also for the whole sample, shown in Figure 2.13 at redshift 0 (top panel) and at $z = 1$ (low panel).

The correlation between mass and concentration approximately follows a power law for the relaxed halos of the ΛCDM model. In the literature, the concentrations would be expected to be somewhat lower if a complete sample is considered that includes disturbed halos. Comparing Figures 2.12 and 2.13 we notice that this expectation is confirmed, but the difference is not very pronounced, only about 5% for the whole mass range. We also note that the normalization $\sigma_8 = 0.8$ used for our simulations slightly lowers the amplitude of the zero point of the relation (Duffy et al., 2008; Macciò et al., 2008) when compared to the WMAP-3 normalization, as halos tend to assemble later with lower σ_8 and/or Ω_m.

When we compare our four simulated cosmologies we find that, as expected, EDE halos of given mass have always higher concentration at a given redshift than models with a cosmological constant: they tend to form earlier and so they have a higher characteristic density. Nevertheless, the differences are not large, they deviate by no more than $\sim 27\%$ at $z = 0$ over the entire mass range we studied for all halos and $\sim 25\%$ for the relaxed one. At higher redshift, the differences are only slightly bigger, of order of $\sim 28\%$ at $z = 1$ for the whole sample, and $\sim 35\%$ for halos in equilibrium configuration, suggesting that we anyway need reliable numerical calibrations and highly accurate observational data to discriminate between the different cosmologies. Interestingly, the average concentration is almost independent of mass when we consider $z \geqslant 2$, as the average concentration of the more massive halos is similar at all redshifts (Gao et al., 2008) and we are then restricted to the exponential tail of the mass function.

The change in concentration normalization relative to the cosmological constant model is well represented by the ratio between the linear growth factor of different models at very high redshift:

$$c_0 \to c_{0,\Lambda\text{CDM}} \frac{D_+(\infty)}{D_{+,\Lambda\text{CDM}}(\infty)}, \tag{2.19}$$

where $c_{0,\Lambda\text{CDM}}$ is the concentration in the ΛCDM model, as suggested by Dolag et al. (2004). In Table 2.2, we compare the ratio between the concentration at $z = 0$ both for the relaxed halos (second column) and for the whole sample (third column) with the ratio between the asymptotic growth factor for the same cosmologies (forth column). The order of magnitude of the two effects is comparable, although the match is not perfect. Here the ratios are computed for $M \sim 4 \times 10^{12} \ h^{-1} M_\odot$, where we have a large number density of halos.
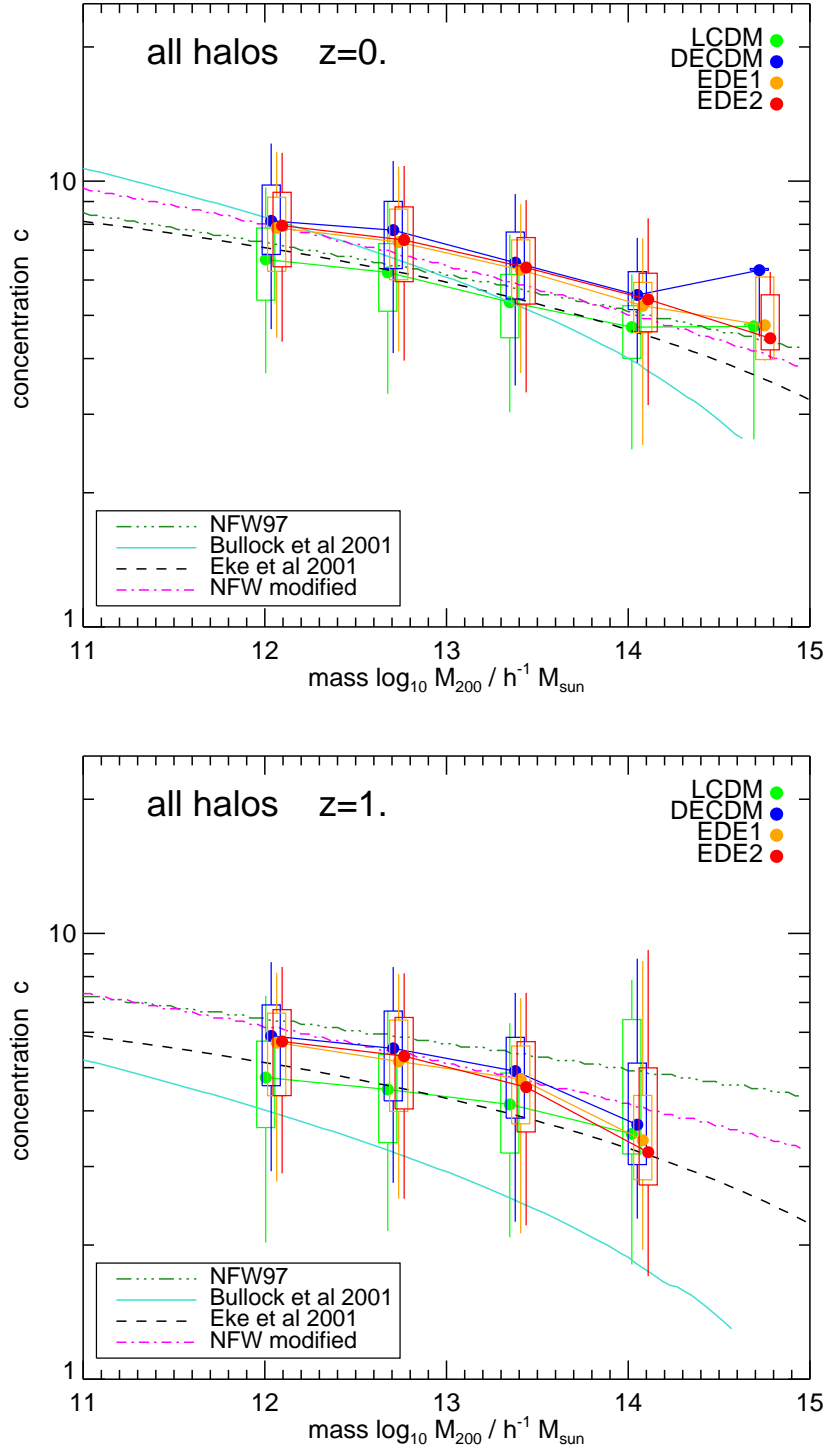
Figure 2.13 Mass-concentration relation for all halos in our simulations. The top panels refers to redshift $z = 0$, while the bottom panel shows the results at $z = 1$. The boxes represent the 25 and 75 percentiles of the distribution with respect to the median value, while the whiskers show the 5 and 95 percentiles. We compare our results with the theoretical expectations from NFW, ENS, B01. Also, a modified NFW prescription with slightly modified parameters as updated by Gao et al. (2008) is shown (see Section 5 for details). The concentration is 5% lower with respect to the relaxed sample at $z = 0$ for the ΛCDM model.

Model	$\dfrac{c_0}{c_{0,\Lambda\mathrm{CDM}}}$	$\dfrac{c_{0,ALL}}{c_{0,ALL,\Lambda\mathrm{CDM}}}$	$\dfrac{D_+(\mathrm{inf})}{D_{+,\Lambda\mathrm{CDM}}(\mathrm{inf})}$
ΛCDM	1.000	1.000	1.000
DECDM	1.256	1.275	1.228
EDE1	1.218	1.232	1.229
EDE2	1.255	1.273	1.252

Table 2.2 Concentration and asymptotic growth factor in the four different cosmologies studied here. The ratio between the concentration parameters at redshift $z = 0$ refers to a mass of $M \sim 4 \times 10^{12}\ h^{-1} M_\odot$ that corresponds to the mass range that contains the majority of our halos. For each model (first column) we give the c_0 parameter relative to ΛCDM, taking into account the relaxed halos (second column) or the whole sample (third column). Finally, in the last column we show the linear growth factor at infinity relative to the ΛCDM cosmology.

It is interesting to compare the concentrations we measure with the various theoretical predictions that have been made for this quantity. We investigate three popular descriptions for the concentration: the classic Navarro, Frenk & White model (hereafter NFW), the model of Bullock et al. (2001, hereafter B01), and that of Eke et al. (2001, hereafter ENS). Finally, we also plot the new modified version of the original Navarro Frenk and White model, as recently proposed by Gao et al. (2008). Both the B01 model and the standard NFW have two free parameters that have been tuned to reproduce simulation results. In the original NFW prescription, the definition of the formation time of a halo is taken to be the redshift at which half of its mass is first contained in a single progenitor: $F = 0.5$. The second parameter is the proportionality constant, $C = 3000$, that relates the halo density scale to the mean cosmic density at the collapse redshift z_{coll}. Recently, Gao et al. (2008) noticed that the evolution of the mass-concentration relation with redshift can be approximated much better by setting $F = 0.1$. The B01 model adopts as collapse redshift the epoch at which the typical collapsing mass fulfills $M_*(a_c) = F\, M_{\mathrm{vir}}$, with $F = 0.01$. They further assume that the concentration is a factor $K = 3.4$ times the ratio between the scale factor at the time the halo is identified and the collapse time. For K and F we use the values that are indicated as the best parameters by Macciò et al. (2007). Finally, we compute the ENS prescriptions considering the effective amplitude of the power spectrum at the scale of the cluster mass. This quantity, rescaled for the linear growth factor of the simulated cosmology, has to be constant. In this case, only one parameter, $C_\sigma = 28$, is needed. Bullock et al. (2001) and Eke et al. (2001) refer to the virial radius as the one including an overdensity given by the generalized top hat collapse model. We have appropriately adapted these models such that the concentration of a halo is defined instead relative to radius r_{200}, as in the NFW model.

Aside from B01, all three other model predictions yield concentrations that agree reasonably well with the measured values at $z = 0$. The B01 model underpredicts the relation at high masses, where it gives has a sharp decline of the relation for $M\, 10^{13}\ h^{-1}\mathrm{M}_\odot$ which is not seen in the simulations. In contrast, the NFW model is

in reasonable agreement with the data at $z = 0$ for both halo samples. However, at $z = 1$ the evolution predicted by the NFW model is less than what we find numerically, even when we consider the revised formulation proposed by Gao et al. (2008) (indicated as NFW modified). The NFW model with the new fitting parameters yields a reasonable fit at the high mass end, but performs a bit worse than the original formulation at $z = 0$, specially at low masses. Unfortunately, for the NFW model the normalization is model dependent, so we cannot really capture all the effects due to different cosmological parameters we use. Finally, the dashed black line in each plot shows the ENS model. This prescription gives the best match with our results and has been able to reproduce the slope of the concentration-mass relation even at higher redshift.

At a fixed mass, halos in the EDE cosmology are significantly less concentrated than their counterparts in the ΛCDM cosmology. It is interesting to notice that the ENS model reproduces these differences quite well, without modifications of the original prescription. In Figure 2.14, we plot for each simulation the corresponding theoretical expectation (dashed lines) for the sample of relaxed halos at $z = 0$. For a low density universe the scaling of the linear growth factor with redshift leads to a greater difference between the models. Dark halo concentrations depend both on the redshift evolution of δ_c and the amplitude of the power spectrum on mass scales characteristic for the halo.

These results for the concentration are particularly important since they demonstrate that quintessence cosmologies with the same equation-of-state at present, but different redshift evolution, can produce measurable differences in the properties of the non-linear central regions of cluster-sized halos. However, the prospects to observationally exploit these concentration differences to distinguish different dark energy cosmologies are sobering. For one, the systematic differences we measure for the concentrations are quite small compared to the statistical errors for the mean concentration, while at the same time the theoretical algorithms for predicting the halo concentration perform quite differently already for the ΛCDM cosmology. Furthermore, directly measuring halo concentrations in observations is not readily possible as it requires an accurate knowledge of the virial radius of a halo, a parameter which is poorly constrained from observations. It therefore remains to be seen whether the effects of dark energy on the non-linear structure of dark halos can be turned into a powerful tool to learn about the nature of dark energy.

2.6 Counting halos by velocity dispersion

As we have seen, the different evolution of the halo mass function is in principle a very sensitive probe of the expansion history of the universe, especially when the massive end of the mass function is probed. Obtaining absolute mass estimates from observations is however problematic, and fraught with systematic biases and
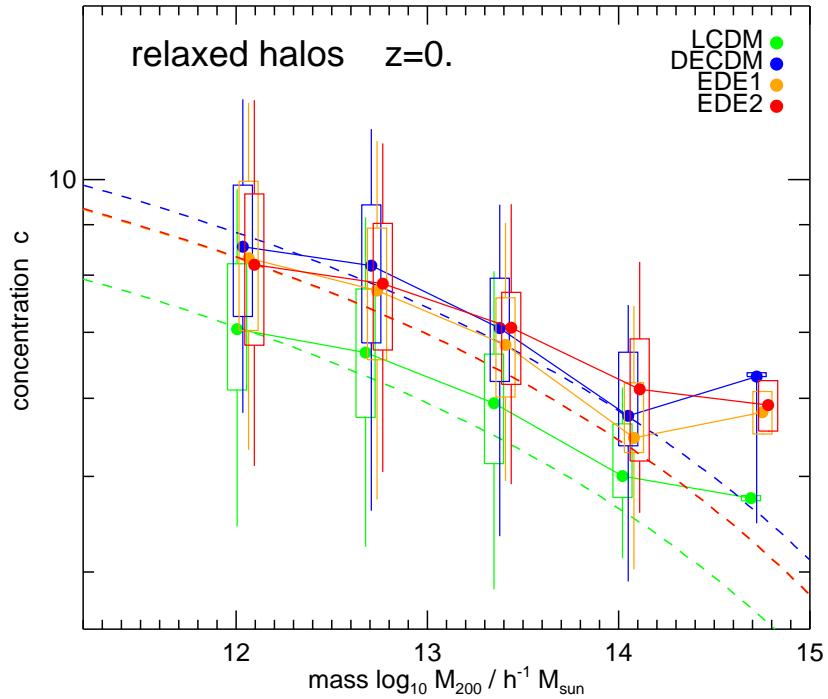
Figure 2.14 Mass-concentration relation for relaxed halos today. Here we show the agreement between simulation results (symbols) and theoretical predictions from ENS (dashed lines), both for the ΛCDM and EDE cosmologies. To this end we solve Eqn. (13) and (16) of Eke et al. (2001). The differences between the four cosmologies are due mostly to the differences in the growth factor evolution and consequently in the amplitude of the power spectrum. The ENS formula works quite well also for EDE models without modifications of the original prescription.
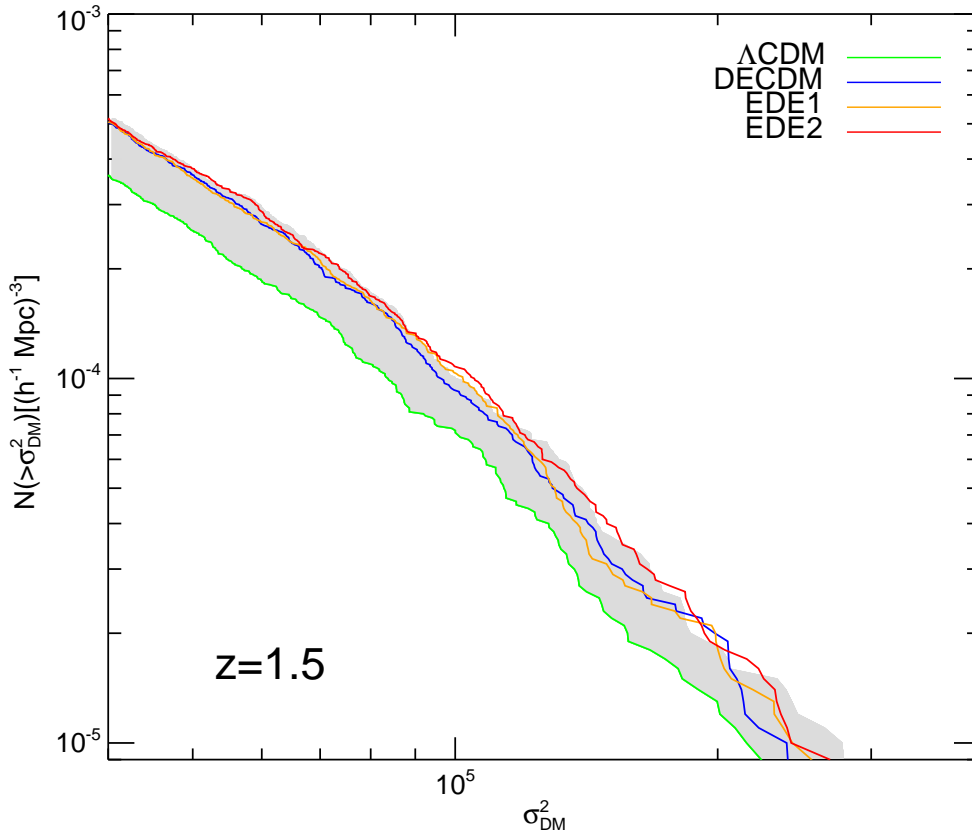
Figure 2.15 The velocity function $n(\sigma)$ as a function of halo mass, for all satellites inside r_{200}. The shaded area indicates the differences between a ΛCDM model with $\sigma_8 = 0.8$ and the same model with $\sigma_8 = 0.9$. It is interesting to remark that this EDE models could justify a higher normalization cosmology.

uncertainties. It is therefore important to look for new ways to count halos which are more readily accessible by observations.

One such approach lies in using the motion of galaxies in groups or clusters of galaxies to measure the line-of sight velocity dispersion, which in turn can be cast into an estimate of the total virial mass of the host halo. This relies on the assumption that the dynamics of the cluster or group galaxies is tracing out the dark matter halo potential.

Cluster and group galaxies can be identified with dark matter sub-structures in N-body simulations (Springel et al., 2001a; Vale and Ostriker, 2004). Employing the bulk velocities of sub-halos as a simulation proxy for real galaxy velocities, we can hence build a velocity profile for any isolated halo, and estimate a line-of-sight velocity dispersion, similarly as it is done for observed group catalogues of galaxies. This allows then to directly count halos (i.e. galaxy groups) as a function of line-of-sight velocity dispersion, bypassing the problematic point of assigning halo mass estimates.
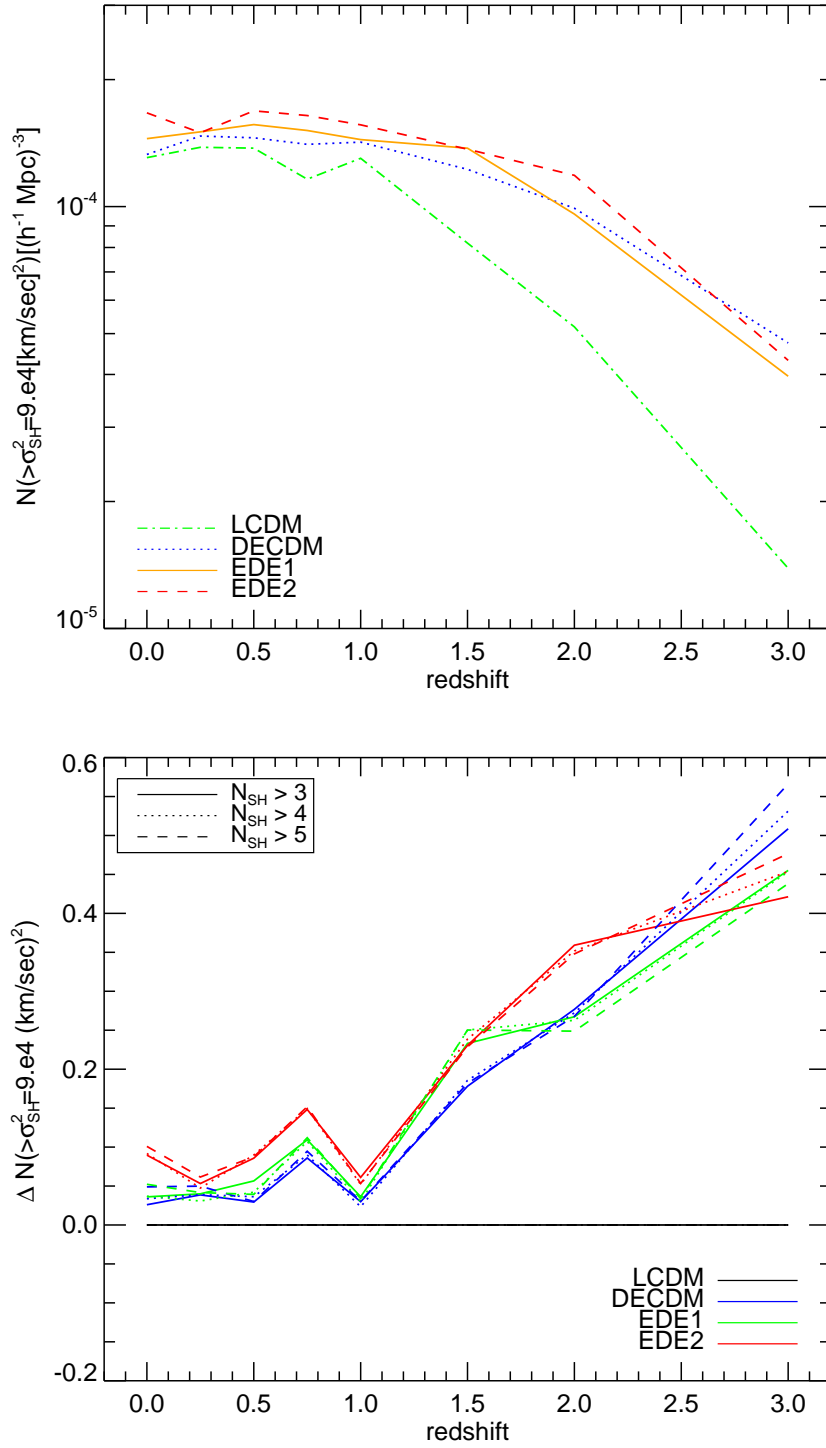
Figure 2.16 Left panel: Comparison of the redshift evolution of the velocity dispersion function for all four cosmologies we simulated (ΛCDM, DECDM, EDE1, and EDE2). Here the cumulative count of groups with velocity dispersion above $\sigma = 300\,\mathrm{km\,s^{-1}}$ was used to measure the amplitude of the velocity dispersion function. Right panel: Differences in the number count when only halos with more than 3 (solid line), 4 (dotted line) or 5 (dashed line) substructures are selected.

In Figure 2.15, we show our estimated cumulative velocity dispersion function for our four different cosmologies at redshift $z = 1.5$. This graph can be interpreted as being a different representation of the halo mass function, except that it is in principle directly accessible by observations. For this measurement, we have derived the information on the velocities from the SUBFIND algorithm directly implemented in GADGET-3, which can find subhalos embedded in dark matter halos.

An important aspect of this statistic is that it does not rely on the often ambiguous definition of a group mass. Instead, it can be directly measured and is more readily accessed by observations. In fact, studies based on the DEEP2 survey (Lin et al., 2004; Davis et al., 2005; Conroy et al., 2007) indicate that, if combined with both the velocity dispersion distribution of clusters from the Sloan Digital Sky Survey and independent measurements of σ_8, they will be able to constrain w to within approximately 1% accuracy. This method is almost independent of cosmological parameters, with the exception of σ_8, since a change in normalization can shift the space density of halos as a function of mass by a similar amount as done by the EDE models. This is illustrated in Figure 2.15 by the shaded area, which represents the change of the velocity dispersion function when σ_8 is increased from 0.8 (green line) to 0.9 (upper limit of the shaded area). The velocity distribution function of the EDE models then approaches the one that we would measure for a ΛCDM model with higher σ_8.

These kind of studies have strong motivations both from the observational and theoretical point of view: there is little scatter between host galaxy luminosity and dark matter halo virial mass and the velocity difference distribution of satellites and interlopers can be modeled as a Gaussian and a constant, respectively (Conroy et al., 2005; Faltenbacher and Diemand, 2006).

Figure 2.16 (left panel) shows the cumulative number of groups with velocity dispersion above a given value, as a function in redshift for the different models. We decided to count halos above a velocity dispersion of $300\,\mathrm{km\,s^{-1}}$, where accurate measurements can be expected also from observations. Note that there is already a very large difference between ΛCDM and EDE at redshift $z = 1$. We find that there is almost no evolution in the cluster number in the dark energy models, while ΛCDM drops by a factor of nearly 10 up to redshift $z = 3$. What is especially important here is the relative difference between the number counts of the two different cosmologies. The fact that we do not need to introduce the mass in this comparison give us the advantage of having no error derived from the particular measurement procedure adopted for the mass. At a fixed velocity dispersion, we can directly probe the growth of the structure at each redshift, which depends on the equation of state parameter w. The slower evolution of the cluster population in EDE models is exactly what is expected to be observed also from Sunyaev-Zeldovich studies of large samples of clusters of galaxies. Combined with probes of the cluster internal velocity dispersion we can hence hope to be able to derive stringent cosmological

constraints.

We also remark that the relative difference between the number of objects within these four simulations seems to be a quite robust statistic which is invariant with respect to details of the measurement procedure. For example, in Figure 2.16 (right panel), we change the number of considered subhalos in the halos to be a minimum of 3, 4, and 5, but the velocity dispersion function relative to the ΛCDM cosmology is essentially unchanged. In practice, the number of observable satellites per host halo suffers from limitations imposed by the magnitude limit of the survey. Our results suggest that the measured velocity dispersion should however be relatively insensitive to this selection effect.

Finally, we have also studied a few properties of the largest substructures in halos to see whether there is a difference in EDE cosmologies. In Figure 2.17, the small diamonds indicate the values of the ratio between M_1 (the mass of the most massive subhalo) and M_{200} (the mass within a sphere of density 200 times the critical value at redshift 0) for the first 200 most massive halos at redshift $z = 3$. The filled circles represent the median of the distribution, computed in bins of 50 halos each, while the error bars mark the 20-th and 80-th percentiles of the distribution. There is almost no dependence on parent halo mass, but we can notice a small, but systematic tendency for the ΛCDM subhalos to be slightly more massive. The dependence is quite weak, yet this behaviour is clear even if the mass of the progenitor M_{200} tends to be lower on average at this high redshift. This is symptomatic of the fact that the ΛCDM substructures are formed at lower redshift with respect to what happens in the EDE models. This is also consistent with expectations based on the observed dependence of substructure mass fraction on halo mass (e.g. De Lucia et al., 2004). Once accreted onto a massive halo, subhalos suffer significant stripping, an effect that is more important for substructures accreted at higher redshift, making the subhalos in the EDE models less massive on average.

2.7 Conclusions

In this study we have analyzed non-linear structure formation in a particular class of dark energy cosmologies, so called *early dark energy* models where the contribution of dark energy to the total energy density of the universe does not vanish even at high redshift, unlike in models with a cosmological constant and many other simple quintessence scenarios. Our particular interest has been to test whether analytic predictions for the halo mass function still reliably work in such cosmologies. As the evolution of the mass function is one of the most sensitive probes available for dark energy, this is of crucial importance for the interpretation of future large galaxy cluster surveys at high redshift. The mass function of EDE models is also especially interesting because analytic theory based on extensions of the spherical collapse model predicts that the mass function should be significantly modified
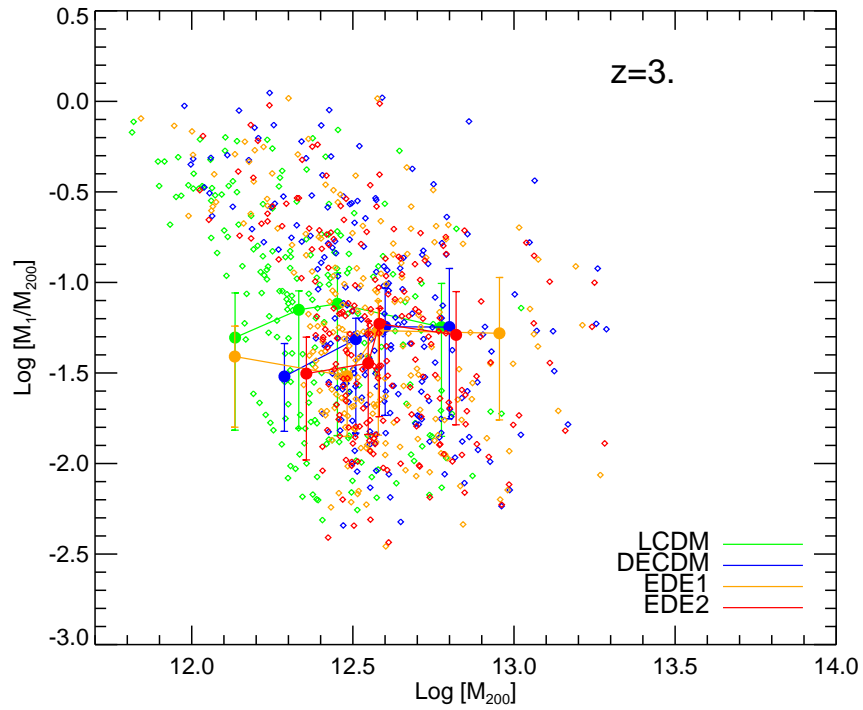
Figure 2.17 Ratio of the mass of the two most massive substructures with respect to the mass of the parent halo. The small diamonds refer to individual halos, while the filled circles are the median values. The error bars mark the 20th and 80th percentiles of the distributions.

(Bartelmann et al., 2006), and in particular be characterized by a different value of the linear overdensity δ_c for collapse, as well as a slightly modified virial overdensity.

We have carried out a set of high-resolution N-body simulations of two EDE models, and compared them with a standard ΛCDM cosmology, and a model with a constant equation of state equal to $w = -0.6$. Interestingly, we find that the universality of the standard Sheth & Tormen formalism for estimating the halo mass function also extends to the EDE models, at least at the $\sim 15\%$ accuracy level that is reached also for the ordinary ΛCDM model. This means that we have found good agreement of the standard ST estimate of the abundance of DM halos with our numerical results for the EDE cosmologies, *without* modification of the assumed virial overdensity and the linear density contrast threshold. This disagrees with the theoretical suggestions based on the generalized top-hat collapse. In fact, if we instead use the latter as theoretical prediction of the halo mass function, the deviations between the prediction and the numerical results become significantly larger. We hence conclude that the constant standard value for the linearly extrapolated density contrast can be used also for an analysis of early dark energy cosmologies. Very recently, similar results were also obtained by Francis et al. (2008), who studied the same problem in cosmological simulations with somewhat smaller mass resolution.

This results on the mass function appear to hold over the whole redshift range we studied, from $z = 0$ to $z = 3$. Since our simulations were normalized to the same σ_8 today, their mass functions and power spectra agree very well today, but towards higher redshift there are significant differences, as expected due to the different histories of the linear growth factor in the different cosmologies. In general, structure in the EDE cosmologies has to form significantly earlier than in ΛCDM to arrive at the same abundance today. For example, already by redshift $z = 3$, the abundance of galaxy clusters of mass $M = 5 \times 10^{12} \, h^{-1} \mathrm{M}_\odot$ is higher in EDE1 by a factor of ~ 1.7 relative to ΛCDM.

The earlier formation of halos in EDE models is also directly reflected in the concentration of halos. While for a given σ_8 we find the same abundance of DM halos, the different formation histories are still reflected in a subtle modification of the internal structure of halos, making EDE concentrations for all halo masses and redshifts considered slightly higher. The difference is however quite small, but it would, for example, lead to a higher rate of dark matter annihilation in halos.

Another relationship that appears to accurately hold equally well in ΛCDM as in generalized dark energy cosmologies is the virial scaling between mass and dark matter velocity dispersion that Evrard et al. (2008) has found. In fact, we find that their normalization of this relation is accurately reproduced by all of our simulations within the measurement uncertainties, independent of cosmology. This also suggests that possible differences in the virial overdensity of EDE halos must be very small, and that presumably the relationship between total Sunyaev-Zeldovich decrement and halo mass is unmodified as well.

We show that counting the number of halos as a function of the line-of-sight velocity dispersion (of subhalos or galaxies), both in simulations and observations, can probe the growth of structures with redshift, and so put powerful constraints on the equation of state parameters. This goal can be achieved by just identifying and counting groups in galaxy survey data such as DEEP2, and by comparing them with high-resolution N-body simulations. Precision measurements with this technique will still require accurate calibrations to deal with complications such as a possible velocity bias or selection effects in observational surveys. However, Davis et al. (2005) suggest that the DEEP2 survey alone has the power to constrain w to an accuracy of 20% using velocity dispersion data, which illustrates the promise of this technique. In combination with other independent data, such as X-ray temperature and SZ decrement data, the constraints could be improved to an accuracy of 5%, without the need to invoke a model for the ambiguous total mass of a halo.

Distinguishing a time-varying dark energy component from the cosmological constant is a major quest of the present theoretical and observational astronomy. One approach is to rely on classical cosmological tests of the Hubble diagram, e.g. by pushing the supernova type Ia observations to much higher redshift. Another quite direct geometrical probe is the observation of baryonic acoustic oscillations in the matter distribution at different redshifts. Finally, the linear and non-linear evolution of cosmic structures provides another opportunity to constrain dark energy. In this work we have used numerical N-body simulations to examine the difference in structure growth in early dark energy cosmologies. We have seen that such simulations are essential to test the predictions of more simplified analytic models, and to calibrate observational tests that try to constrain the properties of dark energy with the abundance and internal structure of dark matter halos. Our results show clearly that the effects due to dynamical dark energy tend to be quite subtle, and can only be cleanly distinguished from ordinary ΛCDM in high accuracy simulations. This poses new challenges to improve the precision of future generations of simulations, and at the same time emphasizes the immense observational task to arrive at sufficiently precise data at high redshift to constrain the dark side of the universe with the required accuracy.

The Sunyaev Zeldovich effects in hydrodynamical simulations of Early Dark Energy models

3.1 Introduction

Current cosmological observations, such as the temperature fluctuations in the Cosmic Microwave Background (CMB), the redshift measurements from Type Ia Supernovae (SNIa), and the Baryonic Acoustic Oscillations (BAO) data, consistently lead to a picture where the Universe has entered a period of *accelerated* expansion. This can be explained if the energy density at present is dominated by a dark energy component with negative pressure, roughly accounting for 70% of the total energy budget.

The simplest form of dark energy is the cosmological constant Λ, which is characterized by a time-independent equation of state parameter and is invoked in the highly successful, standard ΛCDM model for cosmic structure formation. However, many attractive alternative models for the dark energy have been advanced, including e.g. a slowly rolling scalar field (Ratra and Peebles, 1988) known as quintessence. Those models have the advantage to offer an explanation for the fundamental fine-tuning and coincidence problems that affect the simpler cosmological constant scenario.

A major class of dark energy scenarios is governed by scalar fields with global attractor solutions. The fields sub-dominantly "track" the dominant component of the cosmological fluid, and lead to an almost constant ratio between the fractional dark energy to the critical density at early times. In the particularly interesting

class of so-called Early Dark Energy (EDE) models, we expect a non-negligible dark energy contribution even up to the last scattering surface, and consequently a very different structure formation history. Several studies (Bartelmann et al., 2006; Grossi and Springel, 2009; Francis et al., 2009a) have shown that early dark energy indeed strongly influences the growth of cosmic structures. This translates into a slower evolution of the cosmic structures at late times, and may affect the value of the overdensity at virialization, Δ_v.

A natural way to constrain the expansion history of the Universe and to prove the presence of early dark energy lies in studying the distribution of clusters as a function of mass and redshift (e.g. Haiman et al., 2001). In fact, it is well known that cluster counts as a function of their mass are exponentially sensitive to the amplitude of the linear density field and hence to the dark energy equation of state. Unfortunately, the mass of clusters is not a direct observable and it is very difficult to acquire a sufficiently large sample of objects covering the high redshift range in order to draw quantitative conclusions on the nature of dark energy. The first problem can be overcome by using scaling relations that allow an estimate of the mass of the clusters. Typical proxies include the Sunyaev Zeldovich flux decrement, the X-ray temperature and surface brightness, and the weak lensing shear. Among these measures, the thermal Sunyaev Zeldovich effect appears particularly attractive. It allows the detection of galaxy clusters by measuring the distortion they imprint on the background CMB. This technique should in principle yield reliable estimates of the cluster mass, because the integrated SZ flux is a direct indicator of the total energy in the intra-cluster medium (ICM). Furthermore, the SZ distortion can be seen to much larger distances than the X-ray emission. It is therefore important to study this relation further and to identify the sources of the scatter between the observed quantities and the cluster mass.

The Sunyaev Zeldovich effect is presently actively pursued as a method to detect galaxy clusters till high redshift, with the goal to directly measure the evolution of the cluster mass function. In fact, the signal strength is not dimmed with redshift like in optical or X-ray surveys, and it does not suffer significantly from projection effects, nor from a sensitivity to the spatial distribution of the hot intra-cluster gas. Current experiments like the ones carried out with the South Pole Telescope (SPT Ruhl, 2004) and the Atacama Cosmology Telescope (ACT Kosowsky, 2003) are therefore surveying the microwave sky in order to develop large cluster catalogues. Optical deep field observations that are planned as follow-up measurements (see, e.g. PanSTARRS, BOSS,LSST, ADEPT, EUCLID) promise to increase the power of the data considerably and should help to remove certain statistical uncertainties.

The thermal SZ effect can also be detected statistically as a secondary anisotropy in the CMB power spectrum, since it is the dominant contribution at $\ell > 2000$. The current measurements of the small scale anisotropy by instruments like the Cosmic Microwave background Imager (CBI Mason et al., 2003), the Berkeley-

Illinois-Maryland Array (BIMA Dawson et al., 2002), and the Arcminute Cosmology Bolometer Array Receiver (ACBAR Kuo et al., 2004) indicate an excess in the power spectrum at high multipoles. Explaining these measurements through the Sunyaev Zeldovich effect would however require a higher cluster abundance than the one predicted in the standard ΛCDM cosmological model for a value of σ_8 close to the one deduced from the WMAP 5-year data: $\sigma_8 = 0.812^{+0.026}_{-0.026}$ (Komatsu et al., 2009b). EDE models may help to solve this apparent discrepancy, because they feature a higher relative abundance of objects at high redshift, which would enhance the SZ- signal even if the density fluctuations have the same amplitude today. Also, the observed strong lensing cross section is an order of magnitude larger than predicted by ΛCDM (Dalal et al., 2005), and one would be forced to increase σ_8 to a value close to unity to explain this result. Again, early dark energy could help in solving this discrepancy, which stems mainly from the fact that the high redshift clusters are not sufficiently abundant in the standard ΛCDM model. Other indirect evidences for more advanced structure formation at high redshift are the large observed values for the concentration parameter and Einstein radii (Broadhurst and Barkana, 2008), radio observations of clusters at high redshift (Venemans et al., 2007), and also the recent analysis of the Spitzer Space Telescope observations (Magliocchetti et al., 2007) that seems to indicate a considerably larger cluster number density and an higher level of clustering.

In this Chapter we carry out a study of the impact of an early dark energy component on the Sunyaev Zeldovich effect, considering a set of 10 hydrodynamical simulations that cover a wide range of viable dark energy cosmologies. We perform hydrodynamic simulations of cluster formation and evolution assuming a simple non-radiative model, both to cleanly disentangle the dark energy effects and to keep the large simulation set computationally feasible. We generate a set of synthetic maps both of the thermal and the kinetic SZ effect to capture the effects of projection and clustering of the clusters. Our main purpose is to achieve a good theoretical understanding of the SZ signal in the EDE cosmologies and to examine in a quantitative way the extent to which the data can be used to discriminate against a cosmological constant.

Previous works (Sadeh et al., 2007; Rephaeli and Sadeh, 2008) have analyzed the effect of early dark energy on the SZ power spectra using analytical tools instead of numerical simulations. In particular, they assessed the feasibility of reproducing the observed high level of SZ-power, finding that an early dark energy contribution above the current observational limits is apparently required in order to solve the "CBI anomaly" and to recover the observed excess in the power spectrum. Forecasts for the distribution of the sources in the SPT, ATC and Planck cluster samples (Waizmann and Bartelmann, 2009; Fedeli et al., 2009) have supported the expectation of an increased abundance of clusters in the EDE cosmologies. Also in this case the authors used analytic estimates to quantify the SZ signal, and they

considered a number of cosmological models that differed not only in their early dark energy contribution, but also in other parameters of the underlying cosmology. The choice for the latter has unfortunately a strong influence on whether or not a concrete detection of early dark energy seems feasible. Our numerical work in this study provides for important tests of these earlier analytical studies. The latter make use of theoretical results that suggest important modification of the spherical collapse threshold and expected virial overdensity in early dark energy cosmologies (Bartelmann et al., 2006), but recent N-body work has not confirmed these predictions (Grossi and Springel, 2009; Francis et al., 2009a,b). This stresses the importance of explicit numerical modeling for studying the non-linear regime of EDE cosmologies, and for checking analytic predictions, a task that we address in this Chapter.

To fully exploit the statistical power of the upcoming SZ surveys it is important to calibrate the relation between the integrated SZ flux-decrement and the total cluster mass with a precision comparable to the statistical uncertainties expected from observations. On the theoretical side, a number of groups have studied the SZE scaling relations using semi-analytical models (McCarthy et al., 2003), and cosmological simulations (White et al., 2002; da Silva, 2004; Nagai, 2006; Sehgal et al., 2007). They all find a slope in good agreement with the prediction of a self-similar model. Since gravity does not have a preferred scale, we expect clusters of different sizes to be approximately scaled versions of each other as long as gravity only determines the ICM evolution and there is no preferred scale in the underlying cosmological model. It is important to understand how closely clusters actually follow this model, how well they behave as "SZ standard candles", and how large the intrinsic dispersion in the Y-M correlation is. The Y-M correlation is a fundamental tool to use observations of the SZ signal as a tracer of the cluster mass, and any dependence it may have on cosmological parameters need to be accurately understood in order to avoid possible biases. In this work we hence extend the analysis of the Y-M relation to the early dark energy case, and we study its scatter in a similar way as done in Shaw et al. (2009).

The Chapter is organized as follows. In Section 2 we provide a short introduction to the SZ effect, and we present the relevant scaling laws predicted by a self-similar cluster model. The modeling of the different cosmological models with hydrodynamical simulations and the techniques used to compute the simulated maps and their contaminants are described in Section 3. Then, in Section 4 we investigate the global properties of the thermal and kinetic SZ effect for EDE models, given in terms of statistical properties of the maps and source number counts. In Section 5 we present forecasts for future measurements of the SZ number counts; in particular, we discuss the specific case of the SPT wide survey. The full investigation of mass-flux scaling relation and the details of the intrinsic scatter due to variations in the cluster mass definition are outlined in Section 6. Section 7 is concerned with

a study of the SZ power spectra predicted for the standard ΛCDM and EDE models, compared with the BIMA, CBI and ACBAR observational results. Finally, we summarize our results and discuss our conclusions in Section 8.

3.2 The Sunyaev-Zeldovich effects

Compton scattering of the cosmic microwave background (CMB) radiation by intervening hot plasma slightly modifies the incident Planck spectrum, imprinting on it a unique spectral signature: the Sunyaev Zeldovich effect. The redshift-independent nature of this physical process makes it a potentially powerful tool to probe the structure formation of the Universe at early times and in particular to obtain a direct measurement of the evolution of the number density of clusters at high redshift (e.g. Carlstrom et al., 2002). An extensive discussion can be found in several reviews (Rephaeli, 1995; Carlstrom et al., 2002; Rephaeli et al., 2005), below we summarize only the most important relations.

3.2.1 Thermal SZE

The thermal Sunyaev Zeldovich (tSZ) effect is one of the most important sources of secondary anisotropies of the CMB on small scales. It is the result of the inverse Compton scattering of the CMB photons by the non-relativistic electron gas within clusters and groups of galaxies. On average, scattering on the thermal distribution of electrons inside the intergalactic medium boosts the energy of the CMB photons, resulting in a small ($< 1\,\mathrm{mK}$) systematic shift of photons from the Rayleigh-Jeans to the Wien side of the frequency spectrum. For a given line-of-sight, the change in the spectral intensity can be expressed in terms of the Compton y-parameter, defined as:

$$y \equiv \frac{k_B\,\sigma_T}{m_e\,c^2} \int \mathrm{d}l\, n_e(T_e - T_{\mathrm{CMB}}) \;, \tag{3.1}$$

where σ_T is the Thomson-scattering cross section, $m_e c^2$ is the electron rest mass energy, c is the light speed, n_e is the electron number density, and T_e and $T_{\mathrm{CMB}} = 2.726$ K are the electron and CMB temperatures, respectively. If we express the effect as a temperature change at a dimensionless frequency $x \equiv h\,\nu/(k_B T_{\mathrm{CMB}})$, we have:

$$\frac{\Delta T}{T_{\mathrm{CMB}}} = y\, g_\nu(x) \;. \tag{3.2}$$

The spectral dependence of the Sunyaev Zeldovich effect on the observation frequency is described by the function

$$g_\nu(x) = \left(x\, \frac{e^x + 1}{e^x - 1} - 4 \right) \;, \tag{3.3}$$

which is zero at the crossover frequency $\nu_0 = 2.726$, negative below this characteristic frequency and positive above it. It is important to note that in the Rayleigh-Jeans (RJ) limit ($x \ll 1$) this expression reduces to $g_\nu(x) \simeq -2$. The particular frequency dependence of the tSZ effect makes it possible to disentangle this process from the kinetic SZ effect described below.

3.2.2 Kinetic SZE

The kinetic Sunyaev Zeldovich (kSZ) effect arises when the hot plasma that causes the tSZ effect is moving relative to the CMB rest frame. Such peculiar motions of the cluster as a whole lead to an additional Doppler effect that manifests itself in an observable distortion of the CMB spectrum. In the non-relativistic limit, the intensity of the kinematic component of the effect can be expressed in terms of the b-parameter, defined as:

$$b \equiv \frac{\sigma_T}{c} \int dl \, n_e \, v_r \, ,$$
(3.4)

where v_r is the line of sight component of the peculiar velocity of the gas element. The resulting temperature fluctuation is then $\Delta T/T = -b$, which is positive if the cluster is moving away from the observer, negative if it is approaching. Unlike the tSZ effect, the kSZ effect is independent of the observational frequency, a fact that can be used to disentangle the two distortions. Observationally, the kSZ effect provides an interesting possibility to measure the line-of-sight component of the peculiar velocity of clusters.

3.2.3 Self-similar scaling relations

In the absence of any non-gravitational heating and cooling processes, we can assume that clusters form an approximately self-similar family of objects. In such self-similar models, the virial temperature is expected to scale with the mass like

$$T_{\rm vir} \propto [M_{\rm vir} E(z)]^{2/3},$$
(3.5)

where $E(z)$ is the redshift-dependent Hubble parameter for a generic dark energy cosmology, and $M \equiv 4\pi r_\Delta^3 \Delta_c \rho_{\rm crit}/3$ is the halo mass enclosed within a virial over-density Δ_c times the critical density $\rho_{\rm crit}$. We assume that the system is in virial equilibrium, and that the mean density scales as $\rho \propto (1+z)^3$. Isothermal clusters satisfy the relation:

$$Y \propto f_{\rm gas} M_{\rm halo} T,$$
(3.6)

where $f_{\rm gas}$ is the gas mass fraction of the cluster. Applying Equation (3.5) to this relation, we then have:

$$Y \propto f_{\rm gas} M_{\rm vir}^{5/3} E(z)^{2/3}.$$
(3.7)

110

This describes the scaling, with mass and redshift, of the total Comptonization parameter Y of a cluster. In practice, we expect to observe some deviations from the self-similar expectation, because clusters are not strictly isothermal and are not always in thermal equilibrium, and the gas fraction f_{gas} may vary with redshift. In what follows, we will use simulations to calibrate the correlation between galaxy clusters mass and Sunyaev Zeldovich effect in EDE cosmologies.

3.3 Models and method

To derive accurate cosmological constraints from the global properties of the tSZ and kSZ effects we need to produce realistic models for the gas contributing along the line-of-sight of a fiducial observer to the last scattering surface of the CMB. In this work we use the outputs of high-resolution hydrodynamical simulations to construct past light-cones and mock maps of the induced y and b parameters. We analyze how ongoing and future SZ survey would be affected by models that allow for early dark energy, which requires a good understanding of the relation between observed and intrinsic properties of clusters in our simulated catalogues. Below we summarize our methodology and assumptions we use in studying these questions.

3.3.1 Early dark energy models

Dark energy influences the expansion history of the Universe as well as the growth history of cosmic large-scale structure. For a comprehensive analysis, we therefore select a variety of dark energy models with different physical properties. An overview of the characteristics of all the cosmologies studied in this Chapter is given in Table 3.1.

An important class of dark energy behavior is represented by the quintessence models, which start dynamical and approach a cosmological constant during their evolution. The tracking models are particularly attractive as they, at least in part, solve the fine-tuning and the coincidence problems of the standard ΛCDM cosmology. As specific models of such dark energy scenarios we study the so-called Early Dark Energy (EDE) models.

In EDE models, the impact of dark energy on structure formation is expected to be particularly strong because of the presence of a non-negligible dark energy component even at very high redshift, unlike in most other alternative models with a time-varying equation of state. Unlike in the ΛCDM model, the vacuum quintessence energy density, $\rho_Q(z)$, is redshift dependent:

$$\rho_Q = \rho_{Q_0}(1+z)^{3[1+w(z)]}, \tag{3.8}$$

where $w(z)$ is the equation of state parameter ($w(z) = -1$ at all times for a cosmo-

logical constant).

We adopt the parametrization of Wetterich (2004) to set up a first set of models, labeled EDE1, EDE2 and EDE2P in our notation, that allow for a non-trivial amount of dark energy at early times. The equation of state parameter for these models can be computed from the fitting formula:

$$w(z) = \frac{w_0}{(1 + by)^2},$$ (3.9)

where

$$b = -\frac{3w_0}{\ln\left(\frac{1/\Omega_{\mathrm{de,e}}}{\Omega_{\mathrm{de,e}}}\right) + \ln\left(\frac{1-\Omega_{m,0}}{\Omega_{m,0}}\right)},$$ (3.10)

$y = \ln(1 + z) = -\ln a$, and $\Omega_{\mathrm{de,e}}$ quantifies the early quintessence density. These are the same specific models investigated by Grossi and Springel (2009).

As a second dark energy scenario, we consider the parametrization proposed by Doran and Robbers (2006), in the form of our models EDE3DR and EDE3P. Instead of parametrizing $w(a)$, the authors derived an expression for the evolution of the density of the dark energy fluid:

$$\Omega_{\mathrm{de}}(a) \equiv \frac{\Omega_{\mathrm{de},0} - \Omega_{\mathrm{de,e}}\left(1 - a^{-3w_0}\right)}{\Omega_{\mathrm{de},0} + \Omega_{m,0}a^{3w_0}} + \Omega_{\mathrm{de,e}}\left(1 - a^{-3w_0}\right).$$ (3.11)

Here $\Omega_{\mathrm{de},0}$ is the fractional energy density today, while $\Omega_{\mathrm{de,e}}$ represents again the early contribution. The corresponding equation of state evolves from $w(a > a_{eq}) = 0$ during matter domination, to w_0 today. This new formulation has several advantages. A simple analytic expression for $\Omega_{\mathrm{de}}(a)$ allows one to compute very easily several cosmological quantities, particularly the evolution of the Hubble rate. Moreover, the non-vanishing dark energy density at early time arises as a natural parameter to solve the fine-tuning between dark matter and dark energy today. Finally, when compared to observational constraints, these interpolated models allow for a higher value of the average amount of dark energy during the epoch of structure formation (see also Doran et al., 2007):

$$\bar{\Omega}_{\mathrm{de,sf}} = -\ln a_{\mathrm{eq}}^{-1} \int_{\ln a_{\mathrm{eq}}}^{0} \Omega_{\mathrm{de}}(a)\,\mathrm{d}\ln a.$$ (3.12)

We also explore in this study the 'mocker models' proposed by Linder (2006), in which the dark energy acts similar to matter at early times before transitioning to drive the accelerated expansion. The two mocker models we examine here (EDE3 and EDE4) are the same ones as studied in Xia and Viel (2009) and fit the constraints from CMB and lower redshift SNIa very well. In particular, they produce a smooth derivative with respect to redshift for the equation of state at late times.

For these models the parametrization reads:

$$w(a) \;=\; -1 + \left[1 - \frac{w_0}{1 + w_0}a^C\right]^{-1}, \tag{3.13}$$

$$\rho_{\mathrm{de}}(a) \;=\; \rho_{\mathrm{de}}(1)\left[(1 + w_0)a^{-C} - w_0\right]^{3/C}, \tag{3.14}$$

where C characterizes the dynamics of the equation of state parameter, $w' = \mathrm{d}w/\mathrm{d}ln(a) = Cw\,(1+w)$. The amount of dark energy during the structure formation period, $\Omega_{\mathrm{de,sf}}$, lies at the percent level in these cosmologies, similar to the other possible dark energy parameterizations. In particular, a value of $C = 2.5$, the one adopted in the model EDE4, corresponds to $\Omega_{\mathrm{de,e}} \simeq 10^{-6}$.

In addition, we explore the model with dynamical dark energy described in Komatsu et al. (2009b), for brevity K08, with properties similar to those of the 'thawing models' described by Caldwell and Linder (2005). The equation for the evolution of $w(a)$ is here derived under the requirement that $w(a)$ approaches -1 at high redshift, i.e. beyond some transition redshift $z > z_{\mathrm{trans}}$, and that it can be described by a simple linear form, $w(a) = w_0 + (1-a)w_a$, at low redshift. This yields the expression

$$w(a) = \frac{a\tilde{w}(a)}{a + a_{\mathrm{trans}}} - \frac{a_{\mathrm{trans}}}{a + a_{\mathrm{trans}}}, \tag{3.15}$$

for $w(a)$, where

$$1 + w_0 \;=\; \frac{1 + \tilde{w}_0}{1 + a_{\mathrm{trans}}}, \tag{3.16}$$

$$w' \;=\; \frac{\tilde{w}_a}{1 + a_{\mathrm{trans}}} - \frac{a_{\mathrm{trans}}(1 + \tilde{w}_0)}{(1 + a_{\mathrm{trans}})^2}. \tag{3.17}$$

For our model K08, we choose $w_0 = -1.1$ and $w' = 1$, which are found to be the best fitting values inferred by an analysis of the 5-year WMAP distance priors combined with the BAO and SN distance data. As a transition redshift we take $z_{\mathrm{trans}} = 10$, above which $w(a)$ approaches the value -1. The values of w_0 and w' are almost independent of the choice of this quantity, as demonstrated by Komatsu et al. (2009b).

Finally, we consider a model with constant equation of state parameter equal to $w = -0.8$, labeled 'DECDM', and a conventional ΛCDM model, for reference. Throughout the Chapter, we use the labels introduced above to refer to different models.

In Figure 3.1, we show the evolution of the equation of state parameter $w(a)$ up to redshift $z \sim 1000$ in the eight models we consider. It is evident that the mocker models EDE3 and EDE4 approach the cosmological constant case at the present epoch more smoothly than all the other cosmologies. We also notice that the dark energy component in the K08 evolves initially very fast: it reaches a maximum at about $z \sim 3.8$, and is then declining towards a slowly evolving regime.

	$\Omega_{m,0}$	$\Omega_{\mathrm{de},0}$	h_0	σ_8	n_s	w_0	DE param
ΛCDM	0.25	0.75	0.7	0.8	1.0	-1.	0.
DECDM	0.25	0.75	0.7	0.8	1.0	-0.8	0.
EDE1	0.25	0.75	0.7	0.8	1.0	-0.93	$2 \times 10^{-4}(\Omega_{\mathrm{de},e})$
EDE2	0.25	0.75	0.7	0.8	1.0	-0.99	$8 \times 10^{-4}(\Omega_{\mathrm{de},e})$
EDE3	0.25	0.75	0.7	0.8	1.0	-0.972	$1.858(C)$
EDE4	0.25	0.75	0.7	0.8	1.0	-0.95	$2.5(C)$
EDE3DR	0.25	0.75	0.7	0.8	1.0	-0.942	$1.87 \times 10^{-2}(\Omega_{\mathrm{de},e})$
K08	0.25	0.75	0.7	0.8	1.0	-1.1	$1(w')$
EDE2P	0.364	0.636	0.62	0.78	0.99	-0.99	$8 \times 10^{-4}(\Omega_{\mathrm{de},e})$
EDE3P	0.284	0.716	0.686	0.715	0.978	-0.942	$1.87 \times 10^{-2}(\Omega_{\mathrm{de},e})$

Table 3.1 Key parameters of the simulated models. The parameter $\Omega_{\mathrm{de},0}$ describes the amount of dark energy at the present epoch. This term, together with w_0, the value of the equation state parameter today, and $\Omega_{\mathrm{de},e}$, the amount of dark energy at early times, completely describes the models EDE1, EDE2 and EDE2P (see Equation3.10). In the mocker models EDE3 and EDE4, the parametrization reads according to Equation 3.14. Models EDE3RD and EDE3P are constructed directly by rewriting the evolution of the fractional energy density of a cosmological constant in order to include a non-negligible dark energy term at early times (3.11). Finally, in the model K08, w' parametrizes the first derivative of the present day equation of state parameter (3.15).
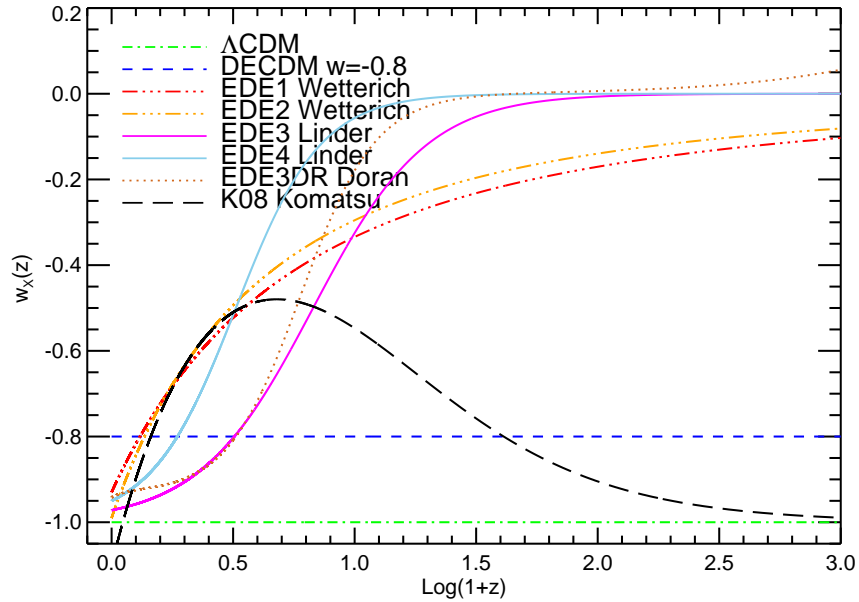
Figure 3.1 Equation of state parameter w shown as a function of redshift for eight different cosmological models considered in this work. In the EDE models, the value of w today is close to that of ΛCDM, but the amount of dark energy at early times is non vanishing, as described by the parametrization (3.9). In contrast, in the model K08 (black long dashed line) the scalar field is moving very slow initially, than $w(z) \sim -1$ also at early times.
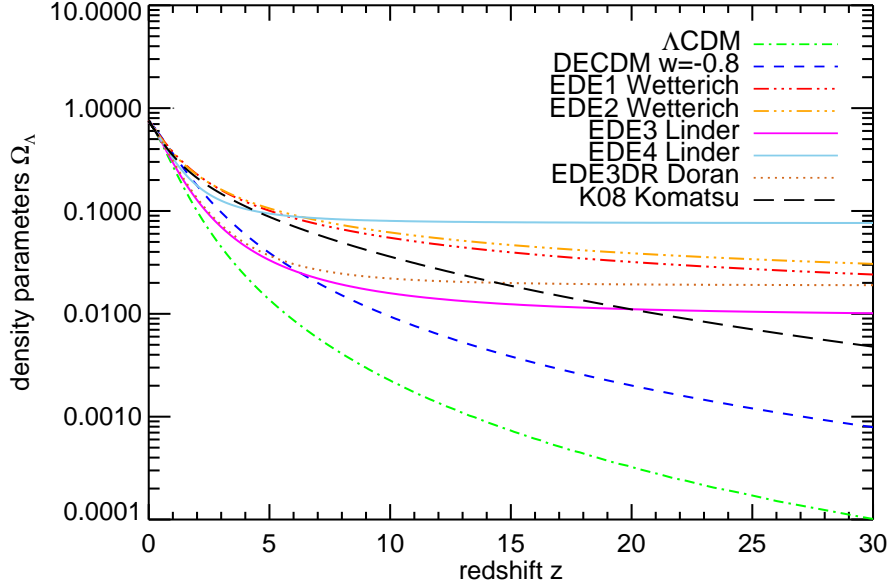
Figure 3.2 Evolution of the density parameters $\Omega_{de}(z)$ for the eight cosmological models studied in this work. At redshift $z = 30$, the dark energy contribution is higher for EDE models compared with a ΛCDM cosmology. In the model EDE4, Ω_{de} is even three orders of magnitude bigger with respect to the cosmological constant case. We observe that at redshift $z < 5$, the effect of EDE on the growth of perturbation is at the per-cent level.
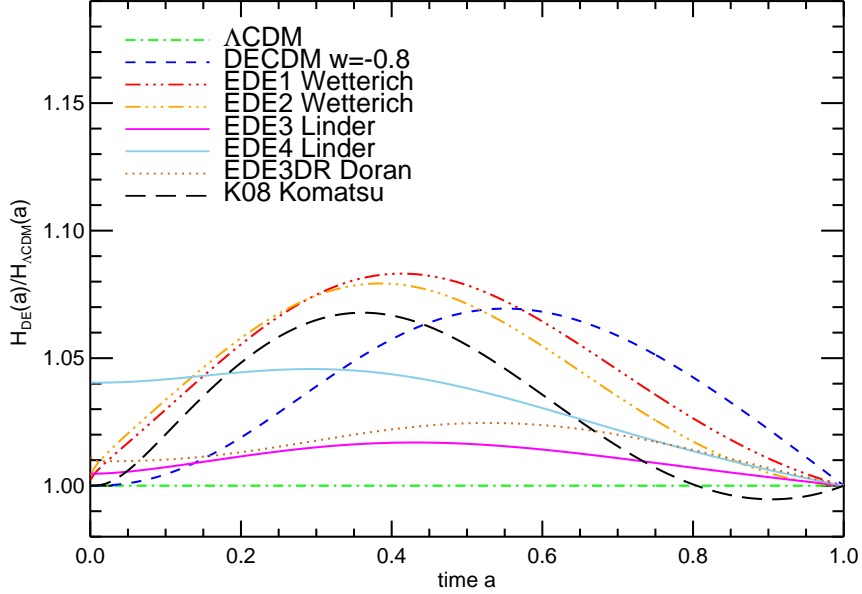
Figure 3.3 Ratio of the Hubble parameter of the quintessence cosmology to that in ΛCDM, as a function of the scale factor a. In the EDE models EDE1 and EDE2 the background evolution differs up to 8% with respect to the standard cosmology, while in the other quintessence models the discrepancies are reduced. This has a strong effect on the evolution of the growth factor.
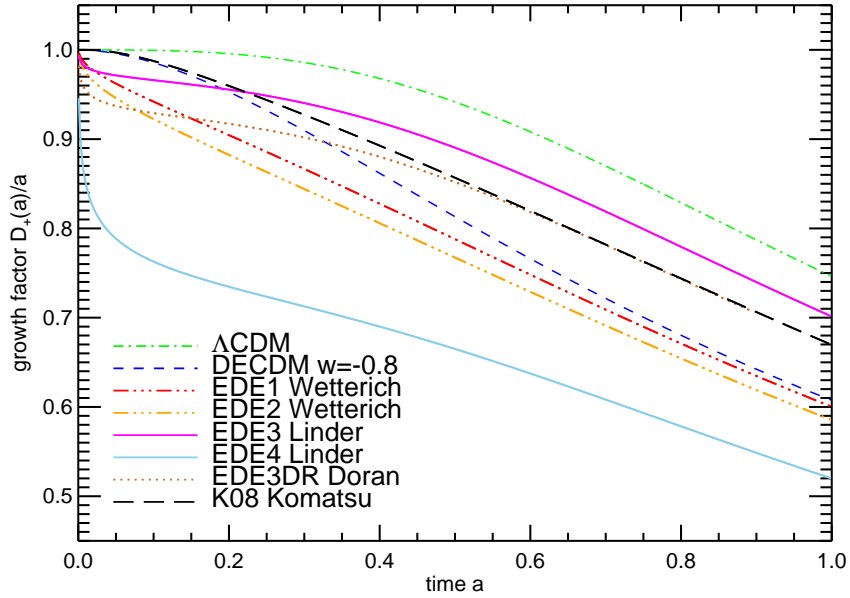
Figure 3.4 Ratio of the growth factor of linear density perturbations and the scale factor a. The growth factor in the eight different cosmologies illustrated here has been normalized to unity at early time, i.e. we here assume that the starting density contrast is the same in all the cosmologies. In particular, the model EDE4, the sky blue solid line, shows a significant difference in the growth factor evolution even with small energy density at high redshift: $\Omega_{de,e} \simeq 10^{-6}$. In all cases, structures have to grow earlier to reach the same abundance as the ΛCDM model today.

3.3.2 The cosmological hydrodynamical simulation

Our starting point for studying the properties of the thermal and kinetic SZ effects in the different cosmologies is a representation of the spatial distribution of the gas mass along the past light-cone. For this purpose, we use a set of high-resolution cosmological simulations including gravitational and non-radiative gas dynamics. Since we did not include radiative cooling and non-gravitational heating processes in the computations, the gas in the clusters may slightly differ in temperature or concentration with respect to a fully realistic model. However, despite this simplification, our simulations can be used to accurately test the self-similar scaling relations introduced in Section 3.2.3, and can be viewed as a first attempt to capture the effects due to different dark energy contributions alone.

For our largest calculations, we followed the evolution of 512^3 dark matter (DM) and 512^3 gas particles from $z = 49$ to $z = 0$, using smoothed particle hydrodynamics (SPH). Unless explicitly stated otherwise, the simulations used a flat cosmological model dominated at present by the presence of dark energy ($\Omega_{\mathrm{m}} = 0.25$, $\Omega_\Lambda = 0.75$ at $z = 0$), with a Hubble parameter $h \equiv H_0/(100 \text{ km s}^{-1} \text{ Mpc}^{-1}) = 0.7$, and baryon density $\Omega_{\mathrm{b}} = 0.044$. The initial conditions were generated by sampling from a cold dark matter (CDM) power spectrum, normalized by assuming $\sigma_8 = 0.8$ for the linearly extrapolated power spectrum today, where σ_8 is r.m.s. matter fluctuation in a sphere of comoving radius $8\,h^{-1}$Mpc. A slightly different normalization and matter density was used in two variants of the EDE models, as listed in Table 3.1, where we give an overview of the parameters of our different cosmological models.

All runs were carried out with periodic boundary conditions in a cubic box with side-length $100\,h^{-1}$Mpc. Correspondingly, the masses of the DM and gas particles are $m_{\mathrm{DM}} = 4.26 \times 10^8 h^{-1} M_\odot$ and $m_{\mathrm{gas}} = 9.1 \times 10^7 h^{-1} M_\odot$, respectively. The Plummer-equivalent gravitational softening length was set to $\epsilon = 4.2\,h^{-1}$kpc in comoving units. We produced approximately one dump per light crossing time through the box, yielding 72 outputs between $z = 10.3$ and $z = 0$. The simulations were run with the cosmological code GADGET-3 (based on Springel et al., 2001b; Springel, 2005), the initial conditions were produced with N-GENIC. Both codes were extended to allow the correct use of a time-variable equation of state.

In Figure 3.2, we show the dark energy fraction as a function of redshift for the four classes of models described in Section 3.3.1. To isolate the dark energy effects, we here compare all models with the same underlying cosmological parameters. It is important to stress that the dark energy parameter is orders of magnitude bigger in these cosmologies with respect to the ΛCDM reference case during recombination and structure formation. In the mocker model we can observe that the energy density Ω_{de} contributes a fixed fraction of the total energy density already at these intermediate redshifts.

According to the Friedmann equation within a flat universe, the expansion rate

for a generalized dark energy cosmology is given by

$$H(a) = H_0 \left[\frac{\Omega_{m,0}}{a^3} + \Omega_{\mathrm{de},0} \exp \left(-3 \int \left[1 + w \left(a \right) \right] \mathrm{d} \ln a \right) \right]^{1/2}, \qquad (3.18)$$

where the density of dark energy changes as a function of the scale factor as:

$$\Omega_{\mathrm{de}}(z) = \Omega_{\mathrm{de},0} \exp \left(-3 \int d \ln a \left[1 + w \left(a \right) \right] \right). \qquad (3.19)$$

For $w = -1$, the case of a cosmological constant is recovered. As can be seen from Figure 3.3, in the models EDE1 and EDE2 we observe the largest differences with respect to the reference ΛCDM case, amounting to slightly more than 8% at redshift $z \sim 1.5$. The effect of all the EDE cosmologies is to accelerate the expansion of the Universe, with the consequence of changing its global geometry. Note that we properly take into account this modification to $H(a)$ in the simulation code and the initial conditions code. In practice, we precompute suitable tables and then interpolate from them for efficiency reasons, since the Hubble rate needs to be evaluated very often by the simulation code.

We also need to calculate the appropriate linear growth factor in the initial condition code in order to set the correct amplitude of the power spectrum at the starting redshift of the simulation (for our models $z_{\mathrm{init}} = 49$). For a general equation of state parameter $w(a)$, the linear growth factor is described by Linder and Jenkins (2003):

$$D'' + \frac{3}{2} \left[1 - \frac{w \left(a \right)}{1 + X \left(a \right)} \right] \frac{D'}{a} + \frac{3}{2} \left[\frac{X \left(a \right)}{1 + X \left(a \right)} \right] \frac{D}{a^2} = 0, \qquad (3.20)$$

where $X \left(a \right)$ is the ratio of the matter density to the energy density:

$$X \left(a \right) = \frac{\Omega_{m,0}}{\Omega_{\mathrm{de},0}} \exp \left[-3 \int_a^1 d \ln a' w \left(a' \right) \right]. \qquad (3.21)$$

Here we define the growth factor as the ratio $D = \delta \left(a \right) / \delta \left(a_i \right)$ of the perturbation amplitude at scale factor a relative to the one at a_i, and we use the normalization condition $D(a_{\mathrm{eq}}) = a_{\mathrm{eq}}$.

In Figure 3.4, we show the evolution of the growth factor divided by the scale factor D/a, for the different dark energy cosmologies investigated in this study. All the models are normalized to unity for $a \sim 0$, so that the linear perturbations have the same density contrast at early times. While in the standard cosmology $D(a) \propto a$ at very high redshift, in all the other models the growth rate is reduced at these times. The suppression starts near the transition redshift $z_{\mathrm{trans}} = 10$ for the K08 model (black dashed line) and the DECDM model (dashed blue line). In the other cosmologies, the difference is present even at higher redshifts, and the discrepancy with respect to the ΛCDM model is largest for EDE4. From the parameterization of equation (3.14), we can deduce that the larger C ($C = 2.5$ for EDE4), the faster
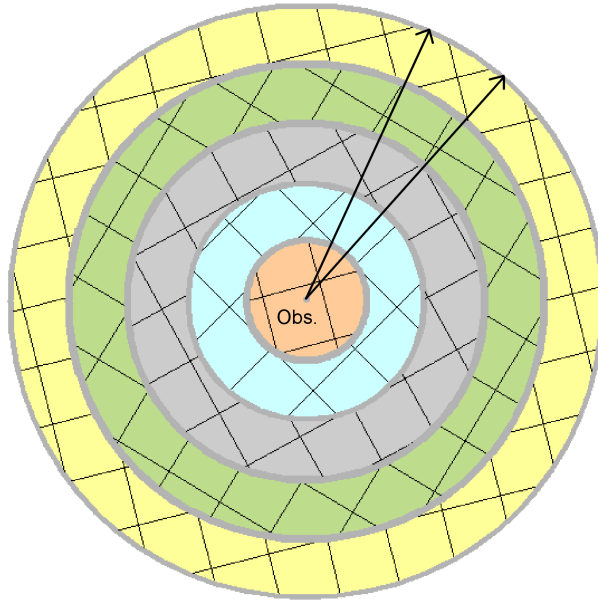
Figure 3.5 Sketch of the adopted stacking and randomization process. The observer is located at the position O at the center of the picture. The passage of CMB photons through the matter distribution of the intergalactic medium in the Universe is followed by stacking together the cosmological box of our simulation at different redshift. Shells of thickness $100\,h^{-1}$Mpc are filled with periodic replicas of the box of size $100\,h^{-1}$Mpc on a side. The difference with respect to the standard procedure to produce light-cone maps is that in this case all boxes (squares) that fall into the same shell are randomized with the same coordinate transformation (rotation and translation), which differs, however, from shell to shell. This method avoids the repetition of the same structures along the line-of-sight, but at the same times produces maps that are continuous everywhere on the sky.

w_{EDE} approaches $w = 0$ at high redshift. An increase in Ω_{sf} on the other hand implies a slow-down in the linear growth rate and consequently leads to a decrease in the value of σ_8 today (Xia and Viel, 2009). This model also shows the highest dark energy contribution at $z > 10$.

3.3.3 The map-making procedure

In order to create realistic maps of the tSZ and kSZ signals produced by the cosmic large-scale structure, we use a similar approach for tessellating the backwards light-cone as described in Carbone et al. (2008a); Zavala et al. (2009). The method is based on the replication of the original simulation box along the line of sight, where at each redshift the simulation output closest to this time is used. In order to avoid that the same structures are repeated along a given line-of-sight, we randomly translate and rotate the simulation box within concentric shells of comoving thickness equal to the simulation box size. Within each of these shells, the same randomization process is applied to a full, coherent tilting of the shell. Unlike in simpler stacking techniques used in the past, this approach has the advantage that

the reconstructed light cone has no discontinuities in the transverse direction. It is therefore ideal to construct maps that are larger than the box size itself, and in particular, it can be used to construct all-sky maps, if desired.

Figure 3.5 gives a sketch of the map-making procedure. The concentric shells represent regions covered by a single simulation output, and within each shell, a different choice for the randomization process is used. We produced dumps spaced by a comoving $100\,h^{-1}\mathrm{Mpc}$ in light travel time for the ΛCDM cosmology, which is also the thickness of our box, so that each shell is covered approximately by one simulation dump (exactly one for our ΛCDM cosmology). However, the map-making code can also deal with an arbitrary spacing of the output times of a given simulation, and will automatically select an optimum use of them for reconstructing the backwards light-cone.

For the projection itself we work in comoving coordinates and take advantage of the periodic boundary conditions of our simulation. For each pixel, we sum up contributions of all the particles that overlap it within their SPH smoothing length. In practice, we first produce partial maps that correspond to those parts of the backwards light-cone that are covered by a particular snapshot dump. The full light-cone is then obtained by adding all partial maps together. In principle, our method can produce arbitrarily large maps, including full sky ones, if desired, but here we focus on smaller maps in order to more easily reach very high angular resolution. In particular, we create maps of two different sizes, one set is 3 square degrees on a side, the other has a field of 12 square degrees on a side. In both cases we consider 4096^2 pixels, corresponding to a resolution of ~ 2.64 and ~ 10.55 arcsec, respectively, and we integrate over the redshift range $0 < z < 9.6$. As we will discuss in more detail in Section 3.4, this range is enough to account for essentially all of the tSZ signal, and especially also for the kSZ effect that is believed to have a non-negligible contribution even for $z > 6$. In order to assess the statistical robustness of our results and the influence of cosmic variance we have created 16 different light-cone realizations with different random number seeds, eight for each resolution.

In order to compute the y and b parameters along each light ray, we need to convert the line-of-sight integral in Equations (3.1) and (3.4) into a discretized expression for the individual SPH particles. Calculating the SZ effect requires knowledge of the number density, temperature, and velocity of the electron distribution. In the non-relativistic limit relevant for the thermal SZ effect, we first compute for each particle the product of pressure and specific volume of the gas:

$$p = (\gamma - 1)(1 - Y_p)mu\mu x_e \,, \tag{3.22}$$

where γ is the ratio of specific heats, $Y_p = 0.24$ is the primordial ^{4}He mass fraction, m the particle mass, u the internal energy per unit mass, μ the mean molecular weight, and x_e the ratio of electron to hydrogen number densities. We use the same

SPH smoothing kernel,

$$W(x) \propto \begin{cases} 1 - 6x^2 + 6x^3, & 0 \leqslant x < 0.5 \ , \\ 2(1-x)^3, & 0.5 < x \leqslant 1 \ , \\ 0, & x > 1, \end{cases}$$

that is used in the simulation code for the computation of hydrodynamical forces for distributing these quantities over the pixels of our maps. In equation (3.23), $x \equiv \Delta\theta/\alpha_i$, where $\Delta\theta$ represents the angular distance between the pixel centre and the projected particle position, and α_i is the angle subtended by the particle smoothing length. We make sure that the sum of the projected smoothing kernels w is normalized to unity for the pixels actually covered by a particle. Then, the contribution to the thermal SZ effect due to the particle α is given by

$$y_{ij} L_{\mathrm{pix}}^2 = \frac{\sigma_T}{m_e c^2} \sum_\alpha p_\alpha w_{\alpha,ij} \ , \tag{3.23}$$

where L_{pix} is the physical size of the pixel at the particle's distance.

We use a similar procedure for constructing the maps of the Doppler b-parameter. The only difference is that in this case the quantity that needs to be distributed over the angular grid is

$$b_{ij} L_{\mathrm{pix}}^2 = \frac{\sigma_T}{c} \sum_\alpha v_{r,\alpha} n_{e,\alpha} w_{\alpha,ij} \ , \tag{3.24}$$

where $v_{r,\alpha}$ is the radial component of the peculiar velocity of the particle α.

As a final remark, in the non-radiative simulations we study here, we do not track the ionization fraction x_e explicitly. Instead, we fixed it to 1.158 for temperatures $T > 10^4$ Kelvin. In other words, we adopt this temperature as a delimiter between cold and completely neutral gas, and fully ionized hot gas. For our simple non-radiative simulations it is necessary to assume that the gas is neutral at very high redshift, otherwise the finite box size of our simulation would lead to a very strong kSZ signal on large angular scales, arising from gas motions described by the largest modes in the simulation box.

3.3.4 Source identification

For our simulations we produced cluster catalogues by running a friends-of-friends (FoF) group finder (e.g., Davis et al. 1985) with a linking length of $b = 0.2$ in units of the mean inter-particle spacing. The FoF algorithm links together all particle pairs separated by less than a distance b and identifies, as halos, candidate groups that contains more than 32 particles. We define the centre of a halo as the position of the minimum of its gravitational potential; this proves very robust and is insensitive to the particle distribution near the outskirts of the halo. The centre
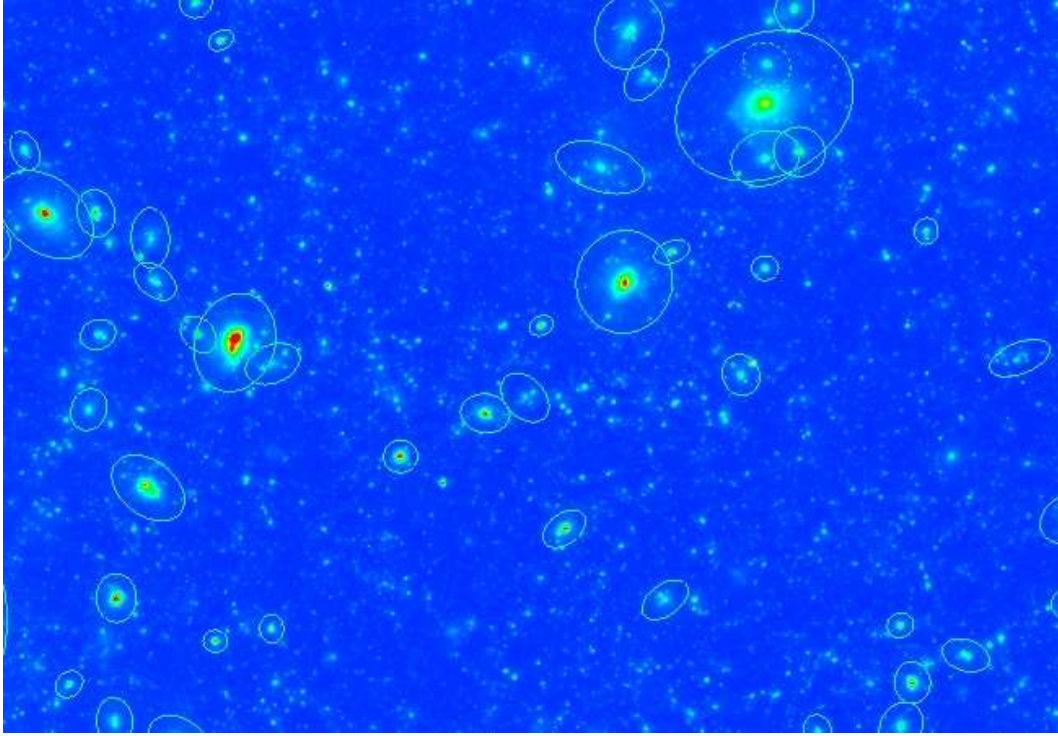
Figure 3.6 Thermal SZ sources identified with `SExtractor`. A circle is drawn for each source, with area equal to the area determined by the source-detection software.
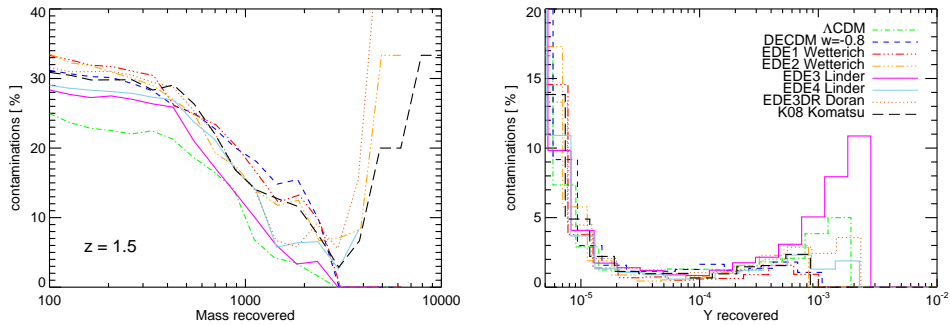
Figure 3.7 Contamination rate of the detected cluster sample as a function of the recovered mass (left panel) and `SExtractor` flux (right panel) for all the different cosmologies we examined. The sources are considered true detections when the peak in the map and the matching cluster from the catalogue are within a 24 pixel distance of each other. At $z = 1.5$ our sample shows only 5% percent contamination from false-positive matches down to $Y = 1.0 \times 10^{-5}$.

defined in this way also coincides closely with the density maximum of the group found with the shrinking sphere method. For each of the halos we also computed spherical overdensity (SO) mass estimates, i.e. the mass enclosed in a sphere with a prescribed mean density $\Delta \times \rho_{\mathrm{crit}}$, where ρ_{crit} is the critical density and Δ describes a characteristic virial overdensity. In particular, we consider the mass M_{200} enclosed within the virial radius, r_{200}, interior to which the density contrast is 200 times the critical density. Where appropriate, we also consider different values of Δ motivated by the generalized spherical collapse model in general cosmologies.

Besides this source identification in the three-dimensional raw simulation data, we independently detected and determined the photometry of extended sources in our SZ maps. To this end we used the software `SExtractor` (Bertin and Arnouts, 1996), a source extraction code based on a connected-pixel algorithm which optimally detects, deblends and measures sources in a given map. The analysis begins with an iterative estimation of the 'sky' background, and then proceeds with an identification of the locations of the brighter sources, building a catalogue of objects from the image map. Thresholding is applied to isolate connected groups of pixels, and to find the approximate positions and shapes of individual detections that will be further processed. A crucial parameter is the threshold level, in particular the minimum number of pixels above the background required before a source is considered as an object. Finally, the total integrated flux for each source is obtained by summing up the contributions of all the pixels centered on the known location of the clusters. The detection itself is more complicated because it depends on the morphology of a cluster. Following the simplest characterization for an extended SZ source, `SExtractor` evaluates the flux inside an elliptical aperture around every detected object, described by a characteristic Kron radius that includes 90% of an object's light. We have tried to optimize the parameter settings of `SExtractor` in order to avoid source confusion and to robustly identify most of the brighter sources at all redshifts.

Figure 3.6 shows a typical source detection map. We have drawn circles with areas equal to the areas of the ellipses matched by `SExtractor` to each identified source. We here used default settings for the detection algorithm but we tuned the detection threshold such that only the more massive halos are found and confusion with the background is avoided, a consideration that becomes especially important for the high redshift partial maps, where we have a dominant contribution from small and faint sources. The threshold cut we apply is 10.5 times the standard deviation on the filtered map (the algorithm estimates the background and noise level automatically). We remark that our maps are in principle noise-free, so what it is interpret here as 'noise' is effectively due to source confusion and alignment of clusters along the line-of-sight.

In a typical coadded map, more than 40% of the total thermal SZ signal can be resolved into isolated sources. For a detailed analysis, we would like to associate

each of the bright sources we observe in the SZ maps with a massive halo in the underlying three-dimensional simulation catalogue. This allows a comparison of the intrinsic halo properties with the quantities that can be extracted from an observed SZ map. From the cluster catalogue derived from the FoF algorithm, we choose a sub-sample of halos with mass $> 10^{12}h^{-1}\mathrm{M}_\odot$ to stay well above our mass limit of $1.3 \times 10^{10}h^{-1}\mathrm{M}_\odot$. All selected clusters contain at least 3500 particles within the virial radius and are hence well resolved. Using again our map making procedure we found all the clusters in the catalogue that fall within a particular map.

We identified as a match all the input clusters that were located within a distance of at most 24 pixels from a `SExtractor` flux peak in the 2D map-plane. This distance corresponds to ~ 1 arcmin, which is the typical cluster size in the 3 square degree maps. We do not allow for multiple catalogue clusters matching a single detection. If no input clusters is found for a given source in the map, we flag the nearest object as a false detection. We have verified that this procedure avoids misclassifications even in the moderately crowded fields at high redshifts, where sometimes several candidates are associated to a single cluster within a larger search radius.

After running through all the candidates, we can identify as true detections in the simulated maps about 90% of the clusters at each redshift with mass above $13h^{-1}\mathrm{M}_\odot$. Figure 3.7 shows the contamination level at $z = 1.5$ in different cosmological models derived as a function of the recovered cluster mass (left panel), and the SZ flux (right panel). The total flux here means the flux decrement integrated by `SExtractor` over the entire cluster profile, which we express just as the Compton-Y parameter, independently of the frequency. Interestingly, the ΛCDM map appears systematically 'cleaner' than the maps of EDE cosmologies, in terms of the fraction of peaks that correspond to real clusters as a function of mass. On the other hand, in the contamination versus flux plot all the models show a sharp decline from $\sim 20\%$ to $\sim 1\%$ in the contamination rate around $Y \sim 10^{-5}$, indicating that confusion effects in our maps are unimportant for bright sources. The maps show a slightly higher contamination level when we consider the biggest objects. In the early dark energy model EDE3 we could not identify one of the extended clusters, and this is the reason of the higher contamination. In general, we note that in order to detect extended clusters, direct profile fitting is a good alternative compared to the peak pixel finding procedure (Sehgal et al., 2007).

If we disregard the slightly higher contamination level at large fluxes due to rare and extended clusters, our sample of detected clusters is 95% complete down to $Y = 2 \times 10^{-5}$ at all redshifts. For the EDE2 model, there are more than 3000 halos more massive than $10^{12}h^{-1}\mathrm{M}_\odot$ in the $z = 1.5$ three-dimensional catalogue for a 3 square degree map. There is still the possibility that some peaks match clusters in the catalogue just by chance alignments. However, we consider only clusters that should give a visible contribution to the Comptonization parameter, and the analysis is performed on single partial maps in the simulation, before to construct

the coadded maps. Then, such misclassification should be very rare.

3.4 Global properties of the SZ signals

In Fig. 3.8, we show typical examples for maps of the Compton y-parameter (upper panels) and Doppler b-parameter (lower panels). The maps are 3 degrees on a side with a pixel resolution of 2.63 arcsec and all refer to the same light-cone realization for the ΛCDM cosmology (left hand panels) and for the EDE1 model(right hand panels). They were produced by coadding a large number (72) of partial maps, each giving the contribution of one of the boxes that we stacked along the photon's path, as described in Section 3.3.3. The total extension of the light-cone realizations corresponds to a comoving distance of approximately $7100\,h^{-1}$Mpc and a redshift interval $0 < z < 9.6$.

It is worth noticing that the partial tSZ maps (see Figure 3.6), that have only $100\,h^{-1}$Mpc depth, show prominent filamentary structure, whereas this is hidden in the full projection by the high background level that arises from the summation of all the structures along the line of sight. The situation is a bit different in the kinetic SZ maps: here the effect is not strongly convergent at high redshifts, and the increase of the contributing material compensates for the low velocity regions, giving an appreciable signal also in the filamentary regions.

In the two thermal SZ maps in the upper panel of Figure 3.8, the signal is dominated by discrete sources. These particular maps feature two nearby large clusters that together contribute for more than 1/4 of the total recovered source flux. This is the only map that shows such a feature. These clusters produce fluctuations in y bigger than $y \sim 10^{-4}$ (yellow regions in the color scale), which correspond to temperature changes in the RJ regime an order of magnitude higher than the primary CMB anisotropies. Massive clusters that generate such strong thermal SZ effects are quite rare. In the map on the left-hand side we recognize a halo with mass $M = 3.9 \times 10^{14} h^{-1} M_{\odot}$ and virial radius $R = 1.2\,h^{-1}$Mpc at redshift $z = 0.068$ (position in pixels: 1614.7, 3753.41), and a smaller peak from a cluster of mass $M = 5.5 \times 10^{14} h^{-1} M_{\odot}$ at redshift $z = 0.17$ (position: 382.209, 480.412). It is also possible to detect a large number of fainter structures with $y \sim 10^{-5}$ (red in the color scale), while filaments between super-clusters and diffuse gas produce fluctuations that can reach at most $y \sim 10^{-6}$ (green regions).

Comparing the map that refers to the ΛCDM cosmology to the EDE1 model (the same color scale is used in the two plots), only few differences are visible. Residuals between the two realizations are located around the higher peaks of the simulated maps. From a theoretical point of view, this is expected, because clusters are particularly sensitive to the linear growth rate δ_c and represent the highest perturbations in the density field (several $\nu = \delta_c D_g(z)/\sigma(M)$, where $\sigma(M)/D_g(z)$ is

the average perturbation amplitude). The peak in the map for the EDE1 model lies in the same positions with respect to the ΛCDM, but corresponds to bigger objects in the simulations. As an example, the extended cluster positioned at (1614.7,3753.41) has a mass $M = 3.9 \times 10^{14}h^{-1}M_\odot$ and the emission is 25% stronger than in the ΛCDM case. In the EDE models, objects form systematically earlier than in the standard cosmology when the power spectrum is normalized to the same value today. To compare, the big peak we can see at the upper right corner of the two maps (position: 3698.88, 3558.27), represents a cluster of mass $M = 3.3 \times 10^{14}h^{-1}M_\odot$ at redshift $z = 0.36$ in the ΛCDM map, while in the EDE1 map we found it already at $z = 0.4$. A typical simulated field contains ~ 25 objects with total integrated flux above 5.0×10^{-2}, and ~ 2000 below that. The number of objects is significantly smaller in the ΛCDM cosmology: this is due to the absence of high-redshift structures as compared to the EDE simulations.

The visual appearance of the two kinetic SZ maps is also really similar, with small differences in the regions where the signal shows negative peaks (blue patches in the map). We notice that there is a considerable displacement between the "bright" and hot sources in the thermal effect and the brightest contribution in the kinetic SZ maps. For example, the peak located in the tSZ map at (1642.11, 835.132), due to a halo of mass $M = 1.1 \times 10^{14}h^{-1}M_\odot$ at $z = 0.07$ and corresponding to the third brightest source in the map, is basically absent in the kinetic map, simply because it does not have a high enough peculiar velocity. More often we find neighborings peaks of opposite sign (blue and yellow regions in the color code map) near the positions of the thermal SZ sources. This can clearly be seen at the location of the two brighter clusters of the map, and probably results from the merging process of substructures, yielding a bipolar variation of the velocities in the main halo. Looking at such positive-negative features may be useful in strategies for identifying clusters and super-clusters in observations (Diaferio et al., 2000).

More quantitatively, we have studied the distribution functions of the kinetic distortion as a function of the thermal SZ signal. To this aim, we binned the pixels of the thermal SZ maps logarithmically in 20 intervals according to their value of the temperature distortion in the RJ limit, and then computed the distribution of the kinetic SZ effect inside each bin. In Figure 3.9, we show the percentage of bins as a function of the kinetic distortion for pixels inside two regions ($1.3 \times 10^{-6} < \Delta T_k/T < 1.9 \times 10^{-6}$ and $1.7 \times 10^{-4} < \Delta T_k/T < 2.5 \times 10^{-4}$) for the ΛCDM and the EDE1 model. The shape of the distribution is quite close to a Gaussian for the bin with fainter objects, while it is more likely to contain large kinetic distortions in pixels with stronger thermal distortions. The non-Gaussian nature of the distribution in this case is particularly evident in the ΛCDM case. Clearly, the shape changes drastically according to whether or not high thermal distortions are included.
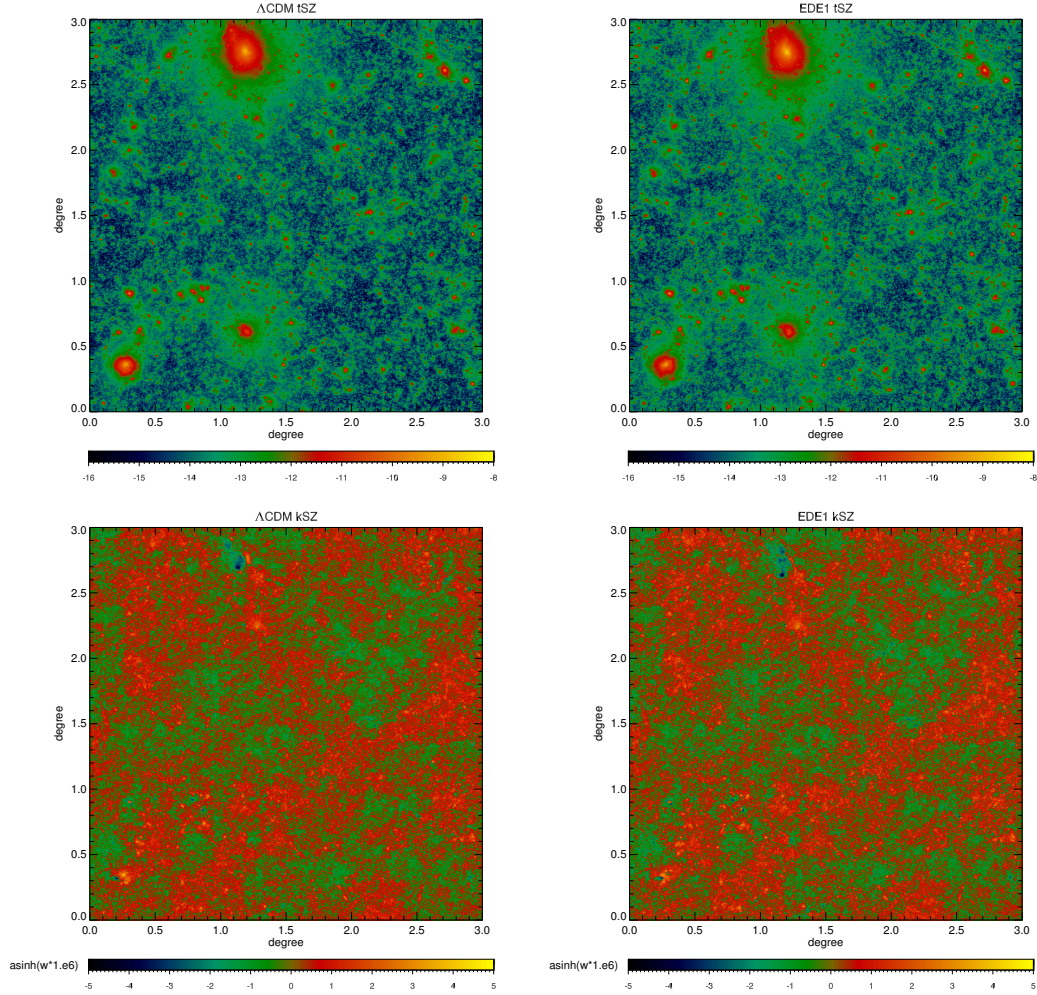
Figure 3.8 Upper panels: Simulated thermal SZ maps, showing the y-parameter in a patch of 3 square degrees. The shading is proportional to $\ln(b)$. The resolution of the map is 2.63 arcsec. The models we show are a ΛCDM cosmology (left panel) and the dark energy model EDE1 (right panel). Lower panels: Simulated kinetic SZ maps, showing the b-parameter in units of $\mathrm{arcsinh}(b \times 10^{-6})$. They refers to the ΛCDM model (left panel) and the EDE1 model (right panel). All the four maps correspond to the same realization of the past light-cone.
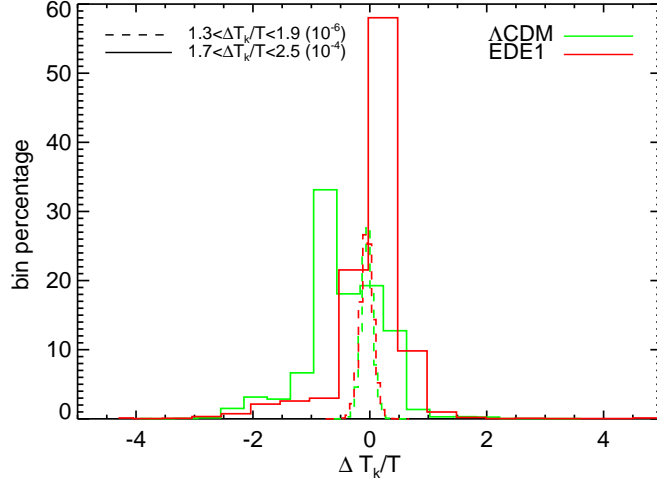
Figure 3.9 Distribution of the kinetic SZ signal within the two redshift bins $1.3 \times 10^{-6} < \Delta T_k/T < 1.9 \times 10^{-6}$ and $1.7 \times 10^{-4} < \Delta T_k/T < 2.5 \times 10^{-4}$ in the RJ limit, both for the ΛCDM (green histograms) and EDE1 models (red histograms). The distribution is well approximated by a Gaussian in the low thermal bin. The dispersion of the kinetic SZ signal increases with higher thermal distortion.

	$y_{\mathrm{mean}} \times 10^{-6}$	$\sigma_{\mathrm{tSZ}}^2 \times 10^{-12}$	s_{tSZ}	$\sigma_{\mathrm{kSZ}}^2 \times 10^{-12}$
ΛCDM	1.553	5.976	14.62	2.118
DECDM	1.738	7.693	15.26	2.703
EDE1	1.787	8.137	14.01	2.912
EDE2	1.768	7.936	13.87	2.851
EDE3	1.608	6.284	13.65	2.285
EDE4	1.685	7.018	13.35	2.545
EDE3DR	1.629	6.425	13.25	2.346
K08	1.711	7.305	13.34	2.659
EDE2P	2.157	9.106	10.98	2.786
EDE3P	1.126	2.737	12.55	1.305

Table 3.2 Mean value of the y parameter for all the simulated cosmological models in units of 10^{-6}. We give also the rms fluctuations of the thermal and kinetic effect in units of 10^{-12}, and the value of the skewness for the thermal effect. The quantities are obtained by averaging over 8 different light-cone maps of 3 square degrees each.

3.4.1 The mean distortion

From the light-cone simulations of the different cosmological models, we can compute the moments of the y and b distortion for the thermal and kinetic maps. In Table 3.2, we report the values obtained averaging over 8 realizations of 3 degrees square map for each cosmology. We can see that all the y_{mean} values are well below the observational constraints reported by the COBE–FIRAS experiment, which sets a 95 per cent upper limit of $y_{\text{mean}} < 1.5 \times 10^{-5}$ (Fixsen et al., 1996). In the ΛCDM model, we obtain a value of $\langle y \rangle = 1.55 \times 10^{-6}$ as the mean of the pixel values in the thermal maps and $\langle b \rangle = 1.78 \times 10^{-7}$ for the kinetic ones. These values are slightly lower than the result of 3.2×10^{-6} obtained by da Silva et al. (2000) and the 2.5×10^{-6} found by White et al. (2002) for pure non-radiative runs, whereas, more recently, Roncarelli et al. (2007) found 1.19×10^{-6} when analyzing simulations that included cooling, star formation and feedback. The main reasons of this discrepancy is the smaller value of σ_8 adopted in our simulations ($\sigma_8 = 0.8$) compared to the first two studies ($\sigma_8 = 0.9$), and the inclusion of extra physics in the third one. The Compton y-parameter scales roughly with $\sigma_8^{\alpha/2}$, with $\alpha \approx 4 - 7$ (see, e.g., Sadeh and Rephaeli, 2004; Diego and Majumdar, 2004). Also, the inclusion of additional physics can affect the results, in particular cooling reduces the contribution of high density gas in groups and clusters, lowering y_{mean} by about 20% .

The mean Comptonization we predict for the EDE model is systematically higher than the one expected in the ΛCDM cosmology. For the EDE1 model we find $y_{\text{mean}} \sim 1.79 \times 10^{-6}$, which is 15% higher with respect to a standard model with the same cosmological parameters. We note however that the lowest and highest values for the distortion are seen in the dark energy model EDE2P and EDE3P, that also adopt a different cosmology. There is almost a factor two difference between these two runs. In fact, the mean y and b parameters are quite sensitive to the σ_8 normalization and to the different Hubble expansion. Both of these cosmologies use a lower power spectrum normalization today, and this effect is dominant in EDE3P, which has the lowest values for the mean, but not in the model EDE2P, since in this model accelerated Hubble expansion dominates. These two cosmologies also show systematically lower skewness and kurtosis. The relative order of the models is exactly the same when we consider the intensity of the kinetic SZ signals instead. Here the increase in the EDE models reflects the impact of the dark energy on the expansion history of the Universe (see Figure 3.3).

In Figure 3.10, we plot the probability distribution of pixel values for both the thermal and kinetic SZ effects. We show as separate curves the results averaged over 8 different light-cone realizations for different cosmological models. The distribution of $\log y$ is nearly symmetric and close to a log-normal function, reflecting the non-Gaussianity of the y parameter (Seljak et al., 2001). Based on the values of the skewness of the distribution we found out that the non-Gaussian effect is almost the same in all cosmologies, and shows only a small shift towards high Comptonization

region in the EDE models.

On the other hand, the probability distribution function for the b parameter in the ΛCDM cosmology is well approximated by a Gaussian, despite the occurrence of rare bright events. A distinctive feature of the dark energy models is a strong depression in the peak of the distribution, and a significant increase of the kurtosis, thus the tails of distribution are more populated. In fact, the kSZ effect has a non-negligible contribution on small-scales coming from high-z clusters, and then the signal from non-linear structures is partly canceled out. However, when considering the distribution of the signal in different redshift slices, we recover the Gaussian shape in all the cosmologies, see Figure 3.11. Since in a given redshift bin there are gas elements both approaching and receding from the observer with equal probability, the kSZ signal has a vanishing expectation value. The two cosmologies of the EDE2P and EDE3P again delimit the upper and lower limits of the pixels values that are obtained. In general, we observe more extended tails in models that show the higher mean Comptonization parameter, and we conclude that the probability to obtain high values of the kinetic signal is enhanced by the accelerated expansion of the Universe in the EDE models.

In Figure 3.12 we plot the differential and integrated contributions as a function of redshifts for the mean y-distortion in all the different cosmologies. These values represent the average over 8 light-cone realizations, and are computed in equally spaced comoving distance intervals of length $100\,h^{-1}$Mpc out to redshift 10. The upper panel shows the peak of the mean y-distortion as a function of redshift. One can notice that there is a large scatter at lower redshift ($z < 1$), mainly due to the probability of finding a very bright cluster in these particular redshift bins. The spikes disappear at higher redshift, since the light-cones include larger comoving volumes at larger distances and then the more massive clusters contribute a smaller fraction of the total mean y-Comptonization. Moreover, large collapsed structures are very rare at higher redshift.

From this plot, we cannot really tell the different models apart, while we can easily trace the differences looking at the integrated distribution of the mean Comptonization, in the lower panel of Figure 3.12. The area under the curves quantifies the cumulative mean distortion at that time. We can notice that close to redshift zero all the cosmologies behave in a similar way, given that they were normalized to the same σ_8 today and they reproduce the same cluster temperature function today. At higher redshift the growth factor evolution is slower for the models with early dark energy, and this anticipates the formation of the structures with respect to a ΛCDM model with the same cosmological parameters. The cumulative effect of the increased hot gas abundance gives rise to a mean thermal distortion systematically larger in the maps that refer to EDE cosmologies. For example, in the ΛCDM case, most of the signal comes from redshifts less than one, and only about 5% of it stems from $z > 3$, in good agreement with previous analysis (see, e.g.,

da Silva et al., 2000). In contrast, in the EDE cases the tail extends to much higher redshift, because structure grows there already. What is remarkable is that at $z > 2$ the contribution to the tSZ effect is non-negligible in the EDE cases. Finally, we observe that at very small redshift, it is the ΛCDM cosmology which gives the greatest signal, even though structures form earlier in the EDE cases. The reason for this is that the ΛCDM cosmology has the greatest volume element at these redshifts, and so a larger amount of gas contributes to the backwards light-cone.

Figure 3.13 shows the differential redshift distribution of σ_{kSZ} (upper panel), averaged over the 8 maps, for the same cosmology analyzed before. The variance provides the complete description of the signal for a Gaussian distribution of the pixel values, therefore the curves give a measurement of its dispersion. We see again that the variance of the SZ signal in all cosmologies comes from a broad range of redshifts out to around 2, and falls off significantly only beyond that. The signal from nearby redshifts is primarily due to clusters with very high peculiar velocities, while at higher redshifts the number of rare events is smaller and the distribution is narrower. In fact, although we averaged over 8 light-cone realizations, we have only one simulation per model, which is not sufficient to completely eliminate the cosmic variance. Integrating the redshift distribution over the maps (lower panel) we see again that we have a more significant contribution from high-redshift sources in the EDE models compared with the ΛCDM model. Unlike for the integrated thermal effect, the gas mass at $z > 6$ still adds important contributions to the total kinetic SZ effect. The distribution is in fact not convergent up to very high redshift. However, the peak of the thermal effect gives us additional information where the strongest kinetic signals in the maps are expected. Finally, the gray dashed line in the plot refers to the model EDE3P. We notice that the integrated variance is reduced by 30% already at redshift $z = 3$. This result confirms the expectation that the kinetic effect is a sensitive function of σ_8.

3.4.2 Plain number counts

We here address the issue of counting the number of discrete sources present in the thermal SZ maps and study how the detection rate is affected by early dark energy. In Figure 3.14, we show the plain number counts obtained with the software `SExtractor` when applied to partial and coadded maps. We first compute the number of detections per square degree obtained by averaging the results for 8 different, fully coadded maps of 3 degrees each (upper left panel). In the lower panel of the plot, we display the residuals between the EDE models and the standard ΛCDM cosmology, computed as $(Y_{\mathrm{DE}} - Y_{\Lambda\mathrm{CDM}})/Y_{\mathrm{DE}}$. The models are quite close to each other, but we can appreciate a 20% differences between the ΛCDM and the EDE1 and EDE2 models in the region of the most massive clusters. This result is in agreement with the visual appearance of the maps, that reveals different features exactly at the locations of the bright sources in the field of view. This is because
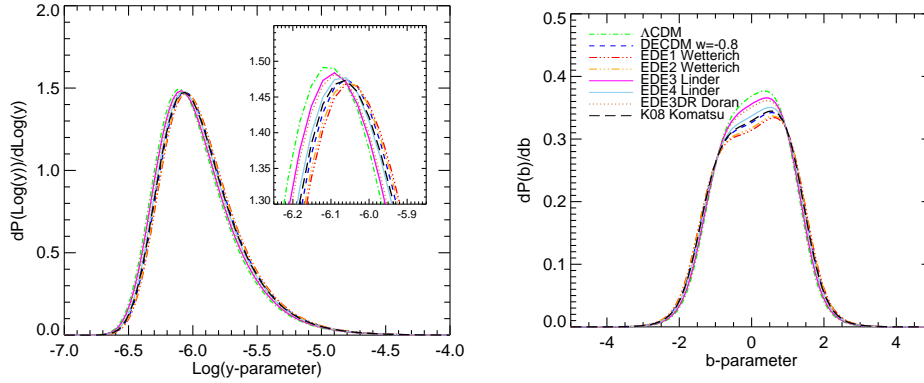
Figure 3.10 Probability distribution of the logarithm of the y-parameter (left panel) and the b-parameter (right panel), obtained considering the $(2.6 \text{ arcsec})^2$ pixels and averaging over 8 different maps realizations. This gives the distribution of the thermal and kinetic signals for a "perfect" experiment. The distribution of the y-parameter is close to a log-normal, while the pixels in the kinetic map have a Gaussian distribution.
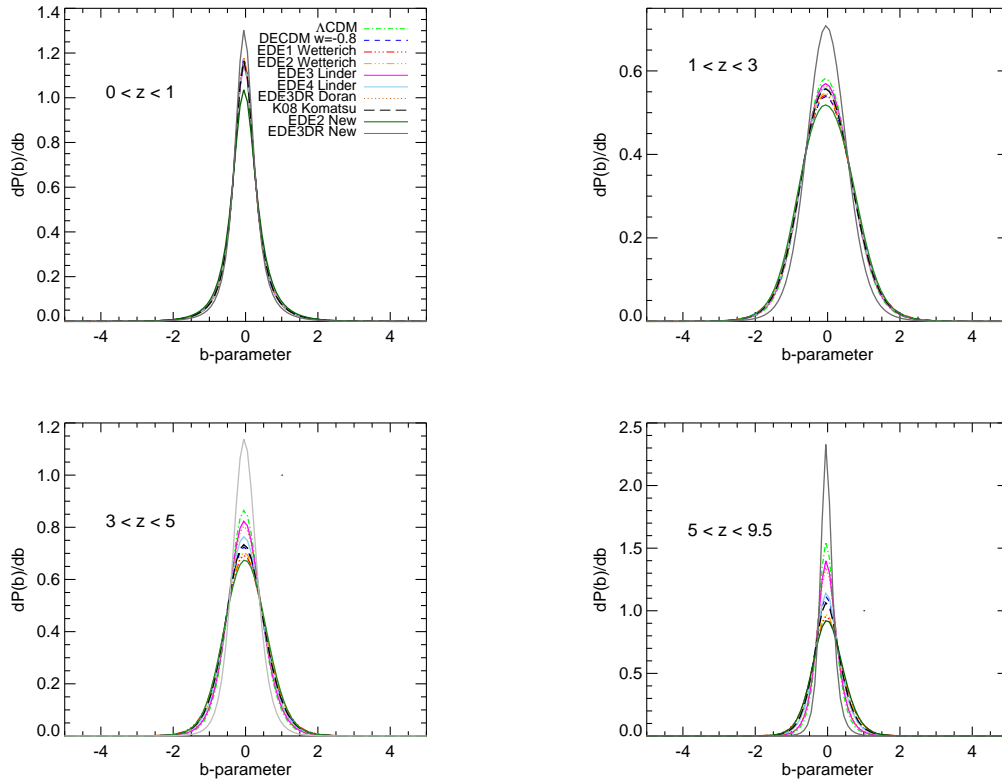
Figure 3.11 The probability distribution of the logarithm of the b-parameter in four different redshifts interval. We can notice that the kSZ signal follows a Gaussian distribution also in the EDE models, when we consider only a smaller fraction of the light-cone.
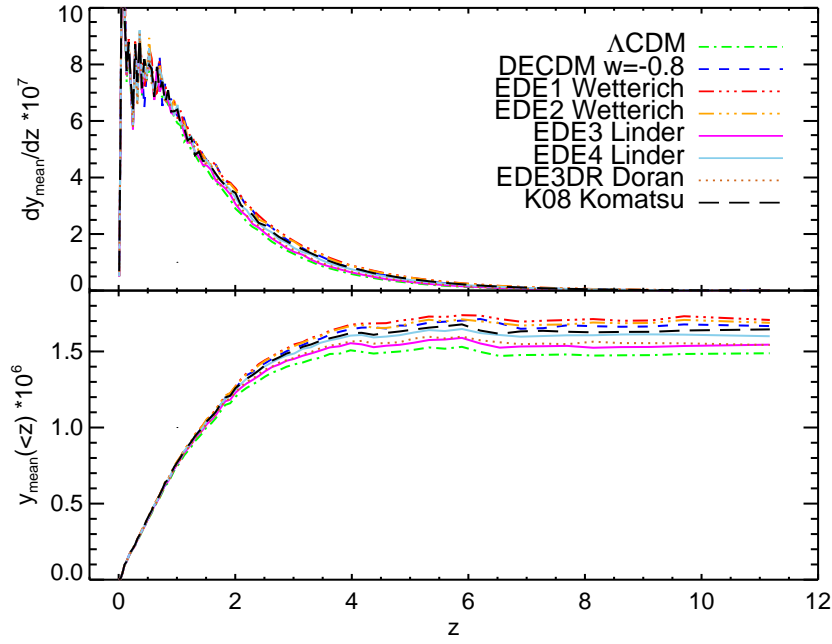
Figure 3.12 Differential contribution per unit redshift to the mean y-distortion over the map, for the ΛCDM simulation (green solid line) and for all the EDE models studied. In each case the thick line is the average over 8 separate map realizations. The upper panel shows the differential contribution per unit redshift, and the lower one the integrated contribution out to redshift $z \sim 10$.
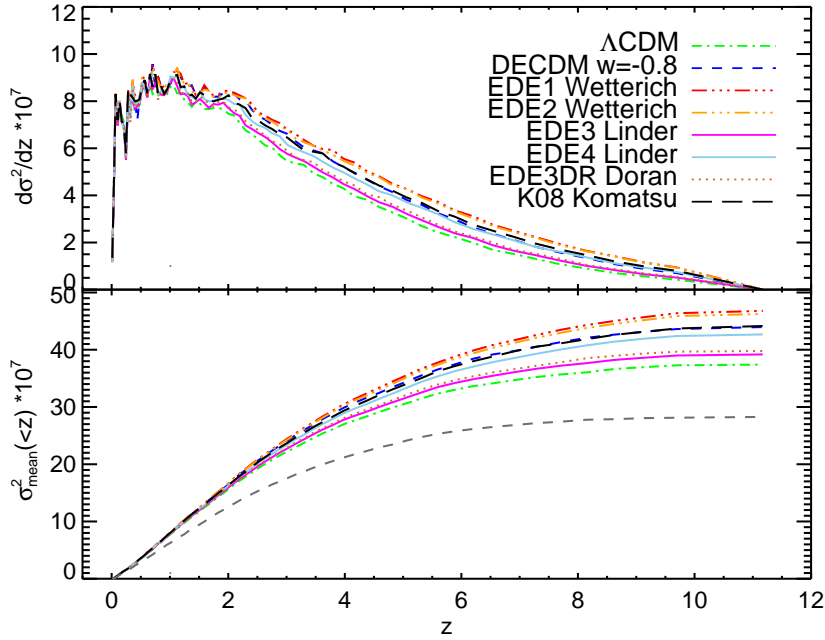
Figure 3.13 Root mean square of the kinetic b-distortion up to redshift $z \sim 10$. The differential (upper plot) and integrated (lower plot) effects are shown for the ΛCDM simulation (green solid line), and for all the EDE models studied. In each case the lines represent the average over 8 separate map realizations. Note that the kinetic effect is not simply additive, thus the quantity $\sigma_k(< z)$ is not simply the integral of the differential contributions. The gray dashed line in the lower panel refers to the model EDE3P. The values given in the plot are in units of 10^{-7}.
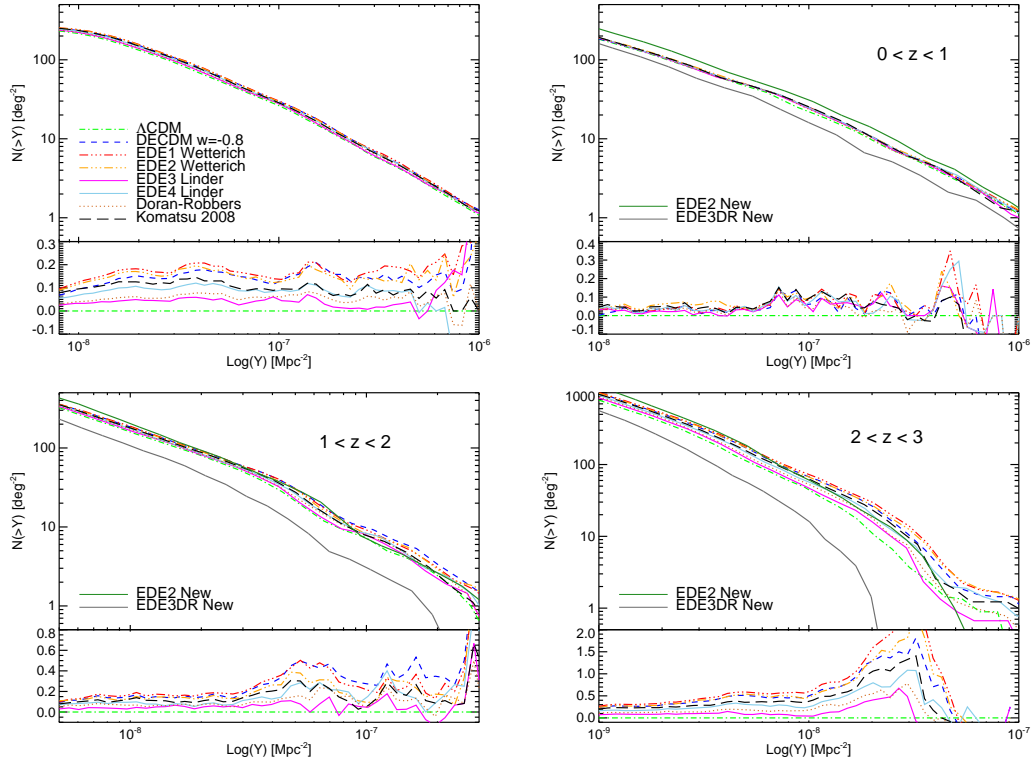
Figure 3.14 Cumulative counts of the thermal SZ sources per square degree detected by `SExtractor` as a function of source strength in the coadded maps in three different frequencies. In order to identify the clusters, we use `SExtractor` with a higher threshold level. The plateau we observe in the distributions corresponds to the limit of detectable sources. We observe a small enhancement in the number counts due to the presence of an early dark energy component.

the most massive clusters of the EDE models form, on average, at higher redshifts than those in a ΛCDM cosmology. The curves flatten out for low values of Y, when we approach the threshold for the detection. The number of fainter sources depends strongly on this detection threshold, as expected. On the other hand, we reassuringly found that the number of bright sources is not affected much by the `SExtractor` parameters. In between, the source number counts can be well approximated by a power law relation, with slope ~ -1.4 for the ΛCDM cosmology, and a slightly less steep slope for the EDE cosmologies.

Next, we consider light cone maps for different redshift intervals (right upper panel and bottom panels of Figure 3.14). In these plots of Figure 3.14 we have also included the results for the models EDE2P and EDE3P (dark green and dark gray solid lines). Models that follow the same underlying cosmology are essentially indistinguishable when the distribution of clusters at $z < 1$ is considered, especially considering the strong effect that a small uncertainty in the cosmological parameters would bring. In the model EDE2P, we can see a 32% increase, while in the EDE3P cosmology the lower σ_8 plays a major role, reducing the number of clusters by one third.

However, it is clearly seen that the degeneracy between the models is reduced when we take the cumulative number counts at higher redshift into account. Here, the increase in the number of detections in the EDE models with respect to the standard scenario is really pronounced. There are almost twice as many massive objects in the redshift interval $2 < z < 3$, and 80% more for $1 < z < 2$. This suggests that the most promising strategy for obtaining stringent constraints on early dark energy is to perform deep cluster surveys together with optical follow-up in order to determine redshift estimates for a large number of clusters. Studying the evolution of the cluster counts as a function of redshift is also promising for distinguishing effects due to the dark energy model from the ones due to different normalization or matter content. Current and future surveys may allow us to draw conclusions about the dark energy content in the Universe even if significant uncertainties in σ_8 remain.

We now consider the abundance of sources as a function of the flux. For each detection, the source strength S_ν is defined as the integrated monochromatic flux decrement, computed over the solid angle of the source:

$$S_\nu = \int_\Omega \Delta B_\nu \, d\Omega = f(x) B_\nu \int_\Omega y(\theta) \, d\Omega. \tag{3.25}$$

Here B_ν is the Planck spectrum of the primary CMB, and $f(x)$ is the spectral function

$$f(x) = x \frac{e^x}{e^x - 1} \left(x \frac{e^x + 1}{e^x - 1} - 4 \right), \tag{3.26}$$

with $x = h\nu/kT_{\mathrm{CMB}}$.

In Figure 3.15, we plot the differential flux distribution computed from the coadded thermal SZ maps as a function of source strength. The results represent the average over 8 different realizations and are normalized to 1 square degree. We quote results for the following frequencies: 143 GHz, 217 GHz, and 353 GHz, which are three relevant Plank channels. The models predict similar cluster counts per square degree at low flux, but, as expected, a higher abundance of clusters at a given flux level is found in the EDE runs. Consistent with the results for the number counts as a function of the Comptonization parameter, in the standard cosmology we find a strong suppression of the peak in the SZ signal, with respect to the EDE simulations. Comparing the differential flux at 143 GHz for the ΛCDM and the EDE1 model, which is the most extreme, we obtain a 16% increase for $S_\nu \sim 1000$. All the other models are in between these two cases.

The signal is dominated by sources between 10^2 and 10^4 mJy at 143 and 352 GHz, and around 10 mJy at 217 GHz, while the contribution by very faint and very bright sources is negligible. The thermal SZ effect does not vanish entirely at $\nu = 217$ GHz, but the brightest sources observed in the other two channels have their fluxes reduced by 3 orders of magnitude. However, at 100 mJy the differences in source count are larger, because the discrepancies are bigger for higher Y values. As a remark, the good agreement at the faint end between the differential flux counts suggests that the simulations already resolve all the sources that contribute significantly to the total Comptonization. At the highest values of y the predictions become uncertain as the low number of sources means that there is significant cosmic variance.

Finally, looking at the angular extent of the single sources on the sky as a function of flux, we found that this property is essentially not affected at all by the presence of early dark energy. The cumulative counts give us the same results for all the cosmology, when the computation of the angular dimension of the source is based on the effective area used by `SExtractor` for the detection. It would be really challenging to discriminate between the dark energy models looking at this statistic.

3.5 Forecasts for galaxy cluster surveys

The first key project for the South Pole Telescope (SPT) is a large survey for galaxy clusters detected by the Sunyaev-Zeldovich effect (SZE) (Ruhl, 2004). The proposed SPT survey area amounts to $\Omega \simeq 4 \times 10^3$ square degrees ($f_{\mathrm{sky}} \simeq 0.097$) and the observations will be in a frequency range between 70 and 300 GHz. The abundance of massive clusters as a function of redshift is highly sensitive to the expansion history of the Universe, then these measurements would provide important constraints on the dark energy equation of state parameter, $w \simeq p/\rho$. It has been recognized by several authors that the high sensitivity and high angular resolution of the SPT will allow the use of such surveys to study the amount and nature of dark energy
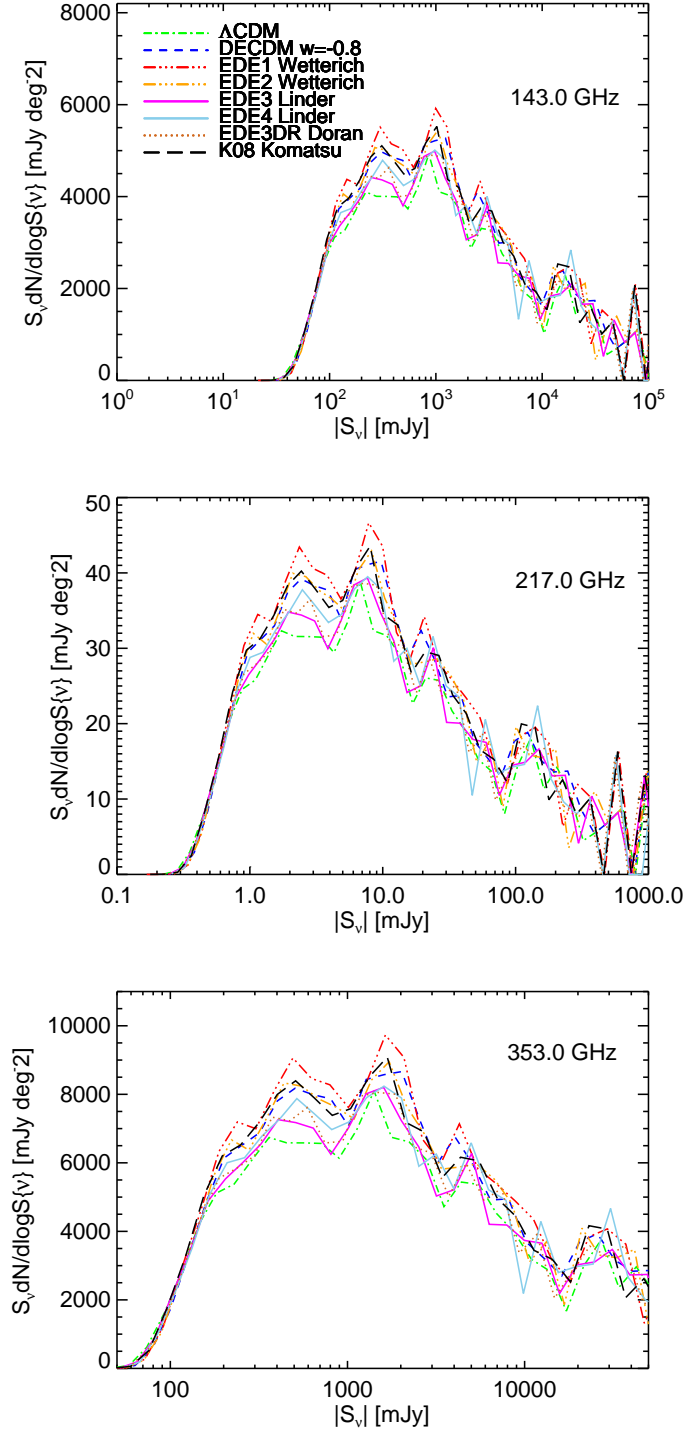
Figure 3.15 Differential flux distribution as a function of source strength for each cosmology averaged over 8 map realizations. The source strength S_ν was defined as the integrated monochromatic flux decrement, integrated over the solid angle of the source, see Equation (3.25). The ΛCDM cosmology shows a suppression of the peak of the SZ source at all frequencies with respect to the EDE models.
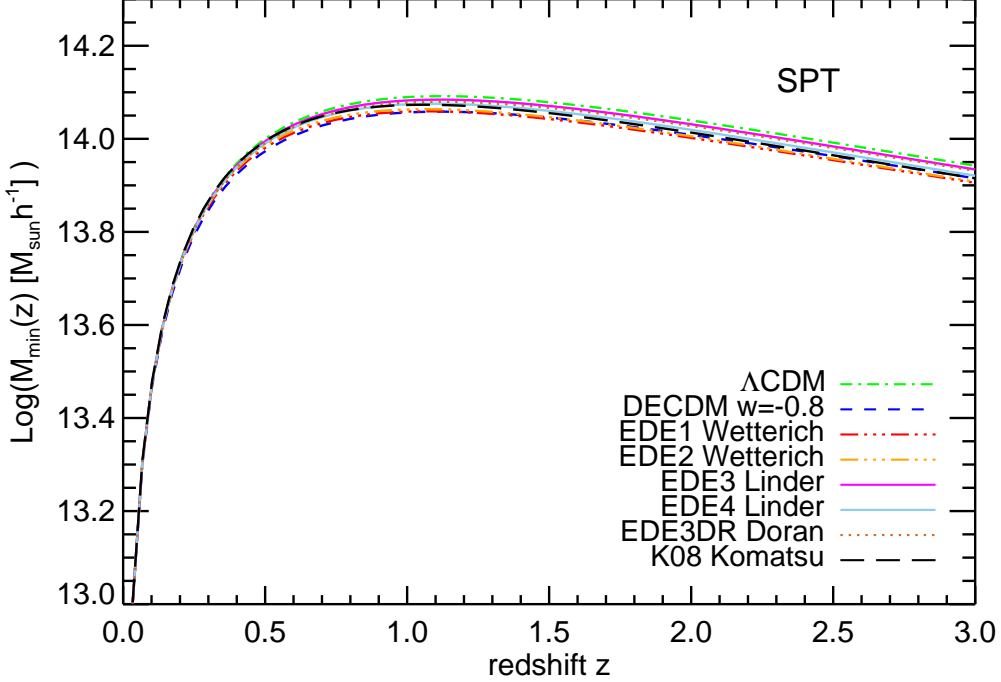
Figure 3.16 Minimum mass for clusters observed in the SPT SZE survey, imposing a threshold flux density of $S_{\nu_0,\text{lim}} \simeq 5$ mJy at a frequency $\nu_0 \equiv 150$ GHz. The green dot-dashed line refers to our fiducial ΛCDM model. In addition, we consider seven different EDE models, as labeled in the plot.

(Haiman et al., 2001; Majumdar and Mohr, 2003; Fedeli et al., 2009).

We model the SPT SZE survey taking into account a limiting SZ flux density of $S_{\nu_0,\text{lim}} \simeq 5$ mJy at a frequency $\nu_0 \equiv 150$ GHz. The mass-flux relation we use is:

$$S_{\nu_0}(M_{200}, z) = 10^\beta \left(\frac{M_{200}}{10^{14} M_\odot} \right)^\alpha \frac{E(z)^{2/3}}{(D_\text{A}(z)/1 \text{ Mpc})^2} |j(\nu)|, \qquad (3.27)$$

where

$$j(\nu) = 2 \frac{(kT_\gamma)^3}{(hc)^2} |f(\nu)|. \qquad (3.28)$$

T_γ is the CMB temperature and $f(\nu)$ is the typical spectral signature of the thermal SZ effect,

$$f(\nu) = \frac{x^4 e^x}{(e^x - 1)^2} \left[x \frac{e^x + 1}{e^x - 1} - 4 \right], \qquad (3.29)$$

with $x \equiv h\nu/kT_\gamma$.

For the SPT catalogue $\nu = \nu_0$, with $\nu_0 \equiv 150$ GHz, then $f(\nu_0) = -3.833$, and we use the best-fit power law index $\alpha = 1.876$ and normalization $\beta = -5.4774$ found by Sehgal et al. (2007) to relate mass and Comptonization parameter.

Figure 3.16 contains a plot of the limiting mass of detectable clusters as a func-

tion of redshift for 8 of the different dark energy cosmologies employed in this work. We can notice that the recovered mass is nearly independent of redshift, and changes very little with cosmology. For a flux limited survey, the limiting mass in Equation (3.27) is sensitive to cosmology through its dependence on the angular diameter distance, $D_A(z)$, and on the Hubble expansion function $E(z)$, that arises in the definition of the virial mass. In fact, clusters form earlier in EDE cosmologies, and in average they have more concentrated dark matter halos. The mass limit we plot is the *virial mass* corresponding to the limiting flux of the survey, thus we incorporate the assumption that the virial relation is invariant in EDE cosmologies, which is supported by recent N-body work (see Grossi and Springel, 2009).

The SPT survey can detect clusters more massive than $\simeq 1 \times 10^{14} h^{-1} M_\odot$ at all redshifts. This corresponds to about 11000 clusters with measured fluxes in our reference ΛCDM model for $0.033 < z < 1.5$. As can be seen from the figure, the minimum mass for detection slightly decreases beyond redshift $z \simeq 1.1$. However, the number of high-mass clusters detectable in the survey at $z > 1.5$ is still strongly limited by the volume considered.

In Figure 3.17 (upper panel) we show the redshift distribution of clusters obtained by averaging 8 different light-cone maps of 12 squared degrees each, for all the models we simulated. We produced a catalogue of clusters with mass $> 10^{13} h^{-1} M_\odot$ from the simulation outputs and then selected the halos contained in our light-cones that are detectable down to a constant SZ decrement of $S_{\nu_0, \text{lim}} \simeq 5 \, \text{mJy}$. Our fields correspond to an effective area of 1152 square degrees, we hence estimate the equivalent all-sky distribution by just multiplying by the fraction of the full solid angle subtended by our simulated maps. The figure reveals that the different cosmologies cause the redshift distribution to decrease less steeply for the EDE models, increasing the number of high-z clusters. When we consider the comoving abundance of clusters (lower plot), we found again an increase in the number of halos for $z > 0.2$, consistently with the surface density results. Taking the same normalization $\sigma_8 = 0.8$ today, the model DECDM shows 25% more objects than the reference ΛCDM model already at $z \simeq 1.5$, while all the others models are in between.

The surface density of clusters depends on the assumed cosmology mainly through the growth factor (see Equation 3.20) and the comoving volume element in solid angle $d\Omega$ and redshift interval dz:

$$dV_C = D_H \frac{(1+z)^2 D_A^2}{E(z)} \, d\Omega \, dz. \tag{3.30}$$

Here

$$D_H \equiv \frac{c}{H_0} = 3000 \, h^{-1} \, \text{Mpc} = 9.26 \times 10^{25} \, h^{-1} \, \text{m}, \tag{3.31}$$

$$H_0 = 100 \, h \, \text{km s}^{-1} \, \text{Mpc}^{-1}, \tag{3.32}$$

and D_{A} is the angular diameter distance at redshift z. $E(z)$ is defined as:

$$
\begin{aligned}
E(z) \;=\;\; & \Omega_{m,0}(1+z)^3 + \Omega_{\mathrm{de},0} \\
& \exp\left(\int_0^z [1 + w(z')]\, \mathrm{d}\ln(1+z')\right) \;.
\end{aligned}
$$

In order to disentangle how these factors contribute to the number and the distribution of clusters we study all the elements separately, and consider also a pair of different cosmologies.

In Figure 3.18, we first compute the cluster abundance of all the clusters above a fixed mass of $M_{\mathrm{min}} = 10^{13} h^{-1} M_{\odot}$ (upper lines) or $M_{\mathrm{min}} = 10^{14} h^{-1} M_{\odot}$ (lower lines), respectively. Results for the eight different dark-energy models are shown, using the same color and line styles as in Figure 3.17. A comparison of the results in Fig. 3.18 and Fig. 3.17 shows that introducing a flux limit mass has the effect of slightly strengthening the dependence on w. We found that, if we would have not included a cosmology dependent mass limit threshold, the pivot point, in which the cluster abundance of the dark energy models overcomes the abundance in the standard model, would be slightly shifted towards a lower redshift, $z = 0.15$ instead of $z = 0.20$. Considering the total number of clusters at a fixed mass, we have the further advantage to remove the uncertainty due to the somewhat arbitrary normalization of the mass-flux relation (see Equation 3.27): then the opposite sensitivity of the volume element and the growth factor completely determine the net effect of the early dark energy contribution.

The upper right panel in Figure 3.18 shows the comoving abundance above a fixed threshold in mass ($M_{\mathrm{min}} = 10^{13} h^{-1} M_{\odot}$) in the range of cosmologies examined here. Looking at the zoomed quantity in the small insets we recover the general trend: for a higher amount of dark energy at early times the number of high-redshift clusters increases. When a constant M_{min} is assumed and we take into account less massive clusters, which offer better statistics, the distribution flattens and the differences are amplified.

The cosmological abundance is exponentially sensitive to the growth factor evolution, but the effect is visible only at redshift $z > 0.5$, because we normalize all models to the same σ_8 today. The lower left plot of Figure 3.18 shows that the growth in models with higher w is bigger with respect to the reference model.

We also notice that the volume element acts in the opposite direction: the reference ΛCDM model has the higher volume, and this tends to balance the increase in the comoving abundance of clusters observed in the dark energy models. This is also why the ordering of the different dark energy models in terms of observed abundance does not reflect precisely their ordering in terms of linear growth power.

The redshift distribution of clusters contains far more information than only constraining the nature of dark energy. Up to now we used the same underlying cosmology in all the runs in order to eliminate all free cosmological parameters with
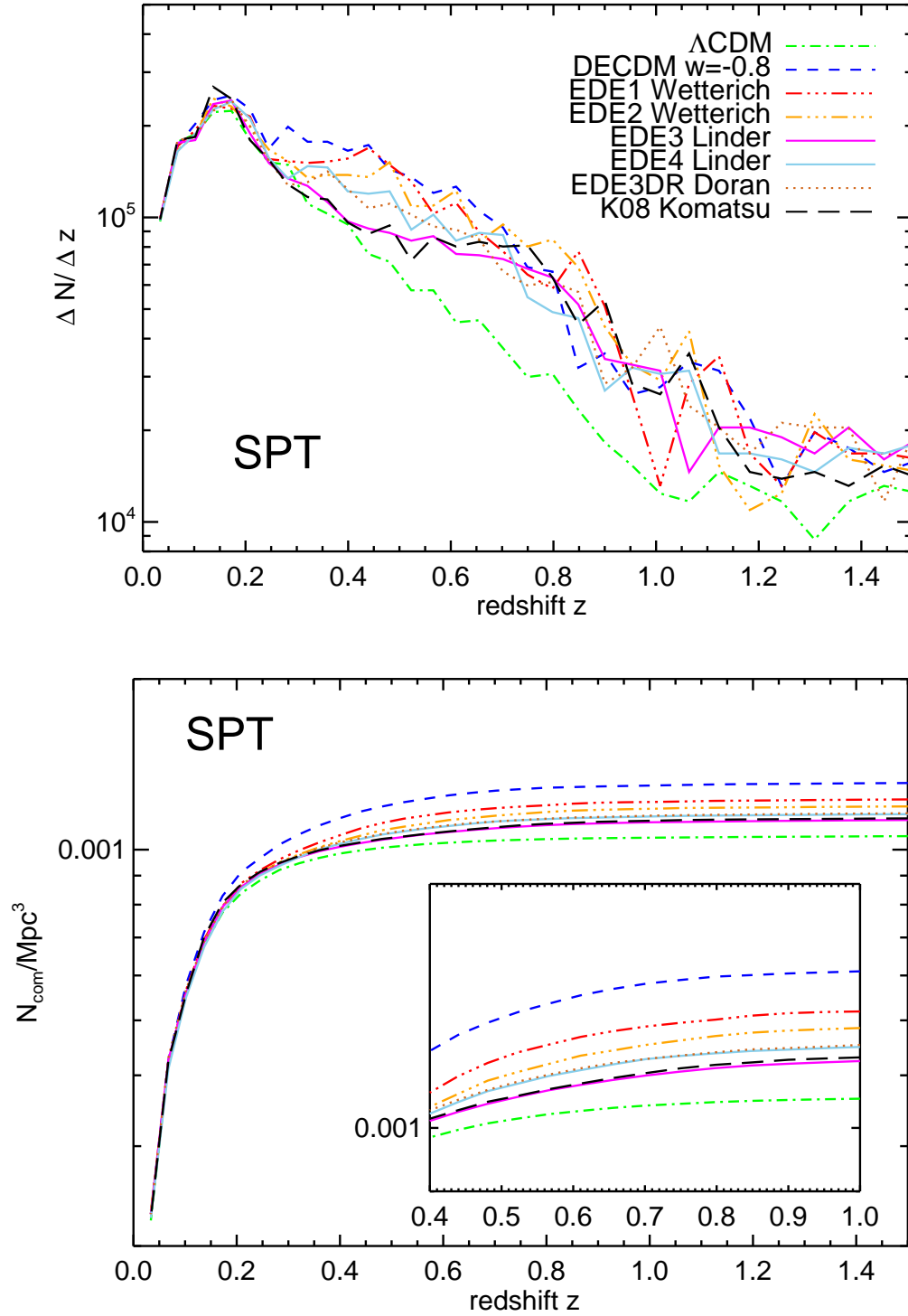
Figure 3.17 Sky-equivalent surface density (upper plot) and cumulative number count (lower plot) of clusters above the limiting flux $S_{\nu_0,\text{lim}} \simeq 5$ mJy, expected for the SPT SZE survey. The corresponding limiting mass for the different cosmologies is shown in Figure 3.16. The clusters were extracted in a 12 deg^2 field, averaging over 8 different maps for each cosmology.
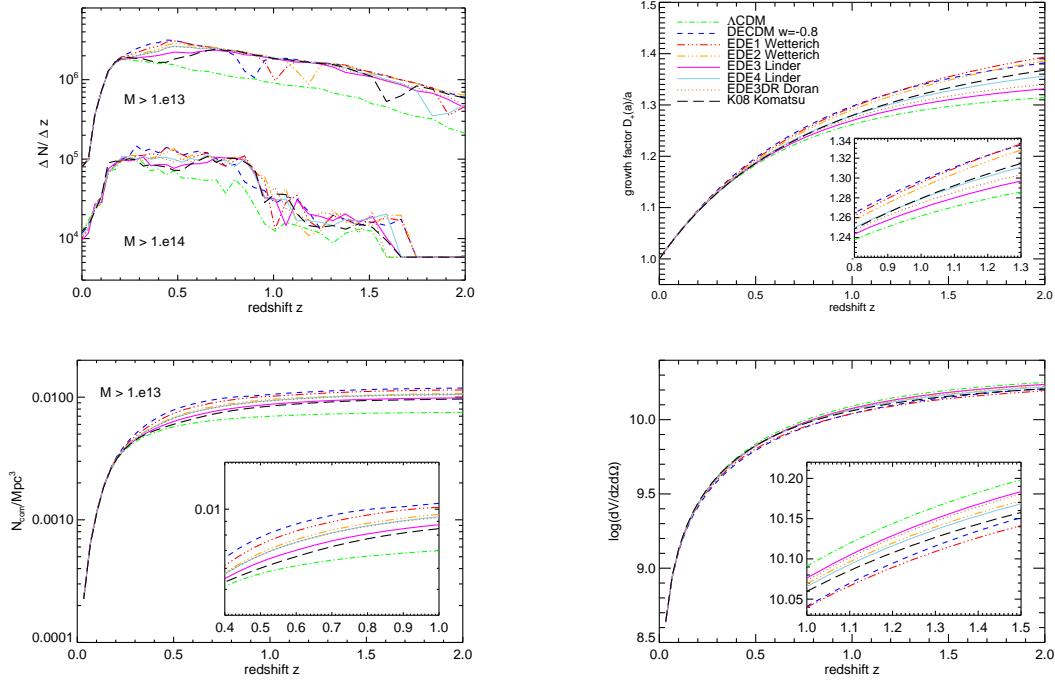
Figure 3.18 Effect of changing dark energy cosmology holding all the other parameters fixed. The four panels show respectively: the expected surface density (sky-equivalent) of clusters above mass $M_{\min} = 10^{13}h^{-1}M_\odot$ and $M_{\min} = 10^{14}h^{-1}M_\odot$ (upper left panel); the evolution of the growth factor in the eight different cosmologies we studied (upper right panel); the comoving abundance of clusters above mass $M_{\min} = 10^{13}h^{-1}M_\odot$ normalized today (lower left panel); and finally the dimensionless comoving volume element (lower right panel). The clusters were extracted in a 12 deg^2 field, averaging over 8 different maps for each cosmology. The different curves are for the eight world models studied here; the solid green curve shows our fiducial flat ΛCDM model.
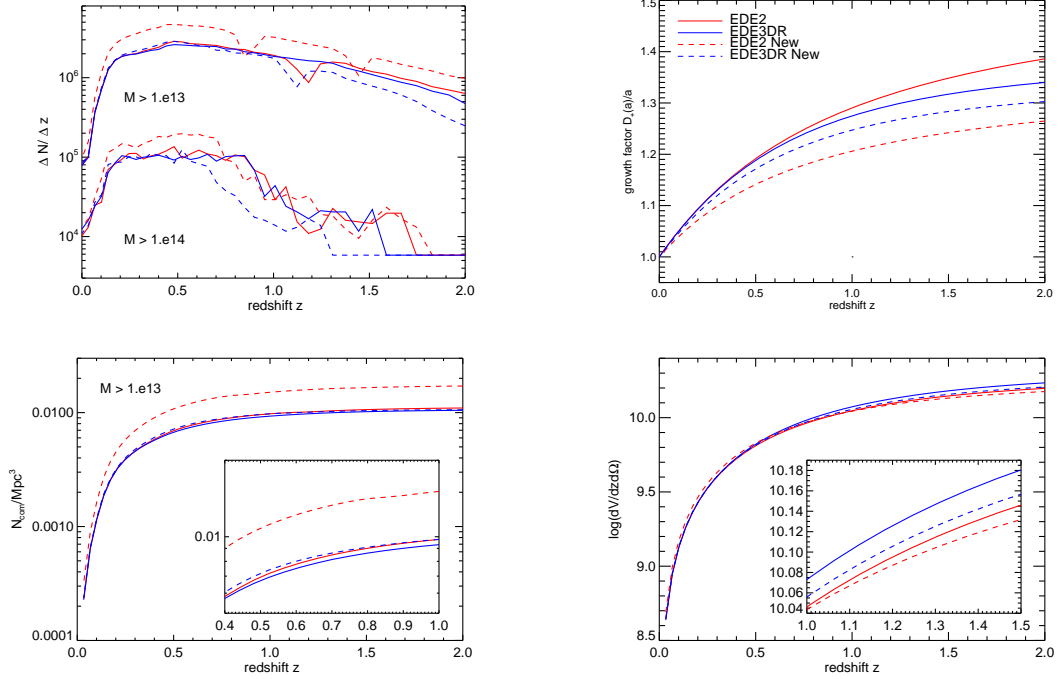
Figure 3.19 Effect of changing the cosmological parameters holding the dark energy cosmology fixed, for the models EDE2 and EDE3. The four panels show respectively: the expected surface density (sky-equivalent) of clusters above mass $M_{\min} = 10^{13}h^{-1}M_{\odot}$ and $M_{\min} = 10^{14}h^{-1}M_{\odot}$ (upper left panel); the evolution of the growth factor (upper right panel); the comoving abundance of clusters above mass $M_{\min} = 10^{13}h^{-1}M_{\odot}$ normalized today (lower left panel); and the effect of the cosmological parameters on the comoving volume element (lower right panel). The clusters were extracted in a 12 deg^2 field, averaging over 8 different maps for each cosmology. The solid curves refer to the original models, while the dashed ones to the modified cosmologies.

the exception of the dark energy contribution. In Figure 3.19, we finally explore also the effects of changing the underlying cosmology. We show the number of clusters $dN/dz\,d\Omega$ in the same 8×12^2 square degrees fields for our standard dark energy models EDE2 and EDE3DR and for two different cosmologies that we call EDE2P and EDE3P. In the latter two models, we change the dark matter density parameter, the Hubble expansion rate today, and the power spectrum normalization. The exact cosmological parameters used are given in Table 3.1. These models are both still in agreement with all current bounds from SN Ia, LSS and CMB data, but we notice that a lower Hubble parameter h, combined with a bigger $\Omega_{m,0}$ lead to an increase of up to 80% in the surface density distribution for the model EDE2P. On the other hand, the comoving abundance is the same for the two Doran-Robbers cosmologies, because the effects of increasing the number of halos is balanced by a 12% decrease in the normalization parameter σ_8.

Several conclusions can be drawn looking at the lower panels of figure 3.19. First, the evolution of the growth function typically reflects the difference in the normalization parameter σ_8, but is not affected by h. A second important feature is that a bigger $\Omega_{m,0}$ reduces $D(a)$ in the model EDE2P. Finally, we analyze the comoving volume element for all different cosmologies, plotted in the lower right panel of Figure 3.19. The increase in the matter density parameter gives a smaller volume element in the two new cosmological models. The Hubble parameter acts in the opposite sense, the volume becomes larger when h is smaller, and this is why the cumulative effect is a very similar decrease for the models EDE2P and EDE3P with respect to the "original" EDE2 and EDE3DR.

We conclude that the sensitivity to various different cosmological parameters like normalization and matter density can be far stronger than the intrinsic differences resulting from dark energy models, even though the shape of the redshift distribution may be unaffected.

3.6 Mass - Compton Y-parameter scaling relation

We now turn to an investigation of the scaling relation between the mass and the Comptonization Y-parameter. To realize the full statistical power of the upcoming SZE surveys, we need to better understand the relation between the SZE observable and the cluster mass as a function of redshift. Making this connection reliably is essential for the use of clusters as cosmological probe.

In this paragraph we address this issue by relating the mass of clusters both with their *intrinsic* SZ effect, and with the one measured directly from the thermal light-cone maps. To identify objects in the light-cone we simply determine the image location of clusters in each of the single redshift slices of the full projection, using the procedure illustrated in section 3.3.4. For each identified cluster, we then

calculate the true and projected value of Y estimated in the following way.

In the first step, we sum up the contribution to the SZ signal due to every gas particle contained inside the virial radius in order to derive the total decrement for that particular cluster. Specifically, we compute:

$$Y_{\text{int}} = (\gamma - 1)(1 - Y_p)\sigma_T \sum_j \mu_j x_j \frac{m_j}{m_e} \frac{u_j}{c^2}, \qquad (3.33)$$

where $\gamma = 5/3$, $Y_p = 24\%$, σ_T is the Thomson cross section, m_e the electron mass, c the speed of light, μ_j is the mean molecular weight of particle j, x_j is the fractional ionization (relative to hydrogen), m_j is the gas particle mass and u_j its internal energy per unit mass. We repeat the summation also over all particles within r_{500} and r_{100} around the potential minimum of the cluster or group. We have always calculated each overdensity radius directly from the three dimensional data of the simulations because we are interested in determining the best scenario for the cluster mass estimation. We derive the concentration of each halo by determining the maximum of its circular velocity curve, which under the assumption of a NFW density profile fully determines the concentration.

Secondly, we have calculated the value of Y_{proj} by integrating the contribution of all the adjacent pixels in the image out to each cluster's projected radius for different fixed fiducial overdensities:

$$Y_{\text{proj}} = d_A(z)^2 Y = d_A(z)^2 \int y \, d\Omega. \qquad (3.34)$$

Here Ω is the solid angle subtended by the object on the sky and the angular scale is converted to Mpc through use of the value of the angular diameter distance, d_A, for each cluster. Defined in this way, Y_{proj} is an intrinsic quantity of the halo, and can be directly compared with the value obtained summing up by all the gas in three dimensions.

In Figure 3.21, we show the two estimates Y_{int} and Y_{proj} as a function of mass for one projected light cone image for the models ΛCDM and EDE1. The value of Y is corrected for redshift since it depends on $E(z)^{-2/3}$, due to the cosmological dependence of the cluster M-T relation. Both the mass and the y-parameter are estimated within R_{200}, the radius where the mean cluster density is 200 times larger than the critical density. We divide the objects identified in the partial maps into four different redshift bins: $z < 0.3, z \in (0.3, 0.6), z \in (0.6, 0.9)$, and $z \in (0.9, 1.5)$. This leaves us with a sample of ~ 1700 halos at $z < 0.3$, and up to ~ 50000 halos in the highest redshift last bin.

We find best fits for the two different cosmologies by fitting all the halos in each redshift interval by a power law relation of the form

$$\frac{Y_{200}}{E(z)^{2/3}} = 10^{\beta} \left(\frac{M_{200}}{10^{14} M_{\odot}} \right)^{\alpha}. \qquad (3.35)$$

The magenta line in the upper panel of Fig. 3.21 is obtained using the fitting parameters derived by Sehgal et al. (2007). The plot clearly shows that the Y-M relation is well represented by a power-law, with slope very close to $\alpha = 5/3$, as predicted by theory (see Equation 3.7). The slope of the relation for ΛCDM and the EDE1 cosmologies is flatter than the value given by Sehgal et al. (2007) since we take a smaller limiting mass compared to them ($M \geqslant 1 \times 10^{12} h^{-1} M_\odot$ instead of $M \geqslant 2 \times 10^{14} M_\odot$). In fact, as the minimum mass of the sample decreases, the index α gets smaller, because the lowest mass halos in the sample, which dominate by number, dominate the Y-M relation.

At a glance, it is clear that the cluster gas component is nearly independent of the dark energy cosmology we are considering. The detailed values of the best fit parameters for normalization β and slope α of the ΛCDM and EDE1 models are given in Table 3.4. Comparing the upper and lower panels of each plot gives us effectively the difference between the true estimate of the integrated SZ effect and the error in the measurements caused by line of sight projection effects. These errors represent the main source of uncertainty in the M-Y relation (White et al., 2002; Melin et al., 2006; Hallman et al., 2006): if we take into account our highest redshift bin, we can see an increase by a factor of 6 in the scatter around the mean value due to projection effects. The majority of the sources shows an increase in the flux estimate due to secondary objects or unbound gas projected into the source region, while a few clusters extend beyond the image clusters and appear to have a lower value of the projected y-parameter.

In Figure 3.20, we show how the virial mass correlates with the SZE signal integrated within a sphere of radius R_{500}. We use the redshift range $0 \leqslant z \leqslant 1.5$ of one light-cone constructed for the ΛCDM and EDE1 cosmology. Sources in each of the four redshift intervals used in the previous plot are ranked by mass and divided in bins of 250 clusters each. Each point represents the mean value over the set of objects, and the error bars give the error around the mean Comptonization parameter. All points clearly trace a power law in the Y-M plane. A departure from that is observed only for high fluxes, in the bins that contain the more massive and nearby clusters. The overall slope of the relation is slightly steeper ($\sim 1.5\%$) than the one obtained when we consider a lower density contrast for the computation of the Comptonization y-parameter.

In general, both the slope and normalization that we measure for these models are in reasonably good agreement with previous works. In particular, the ΛCDM model closely matches the results of Nagai (2006) and Sehgal et al. (2009): the slope and normalization differ by less than 1% in the first case, and by 2.3% and 1.3% in the second, for the same overdensity values. The best-fit lines to $Y_{500} \times E(z)^{-2/3}$ versus M_{200} for all the dark energy cosmologies studied here are shown in the inset of Figure 3.20, and the corresponding parameters are presented in Table 3.3. The shaded area in the embedded panel is the r.m.s. dispersion of the fit for the ΛCDM

model computed as:

$$\sigma_{\log y'} = \sqrt{\frac{1}{N} \sum_i [\log(y_i'/y')]^2}\,, \qquad\qquad (3.36)$$

where $y' = yE(z)^{2/3}$, and y_i' are the individual data points. This dispersion is of the same size as the differences in the best fit line for the dark energy cosmologies. When we compare the average value of the slope, we find no significant departure from one model to the other, confirming the behavior observed by Aghanim et al. (2009). Therefore, using the standard scaling relation calibrated on a ΛCDM model in future surveys should not introduce any additional bias in the derivation of the cluster mass from observables.

Next, we study the evolution of the slope and normalization of the Y-M relation over the redshift range $z < 1.5$ to illustrate the scaling in the different dark energy cosmologies. In Figure 3.22, we present our findings for the $Y_{\rm int}$-M_{200} relation, for all the different cosmologies. The upper panel shows the time variation of the slope α in each partial map for all the cosmological models, while the shaded area corresponds to 1σ departures from that value. One can notice that the slope is consistent with the self-similar scaling at all redshifts, and is constant with time. Also, the models are very close to each other, there is only some small scatter at low redshifts, where our object sample is smaller. The variation of the normalization with time and the 1σ confidence region is presented in the middle panel, while in the bottom panel we show the linear best fit to the β evolution. Again we find no significant departure from the cosmological constant model, but a slightly increased scatter, especially near $z = 0$. However, these oscillations show no systematic dependence on redshift, and are within the intrinsic error and dispersion of the relation. All models show positive evolution of the normalization, confirming expectations (Aghanim et al., 2009).

To illustrate the robustness of our findings with respect to the projected quantity, we repeat the same analysis for the $Y_{\rm proj}$-M_{200} relation. In Figure 3.23 we show the best fit slope and normalization as a function of redshift. The shaded area gives the r.m.s. dispersion for the ΛCDM model, and it is much larger than the one derived from the 3D analysis even for our noise free, high resolution maps. In fact, since the signal is not dimmed by distance and clusters form in high density regions, objects and non-cluster material in proximity to the source can contribute a significant amount to the total signal. The scatter within the models is always much lower than the statistical uncertainties associated to the values. The evolution of the normalization β is steeper with respect to the three dimensional case, because of the larger contribution of the background in the high redshift partial maps. However, these differences are of the same order of magnitude in all models. This means that calibrations that are based on the dynamical properties of the clusters to derive the mass are still valid in the generalized dark energy cosmologies examined in this work.
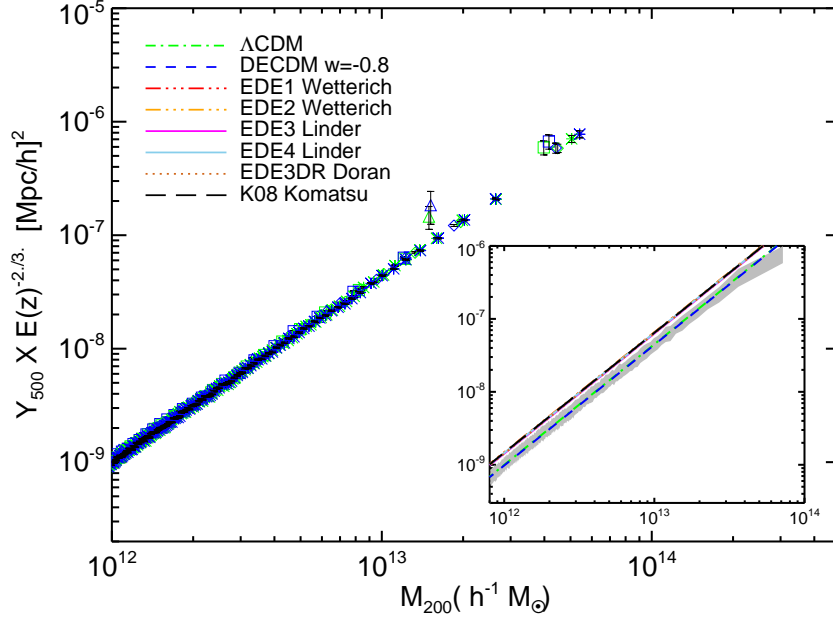
Figure 3.20 Cluster scaling relation between the Compton-Y parameter integrated within a sphere of radius r_{500} and the virial mass M_{200} for the cosmological models ΛCDM and EDE1. The objects of the four redshift intervals considered in Figure 3.21 are divided into bins of 250 clusters. The error bars give the error around the mean in a single bin. The embedded plot shows the best fit relation in the $\log(Y) - \log(M)$ plane for all the cosmological models simulated in this work: the corresponding parameters are listed in Table 3.3. The shaded region gives the r.m.s. dispersion about the best fit line for the ΛCDM model.

Model	α	σ_α	β	σ_β	red. χ^2	clusters
ΛCDM	1.655	0.071	-5.693	0.291	0.032	80010
DECDM8	1.655	0.075	-5.701	0.305	0.031	70447
EDE1	1.644	0.074	-5.540	0.301	0.037	72231
EDE2	1.647	0.074	-5.536	0.299	0.040	73448
EDE3	1.649	0.072	-5.550	0.293	0.039	77316
EDE4	1.647	0.073	-5.542	0.296	0.038	75899
EDE3R	1.648	0.073	-5.549	0.296	0.039	75791
K08	1.644	0.073	-5.544	0.296	0.037	75968

**Table 3.3** Best-fit values for the parameters α and β obtained for the M_{200}-Y_{500} scaling relation, fit using the power-law given in Equation (3.35) and their respective 1σ errors. These results are valid within the redshift range $1.5 < z < 0$, and we considered all the dark energy cosmologies studied in this work. We used these values to trace the Y-M relation in the inset of Figure 3.20.
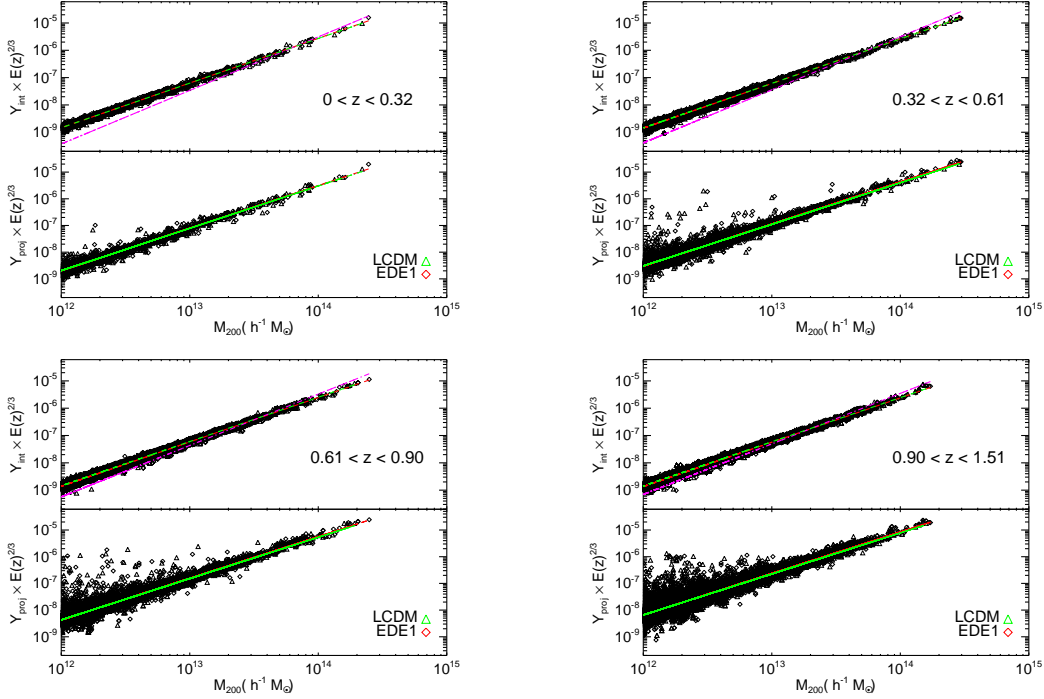
Figure 3.21 The relation between the total decrement, Y, and cluster mass M_{200}. The upper panel shows the decrement calculated from the material within half the virial radius r_{200} for each cluster in the simulation volume in four different redshift regions. The single clusters are indicated by squares and triangles, for the ΛCDM and EDE1 models, respectively. The straight lines indicate the best fit relations in the $\log(Y) - \log(M)$ plane. The magenta lines are traced from the best fit parameters given in Sehgal et al. (2008) in the different redshift intervals. The lower panel shows the decrement obtained directly from the noise free maps by summing pixels centered on the known locations of the clusters. As a remark, we show only clusters whose disk overlapped that of a more massive cluster in the map, and so was identified also in the FoF catalogue.

	$\alpha_{\Lambda\mathrm{CDM}}$	$\sigma_{\alpha,\Lambda\mathrm{CDM}}$	$\beta_{\Lambda\mathrm{CDM}}$	$\sigma_{\beta,\Lambda\mathrm{CDM}}$	clusters$_{\Lambda\mathrm{CDM}}$
$z < 0.3$	1.635	0.025	-5.567	0.102	1769
$z = 0.3 - 0.6$	1.628	0.012	-5.583	0.047	9533
$z = 0.6 - 0.9$	1.622	0.009	-5.599	0.035	19549
$z = 0.9 - 1.5$	1.619	0.006	-5.611	0.023	55233
	α_{EDE1}	$\sigma_{\alpha,\mathrm{EDE1}}$	β_{EDE1}	$\sigma_{\beta,\mathrm{EDE1}}$	clusters$_{\mathrm{EDE1}}$
$z < 0.3$	1.637	0.026	-5.560	0.103	1705
$z = 0.3 - 0.6$	1.632	0.012	-5.584	0.049	8719
$z = 0.6 - 0.9$	1.624	0.009	-5.611	0.036	17851
$z = 0.9 - 1.5$	1.623	0.006	-5.622	0.024	49548

Table 3.4 Best-fit values for the parameters α and β and their respective 1σ errors, obtained by using the power-law scaling relation given in Equation (3.35). These are the values used to trace the green and red lines in the upper panels of Figure 3.21, which refer to the ΛCDM and EDE1 cosmological models, respectively.

149
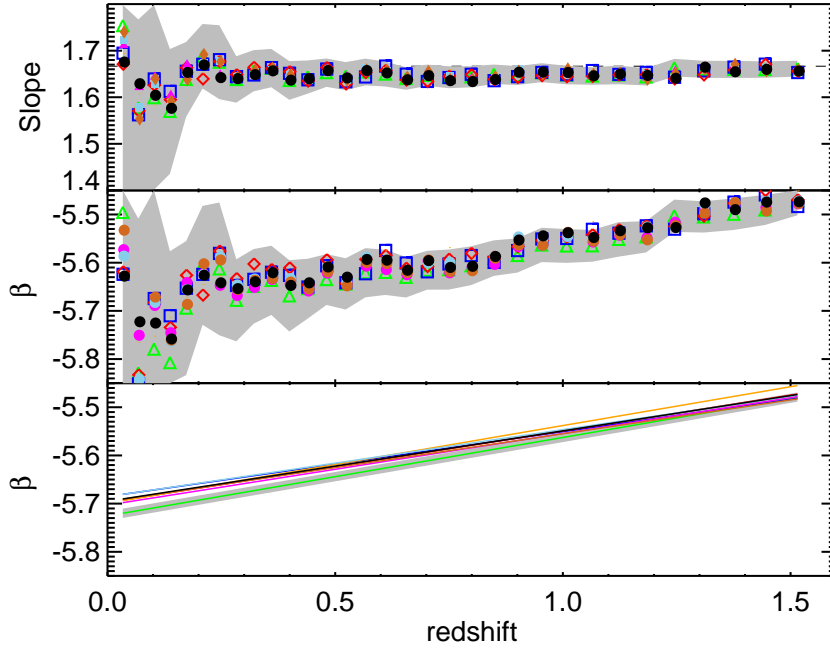
Figure 3.22 Redshift evolution of the normalization and slope of the $Y\text{-}M$ relation for the dark energy cosmologies mutated in this work. The plot refers to the results obtained studying the scaling relation at r_{500} (lower panel, see Equation 3.35). In the upper panel we show the slope of the $Y\text{-}M$ relation derived at the different epochs. The dashed line here indicates the self-similar relation $\alpha = 5/3$. In the middle plot, we show the values of the normalization parameter β. Finally, in the lower panel we trace the best fit lines of the redshift evolution of the normalization parameter. The error bars show the 1-σ confidence region of the best fit normalization parameter and slope at each epoch. We can thus safely assume that the dark energy models here studied have no significant departures with respect to the ΛCDM model.
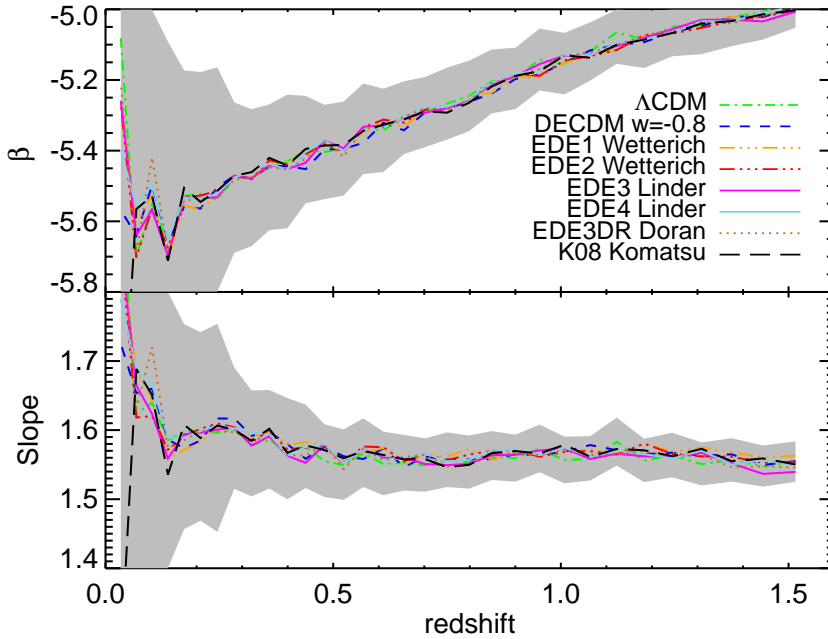
Figure 3.23 Redshift evolution of the normalization and slope of the Y-M relation for all the cosmologies here studied. In the upper plot, we show the evolution of the normalization parameter β, defined in Equation (3.35), and in the lower plot the best fit lines for the slope. These values are obtained from the study of the identified halos in the 2D maps. The shaded area gives the 1σ confidence region of the best fit normalization parameter and slope at each epoch.

3.6.1 Scatter in the Y-M relation

It is important to study the magnitude of the intrinsic scatter about the SZ - mass relation in order to perform accurate corrections to the observable data and to efficiently use the cluster aboundance to constrain the cosmological parameters. Moreover, we have already remarked that the net influence of the projection is to populate the region of high-flux candidates in the Y-M plane: in other words, our Universe appears to have a higher number of high-mass clusters than are actually present. Uncertainties in the "bright" end of the cluster abundance then strongly degrade the dark energy constraints, and this highlights the need to further investigate the robustness of the scaling relations in this contest.

In order to empirically study the minimum scatter in the Y-M relation, we compute the integrated Compton parameter Y_Δ in the projected 2D maps at different radii, corresponding to overdensities within the range $50 \leqslant \Delta \leqslant 2500$, e.g. from a region that is well outside the virial radius computed in the spherical collapse theory up to the inner parts of the cluster. We obtain 16 different measures of M and Y for each of the identified clusters in one of the simulated maps with 3 deg^2 field. Then, we fit the Y-M relation with the power law described in Equation 3.35, assuming as free parameters the normalization and the slope of the scaling. We compute the

scatter around the best fit relation for each set of data in the following way:

$$\sigma_{\mathrm{YM}} = \left(\frac{\sum_{i=1}^{N} (\ln Y_{\Delta_Y} - \ln \hat{Y}_{\Delta_M})_i^2}{N - 2} \right)^{1/2} . \tag{3.37}$$

Here N is the total number of identified clusters in the light-cone, Y_{Δ_Y} is the flux measured within R_{Δ_Y} summing up the pixels in the simulation maps at different radii, while $\hat{Y}_{\Delta_M}$ is the value of the flux computed from the best fit parameters and corresponding to the mass M_{Δ_M}. This procedure is analogous to the one used by Shaw et al. (2009). We took all the clusters in the maps with identified counterparts in the simulation, up to a minimum mass of $M_{\min} = 1 \times 10^{12} h^{-1} M_\odot$ and for redshift $z < 0.5$. For the ΛCDM reference model, this means a sample of more than 7000 clusters.

In total, we studied $16^2 = 256$ different combinations of Δ_Y and Δ_M, and we found that in all cases the power law relation provides a good fit to the data. For a fixed definition of the mass, the slope increases when we compute the Comptonization parameter within a larger overdensity, while it is lower when we fix Δ_Y. For example, at $\Delta_M = 200$, α goes from 1.48 at $\Delta_Y = 50$ to 1.77 at $\Delta_Y = 2500$ for ΛCDM. The normalization presents a more irregular behavior.

Figure 3.24 displays the scatter σ_{YM} around the scaling relation for the ΛCDM cosmologies and the EDE1 model. The curves show very similar features in the two cosmologies, as well as for the other dark energy models. The only difference is a slightly smaller scatter with respect to the cosmological constant case. In general, the deviations around the power law relation, quantified in terms of σ_{YM}, are always smaller in a region close to $\Delta = 200$ both for the mass and the flux values, the minimum being reached for $\Delta_Y = 300$ and $\Delta_M = 300$ in all models. The simulated data show a dispersion that varies between 0.3 and 0.9 when the computation of the mass includes regions outside the virial radius. However, this result depends quite consistently on the halo concentration/substructure content of the sample, and on the particular definition we apply to compute the mass.

In Figure 3.25, we plot the overdensity at which we measure the least scatter in the σ_{YM} plane, and the corresponding value of σ_{YM} as a function of Δ_M. In the right hand plot, we show the results for the ΛCDM and EDE1 cosmologies for two different definitions of the virial mass, to see how variations in this definition affect the final result. Instead of computing the projected radius of the cluster starting from the mass enclosed in a region 200 times overdense with respect to the critical density of the Universe, we repeat the calculations of the mass and Comptonization parameters taking as zero point R_{mean}, the radius that enclose an overdensity 200 times the mean density of the Universe.

A significant contributor to the intrinsic scatter in the Y-M scaling relation are variations in the internal dynamical properties of single clusters. For example,

the abundance of substructures inside the main object varies and can serve as an indicator of the equilibrium state of the halos. Also, scatter in the concentration-mass relation impacts the calibration of the overdensity and explains why the central SZE decrement provides a larger value of σ_{YM} as a function of Δ_{M} with respect to the integrated Comptonization.

In order to quantitatively study the impact of these two effects, we remove from our sample all objects with a substructure fraction $f_S = M_s/M_{\mathrm{vir}} > 0.1$ (here M_s is the total subhalo mass) or which deviate from the concentration mass relation by more than $|\sigma_c| \leqslant 0.05$, where $\sigma_c = \log c - \log(c(M))$ encodes the deviation in the log of the measured value c from the fitted relation $c(M)$ over all the halos at a given redshift. Since the concentration-mass relation is affected by the dark energy cosmology (Dolag et al., 2004; Grossi and Springel, 2009), we recalculate the fit $c(M)$ for each of the models we study. In the left panel of Figure 3.25, we show the variations in σ_{YM} for the full halo sample considering the clusters identified in the 2D maps up to $z = 0.5$ (thick lines), and we recompute the value using only the halos that satisfy our constraints (thin lines). As a general remark, we find that Δ_{Ymin}, the overdensity at which we measure the least scatter, increases more steeply when we exclude these objects, while it is almost constant for the full sample. The scatter has a minimum in proximity of the virial radius, but increase at larger overdensity values. This result is consistent with previous works (Motl et al., 2005; Hallman et al., 2006), which indicate that for larger radii there is a better correlation between the SZE signal and the mass, since the influence of effects at the core are reduced.

Shaw et al. (2009), analyzing isolated massive clusters with analytic gas models and hydrodynamical simulations, found a slope greater than one for the Δ_{Y}- Δ_{M} relation and concluded that the smallest scatter is always obtained by computing Y within a smaller radius than that at which the mass is defined. Here we confirm that the scatter in the $Y_{200} - M_{200}$ relation is bigger by roughly 7% then the one in $Y_{500} - M_{200}$ in the restricted sample, but we find that, in the general case, at larger Δ_M, we need to compute the flux in a larger radius, between R_{200} and R_{500}, to obtain a more accurate estimate of the mass. When we restrict our sample in concentration and substructure content, the scatter is reduced by up to a factor of 2 at higher overdensity, and the value of the minimum decreases by $\sim 15\%$. Interestingly, we find that the substructure selection strongly affects the slope of the Δ_{Ymin}-Δ_{M} fit and the value of σ_{YM}, which decreases by more than 28% at $\Delta_{\mathrm{Y}} = \Delta_{\mathrm{M}} = 500$, while the variation in concentration removes only the remaining 2% of the total scatter. However, the relative importance of the concentration selection increases when we relate the SZE decrement with the mass computed inside a smaller region, and it become dominant for $\Delta_{\mathrm{M}} > 1500$.

Our results have the advantage of considering a very large sample of halos down to a mass of $10^{12}h^{-1}\mathrm{M}_{\odot}$ obtained from high-resolution hydrodynamical simulations
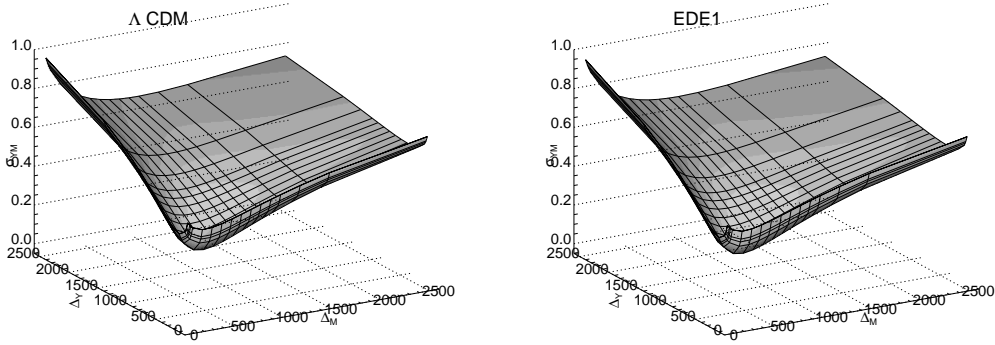
Figure 3.24 The scatter σ_{YM} around the mass-integrated SZE relation for cluster masses measured within the radius defined at virial overdensities in the range $80 < \Delta_M < 2500$, and the integrated SZE measured within the projected radius defined by $80 < \Delta_Y < 2500$. Here we consider all the clusters with mass $M > 10^{12}\,\mathrm{M}_\odot$ contained in the partial 2D maps in the redshift interval $0 < z < 0.5$. The plane shows the same shape for all the different cosmologies we studied.

where foreground/background contamination by structures along the line-of-sight is fully accounted for. We note that we obtain the same results when we repeat the analysis in 3D by computing the contribution of every single gas particle in the simulation individually, but the scatter is then smaller and of the same order of magnitude as found in the work by Sehgal et al. (2009), who claimed a bias in the cluster gas mass of $10 - 20$ per cent when contamination from projection effects is included.

3.7 The SZ angular power spectra

The cluster number counts are directly related to the power spectrum of the SZ signal at different scales, which can hence also be used to constrain the cosmological parameters. Interestingly, early dark energy might offer a natural explanation for the excess in the angular power on scales $\ell \geqslant 2000$ measured by the CBI (Mason et al., 2003), ACBAR (Kuo et al., 2004, 2007; Reichardt et al., 2009), and BIMA (Dawson et al., 2002) experiments. These observations of the CMB spectrum at high multipoles indicate a much higher temperature fluctuation amplitude than expected for a standard cosmology with the normalization $\sigma_8 = 0.812^{+0.026}_{-0.026}$ deduced from the WMAP 5-year data (Komatsu et al., 2009b). This effect is often referred to as "CBI anomaly". Attributing this discrepancy to the SZ effect would require a higher number of massive clusters than expected in the ΛCDM model, an thus an unrealistically high value of the mass variance parameter $\sigma_8 \geqslant 1$ in the ΛCDM cosmology. In this section, we test the viability of these predictions and quantify the effect of different dark energy models on the SZ power spectra of the simulated maps.
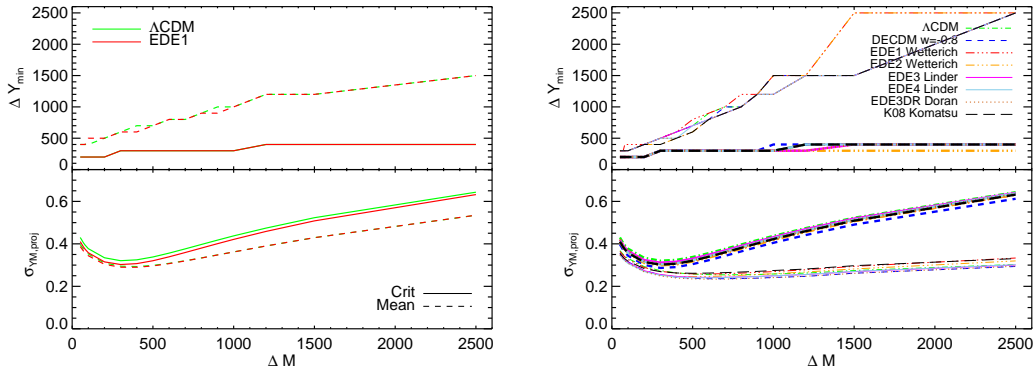
Figure 3.25 Overdensity Δ_{Ymin} for which the scatter is smallest as a function of Δ_{M} (upper panel of each plot) and the corresponding value of σ_{YM} (bottom panel). The variation of this quantity according to the definition of the mass is shown in the left hand plot. On the right hand plot, the thick lines refer to the results for all the dark energy cosmologies considering the full sample of halos, while the thin lines are obtained using only clusters with small substructure content and lower scatter in the concentration-mass relation (see text).

In Figure 3.26, we compare the angular power spectra for both the thermal and kinetic SZ effects with the primary CMB (black solid line). We consider the magnitude of the thermal SZ signal at $\nu = 30$ GHz, that corresponds to $g_\nu(x) = -1.94$ (see Equation 3.3), i.e. near the RJ limit where the effect is maximum. The included points with error bars are the measurements from the ACBAR, CBI and BIMA instruments converted to this frequency. The value $\Delta T = 26.5\,\mu\mathrm{K}^2$ measured at $l = 8748$ is an upper limit. However, recently the results of the Sunyaev Zeldovich Array (SZA Sharp et al., 2009) suggested a lower secondary anisotropy power than previously reported on scales $\ell \sim 4000$, where the thermal signal is expected to be the dominant contribution.

In all maps the tSZ power spectrum peaks at $\ell \simeq 9000$, and it starts to dominate the primary CMB signal at scales of about 4 arcmin. The kSZ signal is about one order of magnitude lower at these scales. However, it is interesting to note that the gap becomes smaller towards higher multipoles: while the tSZ signal looses power for higher ℓ, the kSZ power spectrum is almost flat and should dominate at $\ell > 200000$. This behavior, which is similar to the one obtained by Zhang et al. (2004) and Roncarelli et al. (2007), is a consequence of relevant contributions from high redshift, and therefore smaller objects, that dominate the kSZ effect signal (see Section 3.4). The bending of the power spectra derived from the simulated maps is also due to the fact that the expansion in spherical harmonics is limited by the pixel dimension, and we do not include objects with size comparable to that. Our results are in broad agreement with previous simulated and analytical predictions (Springel et al., 2001a; da Silva et al., 2001; Komatsu and Seljak, 2002), but they are a bit above the results obtained with radiative hydrodynamical simulations. However, we do not expect that the differences become much larger when including

additional physics, hence we can take our results as a basis to test the viability of the early dark energy models.

The comparison between the ΛCDM and the EDE cosmologies indicates that the level of SZ power in the latter is higher than in the standard model, but not yet in good agreement with current measurements of the CMB anisotropy at high multipole values. The magnitude of the differences is very similar for the thermal and kinetic SZ effects, being approximately a factor 1.54 and 1.37 between ΛCDM and EDE1, respectively. The enhancement in the thermal SZ maps for the EDE models is a direct manifestation of the increased cluster abundance in the generalized dark energy models. These results agree qualitatively with the calculations of Sadeh et al. (2007), and the claim that only an unrealistically high value of $\Omega_{\mathrm{de,e}} \sim 0.03$ could compensate for the observed measurements of the CMB anisotropies at high multipole values (Rephaeli and Sadeh, 2008). Unlike in the thermal SZ maps, we note that all the kinetic maps tend to be dominated by the presence (or absence) of single bright sources at large angular scales. In fact, all cosmologies show some sensitivity to rare features and are affected by the cosmic variance, due to the finite box size and field of view.

The redshift dependence of the power spectrum of the thermal effect is shown in Figure 3.27. In each case, we display the spectrum for the coadded thermal SZ maps obtained considering the contribution of the signal at redshift $z > 0, 1, 2$ and 3 (from top to bottom, and from left to right). We know that if the clusters were randomly positioned in the sky the power spectra of the resulting Poissonian distribution should be flat (Seljak et al., 2001). Then, the angular size of the peak of the distribution gives an indication of the major contributors to the total brightness of the maps in the 4 redshift intervals. At higher redshift, the peak approaches higher values of ℓ, and objects with smaller angular size dominate the signal. Again, the curves represent average values over 8 realizations, while the error bars in the first panel show the field-to-field variance in the maps of the ΛCDM model (green dot-dashed line). The non-Gaussian nature of the thermal SZ signal increases the scatter between the maps by one order of magnitude with respect to the Gaussian expectation, $(2/N)^{1/2}C_l$ (White et al., 2002). This effect is being driven by fields that contain at least one very massive halo at low redshift, and thus have $C_l << \bar{C}_l$, where $\bar{C}_l$ represents the mean value. Anyway, the single maps differ from each other mainly in the amplitude and not in the shape of the power spectrum, since our map-making algorithm replicates the same volume.

As already anticipated, the relative differences in the abundance of high-mass clusters between the ΛCDM and the EDE1 model doubles considering only redshifts $z > 2$ ($\sim 65\%$ at $z > 3$). In fact, the strongest impact on the abundance of high mass clusters is due to the slower evolution of the linear growth factor for the EDE cosmology with respect to a standard ΛCDM and at the present epoch this effect is negligible. However, since the bound gas is the main contributor to the

total signal, the absolute magnitude of the thermal effect decreases up to 3 orders of magnitude for redshift $z > 3$. The comparable amplitude between the models puts strict constraints on the possibility of distinguishing between them by future direct measurements, when we take into account the signal at low redshift and the same underlying cosmological parameters. However, we could confirm or rule out deviations from the standard ΛCDM model by looking at the power derived from sources at high redshifts relative to that from low redshifts, since EDE contribute is stronger in this regime.

Finally, we remark that the ordering of the cosmological models in terms of SZ power is the same as found when looking at the global properties of the SZ signal (Section 3.4). This confirms the expectation that the power spectrum is mainly sensitive to the differences in the Hubble expansion function, especially in the total coadded map, where the dominant contribution comes from low redshift sources. However, larger discrepancies are found when looking at models with different cosmological parameters. The lowered power spectrum normalization σ_8 of the model EDE3P directly translates in reduced SZ power levels, by a factor of more than 2.5 times for $z > 0$ compared with the EDE3DR cosmology. The scaling $C_l \propto \sigma_8^7$ accounts for a factor 2.3 of decrease, and the additional effect is due to the weaker dependence of the spectrum on the Hubble expansion rate. On the other hand, we know that C_l is not very sensitive to the matter density parameter when we consider a flat universe and stay in the range $0.15 < \Omega_m < 0.4$, because the decrease in the comoving volume due to the increase of Ω_m compensates for the effects in the mass function (Komatsu and Seljak, 2002). Since the power spectra for the EDE3P cosmology are much smaller than those for the high-σ_8 EDE3DR model, we can also expect that the former power spectra will be less affected in realistic observation by biasing due to the additional component, beam size and instrument noise levels. The power spectrum measured for the model EDE2P agrees quite well with the EDE2 result at very small angular scales, since the effect of decreasing σ_8 is quite small, a 20% difference is expected from the known approximate scaling, and the Hubble parameter is increased by $\sim 5\%$ already at $z = 1$.

3.8 Conclusions

Observing the dynamical evolution of the dark energy component is one of the primary goals of current and future Sunyaev Zeldovich surveys. SZ methods will provide us with mass estimates for a large sample of clusters up to very high redshift, but they also face fundamental challenges. Among them are the superposition of faint sources in the projected images, the intrinsic scatter in the mass-Comptonization relation, and the evolution and modifications of the SZ signal due to the underlying cosmology. These effects may impose severe limits on the cosmological information that can be extracted from the observations. Detailed numerical
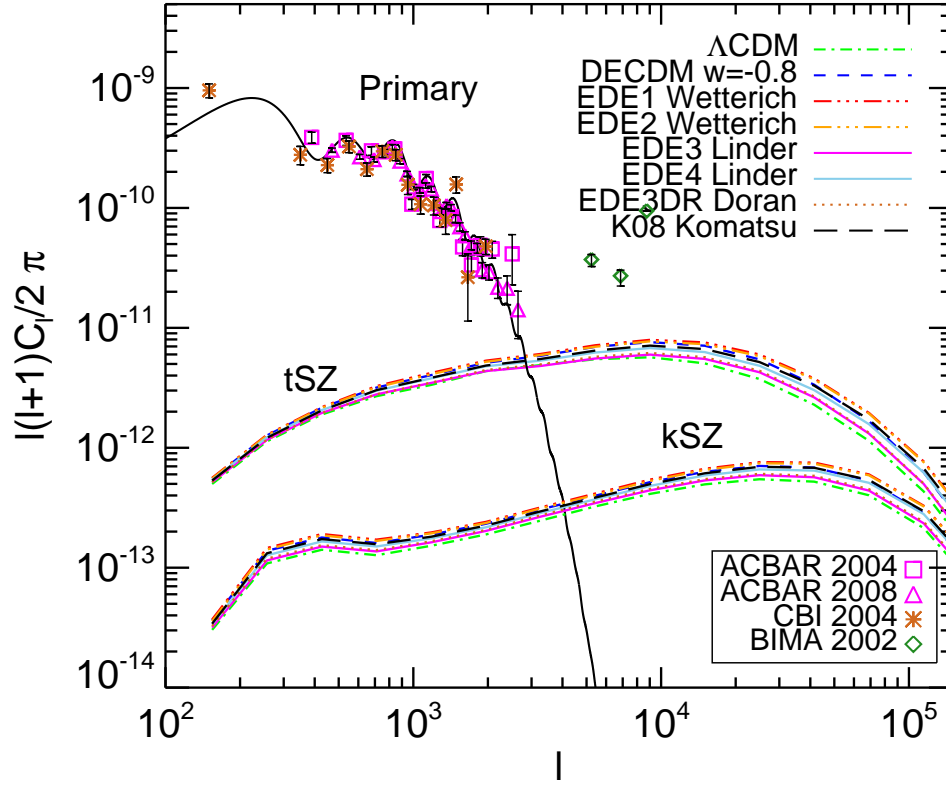
Figure 3.26 Angular power spectra of the $\Delta T/T_{CMB}$ fluctuations induced by the thermal (upper lines) and kinetic (lower lines) SZ effects as a function of the multipole ℓ. The solid line represents the primary CMB signal calculated using CMBFAST and assuming a WMAP-5 cosmological model. The lines represent the average of the power spectra over 8 light-cone maps of three degrees each (both for the tSZ effect and for the kSZ one). The tSZ spectra are computed at the frequency $\nu = 30$ GHz. Also shown is the power excess reported by the ACBAR (squares and triangles), BIMA (diamonds) and CBI (x-symbols) experiments. Note that the BIMA indicated power at $\ell = 8748$ is an upper limit.
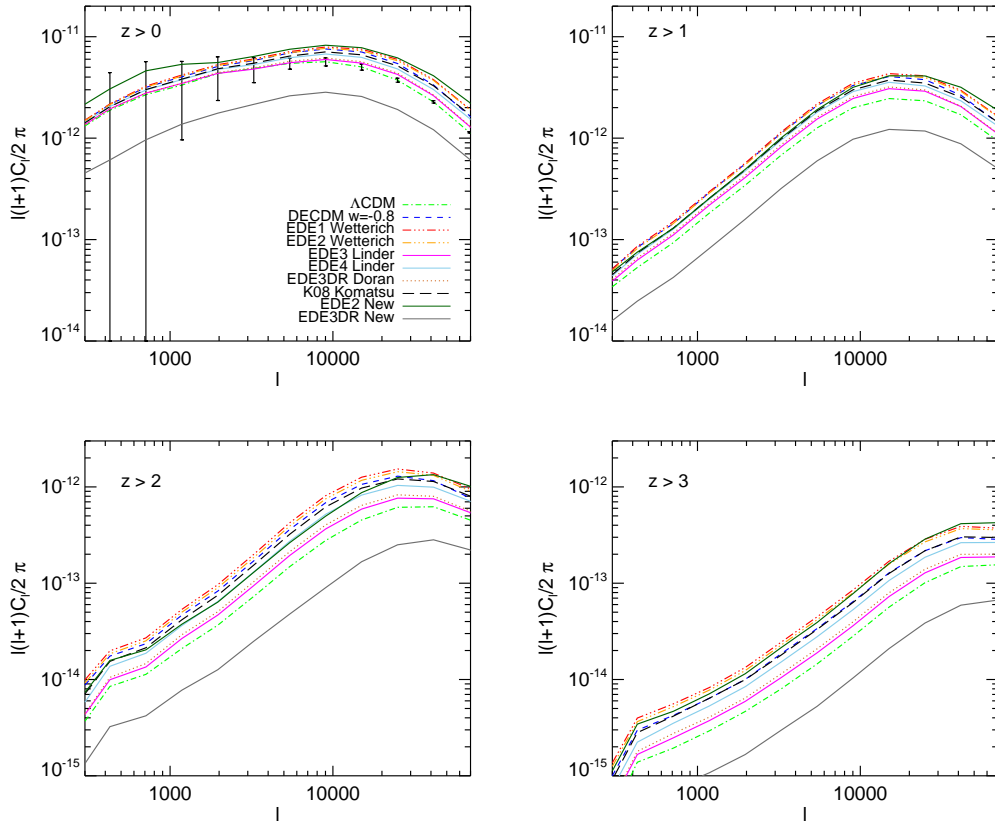
Figure 3.27 Angular power spectrum of the tSZ effect computed in four different redshift intervals. This gives an illustration of the potential of the power spectrum to distinguish between the models if one focuses on the high redshift behavior. The matter power spectrum is plotted for the EDE2 and EDE3DR cosmology and for the same dark energy model but slightly different cosmological parameters (see Table 3.1).

simulations are an essential tool to interpret the upcoming data and to quantify the sensitivity of cluster number counts to the amplitude of the linear density field and hence to the properties of dark energy.

In this Chapter, we present a numerical study of the impact of the dark energy content on the SZ effect, based on the outputs of a comprehensive set of non-radiative gas-dynamical simulations. We have considered a wide variety of dark energy physics besides the cosmological constant. These include a model with constant equation of state parameter for dark energy, $w = -0.8$, three early dark energy models that adopt the parametrization of Wetterich (2004), two EDE models that follow the parametrization of Doran and Robbers (2006), two moker models proposed by Linder (2006) and finally a dynamical dark energy model described in Komatsu et al. (2009b). The majority of these cosmologies has a non-negligible amount of dark energy at early time, but attains the observationally inferred value at present. In earlier work, investigators predicted significant modifications of the spherical collapse density threshold, and thus in the mass function and number counts statistics expected in the non-linear regime of structure formation (Bartelmann et al., 2006). However, numerical simulations, and eventually also improved analytic studies, have not confirmed these expectations (Grossi and Springel, 2009; Francis et al., 2009a,b). Now a much more subtle difference with respect to the familiar territory of the vanilla ΛCDM cosmology is expected. This numerical work addresses the issue of investigating the remaining influence of early dark energy on structure formation, and in particular, of characterizing the prospects to distinguish such cosmologies from ΛCDM with SZ observations.

As a first step, we have used a map-making procedure similar to Carbone et al. (2008a) to construct 16 simulated light-cone images (8 of size 3 square degrees and 8 of 12 square degrees) of the Comptonization and Doppler parameters. Using this data we estimate the expected statistical properties of the kinetic and thermal SZ effect, averaging the results over the set of 8 random lines-of-sight to reduce field-to-field variance. We find that the mean y distortion is systematically higher (up to 15%) in the EDE models with respect to the standard ΛCDM cosmology, for otherwise equal cosmological parameters. The distribution of the pixel values in the thermal SZ effect is close to a log-normal, and the bulk of the signal is contributed across a broad range of redshifts out to 1.5. It is remarkable that, unlike ΛCDM the EDE models have a non-negligible contribution even at $z > 2$. The kinetic SZ effect has a mean close to zero, a nearly Gaussian distribution, and it is dominated by the contribution of high redshift sources. The effect is stronger in EDE models, but it is degenerate with cosmological parameters, in particular with σ_8.

The maps of the thermal SZ effect are dominated by discrete sources. We extracted a catalogue of objects from the 2D images using the software SExtractor and then associated to each of the bright sources a massive halo in the underlying three-dimensional simulation catalogues. We derive a matched sample that is

$\sim 90\%$ complete down to $M = 10^{13}h^{-1}\mathrm{M}_\odot$ and has less than 5% contamination by false detections. Examining the plain number count in the different models, we estimate an increase in the cumulative number counts for the EDE cosmologies up to 20% for the most massive clusters. However, the number of detections even doubles with respect to ΛCDM when we consider only halos in the redshift interval $2 < z < 3$. This result clearly indicates that follow-up optical observations for the determination of the redshifts of massive clusters could make it possible to constrain the cosmological parameters up to the precision necessary to discriminate between ΛCDM and EDE models.

We adopt a limiting flux of $5\,\mathrm{mJy}$ for predicting the expected number and redshift distribution of sources that will be observed by the SPT cluster survey. The effects of the different dark energy models are in general negligible at very low redshift, as confirmed by the study of the mass function distribution in EDE cosmology. Starting from $z > 0.2$, however, we observe an increase in the total comoving abundance of objects that can be detected, due to the fact that increasing the contribution of dark energy slows down structure growth and flattens the redshift distribution of objects. However, the volume element, which is larger in the ΛCDM model, tends to offset this increase, making the net total effect quite small, at variance with what was predicted by analytical models (Bartelmann et al., 2006; Waizmann and Bartelmann, 2009). The differences between the cosmologies never exceed 20%, and are only slightly amplified when a sample of clusters with stricter mass limits is considered. If the local cluster abundance is not known accurately, the sensitivity due to the cosmology, in particular the combined effects of variations in σ_8, h and Ω_m, can easily overcome the differences due to the dark energy physics.

Another interesting aspect that merits investigation is whether the standard scaling laws used to convert the observables into physical quantities like mass are still valid in general dark energy cosmologies. We find that the best fit slope and normalization of the Comptonization-mass relation of all the models studied here is consistent with the results for ΛCDM. This closely matches the outcomes of previous works (Nagai, 2006; Sehgal et al., 2009). All models follow the self-similar expectation accurately, both when we compute the flux directly by summing up the contribution of the gas particles in the simulations, or when we compute it from the 2-dimensional maps. These findings suggest that differences in the virial overdensity of the EDE halos must be very small and do not matter as far as the scaling relations are concerned. Reassuringly, this supports the validity of cosmological constraints derived from cluster counts that use SZ decrements combined with the scaling relations.

To asses the impact of the definition of the cluster mass on the Y-M relation, we compute the scatter around the fitted power law for different combinations of Y_Δ- M_Δ, where Δ designates the overdensity relative to the critical density, which we vary between 50 and 2500. In each case we integrated the SZ flux within the

2D radius that corresponds to the 3D radius of the chosen fiducial overdensity. We find that the deviations with respect to the power law are smallest in proximity of the virial radius for both the mass and the flux values, with a minimum occurring for $\Delta_M = \Delta_Y = 300$. This result is consistent with indications that at larger radii there is a better correlation between mass and the Comptonization parameter (Motl et al., 2005; Hallman et al., 2006), but does not confirm a more recent finding that indicated that the least scatter is always obtained when the flux is measured at smaller radii than the mass (Shaw et al., 2009). However, we note that deviations from isothermality and hydrostatic equilibrium can have a strong impact on the Y-M relation. If we restrict the sample to smaller variations in the halo host concentrations and the fraction of substructures we find a significantly reduced scatter at small radii in the $\Delta_Y - \Delta_M$ plane.

Our SZ power spectrum analysis shows that the thermal SZ effect dominates the primary CMB anisotropies for $l \geqslant 2000$, and is about one order of magnitude larger than the kinetic one. We find an increase in the power of both signals in early dark energy cosmologies, but the maximum values are still below current observational measurements of the small scale anisotropy with the BIMA, CBI and ACBAR instruments. In fact, the dependence on dark energy is very weak when compared to the one on σ_8, which must be independently estimated to disentangle the influence of dark energy models. The differences between the ΛCDM and the EDE1 cosmologies, which represent the two most extreme cases, is a factor 1.54 for the thermal SZ power spectrum and a factor 1.37 for the kinetic one. The degeneracy among the models is reduced when only the high redshift signal is considered in the computation of the power spectrum. It is interesting to remark that the relative ordering of the cosmological models and thus the differences with respect to the ΛCDM case directly reflect the behavior of the Hubble expansion rate and depend only marginally on the growth rate, especially when we consider the total coadded maps that are dominated by low redshift objects. Naturally, there is some dependence of the SZE signal on the details of the ICM physics (heating, cooling, conduction) that we have not taken into consideration in this analysis, but it appears unlikely that these extra physics will substantially increase the relative differences between the models we have found.

In conclusion, our analysis confirms the power of the SZ effect as a probe to distinguish early dark energy cosmology, in particular with respect to the number of SZ clusters that are observed at high redshift. However, the degeneracy with other cosmological parameters is severe and could compromise the ability of future SZ cluster surveys, like those carried out at the SPT, or of power spectrum measurements, to derive robust statements about the dark energy content and its evolution. In any case, the full realization of this potential requires not just an understanding of the observational selection effects and uncertainties, but it is also essential to incorporate information from multiple observables in order to constrain the early

dark energy. Our calculations underscore the importance of limiting the uncertainties in other cosmological parameters, especially σ_8, before strong constraints on dark energy become possible. To distinguish reliably among the rich set of possible dark energy scenarios requires major advances in several cosmological probes (BAO data, CMB observations, supernovae calibrations), especially for models like the ones we have studies, which for extended periods of time behave very similarly to the cosmological constant in ΛCDM.

On the positive side, our results imply that the integrated Comptonization is a good indicator of the cluster mass also in non-standard dark energy cosmologies, and residual uncertainties in the Y-M relation can be removed with an accurate study of the cluster sample properties and projection effects. Thus surveys based on the SZ effect will definitely open a new window onto the high redshift Universe, thanks to the unique redshift-independence of the SZ selection, and they will have an invaluable role for 'precision' cosmology, even if they alone may not be able to solve the dark energy conundrum.

4

Large-scale non-Gaussian mass function and halo bias

4.1 Introduction

Constraining primordial non-Gaussianity offers a powerful test of the generation mechanism of cosmological perturbations in the early universe. While standard single-field models of slow-roll inflation lead to small departures from Gaussianity, non-standard scenarios allow for a larger level of non-Gaussianity (Bartolo et al., 2004). The standard observables to constrain non-Gaussianity are the Cosmic Microwave Background (CMB) and the Large Scale Structure (LSS) of the Universe. A powerful technique is based on the abundance (Koyama et al., 1999; Robinson et al., 2000; Matarrese et al., 2000; Verde et al., 2001; Lo Verde et al., 2008) and clustering (Grinstein and Wise, 1986; Matarrese et al., 1986; Lucchin et al., 1988) of rare events, such as dark matter density peaks, as they trace the tail of the underlying matter distribution. Theoretical predictions on various observational aspects of non-Gaussianity have been extensively tested against N-body simulations, leading to different and sometimes conflicting results (Kang et al., 2007; Grossi et al., 2007; Dalal et al., 2008; Desjacques et al., 2009; Pillepich et al., 2008).

Dalal et al. (2008) and Matarrese and Verde (2008) showed that primordial non-Gaussianity affects the clustering of dark matter halos inducing a scale-dependent bias on large scales. Not only this effect has been already exploited to place stringent constraints on non-Gaussianity (Slosar et al., 2008; Afshordi and Tolley, 2008), but also it is particularly promising for constraining non-Gaussianity from future surveys, which will provide a large sample of galaxy clusters over a volume comparable to the horizon size (e.g., DES, PanSTARRS, BOSS, LSST, ADEPT, EUCLID)

(Dalal et al., 2008; Carbone et al., 2008b; Afshordi and Tolley, 2008; Seljak, 2009). Bartolo et al. (2005) showed that even for small primordial non-Gaussianities, the evolution of perturbations on super-Hubble scales yields extra contributions. The amplitude of these contributions is comparable to the forecasted errors of some planned surveys, opening up the possibility of measuring them.

In light of this, it is important to use N-body experiments to test the validity of theoretical predictions for halo-bias in non-Gaussian framework. Indeed, all proposed analytic biasing expressions have been derived in the extended Press-Schechter framework which assumes spherical collapse dynamics, sharp k-space filtering and Gaussian initial conditions. The validity of the extrapolation of the extended Press-Schechter approach to the non-Gaussian case can be tested independently by considering also the halo mass function. It is thus also important to test and calibrate on N-body simulations the predictions of the non-Gaussian halo mass function (Kang et al., 2007; Grossi et al., 2007; Dalal et al., 2008) and of the non-Gaussian halo bias simultaneously. This is what we set out to do here.

In this Chapter we start by reviewing the analytic predictions for the Gaussian and non-Gaussian halo abundance and clustering (§2). In §3 we describe the numerical simulations with Gaussian and non-Gaussian initial conditions. In §4 we present the test for the non-Gaussian mass function. In §5 and 6 we test the analytic predictions of Gaussian and non-Gaussian large scale bias against N-body simulations. In §7 we compare our results with the literature. Finally, we conclude in §8.

4.2 Formulation of the non-Gaussian halo abundance and clustering

Deviations from Gaussian initial conditions are commonly parametrized in terms of the dimensionless f_{NL} parameter (Salopek and Bond, 1990; Gangui et al., 1994; Verde et al., 2000; Komatsu and Spergel, 2001):

$$\Phi = \phi + f_{\mathrm{NL}}(\phi^2 - \langle \phi^2 \rangle),$$ (4.1)

where Φ denotes the gravitational potential and ϕ is a Gaussian random field. As noted by e.g., Lo Verde et al. (2008), Afshordi and Tolley (2008) and Pillepich et al. (2008), different authors use different conventions. Here Φ denotes Bardeen's gauge-invariant potential which, on sub-Hubble scales, reduces to the usual Newtonian peculiar gravitational potential but with a negative sign. In addition, there are two conventions for normalizing Eq. (4.1): the LSS and the CMB one. In the LSS convention Φ is linearly extrapolated at $z = 0$. In the present Chapter we use this convention. In the CMB convention Φ is instead primordial: thus $f_{\mathrm{NL}} = [g(z = \infty)/g(0)]f_{NL}^{CMB} \sim 1.3 f_{NL}^{CMB}$, where $g(z)$ denotes the linear growth suppression factor

in non Einstein-de-Sitter Universes.

4.2.1 Formulation of the non-Gaussian mass function: Extended Press-Schechter approach

In the Press-Schechter framework, one considers the density contrast field evaluated at some early time, far before any scale of interest has approached the nonlinear regime, but extrapolated to the present day using linear perturbation theory. Then one considers the height of the critical density threshold as a function of time. In that way, the collapse of a halo at redshift $z \neq 0$ corresponds to the $z = 0$ density fluctuation crossing a barrier of height $\delta_c(z) = \Delta_c D(z = 0)/D(z)$, where $\Delta_c \sim \delta_c(z = 0)$ (this is an equality only in an Einstein de Sitter Universe); we use $D(z = 0) = 1$, $D(z) = g(z)/g(0)(1+z)^{-1}$. We should recall here that, even in linear theory, the normalized skewness of the density field, $S_3 \equiv \langle \delta^3 \rangle / \langle \delta^2 \rangle^2$, depends on redshift $\propto 1/D(z)$, however in the Press-Schechter framework one should use the linear $S_3(z = 0)$, in what follows $S_3 \equiv S_3(z = 0)$. Note also that in general the skewness can be written as $S_3 \equiv f_{\rm NL} S_3^{(1)}$, where $S_3^{(1)}$ denotes the skewness in units of $f_{\rm NL}$, care must be exercised in the interpretation of $f_{\rm NL}$: if $S_3^{(1)}$ is that of the density field linearly extrapolated at $z = 0$, f_{NL} must be the LSS one and *not* the CMB one.

Generalization of the mass function to non-Gaussian initial conditions within the Press-Shechter formalism has been presented in Matarrese et al. (2000) and Lo Verde et al. (2008). Both references start by computing an expression for the non-Gaussian probability density function of the smoothed dark matter density field, then obtain the level excursion probability. In the Press-Shechter approach the mass derivative of the level excursion probability is the key ingredient to obtain the mass function expression and is the term that gets modified in the presence of primordial non-Gaussianity. In this derivation, several approximations are made. Both approaches assume that deviations from Gaussianity are small.

Matarrese et al. (2000) use first the saddle-point approximation to compute the level excursion probability and then truncate the resulting expression at the skewness. They obtain:

$$
n(M, z) = 2 \frac{3 H_0^2 \Omega_{m,0}}{8 \pi G M^2} \frac{1}{\sqrt{2\pi}\sigma_M} \exp\left[-\frac{\delta_*^2}{2\sigma_M^2}\right] \times \tag{4.2}
$$

$$
\left| \frac{1}{2} \frac{\delta_c^2}{3\sqrt{1 - S_{3,M}\delta_c/3}} \frac{dS_{3,M}}{d\ln M} + \frac{\delta_*}{\sigma_M} \frac{d\sigma_M}{d\ln M} \right|
$$

where σ_M denotes the *rms* value of the density field, the subscript M denotes that the density field has been smoothed on a scale $R(M)$ corresponding to $R(M) = [M3/(4\bar\rho_M)]^{1/3}$, and $\delta_* = \delta_c \sqrt{1 - \delta_c S_{3,M}/3}$.

Lo Verde et al. (2008) instead first approximate the probability density function

using the Edgeworth expansion, then perform the integral of the level excursion probability exactly on the first few terms of the expansion. They obtain:

$$
\begin{aligned}
n(M, z) \;\; = \;\; & 2 \frac{3 H_0^2 \Omega_{m,0}}{8 \pi G M^2} \frac{1}{\sqrt{2\pi} \sigma_M} \exp\left[-\frac{\delta_c^2}{2\sigma_M^2} \right] \times \\
& \left[\frac{d \ln \sigma_M}{dM} \left(\frac{\delta_c}{\sigma_M} + \frac{S_{3,M} \sigma_M}{6} \left(\frac{\delta_c^4}{\sigma_M^4} - 2\frac{\delta_c^2}{\sigma_M^2} - 1 \right) \right) \right. \\
& \left. + \frac{1}{6} \frac{dS_{3,M}}{dM} \sigma_M \left(\frac{\delta_c^2}{\sigma_M^2} - 1 \right) \right]
\end{aligned}
\tag{4.3}
$$

Note that in the limit of small non-Gaussianity and rare events, the ratio of the non-Gaussian mass function to the Gaussian one for both expressions reduces to:

$$
\mathcal{R}_{NG} \equiv \frac{n(M, z | f_{\mathrm{NL}})}{n(M, z | f_{\mathrm{NL}} = 0)} \longrightarrow 1 + S_{3,M} \frac{\delta_c^3}{6\sigma_M^2} .
\tag{4.4}
$$

It is important to bear in mind that in Eqs. (4.3)-(4.4), the redshift dependence is enclosed only in δ_c (and not in S_3). In the spirit of the "CMB" convention instead, where the gravitational potential is normalized deep in the matter era, one should make sure that all the relevant quantities are correctly extrapolated linearly at $z = 0$, keeping in mind that the gravitational potential slowly evolves in a non Einstein de Sitter Universe.

The major limitations in both derivations are the assumption of spherical collapse and the sharp k-space filtering. In addition, the excursion set improvement on the interpretation of the original Press-Shechter swindle, suggests that this derivation relies on the random-phase hypothesis Sheth (1998), which is clearly not satisfied for non-Gaussian initial conditions even for sharp k-space filtering.

Verde et al. (2001) and Lo Verde et al. (2008) addressed this issue by using the analytical approach to compute the fractional non-Gaussian *correction* to the Gaussian mass function $\mathcal{R}_{NG}$, and used the Sheth and Tormen (1999) mass function to model the Gaussian mass function. This approach is potentially promising, but needs to be calibrated on numerical experiments.

In particular, one may argue that the same correction that in the Gaussian case modifies the collapse threshold and thus the form of the mass function from Press and Schechter (1974) to Sheth et al. (2001) and Sheth and Tormen (2002), may apply to the non-Gaussian correction. In the Gaussian case this is usually referred to as the correction due to ellipsoidal collapse (Lee and Shandarin, 1998). While this interpretation has recently been disputed (see e.g., Robertson et al. (2009)), we will maintain the same nomenclature here. For rare events, high peaks ($\delta_c/\sigma_M \gg 1$) and small f_{NL}, this is equivalent to lower δ_c by a factor $\sqrt{q}$ with $q = 0.75$.

In summary we propose that the non-Gaussian mass function $n(M, z, f_{NL})$ should be re-written in terms of the Gaussian one $n_G^{sim}(M, z)$ –given by tested fits to sim-

ulations e.g., Sheth and Tormen (1999); Reed et al. (2003); Warren et al. (2006); Jenkins et al. (2001)–, multiplied by a non-Gaussian correction factor:

$$n(M, z, f_{NL}) = n_G^{sim}(M, z) \times \mathcal{R}_{NG}(M, z, f_{NL}) \qquad (4.5)$$

where $R_{NG}(M, z, f_{NL})$ takes two different forms in the Matarrese et al. (2000) and Lo Verde et al. (2008) approximations. For the Matarrese et al. (2000) case

$$R_{NG}(M, z, f_{NL}) = \exp\left[\delta_{ec}^3 \frac{S_{3,M}}{6\sigma_M^2}\right] \times \qquad (4.6)$$

$$\left|\frac{1}{6} \frac{\delta_{ec}^2}{\sqrt{1 - \delta_{ec}S_{3,M}/3}} \frac{dS_{3,M}}{d\ln\sigma_M} + \frac{\delta_{ec}\sqrt{1 - \delta_{ec}S_{3,M}/3}}{\delta_{ec}}\right|$$

and for the Lo Verde et al. (2008) case:

$$R_{NG}(M, z, f_{NL}) = 1 + \frac{1}{6}\frac{\sigma_M^2}{\delta_{ec}} \times \qquad (4.7)$$

$$\left[S_{3,M}\left(\frac{\delta_{ec}^4}{\sigma_M^4} - 2\frac{\delta_{ec}^2}{\sigma_M^2} - 1\right) + \frac{dS_{3,M}}{d\ln\sigma_M}\left(\frac{\delta_{ec}^2}{\sigma_M^2} - 1\right)\right]$$

where δ_{ec} denotes the critical density for ellipsoidal collapse, which for high peaks is $\delta_{ec} \sim \delta_c\sqrt{q}$ with $q = 0.75$.

4.2.2 Formulation of the non-Gaussian large scale halo bias

For the case of "local" primordial non-Gaussianity Eq. (4.1), the analytical expression for the large-scale non-Gaussian bias has been derived in five different ways, obtaining always basically the same result. Dalal et al. (2008) considered the Laplacian of Φ in the vicinity of rare, high peaks, considering that the resulting $\nabla^2\Phi$ is proportional to the peaks overdensity; they also generalized to local non-Gaussianity the Kaiser (1984) argument of high-peaks bias in order to derive its non-Gaussian version. Matarrese and Verde (2008) derived the halo bias formula in general non-Gaussian cases specified by an expression for the bispectrum. Slosar et al. (2008) adopted the peak-background split approach (Cole and Kaiser, 1989) for the local non-Gaussian case, showing that the resulting expression relies on the universality of the mass function. Afshordi and Tolley (2008) instead interpreted non-Gaussianity as a modification of the critical density for collapse, in the framework of ellipsoidal collapse. Finally, McDonald (2008) used a renormalized perturbation theory approach to consider at the same time non-linear bias, second-order gravitational evolution and local form of non-Gaussianity. It is encouraging that these different approaches yield a consistent result for the correction to the Gaussian Lagrangian halo bias b_L^G:

$$\frac{\Delta b}{b_L^G} = 2f_{\mathrm{NL}}\delta_c(z)\alpha_M(k) \qquad (4.8)$$

169

where $\alpha_M(k)$ encloses the scale and halo mass dependence –see e.g., Eq. (13) and Fig. 3 of Matarrese and Verde (2008)–. Also in this case the density field is the one extrapolated linearly at $z = 0$, and α_M does not depend on redshift.

Making the standard assumption that halos move coherently with the underlying dark matter, the Lagrangian bias is related to the Eulerian one as $b = 1 + b_L$.

The approximations used to derive this equation are Press-Schechter approach, linear bias, small non-Gaussianity, and in most cases spherical collapse and identification of peaks with halos. It is therefore important to test the validity of Eq. (4.8), with simulations and see if any correction factor needed is indeed due to account for non-spherical collapse. Following the derivation of Matarrese and Verde (2008) we recognize that the correction to the 2-point halo correlation function due to non-Gaussianity (their Eq. (6)) is multiplied by ν^3/σ_M^3 with $\nu = \delta_c/\sigma_M$. In this factor we recognize one Lagrangian Gaussian bias factor to the second power and an extra δ_c/σ_M^2, which denominator was absorbed in the form factor. Recall that, as discussed in §2.1, for "ellipsoidal collapse" and rare events, the Lagrangian Gaussian bias is corrected as $\nu/\sigma_M \longrightarrow q\nu/\sigma_M$ (see Eq. (4.11) below, for high ν). However, the remaining factor is also a Gaussian bias and it should also be corrected by the q-factor.

We conclude that the "non-spherical collapse" modifies Eq. (4.8) to be:

$$\frac{\Delta b}{b_L^G} \simeq 2f_{\mathrm{NL}}\delta_c(z)\alpha_M(k)q \,. \tag{4.9}$$

Note that Afshordi and Tolley (2008) arrived to a similar yet not identical expression when considering ellipsoidal collapse, i.e. they suggest that δ_c should be substituted by the critical density of Sheth et al. (2001), which in our limit would correspond to use $\sqrt{q}$ rather than q in Eq. (4.9).

In §4.6 we will show that Eq. (4.9) correction fits well the simulations.

4.3 N-body simulations

The deviations from Gaussianity we are after become important on very large scales $k \lesssim 0.03\mathrm{h/Mpc}$ and for massive halos. Therefore, one needs to perform N-body simulations on very large boxes, yet with enough resolution to identify massive virialized structures at different redshifts.

Suitable initial conditions have been set up following the method described in Grossi et al. (2008) (see also Grossi et al. (2007); Viel et al. (2009)). In brief, a random realization of a Gaussian gravitational potential, Φ_{L}, normalized to be the one linearly extrapolated at $z = 0$, is generated in Fourier space, then it is inverse-Fourier transformed back to real space and added to the non-Gaussian term, $\Phi_{\mathrm{NL}} = f_{\mathrm{NL}} \left(\Phi_{\mathrm{L}}^2 - \langle \Phi_{\mathrm{L}}^2 \rangle \right)$. The resulting field $\Phi_L + \Phi_{\mathrm{NL}}$ that is linear and at $z = 0$, is
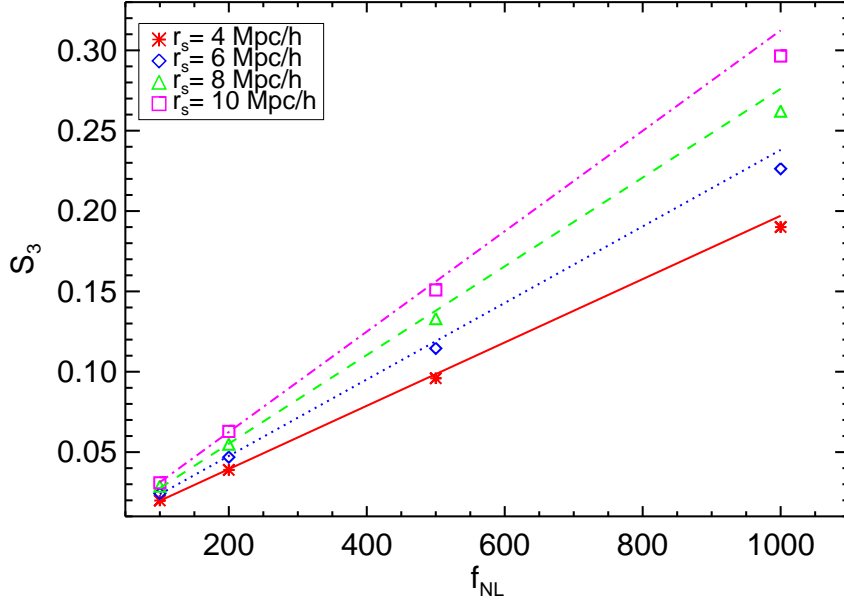
Figure 4.1 Skewness S_3 of the smoothed initial density field for $f_{\rm NL} = 100, 200, 500, 1000$. Symbols show the numerical results of the initial conditions code (averaged over 5 realizations) and are plotted against the analytical predictions for smoothing radii $r_s = 4, 6, 8, 10 Mpc/h$ of a spherical top-hat filter.
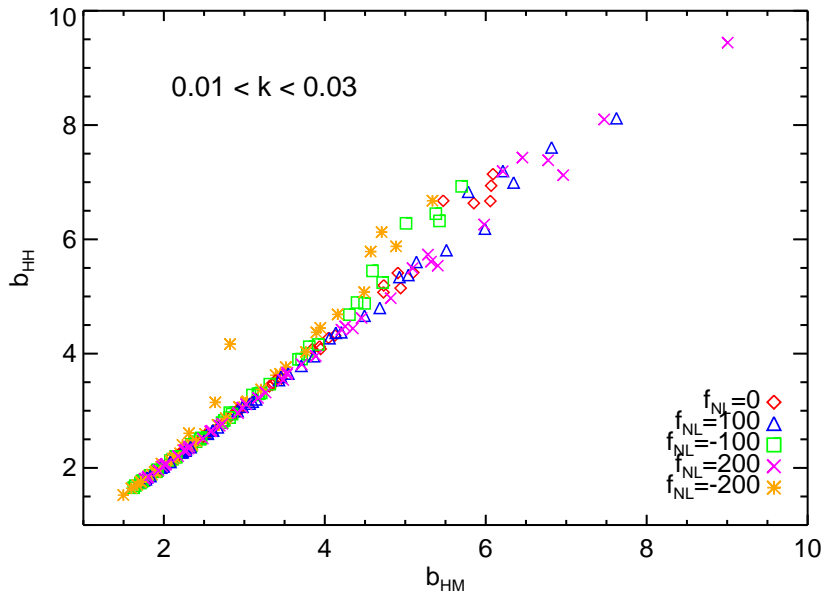
Figure 4.2 The bias of the halo power spectrum b_{hh} compared to the bias of the cross (halo-matter) power spectrum b_{hm}. As expected, when the number density of halos is high there is good agreement between the two quantities. At low halo number densities the two quantities are affected differently by shot noise, with b_{hm} being the least affected.

transformed back in Fourier space. We eventually modulate the power-law spectrum using the transfer function and compute the corresponding density field, which we then scale back to the initial conditions redshift ($z = 60$). The corresponding gravitational potential is then used to displace particles according to the Zeldovich approximation. This method allows one to simulate non-Gaussian models having power spectra which are all consistent with that of the Gaussian case and was already used by Viel et al. (2009).

In order to check the reliability of the initial conditions generation, we have performed a specific test: using 256^3 particles in a box of size 1000 Mpc/h, primordial density fields (extrapolated linearly at $z = 0$) were generated and smoothed using spherical top-hat filters of different radii $r_s = 4, 6, 8, 12$ Mpc/h. The smoothed skewness was then extracted from the fields and compared to the analytical prediction for $f_{\mathrm{NL}} = 100, 200, 500, 1000$, as shown in Figure 4.1.

The set of simulations used in this work assumes the 'concordance' ΛCDM model. We fix the relevant parameters consistently with those derived from the analysis of the WMAP 5-year data (Komatsu et al., 2009a): $\Omega_{m,0} = 0.26$ for the matter density parameter, $\Omega_{\Lambda,0} = 0.74$ for the Λ contribution to the density parameter, $h = 0.72$ for the Hubble parameter (in units of 100 km s^{-1} Mpc^{-1}). The initial power spectrum adopts the Cold Dark Matter (CDM) transfer function suggested by Eisenstein and Hu (1998), has a spectral index $n = 0.96$ and is normalized in such a way that $\sigma_8 = 0.8$. In all experiments, performed using the GADGET-2 numerical code (Springel, 2005), switching off the hydrodynamical part, we consider a box of (1200 Mpc/h)^3 with 960^3 particles: the corresponding particle mass is then $m \approx 1.4 \times 10^{11} h^{-1} M_\odot$. The gravitational force has a Plummer-equivalent softening length of $\epsilon_l = 25 h^{-1}$ kpc. The runs produced 15 outputs from the initial redshift ($z = 60$) to the present time. The 5 simulations consider different amounts of primordial non-Gaussianity, parametrized by the f_{NL} parameter: $f_{\mathrm{NL}} = 0$ (i.e. the reference Gaussian case) and $f_{\mathrm{NL}} = \pm 100, \pm 200$. The catalogues of dark matter haloes are extracted from the simulations using the standard friends-of-friends algorithm adopting a linking length of 0.2 times the mean interparticle distance; only objects with at least 32 particles are considered.

We thus measure the halo bias in the simulations as

$$b_s(k, M, z) = b_{hm} \equiv \frac{P_{hm}(k, z, M)}{P_{mm}(k, z)} \, , \tag{4.10}$$

where $P_{hm}(k, z, M)$ denotes the cross-power spectrum of dark matter with halos of mass M at scale k, and for the simulation snapshot at redshift z. Similarly $P_{mm}(k, z)$ denotes the dark matter power spectrum. Here and hereafter the subscript s denotes quantities measured from the simulation.

In principle, the quantity one is interested in would be the bias of the halo power spectrum $b_{hh} = \sqrt{P_{hh}/P_{mm}}$, but b_{hm} is a less noisy quantity (the shot noise of the
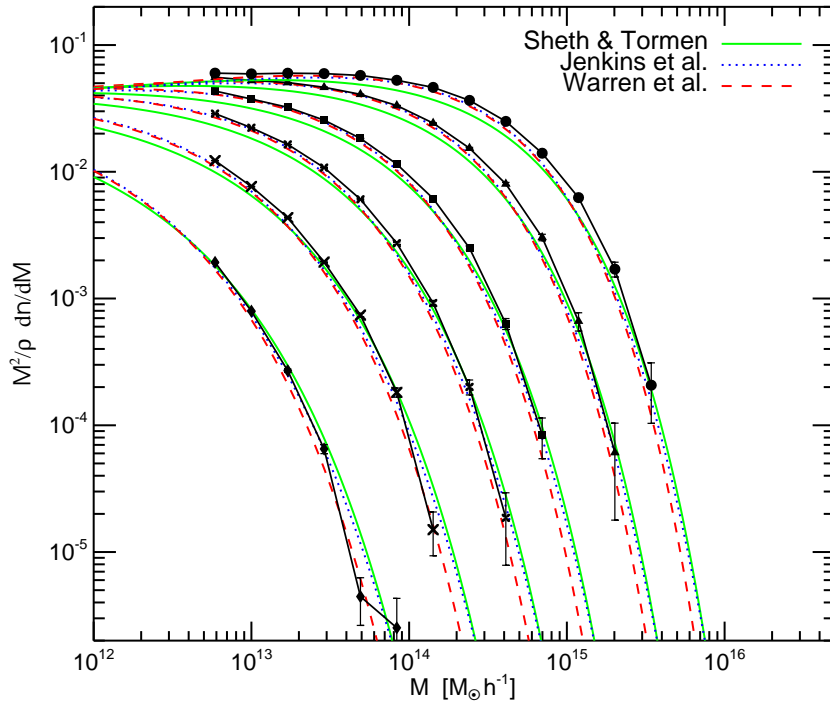
Figure 4.3 Multiplicity mass function for the Gaussian simulation computed using a Friends-of-Friends halo finder. Points denote the simulations results at different redshift: $z = 0, 0.44, 1.02, 1.53, 2.26$ and 3.23 (top to bottom). Solid (green) lines are the Sheth & Tormen (1999) formula, dashed (red) lines are the Warren et al. (2006) one and dotted (blue) are the Jenkins et al. (2001).
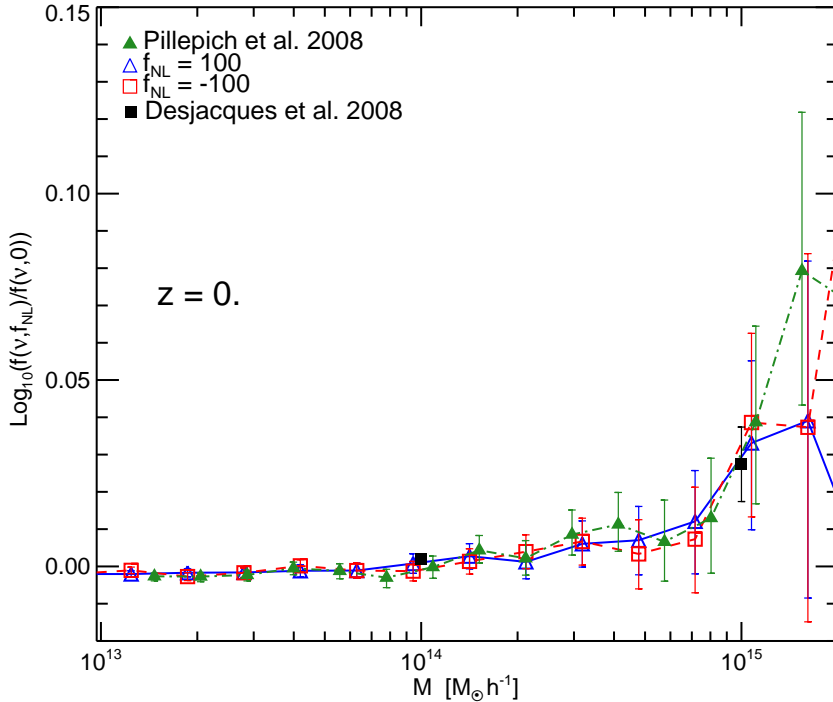
Figure 4.4 Comparison between the halo mass function recovered in our simulations with the work of Desjacques et al. (2009) and Pillepich et al. (2008) at $z = 0$. We show the ratio between our non-Gaussian and Gaussian simulation with $f_{NL} = \pm 100$, few points we read out from Figure 1 of Desjacques et al. (2009)(black points) at the values of ν corresponding to 1×10^{13}, 1×10^{14} and 1×10^{15} $M_{\odot}/h$ and the points from Pillepich et al. (2008). We plot the reciprocal of the results for $f_{NL} = -100$.

finite number of halos is greatly suppressed in the estimate of $P_{hm}(k)$). The quantity b_{hm} is not guaranteed to be identical to b_{hh} if bias has a stochastic component that does not correlate with the matter density field. In Fig. 4.2 we show that this is not the case and that there is good agreement on large scales between b_{hh} and b_{hm}, justifying using the less noisy b_{hm} as an estimator for b_{hh}.

4.3.1 Comparison with independent simulations

In Fig. 4.3 we show the mass function extracted from our Gaussian simulations at the following redshifts: $z = 0.0, 0.44, 1.02, 1.53, 2.26$ and 3.23. We also show three different theoretical predictions (calibrated on N-body simulations): Sheth and Tormen (1999), Jenkins et al. (2001) and Warren et al. (2006), solid, dotted and dashed lines respectively. There is good agreement even at high redshift.

Several groups recently presented N-body simulations, aiming at quantifying the effect of the non Gaussian initial conditions on the halo mass function (Dalal et al., 2008; Pillepich et al., 2008; Desjacques et al., 2009). All these results are obtained for similar cosmological parameters, so that we can compare estimates derived from
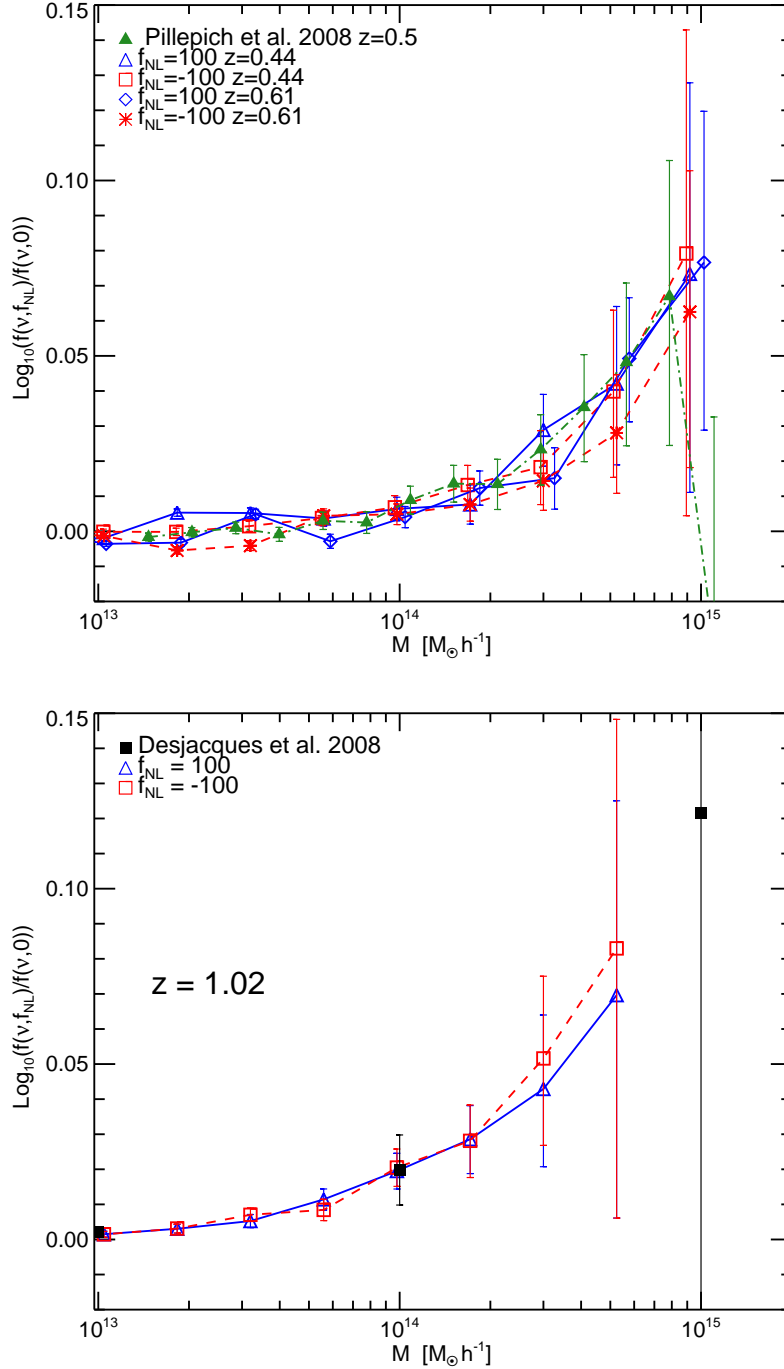
Figure 4.5 Comparison between the halo mass function recovered in our simulations with the work of Desjacques et al. (2009) and Pillepich et al. (2008). In the left panel we show the ratio between the non-Gaussian and Gaussian simulation at redshift 1 for our simulations with $f_{NL} = \pm 100$, three points we read out from Figure 1 of Desjacques et al. (2009)(black points) at the values of ν corresponding to 1×10^{13}, 1×10^{14} and 1×10^{15} $M_\odot/h$. We plot the reciprocal of the results for $f_{NL} = -100$. In the right panel we show the data of Pillepich, Porciani, Hahn (2008) at $z = 0.5$ and we compare them with our simulation results for the two closest available redshifts : $z = 0.44$ and $z = 0.61$ and with Desjacques et al. (2009). All points are rescaled to $|f_{NL} = 100|$ in our notation. The three independent simulations are in good agreement.

175

all the simulations directly. By comparing the results for the individual simulations at $z = 1$, $z \sim 0.5$ and $z = 0$ in Figures 4.4, 4.5 we demonstrate that these results are in agreement among the different groups, once the f_{NL} values are suitably converted to the same convention. Although all simulations use boxes of Giga parsec scales to explore the effect of non-Gaussian initial conditions at the high mass end, the statistical errors at the scale of massive clusters are still large. Therefore, we also report the reciprocal of the results obtained for negative f_{NL} so that they appear in the positive part of the plot, to give an intuitive feeling of the noise within the individual simulations.

In Figure 4.4, we show our simulation results for $f_{NL} = 100$ (blue triangles) and for $f_{NL} = -100$ (red squares) at $z = 0$ compared with data points from Figure 1 of Desjacques et al. (2009) (black points) at the values of ν corresponding to 1×10^{13},1×10^{14} and 1×10^{15} $M_\odot/h$ (as given in their figure caption). Note that, as Desjacques et al. (2009) use $f_{NL} = 100$ in the CMB convention for their simulations, we scaled the points down accordingly by a factor 1.3 to be comparable with our $f_{NL} = 100$. We also show the results for Pillepich et al. (2008) (green points). Here we again apply the re-scaling as before, as their f_{NL} of 82 would correspond to a f_{NL} of ~ 106 in the LSS notation.

In Figure 4.5, the left panel shows the results for Pillepich et al. (2008) (green points) at $z = 0.5$, and our points for the two closest available output times of our simulation ($z = 0.44$ and $z = 0.61$). The right panel shows the comparison at $z = 1$ between our points (blue triangles and red squares) and points from Desjacques et al. (2009) (black squares).

¿From this comparison we conclude that there is remarkable agreement between the three independents simulations, highlighting the robustness of the simulations results. The differences visible at some of the highest mass bins are not significant, given the large error bars present.

4.4 Mass function

We compare the halo mass function of the non-Gaussian simulations with the theoretical predictions of Eqs. (4.5), (4.6) and (4.7) that is, including our *ansatz* for the non-spherical collapse correction: $\delta_c \longrightarrow \sqrt{q}\delta_c$. For clarity we show here the non-Gaussian to Gaussian mass function ratio, i.e. the factor $R_{NG}(M, z)$. The comparison between theory and simulations results is shown in Fig. 4.6 for a few redshift snapshots and for $f_{NL} = \pm 100$, and in Fig. 4.7 for $f_{NL} = \pm 200$ for the same redshifts. Dashed lines are the mass function of Matarrese et al. (2000)–Eq. (4.6) – and dot-dashed lines are that of Lo Verde et al. (2008)–Eq. (4.7)–.

Contrary to Kang et al. (2007) and Dalal et al. (2008), we conclude that both Matarrese et al. (2000) and Lo Verde et al. (2008) are good descriptions of the non-
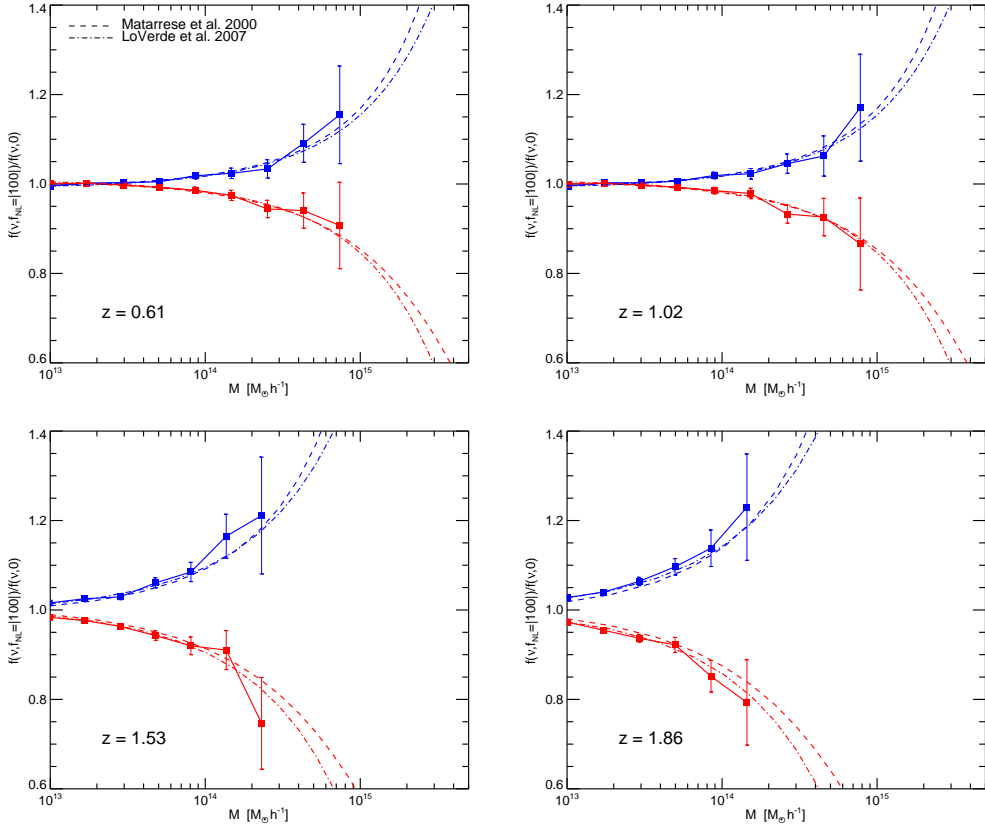
Figure 4.6 Ratio of the non-Gaussian ($f_{NL} = \pm 100$) to Gaussian mass function for different redshift snapshots: top left $z = 0.61$; top right $z = 1.02$; bottom left $z = 1.53$; bottom right $z = 1.86$. The dashed line is the mass function of Matarrese, Verde & Jimenez (2001) and the dot-dashed lines are that of LoVerde et al. (2008), both including the q-correction.
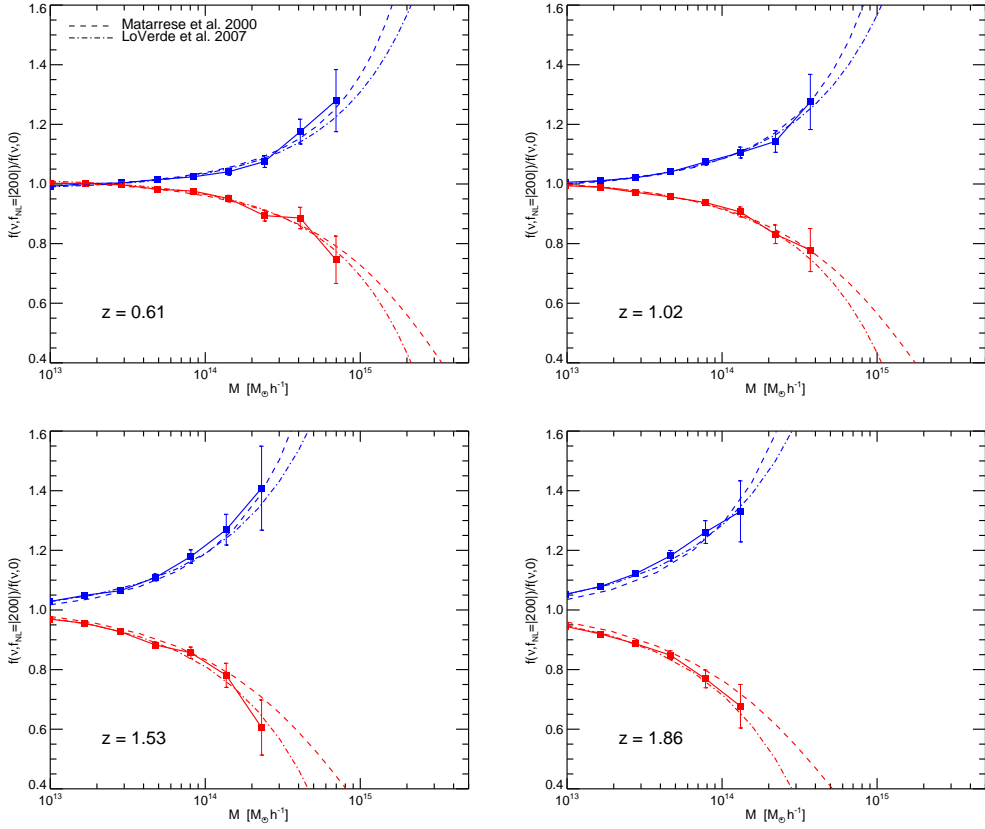
Figure 4.7 Ratio of the non-Gaussian ($f_{NL} = \pm 200$) to Gaussian mass function for different redshift snapshots: top left $z = 0.61$; top right $z = 1.02$; bottom left $z = 1.53$; bottom right $z = 1.86$. The dashed line is the mass function of Matarrese, Verde & Jimenez (2001) and the dot-dashed lines are that of LoVerde et al. (2008), both including our q-correction.

Gaussian correction to the mass function, once the correction for non-spherical collapse is included.

Figs. 4.6 and 4.7 seem to indicate that Lo Verde et al. (2008) may be a better fit for small masses and Matarrese et al. (2000) at high masses. This is not surprising: the Edgeworth expansion works well away from the extreme tails of the distribution (i.e. for moderate δ_c/σ_M), while the saddle-point-approximation used in Matarrese et al. (2000), is expected to work better at the very tails of the distribution (very high δ_c/σ_M). We expect that the mass function of Matarrese et al. (2000) will be a better fit at very high masses or larger f_{NL}. This will be further explored in future work.

4.5 Gaussian halo bias, and the effect of mergers

The large-scale, linear halo Eulerian bias for the Gaussian case is (Mo et al., 1997; Scoccimarro et al., 2001)

$$b^G = 1 + \frac{1}{D(z_o)}\left[\frac{q\delta_c(z_f)}{\sigma_M^2} - \frac{1}{\delta_c(z_f)}\right] + \tag{4.11}$$

$$\frac{2p}{\delta_c(z_f)D(z_o)}\left[1 + \left(\frac{q\delta_c^2(z_f)}{\sigma_M^2}\right)^p\right]^{-1},$$

where $q = 0.75$ and $p = 0.3$, account for non-spherical collapse and are a fit to numerical simulations. Here, σ_M denotes the *rms* value of the dark matter fluctuation field smoothed on a scale R corresponding to the Lagrangian radius of the halos of mass M; z_f denotes the halo formation redshift and z_o denotes the halo observation redshift. As we are interested in massive halos, we expect that $z_f \simeq z_o$. As the non-Gaussian halo bias correction is proportional to $b^G - 1$, the dependence of b^G on whether the selected halos underwent a recent merger (i.e. $z_f \sim z_o$) or are old halos (i.e. $z_f \gg z_o$) affects the amplitude of the non-Gaussian correction (Slosar et al., 2008; Carbone et al., 2008b). Before we trust our simulation to accurately describe the non-Gaussian halo bias we check whether we recover the Gaussian one and whether the linear halo bias approximation is a good description for the scales, redshifts and mass-ranges we are interested in. Gao et al. (2005) show that analytical predictions for the Gaussian halo bias are in reasonable agreement with simulations and that the bias for low-mass halos shows strong dependence on formation time but high mass halos (the ones we are interested in) do not. The halo bias for the Gaussian simulation and the comparison with the theory prediction is shown in Fig. 4.8. Except for the Gaussian halo bias $b_0^G \equiv 1 + \delta_c(z_o)/(\sigma_M^2 D(z_o))$ defined in Efstathiou et al. (1988a) and Kaiser (1984) indicated by the dotted (blue) line, the simulated data agree with the theoretical expectations at different redshifts. In particular, in Fig. 4.8, the black solid line represents the total Gaussian bias of
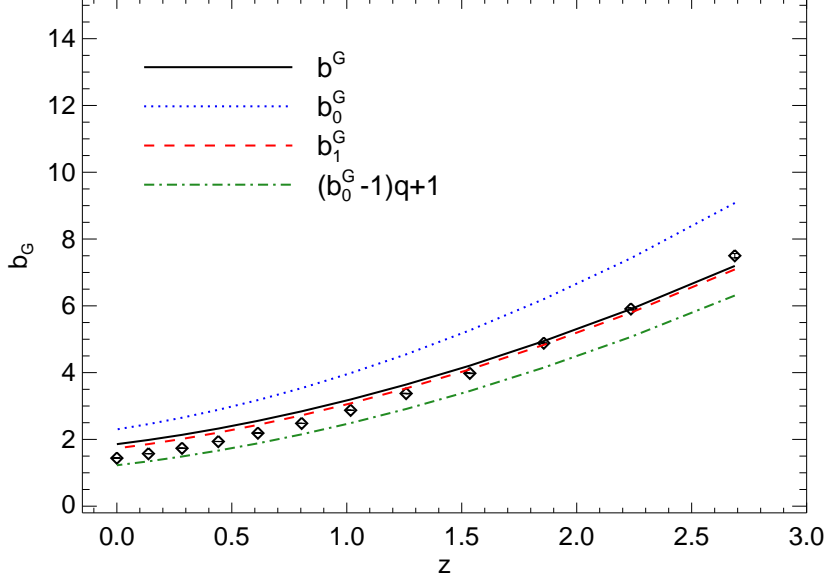
Figure 4.8 Black solid line: the large-scale Gaussian halo Eulerian bias b^G of Eq. (4.11). Blue dotted line: the Gaussian halo bias $b_0^G \equiv 1 + \delta_c(z_o)/(\sigma_M^2 D(z_o))$ as defined in Efsthatiou et al. (1988) and Kaiser (1984). Green dotted-dashed line: $1 + q(b_0^G - 1)$. Red dashed line: the contribution $b_1^G \equiv 1 + [q\delta_c(z_f)/\sigma_M^2 - 1/\delta_c(z_f)]/D(z_o)$ to the total bias of Eq. (4.11).

Eq. (4.11), the dashed (red) line represents the contribution from the first line of Eq. (4.11), and, finally, the dot-dashed (green) line is $1 + q(b_0^G - 1)$. The small difference when using $z_f \sim z_o$ implies that, for the Gaussian halo bias of very massive halos ($M > 10^{13} M_\odot$), it is reliable to assume that the correction from the "non-spherical collapse" can be encapsulated in the factor q in front of $\delta_c(z_o)/(\sigma_M^2 D(z_o))$.

4.6 Non-Gaussian halo bias

Eq. (4.8) shows that the redshift and scale dependence of the non-Gaussian correction can be factorized as a term that depends only on redshift and one that depends only on k and M. The M-dependence is expected to be very weak at large scales ($k < 0.03$ h/Mpc). Here we will test the mass, scale and redshift dependence of the non-Gaussian halo bias and we calibrate its normalization on the simulations.

In Fig. 4.9 we show the dependence on halo mass of $\Delta b/b_L$. We define the quantity

$$\mathcal{R}(M) = \left(\frac{\Delta b}{b_L}\right)_s \left(\frac{\Delta b}{b_L}\right)_{theory}^{-1} , \tag{4.12}$$

where $(\Delta b/b_L)_{theory}$ is given by Eq. (4.8). To study the mass dependence, we evaluate the theory at fixed mass $\widehat{M} = 10^{14} M_\odot$. We compute the bias from the simulations taking halos in six different mass bins. Fig. 4.9 includes only scales
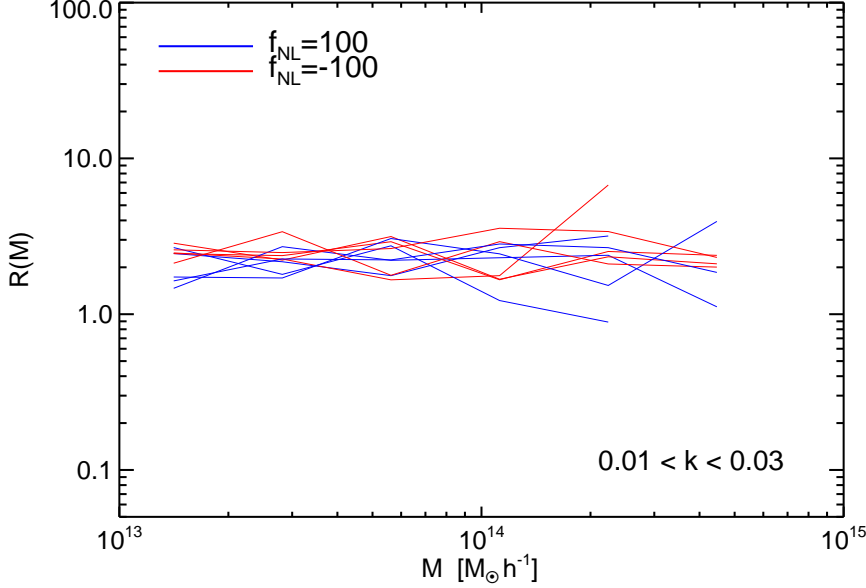
Figure 4.9 Weak mass dependence of $\Delta b/b$ at scales $k < 0.03$ h/Mpc. Different lines correspond to different redshift snapshots between $z = 0$ and $z = 1.5$. The overall normalization is arbitrary.

$k < 0.03$ h/Mpc, different lines correspond to different redshift snapshots between $z = 0$ and $z = 1.5$. As expected, there is no noticeable dependence on halo mass.

Having confirmed the expected weak dependence on halo mass for masses $M > 10^{13} M_\odot/h$ and on scales $k < 0.03$ h/Mpc, we can study the redshift and scale dependence of $\Delta b/b_L$, considering halos of different masses above $10^{13} M_\odot/h$.

The redshift dependence of $\Delta b/b_L$, $(\Delta b/b_L^G)_s[2f_{NL}\alpha_M(k)q]^{-1}$ is shown in Fig. 4.10 where $M > 10^{13} M_\odot/h$ and scales $k < 0.026$ h/Mpc were used. In applying the correction $\delta_c/\sigma_M^2 \longrightarrow q\delta_c/\sigma_M^2$ to $\Delta b/(b_G - 1)$ we have actually corrected b_0^G, i.e. we have employed the same approximation used for the green dot-dashed line of Fig. 8, giving Eq. (4.9). Eq.(9) in fact is only the consequence of our correction to the Gaussian halo bias. Note that the approximation $z_f \sim z_0$ we employed here is expected to hold for rare–massive–halos and Fig. 8 shows that this is a good approximation. A detailed study of the dependence of the non-Gaussian halo bias correction on the formation redshift of the halos will be presented elsewhere.

There seems to be an indication that the q-correction factor for the large-scale bias correction may slightly depend on the value of f_{NL}: in particular the figure shows that it could be slightly smaller than q for f_{NL} large and negative and smaller for f_{NL} large and positive. This is not unexpected: the presence of non-Gaussianity may alter the dynamics of non-spherical collapse (e.g., through tidal forces – see e.g., Desjacques (2008) – or by significantly changing the redshift for collapse with respect to the Gaussian case). At this stage, however, this trend is not highly significant and further study will be left to future work.
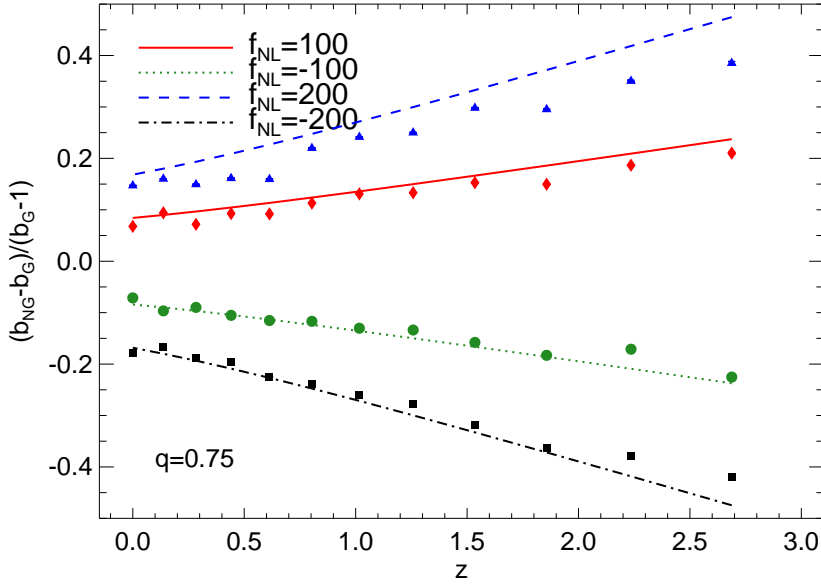
Figure 4.10 The redshift dependence of the non-Gaussian correction to the halo bias: points are the values measured from the simulations, lines are the theoretical predictions, Eq. (4.9). Only $k < 0.026\ h/Mpc$ were used.
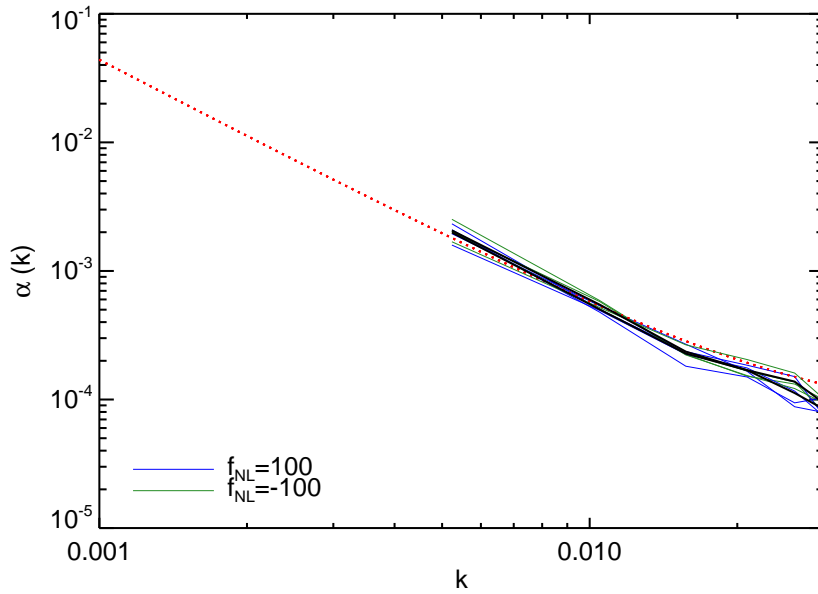
Figure 4.11 Scale dependence of Eq. (4.9). The thin lines correspond to different redshifts for halos with mass above $10^{13} M_\odot/h$ and the thick black line is their average. The dotted line is the theory prediction with $q = 0.75$. At $k > 0.03h/Mpc$ the effect of non-Gaussianity is very small and the measurement become extremely noisy.

Finally, we show the scale dependence of Eq. (4.9), $(\Delta b/b_L^G)_s[2f_{NL}\delta_c(z)q]^{-1}$, in Fig. 4.11. The thin lines correspond to different redshifts and the thick black line to their average. The dotted line is the theory prediction with $q = 0.75$. Note that there is an excellent agreement on the scales of interest, e.g., $k < 0.03\ h/\text{Mpc}$. On smaller scales the effect of non-Gaussianity is very small and the measurement become extremely noisy. These results are in qualitative agreement with the findings of Pillepich et al. (2008).

We conclude that Eq. (4.9), with $q \sim 0.75$, provides a good fit to non-Gaussian simulations.

4.7 Comparison with previous work

After the discussion of §2, it should be clear that if f_{NL}^{CMB} were used in the theoretical predictions or S_3 were *not* linearly extrapolated to $z = 0$, then any constraints on non-Gaussianity so obtained would have to be re-scaled by a factor ~ 1.3. This seems to be the case of some work in the literature. On the other hand the q-correction factor effectively introduces a re-scaling of a factor $\sim 0.75^{3/2} = 0.65$ for the mass function case and 0.75 for the bias case. It is a coincidence that, for the halo bias, $1.3 \times 0.75 \sim 1$, thus the f_{NL} normalization mistake cancels out with the spherical collapse approximation error. This fortuitous cancellation does not happen to the same level in the mass function $0.75^{3/2} \times 1.3 \sim 0.8$, explaining perhaps some of the claimed discrepancy of the simulations with the analytic mass function predictions, and the claimed agreement with the halo bias predictions. Another possible source of inaccuracy would be an inconsistent treatment of the redshift evolution of δ_c and S_3 (see discussion is §2).

In Fig. 4.12 we compare our theoretical predictions with the results presented in Pillepich et al. (2008) and Desjacques et al. (2009). The left panel shows our simulation results at $z = 0$ for $f_{NL} = \pm 100$ and our theoretical predictions. Additionally we show the fit presented by Pillepich et al. (2008), Eqs. (8) and (9), evaluated for the suitable values of f_{NL} accounting for the different notations for f_{NL}. We also adopt our cosmological parameters when converting σ_M to M. The right panel shows the simulation results presented in Pillepich et al. (2008) at z=0 and their fitting formula at $z = 0$ and $z = 1$. We over plot our theoretical models evaluated for their cosmological parameters and for the corresponding values of f_{NL}. Moreover we add the data points from Desjacques et al. (2009) for $z = 0$ and $z = 1$, suitably rescaled by the differences of the f_{NL} value used. The mass function fits of Fig. 12 differ for large masses, in the regime where simulations errors become large; the fits are however consistent given the individual points error-bars.

Our theoretical formulae for the non-Gaussian mass function (Eqs. 5, 6, 7) and for the non-Gaussian halo bias (Eq. 9) are physically motivated expressions that
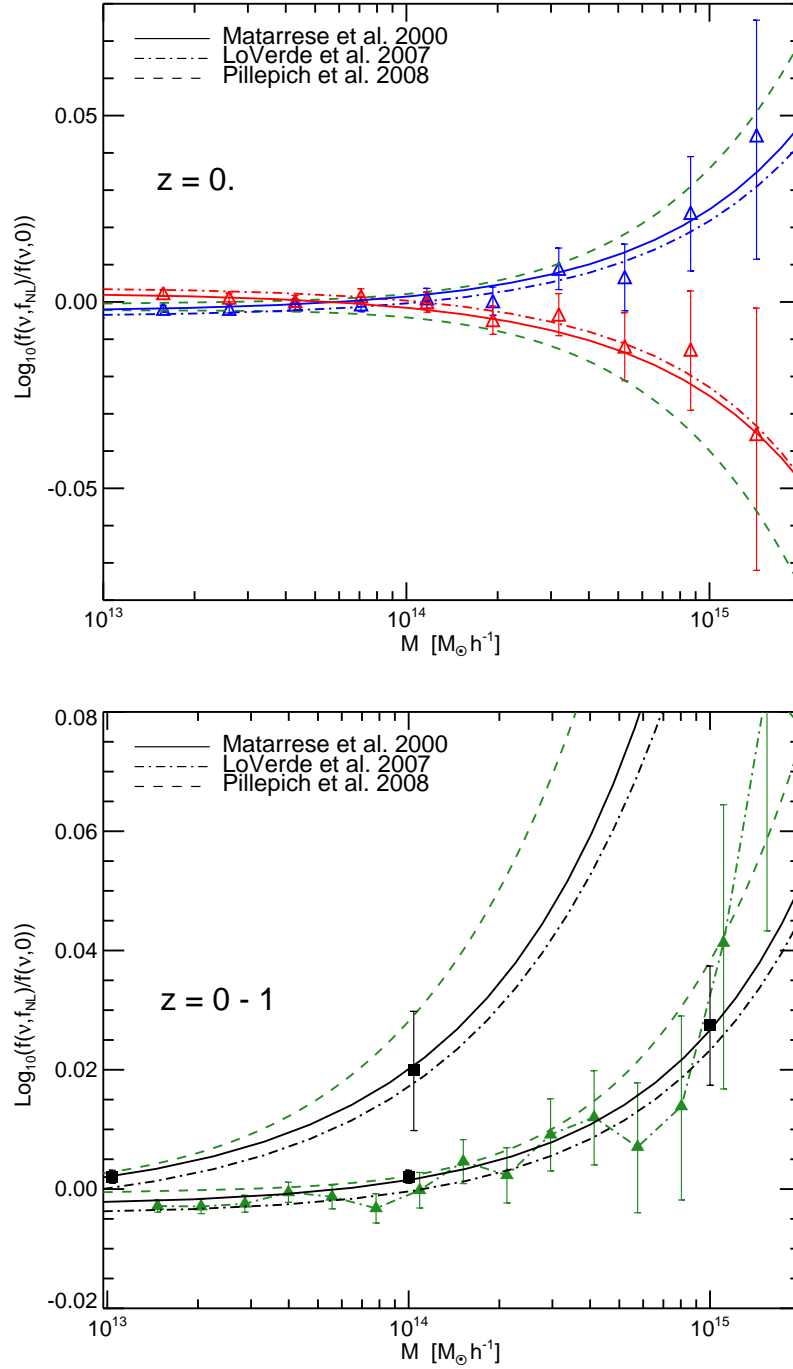
Figure 4.12 Left panel: comparison between simulations points and fits from this work and the polynomial fit of Pillepich et al. (2008). Right panel: Our correction to the Matarrese, Verde & Jimenez (2001) and LoVerde et al (2008) non-Gaussian mass function fits, the polynomial fit of Pillepich, Porciani & Zahn (2009) and points from Desjaques et al (2009) (black squares) and Pillepich, Porciani & Zahn (2009) (green triangles). See text for more details.

Table 4.1 Current and forecasted constraints on f_{NL}^{CMB}

Data/method	Measurements $f_{\mathrm{NL}}, 1-2\sigma$ errors	reference
Photo LRG–bias	$84^{+54+85}_{-101-331}$	Slosar et al. 2008
Spectro LRG–bias	$93^{+74+139}_{-83-191}$	Slosar et al. 2008
QSO - bias	11^{+26+47}_{-37-77}	Slosar et al. 2008
combined	37^{+23+42}_{-26-57}	Slosar et al. 2008
NVSS–ISW	$140^{+647+755}_{-337-1157}$	Slosar et al. 2008
NVSS–ISW	272 ± 127 (2-σ)	Afshordi&Tolley 2008

Data/method	Forecasts $\Delta f_{\mathrm{NL}}(1-\sigma)$	reference
BOSS–bias	18	Carbone et al 2008
ADEPT/Euclid–bias	1.5	Carbone et al. 2008
PANNStarrs–bias	3.5	Carbone et al. 2008
LSST–bias	0.7	Carbone et al. 2008
LSST-ISW	10.	Afshordi&Tolley 2008

have been tested on N-body simulations. They have the advantage over fitting formulae that they can be more robustly interpolated and extrapolated to cosmologies and parameters that have not been directly simulated and they are more robust over parameters ranges where the simulations have low signal-to-noise.

The q-correction we find here has implications for previously reported and forecasted constraints on non-Gaussianity. In Table 1 we report constraints on f_{NL} from the literature rescaled to f_{NL}^{CMB} and corrected for our factor q.

This confirms that constraints on f_{NL} achievable using the non-Gaussian halo bias are competitive with CMB constraints ($f_{NL} \sim 5$ for Planck and $f_{NL} \sim 3$ for a CMBPol-type mission, Babich and Zaldarriaga, 2004; Yadav et al., 2007).

4.8 Conclusions

We have considered $(1.2 \text{ Gpc/h})^3$ size and 960^3 particles N-body simulations with non-Gaussian initial conditions, with non-Gaussianity parameter $f_{NL} = \pm 100$, $f_{NL} = \pm 200$ and a reference Gaussian simulation ($f_{NL} = 0$). The clustering properties and the abundance of the simulation's halos were then compared with independent simulations and theoretical predictions. We find good agreement between different simulations, indicating that the initial conditions set-up is under control. We find that the Press-Schechter-based description of the non-Gaussian correction to the Gaussian mass function of Matarrese et al. (2000) and Lo Verde et al. (2008) is a good fit to the simulations, provided that:

a) The Press-Schechter-based description is used to compute the ratio between Gaussian and non-Gaussian mass function.

b) The critical density δ_c is corrected to account for non-spherical collapse.

This is summarized in our Eq. (4.5) and in Eqs. (4.6) and (4.7) for the non-Gaussian mass functions of Matarrese et al. (2000) and Lo Verde et al. (2008), respectively. For large thresholds this correction is equivalent to a re-scaling of the spherical collapse threshold $\delta_c \times \sqrt{q}$ where $q = 0.75$. The q-correction is thus equivalent to a reduction of f_{NL} by a factor ~ 1.5 because in the mass function, to leading order f_{NL} multiplies δ_c^3.

We find that the non-Gaussian halo bias prescription of Dalal et al. (2008), Matarrese and Verde (2008), Slosar et al. (2008) and Afshordi and Tolley (2008) provides a good description of the scaling of the large-scale halo clustering of the simulations. In particular, we have tested separately the predicted redshift, scale and f_{NL} dependence. The overall amplitude of the effect, however, should be corrected by a factor $\sim q$ which can also be understood in the context of ellipsoidal collapse or as a modification to the excursion set ansatz and the sharp-k space filtering (see Eq. (4.9)). There is an indication that this correction may be slightly dependent on f_{NL}. This is not unexpected, but the signal-to-noise of the effect is too small in the current simulations to draw robust conclusions. We also find that on large ($k < 0.03 \ h/\mathrm{Mpc}$) scales, as expected, the fractional correction to the non-Gaussian halo bias is independent of mass. On smaller scales a dependence on mass is expected, but the simulations do not have sufficient signal-to-noise to verify it. The q-correction to the non-Gaussian halo bias modifies current and forecasted constraints reported in the literature as indicated in our Table 1.

The formulae we presented here for the non-Gaussian mass function (Eq. 5, 6,7) and non-Gaussian halo bias (Eq. 9) are physically motivated expressions which provide good fits to a suite of N-body simulations. As such, they can be more robustly interpolated and extrapolated than simple fitting functions. We confirm that the non-Gaussian halo bias offers a robust and highly competitive test of primordial non-Gaussianity.

5

Concluding remarks

In a radical departure from its history, cosmology has developed into a precise science. Spurred by enormous advances in technology, we can now rigorously address the problems of the origin, evolution and fate of the Universe. The standard cosmological model is the first precise theory that keeps up with all the observational evidences we have and tries to make sense of them all. However, it leaves important questions unanswered.

Without doubt, the most pressing issues are the geometry and composition of our Universe, and the nature of the density perturbations that seeded all the structures we observe. In fact, our knowledge of the mass and energy content of the cosmos is still poor. All we can say is that most of the energy in the Universe is in the form of unknown and invisible components, namely dark matter and dark energy. Dark energy makes up a majority of the total content, and it is responsible for the acceleration of the cosmic expansion. The place of this component in the concordance model of cosmology is supported by several indirect lines of evidence, which, unfortunately, grant us almost no clue about its true identity. The challenge for the next decade is to investigate the very nature of dark energy in the search for a fundamental explanation to the current puzzle. Moreover, mapping the statistical properties of the primordial fluctuations in the density field is a key endeavour in our quest for understanding the dynamics of the early Universe. Despite the simplicity of the inflationary paradigm, the mechanism by which perturbations are generated is not yet fully established and various alternatives have been proposed. Convincing evidence against or for Gaussian initial conditions would rule out many scenarios and point us toward a physical theory for the origin of structures.

In this Thesis, we looked at the large-scale structure of the Universe in order to study in detail alternatives to the standard cosmological model. In fact, while some of the challenges to the current paradigm of structure formation may turn out to be only apparent, others could be real and drive fundamental adjustments

of the model. The main goal of our work has been to establish firm predictions for a range of viable cosmologies and to test well motivated theoretical hypothesis. We have studied the cosmological implications of a variety of early dark energy cosmologies, in search of the fundamental properties of quintessence. In this class of models, the dark energy can contribute a substantial fraction to the total energy density even at early times, and affects strongly the structure formation period. We also considered the effect of non-Gaussian features in the primordial fluctuation field on the late-time clustering of matter, modelling departures from Gaussianity with quadratic non-linearities quantified by the parameter f_{NL}. We made extensive use of numerical simulations to hunt for fingerprints of early dark energy and non-Gaussianity in the fine details of the cosmic structure formation. These simulations were crucial to test the results of more simplified analytic treatments and highlight cosmological probes which would be useful to distinguish the models we investigate from the vanilla ΛCDM scenario. In the following, we conclude the presentation of this Thesis by summarizing our main achievements and discussing their future prospects.

In the first part of this work, we have studied the impact of Early Dark Energy (EDE) on non-linear structure formation and we examined whether its contribution can be detected by statistical methods. Our particular interest has been to test if analytical predictions for the halo mass function still reliably work in such cosmologies, but we also investigated other aspects of structure formation. To this end we have extended the implementation of EDE to the simulation and initial condition codes and then carried out a series of N-body experiments to compare these models with a standard cosmology.

We began by studying the mass function statistic over the whole redshift range accessible with the accuracy required to make reliable predictions. Since our simulations were normalized to the same σ_8 today, their mass functions and power spectra agree very well at $z = 0$, while towards higher redshift we found significant differences, as expected due to the slower evolution of the linear growth factor in the EDE models compared to ΛCDM. Therefore, we can only hope to distinguish different cosmological models with very deep and accurate cluster surveys. In general, we observed that structures in EDE cosmologies have to form significantly earlier than in ΛCDM to reach the same abundance today. From a quantitative analysis, we found that the universality of the standard Sheth-Tormen formalism for estimating the halo mass function carries over to EDE models, at least at the 15% accuracy level that is reached also for the ordinary ΛCDM cosmology. This is a central result of our investigation, and disagrees with previous theoretical suggestions by Bartelmann et al. (2006) based on the generalized top-hat collapse model, which predicts that the virial overdensity and the linear threshold density for collapse should be strongly modified in EDE cosmologies. We concluded that, independently of the mass definition we consider, the constant standard value for the

linearly extrapolated density contrast can be safely used to predict the numerical results in EDE models.

We also investigated new ways to probe the mass function which are easily accessible by observational data and do not rely on the particular measurement procedure adopted to define a group mass. In particular, we showed that counting the number of halos as a function of the line of sight velocity dispersion (of subhalos or galaxies), both in simulations and observations, we can probe the growth of structures with redshift and so put powerful constraints on the equation of state parameter. This goal can be achieved by just identifying and computing groups in galaxy survey data such as DEEP2 (Davis et al., 2005), and by comparing them with mock catalogues from simulations. We found that the relative difference in the number of groups at a given redshift is amplified when we consider the velocity dispersion and is relatively insensitive to selection effects. Differences between the EDE models and the standard scenario can be demonstrated also by looking at the present day data, if we consider observables that are sensitive to the concentration distribution. Analysing the simulations, we noticed that EDE halos of a fixed mass have always a higher characteristic density, and therefore higher concentration, than their counterparts in a ΛCDM cosmology. Nevertheless, the differences are not very large and it will be difficult to measure them with direct observations.

On the other hand, comparing the EDE simulations with theory, we found that several analytic formulae, calibrated on the ΛCDM model, appear to hold equally well in generalized EDE models. Besides the existing fitting formula for the mass function, the Eke et al. (2001) model for the concentration relation describes the magnitude of the effect well in the generalized cosmologies. Specifically, we noticed that the change in the concentration normalization relative to the cosmological constant case is well represented by the ratio of the linear growth factor of different models at very high redshift, as suggested by Dolag et al. (2004). Finally, we tested the virial relation between mass and dark matter velocity dispersion for the EDE cosmologies, finding an excellent agreement with the results for a ΛCDM model as calibrated by Evrard et al. (2008). This is an additional proof that the differences, if any, in the virial overdensity of EDE halos should be small, and therefore the calibration of dynamical mass estimates from internal cluster dynamics does not need to be changed in these cosmologies.

To conclude, we found that the EDE component does not affect the fine details of the non-linear structure formation. This is basically good news because we can hence probe these alternative cosmologies by looking only at the evolution of the growth of the structures with time. It also reduces the degeneracy between the possible cosmological parameters that could vary for EDE. On the other hand, our numerical simulations clearly proved that the differences between EDE models and a ΛCDM cosmology are smaller than previously expected. This highlights the need to improve the accuracy of the next generation of simulations and observations, to

allow the different scenarios to be distinguished.

As part of our search for a sizable effect of the EDE component on the large-scale structure of the Universe, we directed the second part of this Thesis specifically to the study of the Sunyaev Zeldovich (SZ) effect in different cosmological models. We considered a wider range of parametrizations for the evolution of the dark energy density and its equation of state, hoping to capture the important physical properties of quintessence. Our study included the families of early dark energy cosmologies parametrized by Wetterich (2004); Doran and Robbers (2006); Linder (2006), and models that by construction do not have an early dark energy component, in order to assess potential differences in the inferred parameter bounds on the standard cosmology. We used non-radiative hydrodynamical simulations to calculate the large-scale properties of the SZ effect, considering both the thermal and kinetic component and concentrating on an analysis of their statistical properties. We developed a new methodology to construct realistic light-cone images of the Comptonization and the Doppler parameters from the simulation snapshots, yielding sky maps that avoid repetition of structures along the line-of-sight and are free of discontinuities in the transverse direction.

With regard to the results, the maps that refer to EDE cosmologies showed a mean y distortion that are systematically higher (up to 15%) with respect to the ΛCDM cosmology. Consistent with expectations, we found that in the EDE models the tails of the thermal SZ signal extend till high redshift, since structures grow much earlier there, while at redshift zero the mean distortion is comparable with the one obtained for a standard cosmology. Also in the case of the kinetic SZ effect, the occurrence of rare bright events at early times in the EDE models increases the variance of the signal at high redshift, given that all cosmologies were normalized to the same σ_8 today. Of most interest in this context is also the analysis of the angular power spectrum of the SZ effect. We found that EDE can help in reconciling the observational indications of an excess in the angular power at small scales, as measured by the Cosmic Microwave background Imager (CBI Mason et al., 2003), the Berkeley-Illinois-Maryland Array (BIMA Dawson et al., 2002), and the Arcminute Cosmology Bolometer Array Receiver (ACBAR Kuo et al., 2004) experiments, with the indication of a low normalization cosmology. Temporal variations of the dark energy density provides a way for generating an enhanced cluster aboundance at early time and thus a higher amplitude of the thermal and kinetic SZ power spectrum. However, for viable dark energy models the level of the thermal SZ power then still falls short of current measurements. Interestingly, we discovered that the magnitude of the effect is mainly sensitive to the differences in the Hubble expansion function and depends only marginally on the growth rate, considering the same $sigma_8$.

We have already emphasized that an important guide for the study of the dependencies of the large-scale structure on cosmological parameters is the number counts

of galaxy clusters as a function of time. The SZ effect is independent of redshift and thus provides a powerful probe of the cluster gas, especially for high redshift objects. In our work, we accurately extracted simulated catalogues of clusters from the SZ maps and we examined the plain number counts in different models. We found that the number of detections for EDE models with respect to the ΛCDM cosmology almost doubles when we consider only halos in the redshift interval $2 < z < 3$. Therefore, the use of deep galaxy cluster surveys, combined with follow up optical observations to derive the redshifts of massive halos, could make it possible to discriminate between different cosmologies. For what concerns the observational aspects, we analyzed in details the possibility of constraining dark energy cosmologies with the ongoing South Pole Telescope SZ survey (SPT Ruhl, 2004). We first compared the comoving abundance of all clusters contained in the simulated maps above the limiting flux of the survey. Then, we examined separately the dependence of the surface density on the cosmology through the opposite contributions of the growth function and the volume element. We observed that the presence of early dark energy flattens the redshift distribution of objects, with an increase of at most 20% in the number of halos at high redshift. Again, the net effect is quite small, in contrast to what has been predicted by recent forecasts for the SZ effect based on analytic estimates to quantify the signal (Waizmann and Bartelmann, 2009; Fedeli et al., 2009). Once a subset of cosmological parameters, for instance Ω_M, σ_8 and h, are accurately determined by other measurements, and therefore kept fixed, we might be able to highlight the specific contribution of the different dark energy history. Otherwise, the sensitivity due to the cosmology can be stronger than the intrinsic differences in the models and severely hamper our ability to constrain them. We directly quantify this effect with a subset of simulations which adopt different cosmological parameters.

Galaxy clusters are indeed a very promising indicator for constraining the amount of dark energy and its time evolution. But in using this probe effectively, the need arises to relate observational properties, specifically the thermal SZ effect, to intrinsic quantities, such as the mass. With regards to this particular problem, we used the simulated maps in order to fine-tune the known Y-M scaling relation and to improve its precision. We found that all models follow the self-similar scaling independently on whether we consider the intrinsic effect, i.e. the one computed directly from the halos in the simulation, or the results obtained from the SZ maps. Also in the latter case, the scatter between the different cosmologies was always lower than the statistical uncertainties due to the projection effects. This is a strong indication that mass calibrations derived using the SZ decrement, combined with scaling relations, are still valid in the generalized dark energy cosmologies examined in this work. We pursued the association between mass and Comptonization parameter even further, investigating the impact of different theoretical approaches to define the boundaries of a halo. We noticed that the scatter in the relationship reaches a minimum when both the flux and the mass values are integrated out to a radius in

proximity of the virial radius of the halos. These results give a first indication on the optimal angular size on which to measure the correlation. As a natural extension of the analysis we presented here, in the future we plan to produce mock maps and extract synthetic galaxy clusters from numerical simulations that more closely mimic the observational selection effects of future and current data-sets. This requires, on one hand, to improve the accuracy of the simulations by adding more complicated baryon physics to them, and then, to fed the results to specific analysis pipelines for observational instruments. Projects that will improve our understanding of the dominant systematic effects in dark energy measurements are really decisive for "precision" cosmology.

Although constraining dark energy is perhaps the leading motivation for much of the current interest in cluster surveys, it has been recognized that slight deviations from Gaussianity in the primordial matter distribution may cause a significant change in the high mass tails of the halo mass function. In the third part of this Thesis, we investigated the extent to which non-Gaussian (NG) initial conditions can affect the abundance and the clustering of dark matter halos, in particular when considered within the limits allowed by present and future CMB observations. We studied a specific form of non-Gaussianity of the local type, where departures from Gaussianity are modelled in position space through a quadratic contribution in the primordial gravitational potential and the degree of non-linearity is parametrized in terms of the constant f_{NL}. The most recent analysis of the Microwave Anisotropy Probe (WMAP) 5-yr temperature fluctuation maps shows that the primordial NG signal on the very large scales probed by CMB is tiny (Komatsu et al., 2009b). Yet, the latest claims of a positive detection of NG features in the WMAP 3-yr data reported by Yadav et al. (2007) have renewed the interest in NG models, shifting the focus towards smaller scales where NG features can only be spotted through the analysis of the LSS of the Universe at much lower redshifts. In this framework, we used very high resolution experiments trying to bridge the gap between theoretical analytical predictions, that involve simplifying hypothesis, and LSS-based observations, where the non-linear effects play a non-negligible role. We obtained two major results.

First, we have studied the evolution of massive dark matter haloes in NG scenarios quantified by the mass function, and compared them with analytical predictions. We were particularly interested in this statistic because the presence of primordial non-Gaussianity enhances or suppresses the high peak tail of the multiplicity function, depending to the sign of the non-linearity parameter f_{NL}. We found that the number density of massive objects increases with f_{NL}, as expected, and the differences between models is larger at higher redshift, confirming that the occurrence of massive objects at early epochs provides a significant observational test for NG models. Various attempts to compute analytically the effect of primordial non-Gaussianity on the mass function exist in the literature, based on exten-

sions of the Press-Schechter theory; we considered here the formalism presented in Matarrese et al. (2000) and Lo Verde et al. (2008). Both approaches assume that the deviations from Gaussianity are small, but major limitations are the use of the spherical collapse model and the random-phase hypothesis, which is clearly not satisfied for NG initial conditions, and the assumption of sharp k-space filtering. Surprisingly, we discovered that these analytic models fit the results of our simulations very well over the full range of $f_{\rm NL}$ and out to high redshift, provided that we correct the critical density, that enters in the analytic predictions, to account for non-spherical collapse dynamics. This is equivalent to rescaling the spherical collapse threshold by a factor $\sqrt{q}$, where $q = 0.75$. While we first obtained this result from the fit to the simulation data, it is worth noticing that, very recently, a rigorous physical interpretation of the q-factor introduced in this Thesis has been presented by Maggiore and Riotto (2009). In their work, the correction is derived in terms of the diffusing barrier model, which is responsible for modifications also of the Gaussian mass function. Moreover, our result has the important consequence that, once we have rescaled the density threshold, we can use an analytical model to provide accurate predictions for the halo aboundance in NG scenarios, spanning a range of $f_{\rm NL}$ well beyond the current WMAP constraints, without relying on time-consuming numerical experiments. On the other hand, the deviations from the Gaussian model we observed are more modest than what expected, which makes it even more difficult to spot non-Gaussianity from the analysis of the large-scale structure.

As a second line of investigation, we tested the validity of our approach by calibrating also the predictions of the NG halo bias. Computing the cross and auto-power spectrum from a suite of N-body simulations, we showed, both analytically and numerically, that non-Gaussianity leads to a strong scale dependence of the bias of dark matter halos. This effect, first reported by Dalal et al. (2008), was measured here with a greater accuracy thanks to the high resolution of the runs, in which we simulated a very large cosmological region, of 1200 Mpc on a side. In fact, the deviations from Gaussianity would only be seen on very large scale, and thus it becomes fundamental to perform N-body simulations on large boxes. We found a remarkably good agreement between our numerical results and the analytic prescriptions for the NG halo bias, provided we correct the overall amplitude of the effect by the q-factor, which arises again by the modification of the density contrast in the theoretical formulation. It is very important to precisely quantify this effect, since corrections to the bias modify current and forecasted constraints reported in the literature. Measurements of the power spectrum of biased objects provide a new and very powerful avenue to detect and quantify non-Gaussianity. In fact, the scale dependence of the bias is a unique signature of NG models, and future surveys can potentially obtain constraints comparable and even narrower than the existing CMB limits. On the observational side, Slosar et al. (2008) have recently applied this new method to a wide range of data-sets, obtaining limits for

f_{NL} comparable to the best previous estimates. However, there are several issues that require further investigation. In the future, this methodology needs to be tested in N-body simulations using large scale tracers comparable to the one used in observational analyses. Moreover, it is necessary to investigate whether the halo bias depends on parameters other than the mass, in particular the effects of the merger history of the halos, or any other unexpected variables which may arise.

Certainly many of the non-standard models we explored here are essentially equally successful as the ΛCDM paradigm when compared to current data. Indeed, one implication of the results presented here is precisely that both EDE and NG cosmologies will be much more difficult to detect than previously though. This finding provides a cautionary tale for survey design, and strongly highlights that we cannot rely on the assumption that any part of our investigation is simply disconnected to the others. On the other hand, numerical experiments play a crucial role in determining robust predictions for the complex outcome of non-linear structure formation, and in disentangling the contribution of complementary effects. The work presented in this Thesis further confirms the importance of the interplay between simulations and observations in cosmology. We have given several concrete examples of cosmological probes that can highlight the diversity of models and guide the exploration of possible physics. This will be particularly relevant in the development of new and ongoing observational projects. In fact, over the coming years, microwave experiments and high redshift surveys will provide a wide range of new data which will bring further precision to cosmological studies.

Given the encouraging results we obtained from the concordance model of cosmology, there seems to be little room left for dramatic revision of the theory. An indicator of the progress being made in the large-scale structure problem is the difficulty to formulate convincing alternatives to ΛCDM. Therefore, the models recently proposed to alleviate problems of the standard scenario can be used for an important consistency test of our understanding of the data. Given the presence of systematic trends in observations which are not directly reflected in the ΛCDM parameters, we can naively expect that one of these cosmologies might exhibit a significantly better fit. However, we should not lose sight of the fundamental motivation for developing a standard model and keep looking for deviations from it, which is to find the true underlying physical theory governing the Universe's history. In fact, since the cosmological parameters depend on fundamental cosmological aspects, we have really the possibility of learning much about the composition and evolution of the cosmos from them. We need to make sure that the predictions of the theory are at least equally precise as the precision of all observational data we have, in order to realize the prospects of taking the next steps towards a solution of the cosmological puzzles.

Acknowledgments

This research project would not have been possible without the mentorship of numerous outstanding individuals both within the Max Planck Institute for Astrophysics and outside it.

First and foremost, I would like to thank Dr. Volker Springel, who has been a fantastic advisor to me and, in spite of his numerous personal projects, always had time to concentrate on the details of my work. Not only he offered me invaluable assistance and constructive guidance throughout the PhD project, but he has also supported me tremendously in every circumstance. I deeply thank Dr. Klaus Dolag, for having always pushed me ahead with his constant reassuring smile and his confidence, almost blind confidence, in my capability. He is the one who initiated me into the world of numerical simulations and during all these years has generously spent his time and shared his knowledge, helping me to complete my project with the best possible results. I was very lucky to have the opportunity to work with people I strongly admire.

I would like to take this opportunity also to thank Prof. Dr. Lauro Moscardini and the entire group of my Italian collaborators. It was a real pleasure for me to work with them. My gratitude goes to Prof. Dr. Simon White for taking academic interest in this study as well as providing valuable suggestions that improved the quality of this work. In general, during my time as a PhD student, I have been surrounded by wonderful colleagues. I therefore would like to thank them all for creating such a splendid atmosphere.

I want to express my very special gratitude to my brother, his wife and my beloved nieces and nephew, who gave me the extra strength to face the mostly happy, but sometimes heavy moments during these years. I dedicate this work to my parents, who through my childhood and study career had always encouraged me to follow my heart and inquisitive mind in any direction they took me.

Bibliography

N. Afshordi and A. J. Tolley. Primordial non-Gaussianity, statistics of collapsed objects, and the integrated Sachs-Wolfe effect. *Phys. Rev. D*, 78(12):123507–+, Dec. 2008. doi: 10.1103/PhysRevD.78.123507.

N. Aghanim, A. C. da Silva, and N. J. Nunes. Cluster scaling relations from cosmological hydrodynamic simulations in a dark-energy dominated universe. *A&A*, 496:637–644, Mar. 2009. doi: 10.1051/0004-6361/200810692.

A. Albrecht and C. Skordis. Phenomenology of a Realistic Accelerating Universe Using Only Planck-Scale Physics. *Physical Review Letters*, 84:2076–2079, Mar. 2000. doi: 10.1103/PhysRevLett.84.2076.

L. Amendola. Coupled quintessence. *Phys. Rev. D*, 62(4):043511–+, Aug. 2000. doi: 10.1103/PhysRevD.62.043511.

L. Amendola, M. Baldi, and C. Wetterich. Quintessence cosmologies with a growing matter component. *Phys. Rev. D*, 78(2):023015–+, July 2008. doi: 10.1103/PhysRevD.78.023015.

C. Armendariz-Picon, V. Mukhanov, and P. J. Steinhardt. Dynamical Solution to the Problem of a Small Cosmological Constant and Late-Time Cosmic Acceleration. *Physical Review Letters*, 85:4438–4441, Nov. 2000. doi: 10.1103/PhysRevLett.85.4438.

D. Babich and M. Zaldarriaga. Primordial bispectrum information from CMB polarization. *Phys. Rev. D*, 70(8):083005–+, Oct. 2004. doi: 10.1103/PhysRevD.70.083005.

N. A. Bahcall and R. Cen. The mass function of clusters of galaxies. *ApJL*, 407: L49–L52, Apr. 1993. doi: 10.1086/186803.

N. A. Bahcall and X. Fan. The Most Massive Distant Clusters: Determining Omega and delta 8. *ApJ*, 504:1–+, Sept. 1998. doi: 10.1086/306088.

J. M. Bardeen, J. R. Bond, N. Kaiser, and j. . ApJ. k. . C. y. . . m. . m. v. . . p. . . d. . . a. . h. a. . P. Szalay, A. S. title = "The statistics of peaks of Gaussian random fields".

M. Bartelmann, M. Doran, and C. Wetterich. Non-linear structure formation in cosmologies with early dark energy. *A&A*, 454:27–36, July 2006. doi: 10.1051/0004-6361:20053922.

N. Bartolo, S. Matarrese, and A. Riotto. Oscillations during inflation and the cosmological density perturbations. *Phys. Rev. D*, 64(8):083514–+, Oct. 2001. doi: 10.1103/PhysRevD.64.083514.

N. Bartolo, E. Komatsu, S. Matarrese, and A. Riotto. Non-Gaussianity from inflation: theory and observations. *Phys. Rep.*, 402:103–266, Nov. 2004. doi: 10.1016/j.physrep.2004.08.022.

N. Bartolo, S. Matarrese, and A. Riotto. Signatures of primordial non-Gaussianity in the large-scale structure of the universe. *Journal of Cosmology and Astro-Particle Physics*, 10:10–+, Oct. 2005. doi: 10.1088/1475-7516/2005/10/010.

E. Bertin and S. Arnouts. SExtractor: Software for source extraction. *A&A Supp.*, 117:393–404, June 1996.

P. Bode, N. A. Bahcall, E. B. Ford, and J. P. Ostriker. Evolution of the Cluster Mass Function: GPC3 Dark Matter Simulations. *ApJ*, 551:15–22, Apr. 2001. doi: 10.1086/320077.

J. R. Bond, S. Cole, G. Efstathiou, and N. Kaiser. Excursion set mass functions for hierarchical Gaussian fluctuations. *ApJ*, 379:440–460, Oct. 1991. doi: 10.1086/170520.

T. J. Broadhurst and R. Barkana. Large Einstein radii: a problem for ΛCDM. *MNRAS*, 390:1647–1654, Nov. 2008. doi: 10.1111/j.1365-2966.2008.13852.x.

G. L. Bryan and M. L. Norman. Statistical Properties of X-Ray Clusters: Analytic and Numerical Comparisons. *ApJ*, 495:80, Mar. 1998. doi: 10.1086/305262.

J. S. Bullock, T. S. Kolatt, Y. Sigad, R. S. Somerville, A. V. Kravtsov, A. A. Klypin, J. R. Primack, and A. Dekel. Profiles of dark haloes: evolution, scatter and environment. *MNRAS*, 321:559–575, Mar. 2001.

R. R. Caldwell. A phantom menace? Cosmological consequences of a dark energy component with super-negative equation of state. *Physics Letters B*, 545:23–29, Oct. 2002. doi: 10.1016/S0370-2693(02)02589-3.

R. R. Caldwell and E. V. Linder. Limits of Quintessence. *Physical Review Letters*, 95(14):141301–+, Sept. 2005. doi: 10.1103/PhysRevLett.95.141301.

R. R. Caldwell, R. Dave, and P. J. Steinhardt. Cosmological Imprint of an Energy Component with General Equation of State. *Physical Review Letters*, 80:1582–1585, Feb. 1998. doi: 10.1103/PhysRevLett.80.1582.

C. Carbone, V. Springel, C. Baccigalupi, M. Bartelmann, and S. Matarrese. Full-sky maps for gravitational lensing of the cosmic microwave background. *MNRAS*, 388:1618–1626, Aug. 2008a. doi: 10.1111/j.1365-2966.2008.13544.x.

C. Carbone, L. Verde, and S. Matarrese. Non-Gaussian Halo Bias and Future Galaxy Surveys. *ApJL*, 684:L1–L4, Sept. 2008b. doi: 10.1086/592020.

J. E. Carlstrom, G. P. Holder, and E. D. Reese. Cosmology with the Sunyaev-Zel'dovich Effect. *ARA&A*, 40:643–680, 2002. doi: 10.1146/annurev.astro.40.060401.093803.

S. M. Carroll, W. H. Press, and E. L. Turner. The cosmological constant. *ARA&A*, 30:499–542, 1992. doi: 10.1146/annurev.aa.30.090192.002435.

M. Chevallier and D. Polarski. Accelerating Universes with Scaling Dark Matter. *International Journal of Modern Physics D*, 10:213–223, 2001. doi: 10.1142/S0218271801000822.

S. Cole and N. Kaiser. Biased clustering in the cold dark matter cosmogony. *MNRAS*, 237:1127–1146, Apr. 1989.

S. Cole, W. J. Percival, J. A. Peacock, P. Norberg, C. M. Baugh, C. S. Frenk, I. Baldry, J. Bland-Hawthorn, T. Bridges, R. Cannon, M. Colless, C. Collins, W. Couch, N. J. G. Cross, G. Dalton, V. R. Eke, R. De Propris, S. P. Driver, G. Efstathiou, R. S. Ellis, K. Glazebrook, C. Jackson, A. Jenkins, O. Lahav, I. Lewis, S. Lumsden, S. Maddox, D. Madgwick, B. A. Peterson, W. Sutherland, and K. Taylor. The 2dF Galaxy Redshift Survey: power-spectrum analysis of the final data set and cosmological implications. *MNRAS*, 362:505–534, Sept. 2005. doi: 10.1111/j.1365-2966.2005.09318.x.

P. Coles and L. Chiang. Characterizing the nonlinear growth of large-scale structure in the Universe. *Nature*, 406:376–378, July 2000. doi: 10.1038/35019009.

C. Conroy, J. A. Newman, M. Davis, A. L. Coil, R. Yan, M. C. Cooper, B. F. Gerke, S. M. Faber, and D. C. Koo. The DEEP2 Galaxy Redshift Survey: Probing the Evolution of Dark Matter Halos around Isolated Galaxies from z˜1 to z˜0. *ApJ*, 635:982–989, Dec. 2005. doi: 10.1086/497677.

C. Conroy, F. Prada, J. A. Newman, D. Croton, A. L. Coil, C. J. Conselice, M. C. Cooper, M. Davis, S. M. Faber, B. F. Gerke, P. Guhathakurta, A. Klypin, D. C. Koo, and R. Yan. Evolution in the Halo Masses of Isolated Galaxies between z ˜ 1 and z ˜ 0: From DEEP2 to SDSS. *ApJ*, 654:153–171, Jan. 2007. doi: 10.1086/509632.

A. C. da Silva, D. Barbosa, A. R. Liddle, and P. A. Thomas. Hydrodynamical simulations of the Sunyaev-Zel'dovich effect. *MNRAS*, 317:37–44, Sept. 2000. doi: 10.1046/j.1365-8711.2000.03553.x.

A. C. da Silva, D. Barbosa, A. R. Liddle, and P. A. Thomas. Hydrodynamical simulations of the Sunyaev-Zel'dovich effect: the kinetic effect. *MNRAS*, 326: 155–163, Sept. 2001. doi: 10.1046/j.1365-8711.2001.04580.x.

A. J. C. da Silva. SZ scaling relations in Galaxy Clusters: Results from hydrodynamical N-body simulations. *Ap&SS*, 290:167–176, Feb. 2004. doi: 10.1023/B: ASTR.0000022172.80206.d6.

N. Dalal, J. F. Hennawi, G. Holder, and P. Bode. Strong Lensing by Galaxy Clusters and ΛCDM. In Y. Mellier and G. Meylan, editors, *Gravitational Lensing Impact on Cosmology*, volume 225 of *IAU Symposium*, pages 193–201, June 2005. doi: 10.1017/S1743921305001997.

N. Dalal, O. Doré, D. Huterer, and A. Shirokov. Imprints of primordial non-Gaussianities on large-scale structure: Scale-dependent bias and abundance of virialized objects. *Phys. Rev. D*, 77(12):123514–+, June 2008. doi: 10.1103/PhysRevD.77.123514.

M. Davis, G. Efstathiou, C. S. Frenk, and S. D. M. White. The evolution of large-scale structure in a universe dominated by cold dark matter. *ApJ*, 292:371–394, May 1985. doi: 10.1086/163168.

M. Davis, B. F. Gerke, J. A. Newman, and the Deep2 Team. Constraining Dark Energy with the DEEP2 Redshift Survey. In S. C. Wolff and T. R. Lauer, editors, *Observing Dark Energy*, volume 339 of *Astronomical Society of the Pacific Conference Series*, page 128, Aug. 2005.

K. S. Dawson, W. L. Holzapfel, J. E. Carlstrom, M. Joy, S. J. LaRoque, A. D. Miller, and D. Nagai. Measurement of Arcminute-Scale Cosmic Microwave Background Anisotropy with the Berkeley-Illinois-Maryland Association Array. *ApJ*, 581:86–95, Dec. 2002. doi: 10.1086/344226.

G. De Lucia, G. Kauffmann, V. Springel, S. D. M. White, B. Lanzoni, F. Stoehr, G. Tormen, and N. Yoshida. Substructures in cold dark matter haloes. *MNRAS*, 348:333–344, Feb. 2004. doi: 10.1111/j.1365-2966.2004.07372.x.

V. Desjacques. Environmental dependence in the ellipsoidal collapse model. *MNRAS*, 388:638–658, Aug. 2008. doi: 10.1111/j.1365-2966.2008.13420.x.

V. Desjacques, U. Seljak, and I. T. Iliev. Scale-dependent bias induced by local non-Gaussianity: a comparison to N-body simulations. *MNRAS*, 396:85–96, June 2009. doi: 10.1111/j.1365-2966.2009.14721.x.

A. Diaferio, R. A. Sunyaev, and A. Nusser. Large-Scale Motions in Superclusters: Their Imprint in the Cosmic Microwave Background. *ApJL*, 533:L71–L74, Apr. 2000. doi: 10.1086/312627.

J. M. Diego and S. Majumdar. The hybrid SZ power spectrum: combining cluster counts and SZ fluctuations to probe gas physics. *MNRAS*, 352:993–1004, Aug. 2004. doi: 10.1111/j.1365-2966.2004.07989.x.

S. Dodelson, M. Kaplinghat, and E. Stewart. Solving the Coincidence Problem: Tracking Oscillating Energy. *Physical Review Letters*, 85:5276–5279, Dec. 2000. doi: 10.1103/PhysRevLett.85.5276.

K. Dolag, M. Bartelmann, F. Perrotta, C. Baccigalupi, L. Moscardini, M. Meneghetti, and G. Tormen. Numerical study of halo concentrations in dark-energy cosmologies. *A&A*, 416:853–864, Mar. 2004. doi: 10.1051/0004-6361: 20031757.

M. Doran and G. Robbers. Early dark energy cosmologies. *Journal of Cosmology and Astro-Particle Physics*, 6:26–+, June 2006. doi: 10.1088/1475-7516/2006/ 06/026.

M. Doran, J.-M. Schwindt, and C. Wetterich. Structure formation and the time dependence of quintessence. *Phys. Rev. D*, 64(12):123520, Dec. 2001.

M. Doran, K. Karwan, and C. Wetterich. Observational constraints on the dark energy density evolution. *Journal of Cosmology and Astro-Particle Physics*, 11:7, Nov. 2005. doi: 10.1088/1475-7516/2005/11/007.

M. Doran, G. Robbers, and C. Wetterich. Impact of three years of data from the Wilkinson Microwave Anisot ropy Probe on cosmological models with dynamical dark energy. *Phys. Rev. D*, 75(2):023003, Jan. 2007. doi: 10.1103/PhysRevD.75. 023003.

A. R. Duffy, J. Schaye, S. T. Kay, and C. Dalla Vecchia. Dark matter halo concentrations in the Wilkinson Microwave Anisotropy Probe year 5 cosmology. *MNRAS*, 390:L64–L68, Oct. 2008. doi: 10.1111/j.1745-3933.2008.00537.x.

R. Durrer and R. Maartens. Dark energy and dark gravity: theory overview. *General Relativity and Gravitation*, 40:301–328, Feb. 2008. doi: 10.1007/ s10714-007-0549-5.

G. Efstathiou and J. R. Bond. Cosmic confusion: degeneracies among cosmological parameters derived from measurements of microwave background anisotropies. *MNRAS*, 304:75–97, Mar. 1999. doi: 10.1046/j.1365-8711.1999.02274.x.

G. Efstathiou, C. S. Frenk, S. D. M. White, and M. Davis. Gravitational clustering from scale-free initial conditions. *MNRAS*, 235:715–748, Dec. 1988a.

G. Efstathiou, C. S. Frenk, S. D. M. White, and M. Davis. Gravitational clustering from scale-free initial conditions. *MNRAS*, 235:715–748, Dec. 1988b.

D. J. Eisenstein and W. Hu. Baryonic Features in the Matter Transfer Function. *ApJ*, 496:605, Mar. 1998. doi: 10.1086/305424.

D. J. Eisenstein, I. Zehavi, D. W. Hogg, R. Scoccimarro, M. R. Blanton, R. C. Nichol, R. Scranton, H. Seo, M. Tegmark, Z. Zheng, S. F. Anderson, J. Annis, N. Bahcall, J. Brinkmann, S. Burles, F. J. Castander, A. Connolly, I. Csabai, M. Doi, M. Fukugita, J. A. Frieman, K. Glazebrook, J. E. Gunn, J. S. Hendry, G. Hennessy, Z. Ivezić, S. Kent, G. R. Knapp, H. Lin, Y. Loh, R. H. Lupton, B. Margon, T. A. McKay, A. Meiksin, J. A. Munn, A. Pope, M. W. Richmond, D. Schlegel, D. P. Schneider, K. Shimasaku, C. Stoughton, M. A. Strauss, M. Sub-baRao, A. S. Szalay, I. Szapudi, D. L. Tucker, B. Yanny, and D. G. York. Detection of the Baryon Acoustic Peak in the Large-Scale Correlation Function of SDSS Luminous Red Galaxies. *ApJ*, 633:560–574, Nov. 2005. doi: 10.1086/466512.

V. R. Eke, S. Cole, and C. S. Frenk. Cluster evolution as a diagnostic for Omega. *MNRAS*, 282:263–280, Sept. 1996.

V. R. Eke, J. F. Navarro, and M. Steinmetz. The Power Spectrum Dependence of Dark Matter Halo Concentrations. *ApJ*, 554:114–125, June 2001. doi: 10.1086/321345.

N. Espino-Briones, M. Plionis, and C. Ragone-Figueroa. Environmental Effects of Dark Matter Halos: The Clustering-Substructure Relation of Group-Size Halos. *ApJL*, 666:L5–L8, Sept. 2007. doi: 10.1086/521622.

A. E. Evrard, J. Bialek, M. Busha, M. White, S. Habib, K. Heitmann, M. Warren, E. Rasia, G. Tormen, L. Moscardini, C. Power, A. R. Jenkins, L. Gao, C. S. Frenk, V. Springel, S. D. M. White, and J. Diemand. Virial Scaling of Massive Dark Matter Halos: Why Clusters Prefer a High Normalization Cosmology. *ApJ*, 672:122–137, Jan. 2008. doi: 10.1086/521616.

A. Faltenbacher and J. Diemand. Velocity distributions in clusters of galaxies. *MNRAS*, 369:1698–1702, July 2006. doi: 10.1111/j.1365-2966.2006.10421.x.

A. Faltenbacher and W. G. Mathews. The concentration-velocity dispersion relation in galaxy groups. *MNRAS*, 375:313–323, Feb. 2007. doi: 10.1111/j.1365-2966.2006.11295.x.

C. Fedeli, L. Moscardini, and M. Bartelmann. Observing the clustering properties of galaxy clusters in dynamical dark-energy cosmologies. *A&A*, 500:667–679, June 2009. doi: 10.1051/0004-6361/200811477.

P. G. Ferreira and M. Joyce. Cosmology with a primordial scaling field. *Phys. Rev. D*, 58(2):023503, July 1998.

D. J. Fixsen, E. S. Cheng, D. A. Cottingham, R. E. Eplee, Jr., R. B. Isaacman, J. C. Mather, S. S. Meyer, P. D. Noerdlinger, R. A. Shafer, R. Weiss, E. L. Wright, C. L. Bennett, N. W. Boggess, T. Kelsall, S. H. Moseley, R. F. Silverberg, G. F. Smoot, and D. T. Wilkinson. Cosmic microwave background dipole spectrum

measured by the COBE FIRAS instrument. *ApJ*, 420:445–449, Jan. 1994. doi: 10.1086/173575.

D. J. Fixsen, E. S. Cheng, J. M. Gales, J. C. Mather, R. A. Shafer, and E. L. Wright. The Cosmic Microwave Background Spectrum from the Full COBE FIRAS Data Set. *ApJ*, 473:576–+, Dec. 1996. doi: 10.1086/178173.

M. J. Francis, G. F. Lewis, and E. V. Linder. Can Early Dark Energy be Detected in Non-Linear Structure? *ArXiv e-prints, 0808.2840*, Aug. 2008.

M. J. Francis, G. F. Lewis, and E. V. Linder. Can early dark energy be detected in non-linear structure? *MNRAS*, 394:605–614, Apr. 2009a. doi: 10.1111/j. 1365-2966.2008.14286.x.

M. J. Francis, G. F. Lewis, and E. V. Linder. Halo mass functions in early dark energy cosmologies. *MNRAS*, 393:L31–L35, Feb. 2009b. doi: 10.1111/j.1745-3933. 2008.00592.x.

W. L. Freedman. Determination of Cosmological Parameters. *Physica Scripta Volume T*, 85:37–+, 2000. doi: 10.1238/Physica.Topical.085a00037.

W. L. Freedman, B. F. Madore, B. K. Gibson, L. Ferrarese, D. D. Kelson, S. Sakai, J. R. Mould, R. C. Kennicutt, Jr., H. C. Ford, J. A. Graham, J. P. Huchra, S. M. G. Hughes, G. D. Illingworth, L. M. Macri, and P. B. Stetson. Final Results from the Hubble Space Telescope Key Project to Measure the Hubble Constant. *ApJ*, 553:47–72, May 2001. doi: 10.1086/320638.

A. Gangui, F. Lucchin, S. Matarrese, and S. Mollerach. The three-point correlation function of the cosmic microwave background in inflationary models. *ApJ*, 430: 447–457, Aug. 1994. doi: 10.1086/174421.

L. Gao, V. Springel, and S. D. M. White. The age dependence of halo clustering. *MNRAS*, 363:L66–L70, Oct. 2005. doi: 10.1111/j.1745-3933.2005.00084.x.

L. Gao, J. F. Navarro, S. Cole, C. S. Frenk, S. D. M. White, V. Springel, A. Jenkins, and A. F. Neto. The redshift dependence of the structure of massive Λ cold dark matter haloes. *MNRAS*, 387:536–544, June 2008. doi: 10.1111/j.1365-2966.2008. 13277.x.

B. Grinstein and M. B. Wise. Non-Gaussian fluctuations and the correlations of galaxies or rich clusters of galaxies. *ApJ*, 310:19–22, Nov. 1986. doi: 10.1086/ 164660.

M. Grossi and V. Springel. The impact of early dark energy on non-linear structure formation. *MNRAS*, 394:1559–1574, Apr. 2009. doi: 10.1111/j.1365-2966.2009. 14432.x.

M. Grossi, K. Dolag, E. Branchini, S. Matarrese, and L. Moscardini. Evolution of massive haloes in non-Gaussian scenarios. *MNRAS*, 382:1261–1267, Dec. 2007. doi: 10.1111/j.1365-2966.2007.12458.x.

M. Grossi, E. Branchini, K. Dolag, S. Matarrese, and L. Moscardini. The mass density field in simulated non-Gaussian scenarios. *MNRAS*, 390:438–446, Oct. 2008. doi: 10.1111/j.1365-2966.2008.13783.x.

J. E. Gunn and J. R. I. Gott. On the Infall of Matter Into Clusters of Galaxies and Some Effects on Their Evolution. *ApJ*, 176:1–+, Aug. 1972. doi: 10.1086/151605.

Z. Haiman, J. J. Mohr, and G. P. Holder. Constraints on Cosmological Parameters from Future Galaxy Cluster Surveys. *ApJ*, 553:545–561, June 2001. doi: 10.1086/320939.

E. J. Hallman, P. M. Motl, J. O. Burns, and M. L. Norman. Challenges for Precision Cosmology with X-Ray and Sunyaev-Zeldovich Effect Gas Mass Measurements of Galaxy Clusters. *ApJ*, 648:852–867, Sept. 2006. doi: 10.1086/505317.

D. A. Howell, A. Conley, M. Della Valle, P. E. Nugent, S. Perlmutter, G. H. Marion, K. Krisciunas, C. Badenes, P. Mazzali, G. Aldering, P. Antilogus, E. Baron, A. Becker, C. Baltay, S. Benetti, S. Blondin, D. Branch, E. F. Brown, S. Deustua, A. Ealet, R. S. Ellis, D. Fouchez, W. Freedman, A. Gal-Yam, S. Jha, D. Kasen, R. Kessler, A. G. Kim, D. C. Leonard, W. Li, M. Livio, D. Maoz, F. Mannucci, T. Matheson, J. D. Neill, K. Nomoto, N. Panagia, K. Perrett, M. Phillips, D. Poznanski, R. Quimby, A. Rest, A. Riess, M. Sako, A. M. Soderberg, L. Strolger, R. Thomas, M. Turatto, S. van Dyk, and W. M. Wood-Vasey. Type Ia supernova science 2010-2020. *ArXiv e-prints*, Mar. 2009.

G. Hütsi. Acoustic oscillations in the SDSS DR4 luminous red galaxy sample power spectrum. *A&A*, 449:891–902, Apr. 2006. doi: 10.1051/0004-6361:20053939.

N. Jackson. The Hubble Constant. *Living Reviews in Relativity*, 10:4–+, Sept. 2007.

A. Jenkins, C. S. Frenk, S. D. M. White, J. M. Colberg, S. Cole, A. E. Evrard, H. M. P. Couchman, and N. Yoshida. The mass function of dark matter haloes. *MNRAS*, 321:372–384, Feb. 2001.

N. Kaiser. On the spatial correlations of Abell clusters. *ApJL*, 284:L9–L12, Sept. 1984. doi: 10.1086/184341.

X. Kang, P. Norberg, and J. Silk. Can a large-scale structure probe cosmic microwave background-constrained non-Gaussianity? *MNRAS*, 376:343–347, Mar. 2007. doi: 10.1111/j.1365-2966.2007.11435.x.

A. Klypin, A. V. Macciò, R. Mainini, and S. A. Bonometto. Halo Properties in Models with Dynamical Dark Energy. *ApJ*, 599:31–37, Dec. 2003. doi: 10.1086/379237.

E. Komatsu and U. Seljak. The Sunyaev-Zel'dovich angular power spectrum as a probe of cosmological parameters. *MNRAS*, 336:1256–1270, Nov. 2002. doi: 10.1046/j.1365-8711.2002.05889.x.

E. Komatsu and D. N. Spergel. Acoustic signatures in the primary microwave background bispectrum. *Phys. Rev. D*, 63(6):063002–+, Mar. 2001. doi: 10.1103/ PhysRevD.63.063002.

E. Komatsu, J. Dunkley, M. R. Nolta, C. L. Bennett, B. Gold, G. Hinshaw, N. Jarosik, D. Larson, M. Limon, L. Page, D. N. Spergel, M. Halpern, R. S. Hill, A. Kogut, S. S. Meyer, G. S. Tucker, J. L. Weiland, E. Wollack, and E. L. Wright. Five-Year Wilkinson Microwave Anisotropy Probe Observations: Cosmological Interpretation. *ApJS*, 180:330–376, Feb. 2009a. doi: 10.1088/0067-0049/180/2/330.

E. Komatsu, J. Dunkley, M. R. Nolta, C. L. Bennett, B. Gold, G. Hinshaw, N. Jarosik, D. Larson, M. Limon, L. Page, D. N. Spergel, M. Halpern, R. S. Hill, A. Kogut, S. S. Meyer, G. S. Tucker, J. L. Weiland, E. Wollack, and E. L. Wright. Five-Year Wilkinson Microwave Anisotropy Probe Observations: Cosmological Interpretation. *ApJS*, 180:330–376, Feb. 2009b. doi: 10.1088/0067-0049/180/2/330.

A. Kosowsky. The Atacama Cosmology Telescope. *New Astronomy Review*, 47: 939–943, Dec. 2003. doi: 10.1016/S1387-6473(03)00214-8.

M. e. a. Kowalski. Improved Cosmological Constraints from New, Old, and Combined Supernova Data Sets. *ApJ*, 686:749–778, Oct. 2008. doi: 10.1086/589937.

K. Koyama, J. Soda, and A. Taruya. Constraints on a non-Gaussian (χm2) cold dark matter model. *MNRAS*, 310:1111–1118, Dec. 1999. doi: 10.1046/j.1365-8711. 1999.03033.x.

A. V. Kravtsov, A. A. Klypin, and A. M. Khokhlov. Adaptive Refinement Tree: A New High-Resolution N-Body Code for Cosmological Simulations. *ApJS*, 111:73, July 1997. doi: 10.1086/313015.

J. Kujat, R. J. Scherrer, and A. A. Sen. Phantom dark energy models with negative kinetic term. *Phys. Rev. D*, 74(8):083501–+, Oct. 2006. doi: 10.1103/PhysRevD. 74.083501.

C. L. Kuo, P. A. R. Ade, J. J. Bock, C. Cantalupo, M. D. Daub, J. Goldstein, W. L. Holzapfel, A. E. Lange, M. Lueker, M. Newcomb, J. B. Peterson, J. Ruhl, M. C. Runyan, and E. Torbet. High-Resolution Observations of the Cosmic Microwave Background Power Spectrum with ACBAR. *ApJ*, 600:32–51, Jan. 2004. doi: 10.1086/379783.

C. L. Kuo, P. A. R. Ade, J. J. Bock, J. R. Bond, C. R. Contaldi, M. D. Daub, J. H. Goldstein, W. L. Holzapfel, A. E. Lange, M. Lueker, M. Newcomb, J. B. Peterson, C. Reichardt, J. Ruhl, M. C. Runyan, and Z. Staniszweski. Improved

Measurements of the CMB Power Spectrum with ACBAR. *ApJ*, 664:687–701, Aug. 2007. doi: 10.1086/518401.

C. Lacey and S. Cole. Merger rates in hierarchical models of galaxy formation. *MNRAS*, 262:627–649, June 1993.

C. Lacey and S. Cole. Merger Rates in Hierarchical Models of Galaxy Formation - Part Two - Comparison with N-Body Simulations. *MNRAS*, 271:676, Dec. 1994.

J. Lee and S. F. Shandarin. Large-Scale Biasing and the Primordial Gravitational Potential. *ApJL*, 505:L75–L78, Oct. 1998. doi: 10.1086/311607.

A. Liddle. *An Introduction to Modern Cosmology, Second Edition.* May 2003.

A. R. Liddle and R. J. Scherrer. Classification of scalar field potentials with cosmological scaling solutions. *Phys. Rev. D*, 59(2):023509, Jan. 1999.

L. Lin, D. C. Koo, C. N. A. Willmer, D. R. Patton, C. J. Conselice, R. Yan, A. L. Coil, M. C. Cooper, M. Davis, S. M. Faber, B. F. Gerke, P. Guhathakurta, and J. A. Newman. The DEEP2 Galaxy Redshift Survey: Evolution of Close Galaxy Pairs and Major-Merger Rates up to z ˜ 1.2. *ApJL*, 617:L9–L12, Dec. 2004. doi: 10.1086/427183.

E. V. Linder. Dark energy in the dark ages. *Astroparticle Physics*, 26:16–21, Aug. 2006. doi: 10.1016/j.astropartphys.2006.04.004.

E. V. Linder and D. Huterer. How many dark energy parameters? *Phys. Rev. D*, 72(4):043509–+, Aug. 2005. doi: 10.1103/PhysRevD.72.043509.

E. V. Linder and A. Jenkins. Cosmic structure growth and dark energy. *MNRAS*, 346:573–583, Dec. 2003. doi: 10.1046/j.1365-2966.2003.07112.x.

E. V. Linder and G. Robbers. Shifting the Universe: early dark energy and standard rulers. *Journal of Cosmology and Astro-Particle Physics*, 6:4–+, June 2008. doi: 10.1088/1475-7516/2008/06/004.

M. Lo Verde, A. Miller, S. Shandera, and L. Verde. Effects of scale-dependent non-Gaussianity on cosmological structures. *Journal of Cosmology and Astro-Particle Physics*, 4:14–+, Apr. 2008. doi: 10.1088/1475-7516/2008/04/014.

F. Lucchin and S. Matarrese. Power-law inflation. *Phys. Rev. D*, 32:1316–1322, Sept. 1985. doi: 10.1103/PhysRevD.32.1316.

F. Lucchin, S. Matarrese, and N. Vittorio. Scale-invariant clustering and primordial biasing. *ApJL*, 330:L21–L23, July 1988. doi: 10.1086/185196.

A. V. Macciò, C. Quercellini, R. Mainini, L. Amendola, and S. A. Bonometto. Coupled dark energy: Parameter constraints from N-body simulations. *Phys. Rev. D*, 69(12):123516, June 2004. doi: 10.1103/PhysRevD.69.123516.

A. V. Macciò, A. A. Dutton, F. C. van den Bosch, B. Moore, D. Potter, and J. Stadel. Concentration, spin and shape of dark matter haloes: scatter and the dependence on mass and environment. *MNRAS*, 378:55–71, June 2007. doi: 10.1111/j.1365-2966.2007.11720.x.

A. V. Macciò, A. A. Dutton, and F. C. van den Bosch. Concentration, spin and shape of dark matter haloes as a function of the cosmological model: WMAP1, WMAP3 and WMAP5 results. *MNRAS*, 391:1940–1954, Dec. 2008. doi: 10.1111/j.1365-2966.2008.14029.x.

M. Maggiore and A. Riotto. The Halo Mass Function from Excursion Set Theory. III. Non-Gaussian Fluctuations. *ArXiv e-prints*, Mar. 2009.

M. Magliocchetti, L. Silva, A. Lapi, G. de Zotti, G. L. Granato, D. Fadda, and L. Danese. A highly obscured and strongly clustered galaxy population discovered with the Spitzer Space Telescope. *MNRAS*, 375:1121–1132, Mar. 2007. doi: 10.1111/j.1365-2966.2006.11357.x.

R. Mainini, A. V. Macciò, and S. A. Bonometto. Non-linear predictions from linear theories in models with Dark Energy. *New Astronomy*, 8:173–178, Feb. 2003. doi: 10.1016/S1384-1076(02)00226-9.

S. Majumdar and J. J. Mohr. Importance of Cluster Structural Evolution in Using X-Ray and Sunyaev-Zeldovich Effect Galaxy Cluster Surveys to Study Dark Energy. *ApJ*, 585:603–610, Mar. 2003. doi: 10.1086/346179.

M. Manera and D. F. Mota. Cluster number counts dependence on dark energy inhomogeneities and coupling to dark matter. *MNRAS*, 371:1373–1380, Sept. 2006. doi: 10.1111/j.1365-2966.2006.10774.x.

I. Maor. Spherical Collapse with Dark Energy. *International Journal of Theoretical Physics*, 46:2274–2282, Sept. 2007. doi: 10.1007/s10773-007-9344-z.

B. S. Mason, T. J. Pearson, A. C. S. Readhead, M. C. Shepherd, J. Sievers, P. S. Udomprasert, J. K. Cartwright, A. J. Farmer, S. Padin, S. T. Myers, J. R. Bond, and C. R. Contaldi. The Anisotropy of the Microwave Background to l = 3500: Deep Field Observations with the Cosmic Background Imager. *ApJ*, 591:540–555, July 2003. doi: 10.1086/375507.

S. Matarrese and L. Verde. The Effect of Primordial Non-Gaussianity on Halo Bias. *ApJL*, 677:L77–L80, Apr. 2008. doi: 10.1086/587840.

S. Matarrese, F. Lucchin, and S. A. Bonometto. A path-integral approach to large-scale matter distribution originated by non-Gaussian fluctuations. *ApJL*, 310: L21–L26, Nov. 1986. doi: 10.1086/184774.

S. Matarrese, L. Verde, and R. Jimenez. The Abundance of High-Redshift Objects as a Probe of Non-Gaussian Initial Conditions. *ApJ*, 541:10–24, Sept. 2000. doi: 10.1086/309412.

I. G. McCarthy, A. Babul, G. P. Holder, and M. L. Balogh. Cluster Sunyaev-Zeldovich Effect Scaling Relations. *ApJ*, 591:515–525, July 2003. doi: 10.1086/375486.

P. McDonald. Primordial non-Gaussianity: Large-scale structure signature in the perturbative bias model. *Phys. Rev. D*, 78(12):123519–+, Dec. 2008. doi: 10.1103/PhysRevD.78.123519.

J.-B. Melin, J. G. Bartlett, and J. Delabrouille. Catalog extraction in SZ cluster surveys: a matched filter approach. *A&A*, 459:341–352, Nov. 2006. doi: 10.1051/0004-6361:20065034.

H. J. Mo and S. D. M. White. An analytic model for the spatial clustering of dark matter haloes. *MNRAS*, 282:347–361, Sept. 1996.

H. J. Mo, Y. P. Jing, and S. D. M. White. High-order correlations of peaks and haloes: a step towards understanding galaxy biasing. *MNRAS*, 284:189–201, Jan. 1997.

D. F. Mota and C. van de Bruck. On the spherical collapse model in dark energy cosmologies. *A&A*, 421:71–81, July 2004. doi: 10.1051/0004-6361:20041090.

P. M. Motl, E. J. Hallman, J. O. Burns, and M. L. Norman. The Integrated Sunyaev-Zeldovich Effect as a Superior Method for Measuring the Mass of Clusters of Galaxies. *ApJL*, 623:L63–L66, Apr. 2005. doi: 10.1086/430144.

D. Nagai. The Impact of Galaxy Formation on the Sunyaev-Zel'dovich Effect of Galaxy Clusters. *ApJ*, 650:538–549, Oct. 2006. doi: 10.1086/506467.

J. F. Navarro, C. S. Frenk, and S. D. M. White. Simulations of X-ray clusters. *MNRAS*, 275:720–740, Aug. 1995.

J. F. Navarro, C. S. Frenk, and S. D. M. White. The Structure of Cold Dark Matter Halos. *ApJ*, 462:563, May 1996. doi: 10.1086/177173.

J. F. Navarro, C. S. Frenk, and S. D. M. White. A Universal Density Profile from Hierarchical Clustering. *ApJ*, 490:493, Dec. 1997. doi: 10.1086/304888.

A. F. Neto, L. Gao, P. Bett, S. Cole, J. F. Navarro, C. S. Frenk, S. D. M. White, V. Springel, and A. Jenkins. The statistics of Λ CDM halo concentrations. *MNRAS*, 381:1450–1462, Nov. 2007. doi: 10.1111/j.1365-2966.2007.12381.x.

N. J. Nunes and D. F. Mota. Structure formation in inhomogeneous dark energy models. *MNRAS*, 368:751–758, May 2006. doi: 10.1111/j.1365-2966.2006.10166.x.

N. J. Nunes, A. C. da Silva, and N. Aghanim. Number counts in homogeneous and inhomogeneous dark energy models. *A&A*, 450:899–907, May 2006. doi: 10.1051/0004-6361:20053706.

N. Padmanabhan, D. J. Schlegel, U. Seljak, A. Makarov, N. A. Bahcall, M. R. Blanton, J. Brinkmann, D. J. Eisenstein, D. P. Finkbeiner, J. E. Gunn, D. W. Hogg, Ž. Ivezić, G. R. Knapp, J. Loveday, R. H. Lupton, R. C. Nichol, D. P. Schneider, M. A. Strauss, M. Tegmark, and D. G. York. The clustering of luminous red galaxies in the Sloan Digital Sky Survey imaging data. *MNRAS*, 378:852–872, July 2007. doi: 10.1111/j.1365-2966.2007.11593.x.

P. J. Peebles and B. Ratra. The cosmological constant and dark energy. *Reviews of Modern Physics*, 75:559–606, Apr. 2003. doi: 10.1103/RevModPhys.75.559.

P. J. E. Peebles. *The large-scale structure of the universe*. 1980.

P. J. E. Peebles and B. Ratra. Cosmology with a time-variable cosmological 'constant'. *ApJL*, 325:L17–L20, Feb. 1988. doi: 10.1086/185100.

S. e. a. Perlmutter. Measurements of Omega and Lambda from 42 High-Redshift Supernovae. *ApJ*, 517:565–586, June 1999. doi: 10.1086/307221.

A. Pillepich, C. Porciani, and O. Hahn. Halo mass function and scale-dependent bias from N-body simulations with non-Gaussian initial conditions. *ArXiv e-prints*, Nov. 2008.

C. Power, J. F. Navarro, A. Jenkins, C. S. Frenk, S. D. M. White, V. Springel, J. Stadel, and T. Quinn. The inner structure of ΛCDM haloes - I. A numerical convergence study. *MNRAS*, 338:14–34, Jan. 2003. doi: 10.1046/j.1365-8711.2003.05925.x.

W. H. Press and P. Schechter. Formation of Galaxies and Clusters of Galaxies by Self-Similar Gravitational Condensation. *ApJ*, 187:425–438, Feb. 1974.

B. Ratra and P. J. E. Peebles. Cosmological consequences of a rolling homogeneous scalar field. *Phys. Rev. D*, 37:3406–3427, June 1988.

D. Reed, J. Gardner, T. Quinn, J. Stadel, M. Fardal, G. Lake, and F. Governato. Evolution of the mass function of dark matter haloes. *MNRAS*, 346:565–572, Dec. 2003. doi: 10.1046/j.1365-2966.2003.07113.x.

C. L. Reichardt, P. A. R. Ade, J. J. Bock, J. R. Bond, J. A. Brevik, C. R. Contaldi, M. D. Daub, J. T. Dempsey, J. H. Goldstein, W. L. Holzapfel, C. L. Kuo, A. E. Lange, M. Lueker, M. Newcomb, J. B. Peterson, J. Ruhl, M. C. Runyan, and Z. Staniszewski. High-Resolution CMB Power Spectrum from the Complete ACBAR Data Set. *ApJ*, 694:1200–1219, Apr. 2009. doi: 10.1088/0004-637X/694/2/1200.

Y. Rephaeli. Comptonization Of The Cosmic Microwave Background: The Sunyaev-Zeldovich Effect. *ARA&A*, 33:541–580, 1995. doi: 10.1146/annurev.aa.33.090195.002545.

Y. Rephaeli and S. Sadeh. S-Z Power Spectra. *Modern Physics Letters A*, 23:1498–1505, 2008. doi: 10.1142/S0217732308027886.

Y. Rephaeli, S. Sadeh, and M. Shimon. The Sunyaev-Zeldovich effect. In F. Melchiorri and Y. Rephaeli, editors, *Background Microwave Radiation and Intracluster Cosmology*, pages 57–+, 2005.

A. G. Riess, A. V. Filippenko, P. Challis, A. Clocchiatti, A. Diercks, P. M. Garnavich, R. L. Gilliland, C. J. Hogan, S. Jha, R. P. Kirshner, B. Leibundgut, M. M. Phillips, D. Reiss, B. P. Schmidt, R. A. Schommer, R. C. Smith, J. Spyromilio, C. Stubbs, N. B. Suntzeff, and J. Tonry. Observational Evidence from Supernovae for an Accelerating Universe and a Cosmological Constant. *AJ*, 116:1009–1038, Sept. 1998. doi: 10.1086/300499.

A. G. Riess, A. V. Filippenko, W. Li, R. R. Treffers, B. P. Schmidt, Y. Qiu, J. Hu, M. Armstrong, C. Faranda, E. Thouvenot, and C. Buil. The Rise Time of Nearby Type IA Supernovae. *AJ*, 118:2675–2688, Dec. 1999. doi: 10.1086/301143.

A. G. Riess, L. Macri, S. Casertano, M. Sosey, H. Lampeitl, H. C. Ferguson, A. V. Filippenko, S. W. Jha, W. Li, R. Chornock, and D. Sarkar. A Redetermination of the Hubble Constant with the Hubble Space Telescope from a Differential Distance Ladder. *ApJ*, 699:539–563, July 2009. doi: 10.1088/0004-637X/699/1/539.

A. G. e. a. Riess. Type Ia Supernova Discoveries at z ¿ 1 from the Hubble Space Telescope: Evidence for Past Deceleration and Constraints on Dark Energy Evolution. *ApJ*, 607:665–687, June 2004. doi: 10.1086/383612.

B. E. Robertson, A. V. Kravtsov, J. Tinker, and A. R. Zentner. Collapse Barriers and Halo Abundance: Testing the Excursion Set Ansatz. *ApJ*, 696:636–652, May 2009. doi: 10.1088/0004-637X/696/1/636.

J. Robinson and J. E. Baker. Evolution of the cluster abundance in non-Gaussian models. *MNRAS*, 311:781–792, Feb. 2000. doi: 10.1046/j.1365-8711.2000.03109.x.

J. Robinson, E. Gawiser, and J. Silk. Constraining Primordial Non-Gaussianity with the Abundance of High-Redshift Clusters. *ApJ*, 532:1–16, Mar. 2000. doi: 10.1086/308549.

M. Roncarelli, L. Moscardini, S. Borgani, and K. Dolag. The Sunyaev-Zel'dovich effects from a cosmological hydrodynamical simulation: large-scale properties and correlation with the soft X-ray signal. *MNRAS*, 378:1259–1269, July 2007. doi: 10.1111/j.1365-2966.2007.11914.x.

J. e. a. Ruhl. The South Pole Telescope. In C. M. Bradford, P. A. R. Ade, J. E. Aguirre, J. J. Bock, M. Dragovan, L. Duband, L. Earle, J. Glenn, H. Matsuhara, B. J. Naylor, H. T. Nguyen, M. Yun, and J. Zmuidzinas, editors, *Society of Photo-Optical Instrumentation Engineers (SPIE) Conference Series*, volume 5498 of *Society of Photo-Optical Instrumentation Engineers (SPIE) Conference Series*, pages 11–29, Oct. 2004. doi: 10.1117/12.552473.

S. Sadeh and Y. Rephaeli. S-Z anisotropy and cluster counts: consistent selection of sigma8 and the temperature-mass relation. *New Astronomy*, 9:373–382, June 2004. doi: 10.1016/j.newast.2004.01.001.

S. Sadeh, Y. Rephaeli, and J. Silk. Cluster abundances and Sunyaev-Zel'dovich power spectra: effects of non-Gaussianity and early dark energy. *MNRAS*, 380: 637–645, Sept. 2007. doi: 10.1111/j.1365-2966.2007.12091.x.

D. S. Salopek and J. R. Bond. Nonlinear evolution of long-wavelength metric fluctuations in inflationary models. *Phys. Rev. D*, 42:3936–3962, Dec. 1990. doi: 10.1103/PhysRevD.42.3936.

A. G. Sánchez and S. Cole. The galaxy power spectrum: precision cosmology from large-scale structure? *MNRAS*, 385:830–840, Apr. 2008. doi: 10.1111/j. 1365-2966.2007.12787.x.

R. Scoccimarro, R. K. Sheth, L. Hui, and B. Jain. How Many Galaxies Fit in a Halo? Constraints on Galaxy Formation Efficiency from Spatial Clustering. *ApJ*, 546:20–34, Jan. 2001. doi: 10.1086/318261.

E. Sefusatti, C. Vale, K. Kadota, and J. Frieman. Primordial Non-Gaussianity and Dark Energy Constraints from Cluster Surveys. *ApJ*, 658:669–679, Apr. 2007. doi: 10.1086/511331.

N. Sehgal, H. Trac, K. Huffenberger, and P. Bode. Microwave Sky Simulations and Projections for Galaxy Cluster Detection with the Atacama Cosmology Telescope. *ApJ*, 664:149–161, July 2007. doi: 10.1086/518880.

N. Sehgal, P. Bode, S. Das, C. Hernandez-Monteagudo, K. Huffenberger, Y.-T. Lin, J. P. Ostriker, and H. Trac. Simulations of the Microwave Sky. *ArXiv e-prints*, Aug. 2009.

U. Seljak. Extracting Primordial Non-Gaussianity without Cosmic Variance. *Physical Review Letters*, 102(2):021302–+, Jan. 2009. doi: 10.1103/PhysRevLett.102. 021302.

U. Seljak, J. Burwell, and U.-L. Pen. Sunyaev-Zeldovich effect from hydrodynamical simulations: Maps and low order statistics. *Phys. Rev. D*, 63(6):063001–+, Mar. 2001. doi: 10.1103/PhysRevD.63.063001.

M. K. Sharp, D. P. Marrone, J. E. Carlstrom, T. Culverhouse, C. Greer, D. Hawkins, R. Hennessy, M. Joy, J. W. Lamb, E. M. Leitch, M. Loh, A. Miller, T. Mroczkowski, S. Muchovej, C. Pryke, and D. Woody. A Measurement of Arcminute Anisotropy in the Cosmic Microwave Background with the Sunyaev-Zel'dovich Array. *ArXiv e-prints*, Jan. 2009.

L. D. Shaw, O. Zahn, G. P. Holder, and O. Doré. Sharpening the Precision of the Sunyaev-Zel'dovich Power Spectrum. *ApJ*, 702:368–376, Sept. 2009. doi: 10.1088/0004-637X/702/1/368.

R. K. Sheth. An excursion set model for the distribution of dark matter and dark matter haloes. *MNRAS*, 300:1057–1070, Nov. 1998. doi: 10.1046/j.1365-8711. 1998.01976.x.

R. K. Sheth and G. Tormen. Large-scale bias and the peak background split. *MNRAS*, 308:119–126, Sept. 1999.

R. K. Sheth and G. Tormen. An excursion set model of hierarchical clustering: ellipsoidal collapse and the moving barrier. *MNRAS*, 329:61–75, Jan. 2002. doi: 10.1046/j.1365-8711.2002.04950.x.

R. K. Sheth, H. J. Mo, and G. Tormen. Ellipsoidal collapse and an improved model for the number and spatial distribution of dark matter haloes. *MNRAS*, 323:1–12, May 2001. doi: 10.1046/j.1365-8711.2001.04006.x.

A. Slosar, C. Hirata, U. Seljak, S. Ho, and N. Padmanabhan. Constraints on local primordial non-Gaussianity from large scale structure. *Journal of Cosmology and Astro-Particle Physics*, 8:31–+, Aug. 2008. doi: 10.1088/1475-7516/2008/08/031.

R. E. Smith, J. A. Peacock, A. Jenkins, S. D. M. White, C. S. Frenk, F. R. Pearce, P. A. Thomas, G. Efstathiou, and H. M. P. Couchman. Stable clustering, the halo model and non-linear cosmological power spectra. *MNRAS*, 341:1311–1332, June 2003. doi: 10.1046/j.1365-8711.2003.06503.x.

V. Springel. The cosmological simulation code GADGET-2. *MNRAS*, 364:1105–1134, Dec. 2005. doi: 10.1111/j.1365-2966.2005.09655.x.

V. Springel, M. White, and L. Hernquist. Hydrodynamic Simulations of the Sunyaev-Zeldovich Effect(s). *ApJ*, 549:681–687, Mar. 2001a. doi: 10.1086/319473.

V. Springel, N. Yoshida, and S. D. M. White. GADGET: a code for collisionless and gasdynamical cosmological si mulations. *New Astronomy*, 6:79–117, Apr. 2001b. doi: 10.1016/S1384-1076(01)00042-2.

M. Tegmark and M. Zaldarriaga. Separating the early universe from the late universe: Cosmological parameter estimation beyond the black box. *Phys. Rev. D*, 66(10):103508–+, Nov. 2002. doi: 10.1103/PhysRevD.66.103508.

A. Vale and J. P. Ostriker. Linking halo mass to galaxy luminosity. *MNRAS*, 353: 189–200, Sept. 2004. doi: 10.1111/j.1365-2966.2004.08059.x.

B. P. Venemans, H. J. A. Röttgering, G. K. Miley, W. J. M. van Breugel, C. de Breuck, J. D. Kurk, L. Pentericci, S. A. Stanford, R. A. Overzier, S. Croft, and H. Ford. Protoclusters associated with z ¿ 2 radio galaxies . I. Characteristics of high redshift protoclusters. *A&A*, 461:823–845, Jan. 2007. doi: 10.1051/0004-6361:20053941.

L. Verde, L. Wang, A. F. Heavens, and M. Kamionkowski. Large-scale structure, the cosmic microwave background and primordial non-Gaussianity. *MNRAS*, 313: 141–147, Mar. 2000. doi: 10.1046/j.1365-8711.2000.03191.x.

L. Verde, R. Jimenez, M. Kamionkowski, and S. Matarrese. Tests for primordial non-Gaussianity. *MNRAS*, 325:412–418, July 2001. doi: 10.1046/j.1365-8711. 2001.04459.x.

P. T. P. Viana and A. R. Liddle. The cluster abundance in flat and open cosmologies. *MNRAS*, 281:323–+, July 1996.

M. Viel, E. Branchini, K. Dolag, M. Grossi, S. Matarrese, and L. Moscardini. Primordial non-Gaussianities in the intergalactic medium. *MNRAS*, 393:774–782, Mar. 2009. doi: 10.1111/j.1365-2966.2008.14236.x.

J.-C. Waizmann and M. Bartelmann. Impact of early dark energy on the Planck SZ cluster sample. *A&A*, 493:859–870, Jan. 2009. doi: 10.1051/0004-6361:200809990.

L. Wang and P. J. Steinhardt. Cluster Abundance Constraints for Cosmological Models with a Time-varying, Spatially Inhomogeneous Energy Component with Negative Pressure. *ApJ*, 508:483–490, Dec. 1998. doi: 10.1086/306436.

M. S. Warren, K. Abazajian, D. E. Holz, and L. Teodoro. Precision Determination of the Mass Function of Dark Matter Halos. *ApJ*, 646:881–885, Aug. 2006. doi: 10.1086/504962.

N. N. Weinberg and M. Kamionkowski. Constraining dark energy from the abundance of weak gravitational lenses. *MNRAS*, 341:251–262, May 2003. doi: 10.1046/j.1365-8711.2003.06421.x.

S. Weinberg. *Gravitation and Cosmology: Principles and Applications of the General Theory of Relativity.* July 1972.

S. Weinberg. The cosmological constant problem. *Reviews of Modern Physics*, 61: 1–23, Jan. 1989. doi: 10.1103/RevModPhys.61.1.

J. Weller and R. A. Battye. Constraining dark energy using Sunyaev-Zel'dovich cluster surveys. *New Astronomy Review*, 47:775–779, Nov. 2003. doi: 10.1016/S1387-6473(03)00137-4.

C. Wetterich. Cosmology and the fate of dilatation symmetry. *Nuclear Physics B*, 302:668, Oct. 1988.

C. Wetterich. Quintessence - the Dark Energy in the Universe? *Space Science Reviews*, 100:195–206, Jan. 2002.

C. Wetterich. Phenomenological parameterization of quintessence. *Physics Letters B*, 594:17–22, July 2004. doi: 10.1016/j.physletb.2004.05.008.

M. White, L. Hernquist, and V. Springel. Simulating the Sunyaev-Zeldovich Effect(s): Including Radiative Cooling and Energy Injection by Galactic Winds. *ApJ*, 579:16–22, Nov. 2002. doi: 10.1086/342756.

S. D. M. White, G. Efstathiou, and C. S. Frenk. The amplitude of mass fluctuations in the universe. *MNRAS*, 262:1023–1028, June 1993.

E. L. Wright, S. S. Meyer, C. L. Bennett, N. W. Boggess, E. S. Cheng, M. G. Hauser, A. Kogut, C. Lineweaver, J. C. Mather, G. F. Smoot, R. Weiss, S. Gulkis, G. Hinshaw, M. Janssen, T. Kelsall, P. M. Lubin, S. H. Moseley, Jr., T. L. Murdock, R. A. Shafer, R. F. Silverberg, and D. T. Wilkinson. Interpretation of the cosmic microwave background radiation anisotropy detected by the COBE Differential Microwave Radiometer. *ApJL*, 396:L13–L18, Sept. 1992. doi: 10. 1086/186506.

J.-Q. Xia and M. Viel. Early dark energy at high redshifts: status and perspectives. *Journal of Cosmology and Astro-Particle Physics*, 4:2–+, Apr. 2009. doi: 10. 1088/1475-7516/2009/04/002.

A. P. S. Yadav, E. Komatsu, and B. D. Wandelt. Fast Estimator of Primordial Non-Gaussianity from Temperature and Polarization Anisotropies in the Cosmic Microwave Background. *ApJ*, 664:680–686, Aug. 2007. doi: 10.1086/519071.

J. Zavala, V. Springel, and M. Boylan-Kolchin. Extragalactic gamma-ray background radiation from dark matter annihilation. *ArXiv e-prints*, Aug. 2009.

P. Zhang, U.-L. Pen, and H. Trac. Precision era of the kinetic Sunyaev-Zel'dovich effect: simulations, analytical models and observations and the power to constrain reionization. *MNRAS*, 347:1224–1233, Feb. 2004. doi: 10.1111/j.1365-2966.2004. 07298.x.

I. Zlatev, L. Wang, and P. J. Steinhardt. Quintessence, Cosmic Coincidence, and the Cosmological Constant. *Physical Review Letters*, 82:896–899, Feb. 1999. doi: 10.1103/PhysRevLett.82.896.

Curriculum Vitae

Personal Information

First & Last Name: Margherita Grossi
Date of birth: 31st October, 1980
Place of birth: Atina, Italy
Citizenship: Italian/Swiss

Contact Information

Address :   Max-Planck-Institut für Astrophysik
Karl-Schwarzschild-Straße, 1
D-85748 Garching b. München - Germany
E-mail: margot@mpa-garching.mpg.de

Education

Sep 2006 to current   **PhD student in Astrophysics**
Max-Planck-Institut für Astrophysik
Topic: *"Cosmological simulations of non-standard dark energy models as a tool to predict their observational implications"*
Advisors: Prof. Dr. Simon White and Dr. Volker Springel

July 2006   **Laurea in Astronomia (B.Sc. + M.Sc. equivalent)**
University of Bologna(Italy)
Dissertation: *"Cosmic structure formation in models with primordial non-Gaussianity"*
Final grade: 110/110 with distinction
Advisors: Prof. Dr. Lauro Moscardini and Dr. Klaus Dolag

July 1999   **School-leaving Certificate in Humanities**
Liceo classico G.Carducci(Italy)
Final grade: 100/100

Research Interests

Numerical simulations of structure formation
Cosmological probes of Dark Energy
Non-Gaussian world models
Sunyaev Zeldovich effect